NASA-CR-195696

TECTONIC HISTORY OF THE TERRESTRIAL PLANETS

FINAL REPORT
TO THE
NATIONAL AERONAUTICS AND SPACE ADMINISTRATION

IN-91-CR
21 GT.

NASA GRANTS NAGW - 1937

OCTOBER 1989 - MARCH 1993

Sean C. Solomon, Principal Investigator

Department of Earth, Atmospheric, and Planetary Sciences
Massachusetts Institute of Technology
77 Massachusetts Avenue
Cambridge, MA 02139

This is a report of research conducted during the final period under NASA Grants NAGW-1937, "Tectonic History of the Terrestrial Planets". During this period the grant has supported the scientific contributions of a principal investigator, one Postdoctoral Associate (Suzanne E. Smrekar), and two Graduate Research Assistants (Patrick J. McGovern and Noriyuki Namiki) to the NASA Planetary Geology and Geophysics Program.

The simplest way to convey the full scope and principal results of research during the past year is through the papers and abstracts of oral presentations supported by this grant during the final period. Following is a list of 5 papers, one book chapter, and 14 abstracts and extended abstracts that have been published or submitted for publication. This list serves as a table of contents for the bulk of this report.

TABLE OF CONTENTS

(PAPERS AND ABSTRACTS SUPPORTED BY NASA GRANT NAGW-1937 DURING APRIL 1992 - MARCH 1993)

12. Simons, M., and S.C. Solomon, Geoid-to-topography ratios on Venus: A global perspective, in *1993 Spring Meeting, Eos Trans. Amer. Geophys. Un., 74*, Suppl., in press, 1993.

13. Smrekar, S.E. and S.C. Solomon, Gravitational spreading of high terrain in Ishtar Terra, Venus, *J. Geophys. Res., 97*, 16,121-16,148, 1992.

14. Smrekar, S.E., and S.C. Solomon, Constraints on crustal rheology and age of deformation from models of gravitational spreading in Ishtar Terra, Venus, in *Papers Presented to the International Colloquium on Venus*, Pasadena, Calif., pp. 114-116, Lunar and Planetary Institute, Houston, Tex., 1992.

15. Solomon, S.C., Tectonic processes on Venus: Comparisons and contrasts with the Earth, *Amer. Assoc. Petrol. Geol. 1992 Annual Convention Official Program*, Calgary, Canada, p. 124, 1992.

16. Solomon, S.C., The tectonics of Venus: An overview, in *Papers Presented to the International Colloquium on Venus*, Pasadena, Calif., pp. 118-119, Lunar and Planetary Institute, Houston, Tex., 1992.

17. Solomon, S.C., The tectonic and volcanic evolution of Venus: Catastrophic or gradual?, in *1992 Fall Meeting, Eos Trans. Amer. Geophys. Un., 73*, Suppl., 328-329, 1992.

18. Solomon, S.C., Venus: Keeping that youthful look, *Nature, 361*, 114-115, 1993.

19. Solomon, S.C., A tectonic resurfacing model for Venus, in *Lunar and Planetary Science XXIV*, pp. 1331-1332, Lunar and Planetary Institute, Houston, Tex., 1993.

20. Solomon, S.C., The resurfacing controversy for Venus: An overview and a mechanistic perspective, in *1993 Spring Meeting, Eos Trans. Amer. Geophys. Un., 74*, in press, 1993.

21. Squyres, S.W., D.G. Jankowski, M. Simons, S.C. Solomon, B.H. Hager, and G.E. McGill, Plains tectonism on Venus: The deformation belts of Lavinia Planitia, *J. Geophys. Res., 97*, 13,579-13,599, 1992.

FLEXURAL ANALYSIS OF UPLIFTED RIFT FLANKS ON VENUS;

Susan A. Evans, Mark Simons, and Sean C. Solomon, Department of Earth, Atmospheric, and Planetary Sciences, Massachusetts Institute of Technology, Cambridge, MA 02139.

Introduction. Knowledge of the thermal structure of a planet is vital to a thorough understanding of its general scheme of tectonics. Since no direct measurements of heat flow or thermal gradient are available for Venus, most estimates have been derived from theoretical considerations or by analogy with the Earth [1]. The flexural response of the lithosphere to applied loads is sensitive to regional thermal structure. Under the assumption that the yield strength as a function of depth can be specified, the temperature gradient can be inferred from the effective elastic plate thickness [2]. Previous estimates of the effective elastic plate thickness on Venus range from 11-18 km for the foredeep north of Uorsar Rupes [3] to 30-60 km for the annular troughs around several coronae [4,5]. Thermal gradients inferred for these regions are 14-23 K km^{-1} and 4-9 K km^{-1}, respectively [3,4]. In this study, we apply the same techniques to investigate the uplifted flanks of an extensional rift. Hypotheses for the origin of uplifted rift flanks on Earth include lateral transport of heat from the center of the rift, vertical transport of heat by small-scale convection, differential thinning of the lithosphere, dynamical uplift, and isostatic response to mechanical unloading of the lithosphere [6]. The last hypothesis is considered the dominant contributor to terrestrial rift flanks lacking evidence for volcanic activity, particularly for rift structures which are no longer active [6]. In this study, we model the uplifted flanks of a Venusian rift as the flexural response to a vertical end load.

Tectonic Environment. We examine a linear rift system centered at 33°S, 92°E, in an area to the east of Aino Planitia. The feature appears as a linear ridge in Pioneer Venus altimetry and thus has been named Juno Dorsum. However, the increased resolution of Magellan images and topography has established that this feature is actually a linear rift with pronounced flanking highs. The rift is 100 km wide and 450 km long; it has a central depression 1-2 km deep and flanks elevated by as much as 1 km (Figures 1 and 2). The rift connects a 1.5-km-high volcano on its western edge to two coronae, Tai Shan and Gefjun [7], to the east. Despite the presence of the volcano and coronae, both the center of the rift and the adjacent flanks appear to be free of volcanic flows. Juno Dorsum is at the end of a nearly continuous chain of coronae, rifts, and linear fractures which extends eastward and appears to terminate at the northwestern edge of Artemis Corona. The rift appears in Magellan images as numerous ENE-trending lineaments, which we interpret to be normal faults. To the north and south are smooth, radar-dark plains which stand very close to mean planetary elevation.
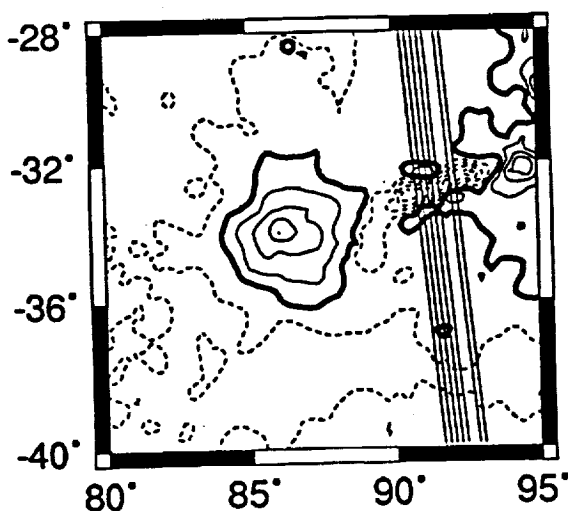
Figure 1. Topographic contour map of the Juno Dorsum region. Thin solid lines denote positive elevation contours, thick solid lines zero elevation, and dashed lines negative elevations. The contour interval is 0.3 km, and the datum is mean planetary radius, 6051.9 km. The rift is located in the center right of the figure, with an unnamed volcano to its west. The north-south-trending lines indicate the tracks of orbits 965-968 and 971-972 (numbers increasing eastward). The orbit tracks make an angle of approximately 75° with the strike of the rift.
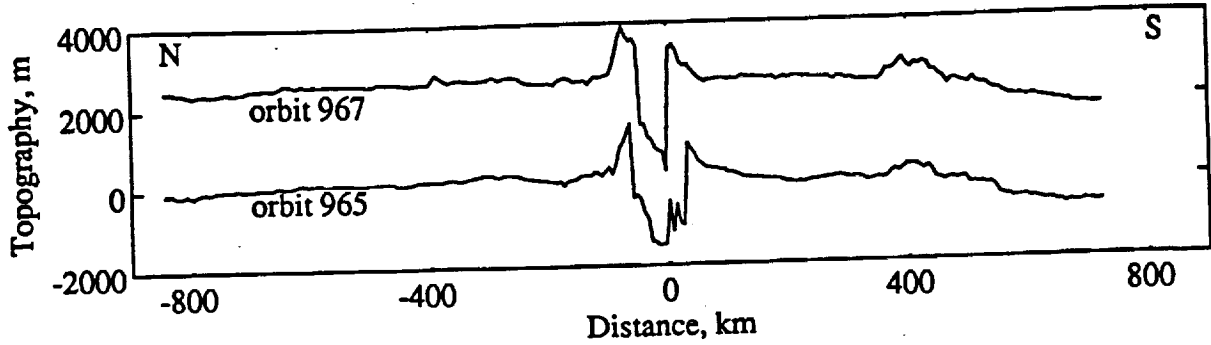
Figure 2. Example orbit profiles over Juno Dorsum; see Figure 1 for location. The rift flanks are elevated 800 to 1000 m above the surrounding plains, and interference from other regional topographic features is minimal. Orbit 967 has been offset vertically by 2500 m for clarity.

We use Magellan altimetric profiles from orbits 965-968 and 970-972 (Figures 1 and 2). While topographic profiles perpendicular to the strike of the rift are preferable, the orbit tracks cross the rift at an angle of approximately 75°, and we can easily make the geometrical correction for this small difference. Profiles from single orbits avoid errors introduced by inter-orbit offsets. As is evident in Figure 2, the topography of the surrounding plains region is rather smooth, and the uplift of the flanks is quite distinct and easy to discern from other regional topography.

Model. We model the uplift of the rift flanks as the flexural response of a thin elastic plate overlying a fluid substratum [8]. We assume that the flexure is of the form

$$w = \exp\left(\tfrac{-x}{\alpha}\right)\left[A\cos\left(\tfrac{-x}{\alpha}\right) + B\sin\left(\tfrac{-x}{\alpha}\right)\right] \tag{1}$$

where w is the vertical deflection of the plate from the regional datum, x is the distance along the profile, and α is the flexural parameter given by

$$\alpha = \left[\frac{E\,T_e^3}{3\,\rho_m\,g\,(1 - v^2)}\right]^{\frac{1}{4}} \tag{2}$$

where E is Young's Modulus (60 GPa), T_e is the elastic plate thickness, ρ_m is the mantle density (3300 kg m^{-3}), g is the gravitational acceleration (8.87 m s$^{-2}$), and v is Poisson's ratio (0.25). The objective is to find the three parameters A, B, and α such that the root mean square (rms) misfit between the observed and calculated topographic profiles is a minimum. Since w depends non-linearly on α, we first fix the value of α, then calculate the best-fitting values of A and B. The flexural parameter is then varied over a range corresponding to an elastic plate thickness of 1 to 50 km, and the procedure is repeated. From the parameters providing the best overall fit we calculate the plate curvature at the first zero-crossing. This curvature and the apparent elastic plate thickness are then used to estimate the thermal gradient from the curves in [3].

We model only the rift flanks, so we remove the central rift depression from the profiles and model each rift flank separately. The location of highest topography in the half profile defines the origin of the horizontal axis. We fit topography up to 350 km from the rift, to avoid modelling the small rise 400 km to the south of the rift (Figures 1 and 2). We also remove the mean elevation and the best-fit linear trend from our profiles before fitting to prevent bias from long-wavelength regional topography.

Results. Of the fourteen profiles obtained in orbits 965-968 and 971-972, we analyze ten which have flanks rising 600-1200 m above the regional mean elevation. Four of these profiles are well fit by elastic plate thicknesses of 8-16 km. For each of these profiles, there is a narrow range of plate thicknesses for which the rms error is small, so the results are well constrained (Figure 3). Three of these profiles produce best-fitting plate thicknesses of 8-9 km, suggesting that the true effective elastic plate thickness may be near the low end of this range. The remaining profiles generally contain more small-scale topographic variation of ± 100 m in amplitude and are equally well fit by a range of plate thicknesses. The fits for all profiles, however, are consistent with elastic plate thicknesses of 8-20 km.
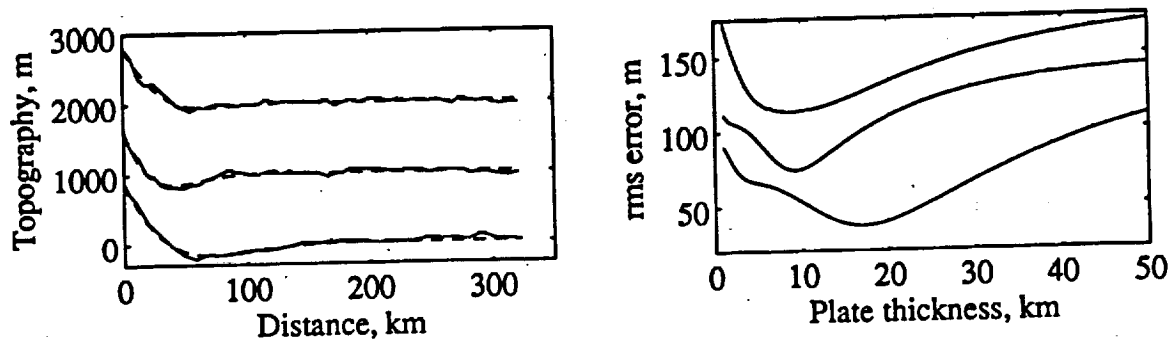

Figure 3. Left: topographic profiles (solid) and best-fit flexural profiles (dashed) for three half profiles; top to bottom are orbit 967, southern flank; orbit 968, southern flank; orbit 968, northern flank. Right: the rms error as a function of elastic plate thickness for the same profiles. Note that the top two profiles are best fit only over a small range of elastic plate thicknesses, whereas the bottom profile can be fit by a broader range of plate thicknesses. All profiles are consistent with elastic plate thicknesses in the range 8-20 km. For clarity, the upper two profiles on the left have been vertically offset by 1000 m and 2000 m, respectively, and the corresponding error curves by 30 and 60 m.

These effective plate thicknesses and the calculated curvatures imply thermal gradients of 15-30 K km^{-1} if the base of the mechanical lithosphere is limited by the ductile strength of olivine [3]. Because the values of elastic lithosphere thickness derived here are comparable to or less than the estimated crustal thickness beneath plains regions on Venus [9,10], the base of the mechanical lithosphere may lie within the crust and be limited by the flow law for lower crustal material. In such a situation, the thermal gradients would be less than the figures given above.

The effective elastic plate thicknesses we derive for the Juno rift structure (8-20 km) are comparable to those obtained for the North Polar Plains at Uorsar Rupes (11-18 km) and both regions involve flexure of the lithosphere beneath plains at elevations near the planetary mean. A general relationship between regional elevation and elastic plate thickness might be expected if regional elevation were controlled by lithospheric thermal structure [11], as in the Earth's oceanic regions. Further analysis of flexure is warranted to determine if such a relationship holds for Venus.

References: [1] S. C. Solomon and J. W. Head, *JGR, 87,* 9236, 1982; [2] M. K. McNutt, *JGR, 89,* 11,180, 1991; [3] S. C. Solomon and J. W. Head, *Geophys. Res. Lett., 17,* 1393, 1991; [4] D. T. Sandwell and G. Schubert, *JGR,* in press, 1992; [5] D. T. Sandwell and G. Schubert, *Science,* submitted, 1992; [6] J. K. Weissel and G. D. Karner, *JGR, 94,* 13,919, 1989; [7] E. R. Stofan et al., *JGR,* in press, 1992; [8] D. L. Turcotte and G. Schubert, *Geodynamics.,* pp. 125-131, 1982; [9] R. E. Grimm and S. C. Solomon, *JGR, 93,* 11,911, 1988; [10] M. T. Zuber and E.M. Parmentier, *Icarus, 85,* 290, 1990; [11] P. Morgan and R. J. Phillips, *JGR, 88,* 8305, 1983.

Patterns of Deformation and Volcanic Flows Associated with Lithospheric Loading by Large Volcanoes on Venus

Patrick J. McGovern and Sean C. Solomon (Dept. of Earth, Atmospheric, and Planetary Sciences, M.I.T., Cambridge, MA 02139)

Magellan radar imaging and topography data are now available for a number of volcanoes on Venus greater than 100 km in radius. These data can be examined to reveal evidence of the flexural response of the lithosphere to the volcanic load. On Venus, erosion and sediment deposition are negligible, so tectonic evidence of deformation around large volcanoes should be evident except where buried by very young flows. Radar images reveal that most tectonic features and flow units on the flanks of these volcanoes have predominantly radial orientations. However, both Tepev Mons in Bell Regio and Sapas Mons in Atla Regio exhibit circumferential graben on their flanks. In addition, images reveal several flow units with an annular character around the north and west flanks of Tepev Mons. This pattern most likely results from ponding of flows in an annular flexural moat. Maat Mons in Atla Regio and Sif Mons in Eistla Regio are examples of volcanoes that lack circumferential graben and annular flows; discernible flow units and fractures on these constructs appear to be predominantly radial. Altimetry data can also provide evidence of flexural response. Tepev Mons is partially encircled by depressions that may be sections of a flexural moat that has not been completely filled. The locations of these depressions generally coincide with the annular flows described above. There is weaker evidence for such depressions around Maat Mons as well. The lack of circumferential tectonic features around most volcanoes on Venus might be explained by gradual moat filling and coverage by radial flows. The depressions around Tepev (and possibly Maat) may indicate that this process is currently continuing. We use analytic models of plate flexure in an axisymmetric geometry to constrain the elastic plate thickness supporting Tepev Mons. If we consider the outer radius of the ponded flows to be the edge of a moat, we find that models with elastic plate thickness of 10-20 km fit best. Finite element models of a volcanic load detached from the underlying lithosphere predict overthrusting and radial normal faulting at the volcano's edge. Such a mechanism for the formation of radial rift zones on Venus volcanoes would make such features analogous to structures on the flanks of volcanoes on Earth.

ESTIMATES OF ELASTIC PLATE THICKNESSES BENEATH LARGE VOLCANOES ON VENUS

Patrick J. McGovern and Sean C. Solomon, Dept. of Earth, Atmospheric, and Planetary Sciences, Massachusetts Institute of Technology, Cambridge, MA 02139.

Introduction. Magellan radar imaging and topography data are now available for a number of volcanoes on Venus greater than 100 km in radius. These data can be examined to reveal evidence of the flexural response of the lithosphere to the volcanic load. On Earth, flexure beneath large hotspot volcanoes results in an annular topographic moat which is partially to completely filled in by sedimentation and mass wasting from the volcano's flanks (see [1, 2]). On Venus, erosion and sediment deposition are considered to be negligible at the resolution of Magellan images [3]. Thus, it may be possible to observe evidence of flexure by the ponding of recent volcanic flows in the moat. We also might expect to find topographic signals from unfilled moats surrounding large volcanoes on Venus, although these signals may be partially obscured by regional topography. Also, in the absence of sedimentation, tectonic evidence of deformation around large volcanoes should be evident except where buried by very young flows.

We have found two examples to date of volcanoes with strong evidence for moat formation and infilling by flows. Radar images of Tepev Mons, a volcano about 125 km in radius near the southwestern corner of Bell Regio, reveal a bright flow unit draped around the northern and western flanks of the volcano. An unnamed volcano at 10°N, 275°E (southwest of Beta Regio) exhibits both circumferential flanking flows and lateral spreading of originally radially trending flows The distal edges of these flows terminate about 240-260 km from the summit. The edges of these flows form an arc of greater than 120° to the north and west of the volcano.

Method. We use analytic solutions in axisymmetric geometry [4] for deflections and stresses resulting from loading of a plate overlying an inviscid fluid. Solutions for a set of disk loads are superimposed to obtain a solution for a conical volcano. The deflection of the lithosphere produces an annular depression or moat, the extent of which can be estimated by measuring the distance from the volcano's edge to the first zero crossing or to the peak of the flexural arch. Magellan altimetry data records (ARCDRs) from data cycle 1 are processed using the GMT mapping and graphics software [5] to produce topographic contour maps of the volcanoes. We then take topographic profiles that cut across the annular and ponded flows seen on the radar images. By comparing the locations of these flows to the predicted moat locations from a range of models, we estimate the elastic plate thickness which best fits the observations, together with the uncertainty in that estimate.

Results. Figure 1 shows two cross sections through Tepev Mons. The areas covered by annular flows are marked with arrows. Figure 2 shows deflections calculated analytically for a conical load of height 10 km and radius 150 km for elastic plate thicknesses T_e of 10 km and 20 km. Arrows denote the predicted approximate extent of a moat due to loading in each model. Note that for the analytic solutions, increasing the elastic plate thickness increases both the maximum depth and the radial extent of the predicted moat. The model in Figure 2a matches the northwestern cross section in Figure 1a. The area of flows in Figure 1b is somewhat larger in radial extent and is better matched by the predicted moat in Figure 2b. Figure 3 shows a cross section through the volcano at 10°N, 275°E. Figure 4 shows calculated deflections for a conical load of height 5 km and radius 250 km, for elastic plate thicknesses of 10 and 20 km. The extent of annular flows is better matched by the smaller thickness.

Discussion. These two volcanoes are apparently atypical of large volcanoes on Venus in that both topography and flow morphology suggest the existence of a flexural moat. On other large shield volcanoes such as Sif Mons and Sapas Mons, topographic evidence of a moat is lacking, and no flows that have convincingly ponded in annular moats can be identified. Large volcanoes that form on or near large rift zones (such as Maat Mons, Ozza Mons, and others) also lack

topographic evidence of a flexural moat. It should be noted that as altimetry data and stereo imaging from later cycles become available, coverage will improve, gaps will be filled in, and it may be possible to identify topographic signatures of moats which have eluded our search to date.

In contrast to Tepev Mons and the construct at 10°N, 275°E, most large volcanoes on Venus are generally characterized by fractures and flow units that have dominantly radial orientations. Given this observation and the assumption that lithospheric flexure has occurred, then the moats must be filled or covered. Mass wasting, through large landslides or slumps such as those discovered off the Hawaiian Islands [2], is one possibility. Moat-filling flows may be covered by later radial flows, a process that may have been repeated many times during volcano growth.

Conclusions. Under the assumption that circumferentially ponded flows surrounding volcanoes have at least partially filled a flexural moat, we can compare the position and extent of the moat to predictions from analytic flexure models. For Tepev Mons, models that fit best have elastic plate thicknesses in the range of 10 to 20 km. For the volcano at 10°N, 275°E, the best fit is obtained for a thickness of about 10 km. These values of elastic plate thickness can be converted to estimates of mechanical plate thickness and thermal gradient [6]. Using parameters appropriate for Venus [7] we obtain thermal gradients values of about 12-25 K/km for Tepev Mons and about 25 K/km for 10°N, 275°E. These gradients are in the range expected if Venus loses most of its internal heat by conduction through a globally continuous, if laterally heterogeneous, lithospheric shell [7].

References. [1] H. W. Menard, *Bull. Amer. Assoc. Petrol. Geol., 40,* 2195, 1956; [2] R.B. Moore et al., *J. Geophys. Res, 94,* 17465, 1989; [3] R. E. Arvidson et al. *Science, 252,* 270, 1991; [4] J. F. Brotchie, *Mod. Geol., 3,* 15, 1971; [5] P. Wessel and W. H. F. Smith, *Eos Trans. AGU, 72,* 441, 1991; [6] M. K. McNutt, *J. Geophys. Res., 89,* 11,180, 1984; [7] S. C. Solomon and J. W. Head, *Geophys. Res. Lett., 17,* 1393, 1990.
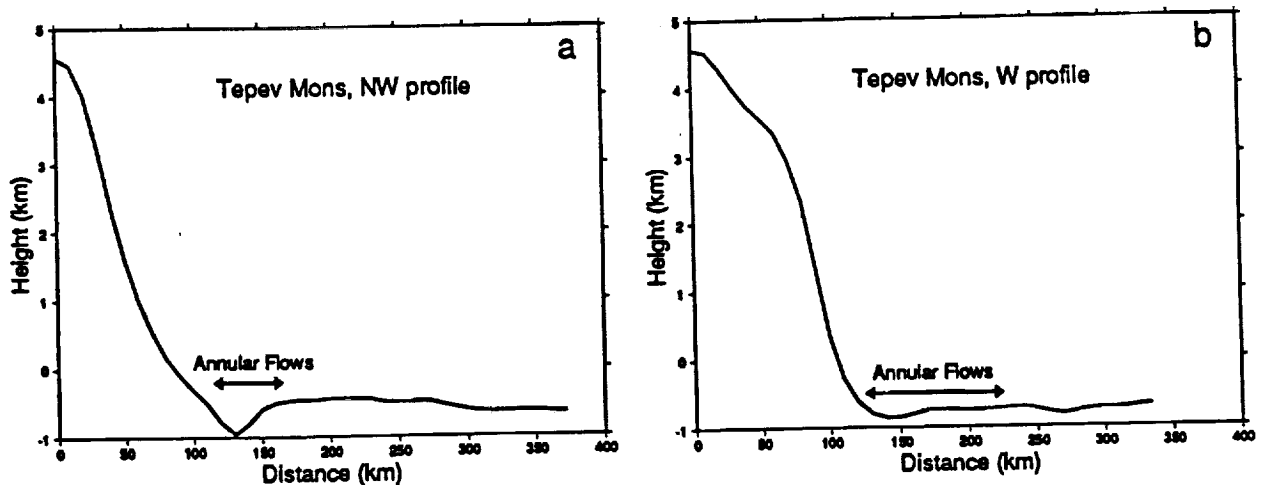
Figure 1. Topographic cross sections through Tepev Mons. (a) Northwestern profile; (b) western profile.
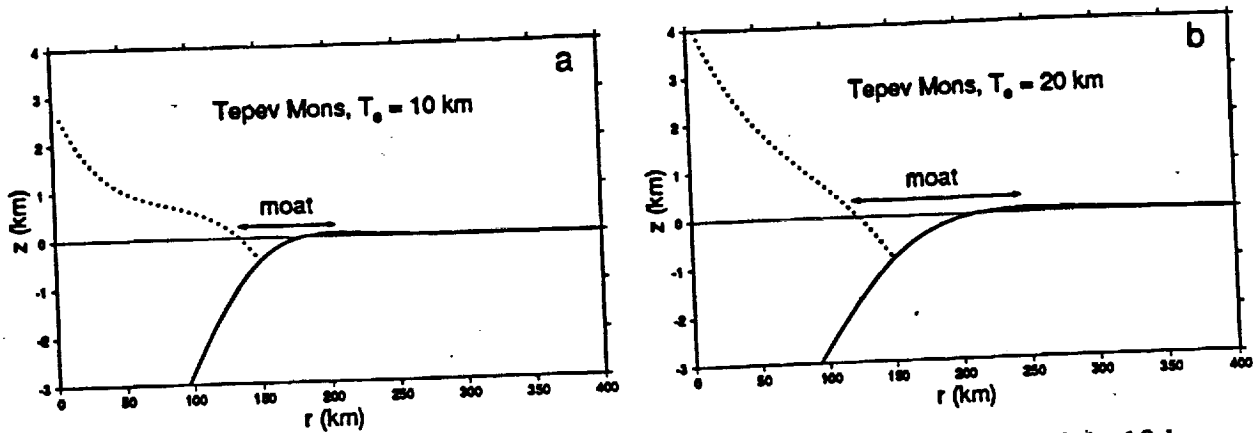
Figure 2. Analytic solutions for lithospheric deflection by a conical load of height 10 km and radius 150 km. The solid line is the deflection solution, while the dotted line includes the topography from the load. (a) $T_e = 10$ km; (b) $T_e = 20$ km.
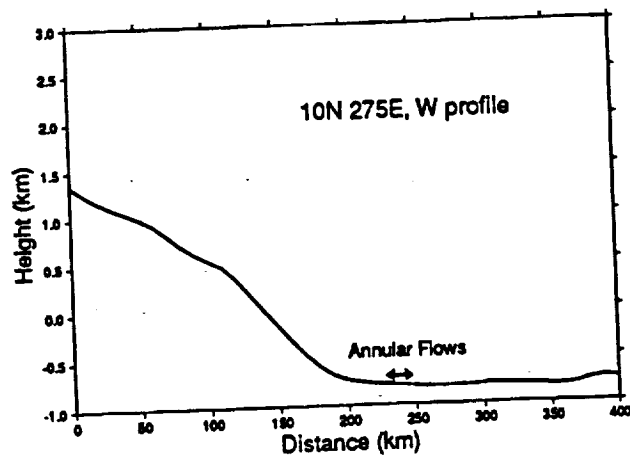
Figure 3. Topographic cross section through the volcano at 10°N, 275°E, extending westward.
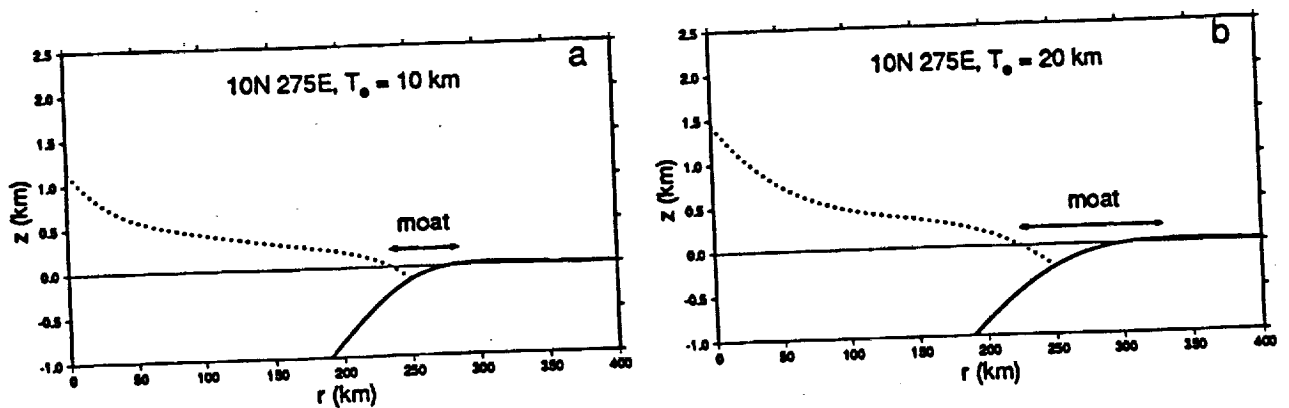
Figure 4. Analytic solutions for lithospheric deflection by a conical load of height 5 km and radius 250 km. Solid line is deflection solution, dotted line includes the topography from the load. (a) $T_e = 10$ km; (b) $T_e = 20$ km.

ASPECTS OF MODELLING THE TECTONICS OF LARGE VOLCANOES ON THE TERRESTRIAL PLANETS;

Patrick J. McGovern, Dept. of Earth, Atmospheric, and Planetary Sciences, Massachusetts Institute of Technology, Cambridge, MA 02139, and Sean C. Solomon, Dept. of Terrestrial Magnetism, Carnegie Institution of Washington, Washington, D. C. 20015.

Introduction. Analytic solutions for the response of planetary lithospheres to volcanic loads have been used to model faulting and infer elastic plate thicknesses [e.g., 1-4]. Predictions of the distribution of faulting around volcanic loads, based on the application of Anderson's criteria for faulting [5] to the results of the models, do not agree well with observations [6,7]. Such models do not give the stress state in the load itself, but only suggest a state of horizontal compressive stress there. Further, these models have considered only the effect of an instantaneously emplaced load. They do not address the time evolution of stresses, nor do they consider the effect of a load which grows. A finite element approach allows us to assign elements to the load itself, and thus permits calculation of the stress state and stress history within the edifice. The effects of episodic load growth can also be treated. When these effects are included, models give much better agreement with observations.

Method. We use the finite element code TECTON [8,9] to construct axisymmetric models of volcanoes resting on an elastic lithospheric plate overlying a viscoelastic asthenosphere. We have implemented time-dependent material properties in order to simulate incremental volcano growth. The viscoelastic layer was taken to extend to a sufficient depth so that a rigid lower boundary has no significant influence on the results. The code first calculates elastic deformations and stresses and then determines the time-dependent viscous deformations and stresses. Time in the model scales as the Maxwell time τ_m in the asthenosphere.

Results. We consider a volcano 25 km in height and 200 km in radius on an elastic lithosphere 40 km thick (parameters approximately appropriate to Ascraeus Mons). The volcano consists of three load increments applied at intervals of $1000 \tau_m$. Contours of maximum deviatoric stress in the fully-grown edifice at the conclusion of flexure ($t = 3000 \tau_m$) are shown in Figure 1. Note that the maximum stress occurs in the lower mid-section of the edifice. We adopt the convention that tension is positive.

Discussion. Simple models of plate flexure due to an instantaneous load predict a state of horizontal compressive stress in the plate beneath the load [1,4] with an increasing magnitude of compression from the middle of the plate upward, and a maximum at the surface. Models with a succession of loads emplaced from the bottom up display a different distribution of stress. The maximum horizontal stress occurs in the lowest (first) load increment and decreases upward with each later load increment. Thus, thrust faults (predicted by simpler models) associated with such stresses would be expected to occur only early in the evolution (or not at all) and would be covered by later units which remain unfaulted. Such a distribution of stresses could also affect the locations and dimensions of magma chambers. A zone of horizontal compression within the edifice would inhibit ascending magma from reaching the summit and thus might cause magma to pool beneath it. Since magma will propagate perpendicular to the direction of least compressive stress, radial propagation of magma in sheet dikes or sills might also occur. The effects of adding fault slip along a basal detachment between edifice and lithosphere (as proposed in models of the flank tectonics of Hawaii [10]) was shown to achieve an even greater reduction in horizontal compressive stress in the edifice [11]. Such a structure may control the growth and evolution of tectonic features surrounding volcanoes on both Mars and Earth [11].

Stresses calculated from planetary loading models have been used, in conjunction with Anderson's criteria for faulting [5], to predict types of faulting that should be observed [1,2,4]. Typically, a zone is found surrounding the load with both the least compressive stress σ_1 and the most compressive stress σ_3 horizontal (assuming that near the surface, σ_{zz} is small and compressive). Application of Anderson's criteria yields a prediction of strike-slip faulting. Such a region surrounding a large load has not heretofore been observed [6,7]. Given the complete stress field in an element in this region from the TECTON solutions, we can plot Mohr diagrams, as in Figure 2, and compare them with a Mohr-Coulomb failure envelope. The Mohr circles grow in

size as flexure proceeds, until the failure envelope is exceeded at about 70 τ_m after first loading. The largest circle shows stresses at the conclusion of flexure. This stress state corresponds to that given by analytic plate models (in which flexure occurs instantaneously). Simply interpreting this final stress state is seen to be misleading for two reasons. First, σ_1 (= σ_{rr}) is much larger than the tensional strength of any rock. Use of a shear failure criterion (such as Mohr-Coulomb) for such a stress state is improper [7]. Use of a tensile failure criterion will predict the formation of tension joints which may be precursors of graben [7]. Second, consideration of the stress history indicates that at the time of first failure, the shear failure criterion is satisfied, with principal stress directions that predict circumferential normal faulting. Formation of these faults would relieve stresses and provide planes of low resistance along which further faulting with a similar orientation would be expected to develop. Thus, the "prediction" of a zone of strike-slip faulting surrounding a lithospheric load, based on simple instantaneously-loaded plate flexure models, is in error.

Conclusions. Simple interpretations of the results from instantaneous load models lead to predictions of lithospheric stress fields that do not match observations. Consideration of the history of stresses in the lithosphere and within the load itself helps to resolve these discrepancies.

References. [1] R.P. Comer *et al.*, *Rev. Geophys.*, *23*, 61, 1985; [2] H.J. Melosh, *Proc. LPS 9*, 3513, 1978; [3] P.J. McGovern and S.C. Solomon, *Inter. Colloq. on Venus*, LPI , p. 68, 1992; [4] R.P. Comer, *GJRAS*, *72*, 101, 1983; [5] E.M. Anderson, *The Dynamics of Faulting*, 1951; [6] M.P. Golombek, *JGR*, *90*, 3065, 1985; [7] R.A. Schultz and M.T. Zuber, *LPS*, *23*, 1247, 1992; [8] H.J. Melosh and A. Rafesky, *GJRAS*, *60*, 333, 1980; [9] H.J. Melosh and A. Rafesky, *JGR*, *88*, 515, 1983; [10] P.W. Lipman *et al.*, *USGS Prof. Pap. 1276*, 45 pp., 1985; [11] P.J. McGovern and S.C. Solomon, *LPS*, *23*, 885, 1992; [12] J. Handin, in *Handbook of Physical Constants*, ed. S.P. Clark, 223, 1966;
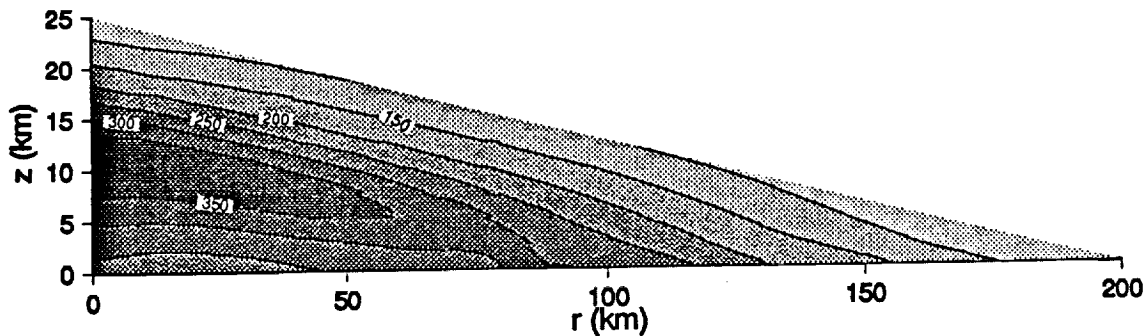
Figure 1. Contours of maximum deviatoric stress (MPa) in the volcanic edifice described above.
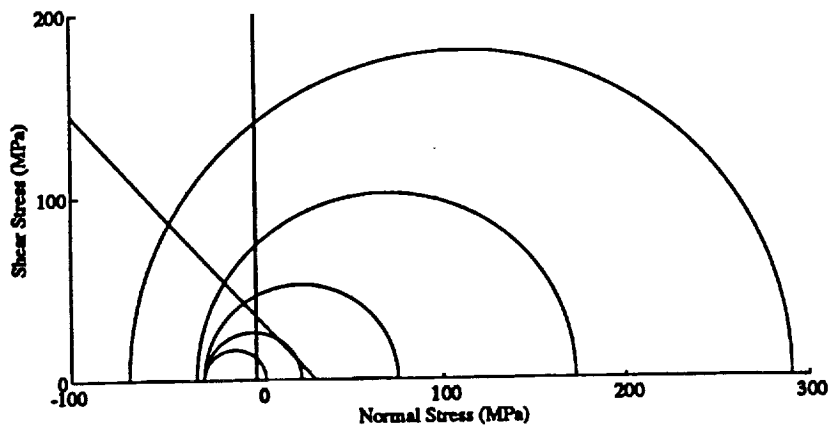
Figure 2. Mohr diagram for element at the top of the lithosphere (stresses calculated at element center: r = 265 km, z = -2.5 km). Diagonal line is Mohr-Coulomb failure envelope for basalt [12] with angle of internal friction ϕ = 49° and cohesion c = 38 MPa. In order of increasing radius, the circles represent stress state at t = 30, 70, 1000, 2000, and 3000 τ_m . When failure envelope is first exceeded (t = 70 τ_m), σ_1 = σ_{rr} and σ_3 =σ_{zz}. At final time shown, σ_1 = σ_{rr} and σ_3 = $\sigma_{\theta\theta}$.

STATE OF STRESS, FAULTING, AND ERUPTION CHARACTERISTICS OF LARGE VOLCANOES ON MARS

Patrick J. McGovern

Department of Earth, Atmospheric, and Planetary Sciences,

Massachusetts Institute of Technology, Cambridge

Sean C. Solomon

Department of Terrestrial Magnetism,

Carnegie Institution of Washington,

Washington, D.C.

ABSTRACT

The formation of a large volcano loads the underlying lithospheric plate and can lead to lithospheric flexure and faulting. In turn, lithospheric stresses affect the stress field beneath and within the volcanic edifice and can influence magma transport. Modeling the interaction of these processes is crucial to an understanding of the history of eruption characteristics and tectonic deformation of large volcanoes. We develop models of time-dependent stress and deformation for the Tharsis volcanoes on Mars. A finite element code is used that simulates viscoelastic flow in the mantle and elastic plate flexural behavior. We calculate stresses and displacements due to a volcano-shaped load emplaced on an elastic plate. Models variously incorporate growth of the volcanic load with time and a detachment between volcano and lithosphere. The models illustrate the manner in which time-dependent stresses induced by lithospheric plate flexure beneath the volcanic load may affect eruption histories, and the derived stress fields can be related to tectonic features on and surrounding Martian volcanoes. After an initial load increment is emplaced, flexurally-induced stresses grow with time and the principal stress directions in the volcano rotate as flexure proceeds. Magma is expected to propagate perpendicular to the least compressive stress axis. As a result of flexure, this axis rotates from a horizontal orientation to a nearly vertical one; thus magma propagation paths will tend to rotate from vertical to horizontal orientations. We suggest that at the later stages of flexure, this effect would tend to favor eruption sites on to the flanks of the volcano rather than the summit. Such a scenario is consistent with the photogeologically determined evolution of the Tharsis Montes. As a result of flexure there are three regions where stresses become sufficiently large to cause failure by faulting (according to the Mohr-Coulomb criterion): at the surface of the plate just outward of the volcano, and at the base of the elastic lithosphere beneath the center of the volcano, and on the upper flanks of the first volcanic load increment. Normal faulting is the dominant mode of failure predicted for the first region, consistent with circumferential graben observed around the Tharsis Montes and with the scarp at the base of Olympus Mons, interpreted as a large-offset, listric normal fault. Normal faulting, mostly radially oriented, is predicted for the second region. Under the premise that failure

in the sub-volcano zone may be strongly influenced by pre-existing weak zones or regional stresses, this feature may have a surface expression in the rifting and the bilateral symmetry of the Tharsis Montes. Failure in the third region is predicted to consist of thrust faulting, oriented mostly circumferentially on the upper flanks with an annulus of radially oriented thrust faulting starting about midway downslope. Concentric terraces, interpreted by some workers as thrust faults, on the upper flanks of Olympus Mons may correspond to the predicted circumferential thrust features. For volcanoes detached from the plate, predicted failure in the edifice takes the form of radial normal faulting at the base. Addition of an extensional stress due to regional topography yields a pattern of predicted faulting which closely matches that observed on the Tharsis Montes. This stress state is also consistent with an interpretation of the aureole deposits of Olympus Mons as the result of gravity sliding along a basal detachment.

Our models also suggest explanations for the lack of strike-slip features, predicted by simple flexural models, around the Tharsis volcanoes. For a given load increment, the first mode of near-surface failure for most of the area immediately outward of the load is circumferential normal faulting and graben formation. As the volcano grows and the flexural response to the increasing load proceeds, the predicted failure mode in a portion of this annular region surrounding the volcano changes to strike-slip faulting. Because normal faulting has been predicted to have taken place earlier, however, it is likely that release of later stresses will occur by reactivation and growth of these normal faults and graben rather than by the formation of strike-slip faults.

INTRODUCTION

The major Tharsis volcanoes of Mars (Olympus Mons and the three Tharsis Montes: Arsia Mons, Pavonis Mons, and Ascraeus Mons) are among the largest known volcanic structures in the solar system. An understanding of the formation and evolution of these structures can provide important constraints on the processes that built and maintained the Tharsis Rise. In addition, the Tharsis volcanoes may be analogues to large hot-spot volcanoes on Earth, such as those of Hawaii. For instance, Kilauea and Olympus Mons have very similar ratios of volcano height to diameter and of basal scarp height to volcano height [*Borgia et al.*, 1990]. Thus studies of the evolution of large Martian volcanoes may yield insight into terrestrial volcanic processes as well. In this paper we utilize finite element models to evaluate the evolution in internal stress and deformation within and surrounding the Tharsis volcanoes, and we discuss how the time-dependent stress field may be relatable to the eruption characteristics of the volcanoes and to the formation of associated tectonic features.

To date the investigation of the evolution of stresses in large volcanoes has taken two paths: models of edifice stresses alone (usually finite element models with rigid bottom boundary conditions), and investigations of flexural stresses in the lithospheric plate supporting the volcano. As examples of the first category of study, *Chevallier and Verwoerd* [1988] used an axisymmetric planar finite element code to investigate the effect of magma chamber and external pressures on stress and eruption histories of hot spot volcanoes, *Dieterich* [1988] modeled stress in volcano rift zones by means of a two-dimensional triangular grid of elements, and *Ryan* [1988] employed a horizontal planar finite element model of the flank of Kilauea to determine displacements and stresses due to dike emplacement. In an example of the second class of study, *Thurber and Gripp* [1988] applied a flexural model to constrain the tectonics of volcano flank motions. *ten Brink and Brocher* [1987] proposed a link between flexural stresses in the lithosphere and eruption history; in their scenario the orientation of flexural stresses beneath a given point on the volcanic chain changes with time as the volcanic load is emplaced and then eroded. Given that magma seeks to propagate along paths perpendicular to the direction of least compressive stress, magma ascent can

be blocked when both principal horizontal stress deviators are compressional. Thus eruption history depends on location along the volcanic chain or on time since volcano formation.

Recent studies have also been carried out on edifice stresses of large Martian volcanoes. *Thomas et al.* [1990] investigated the tectonics of the flanks of Martian volcanoes by means of an incompressible finite-element model. Volcano self-loading and magma chamber effects were included, but lithospheric flexure was not. Thomas and coworkers found that stresses on the flanks of a large volcano are sufficient to cause circumferentially oriented thrust faulting, and they suggested that such thrusting produced the concentric terraces observable high on the flanks of Olympus Mons. *Zuber and Mouginis-Mark* [1992] treated the evolution of the surface of Olympus Mons, using a finite element model to calculate stresses in the summit caldera region caused by different magma chamber locations and geometries for comparison with observed patterns of faulting.

In this paper we study the stress field within a volcano and the lithosphere upon which it rests as a unified system. With such a model formulation we can account explicitly for the interaction between edifice stresses (e.g., due to volcano self-loading) and flexural stresses (a result of the load induced by the volcano on the lithosphere). We include both growth of the volcano and viscoelastic deformation in the asthenosphere, so the problem is intrinsically time-dependent. The calculated displacements yield the subsidence history of the volcano. The orientations of principal stresses and their change with time provide important constraints on possible magma emplacement paths and eruption histories. With the computed stress fields, a failure criterion can be used to predict locations and modes of faulting within and near the volcano. After a short discussion of important geological and geophysical characteristics of the Tharsis volcanoes, we briefly describe the finite element procedure and the modelling assumptions. The results of the numerical computations are next presented, and their potential implications for the evolution of eruption characteristics and the formation of tectonic features are then compared with known constraints on the evolution of the Tharsis volcanoes.

CHARACTERISTICS OF MAJOR THARSIS VOLCANOES

The four major Tharsis volcanoes are the largest of the martian shield volcanoes [e.g., *Greeley and Spudis*, 1981]. Each construct is composed of many overlapping flows and flow units erupted over a period of activity as much as 2-3 Gy. in duration [*Tanaka*, 1986]. The approximate heights and basal diameters are given in Table 1.

The largest of the major Tharsis volcanoes is Olympus Mons (Figure 1). The principal tectonic features associated with Olympus Mons are (1) the summit caldera complex, consisting of a series of circular depressions with complex patterns of faulting, (2) concentric terraces seen on the upper slopes of the volcano, (3) the basal scarp, a nearly vertical cliff surrounding the volcano at a radius of about 300 km, and (4) the aureole deposits, which occupy a vast region dominantly to the northwest of the main shield (downslope from the Tharsis rise [*U. S. Geological Survey*, 1989]). The summit caldera is likely the result of a collapse following withdrawal of magma from a high-level magma chamber [*Mouginis-Mark*, 1981; *Zuber and Mouginis-Mark*, 1992]. As noted earlier *Thomas et al.* [1990] have interpreted the concentric terraces to be thrust faults. The basal scarp has been variously interpreted as a thrust fault [*Morris*, 1981], a listric normal fault [*Francis and Wadge*, 1983], and a fault-propagation fold over a subsurface thrust fault [*Borgia et al.*, 1990]. The aureole deposits are generally held to be disrupted landslide material derived from the slopes of the volcano [*Harris*, 1977; *Lopes et al.*, 1980; *Francis and Wadge*, 1983]. *Tanaka* [1985] proposed that gravity sliding and spreading of the aureole deposits is enabled by a weak basal detachment between aureole and substrate. A layer containing about 10% interstitial or interbedded ice would be sufficiently weak to provide such a detachment.

Tectonic features on the flanks of Hawaiian volcanoes on Earth may provide useful analogues to the Olympus Mons scarp and aureole. Acoustic backscatter images of the Hawaiian Ridge reveal that extensive mass wasting deposits (slumps and debris avalanches) flank all of the major Hawaiian shields [*Moore et al.*, 1989]. A study of focal mechanisms of shallow earthquakes on the southern flanks of Kilauea [*Thurber and Gripp*, 1988] supports the hypothesis that a detachment surface separates the volcanic edifice and the older oceanic crust. By this hypothesis,

the volcano can overthrust the underlying crustal layer, sliding on a decollement of weak oceanic sediments. The slides and slumps, driven by intrusions at the rift zones, detach from the volcano along large-offset listric normal faults [Lipman et al., 1985].

Tectonic features observed on and around the Tharsis Montes volcanoes differ somewhat from those of Olympus Mons. The principal tectonic features associated with these volcanoes are (1) circumferential graben on the lower volcano slopes and the surrounding plains, (2) linear embayments or rifts approximately bisecting each volcano along an axis trending N40°E and serving as sources for flows embaying the northeast and southwest flanks, and (3) lobe-shaped deposits to the west or northwest of the edifice [Scott and Tanaka, 1981; Scott et al., 1981a, b, c]. The Tharsis Montes volcanoes exhibit an approximate bilateral symmetry about a NE-SW-trending axis coinciding approximately with the line connecting their centers. Graben tend to occur on the northwest and southeast flanks of these volcanoes (Figures 2-5), i.e. perpendicular to radial directions broadly orthogonal to the line of the rifts. From photogeological study of Viking Orbiter images, Crumpler and Aubele [1978] proposed the following evolutionary sequence for the Tharsis Montes: (1) construction of the main shield, (2) outbreak of parasitic eruption centers on the volcano flanks along the NE-SW-trending axis, (3) subsidence of the summit and formation of concentric fractures and graben, and (4) formation of a bisecting rift along the NE-SW-trending axis, with rift eruptions leading to flooding of the summit depression and inundation of the rifted flanks. This sequence is most advanced on Arsia Mons; Pavonis Mons has reached stage (3), and Ascraeus Mons stage (2). The morphology and tectonics of the flanks of the Tharsis Montes are described in greater detail by Zimbleman and Edgett [1991]. They propose that the lobate deposits formed by gravity sliding and were further modified by both effusive and pyroclastic volcanic activity.

Prominent rift zones that radiate from the summit calderas are dominant structural features characteristic of Hawaiian shield volcanoes [Peterson and Moore, 1987]. These zones are sites of emplacement of magma drained from the summit magma chamber and indicate an environment of horizontal extension. The rift zones and landslides or slump deposits appear to be causally related,

as described above. The Hawaiian rift zones may be analogues to the radial rifts of the Tharsis Montes.

The thickness of the elastic lithosphere beneath the Tharsis Montes volcanoes has been inferred from the radial distances of their circumferential graben by *Comer et al.* [1985] (see Figures 3-5). Preferred values of elastic lithosphere thickness are around 20 km. Concentric graben are not found around Olympus Mons, however, which led Comer and coworkers to conclude that the thickness of the elastic lithosphere beneath Olympus Mons must be much greater (> 150 km) than beneath the Tharsis Montes. Of course, the actual lithosphere does not behave perfectly elastically; rather its strength is limited by frictional failure at shallow depth and by ductile flow at greater depth. From strength envelope considerations for crustal and mantle material [*McNutt*, 1984], values for elastic plate thickness T_e were converted to estimates of mechanical plate thickness T_m and lithospheric thermal gradient by *Solomon and Head* [1990]. For Olympus Mons, flexurally induced curvature is small and T_m is approximately equal to T_e. The lithospheric thermal gradient is then less than 5 K km^{-1}. For the Tharsis Montes, flexural curvatures are larger, T_m exceeds T_e, and mean thermal gradients (corresponding to the best fitting values of T_m) are in the range 10-14 K km^{-1}. Upper and lower bounds on T_e for the Tharsis Montes from *Comer et al.* [1985] allow a range of thermal gradients from 7-27 K km^{-1}.

METHOD

We use the finite element program TECTON [*Melosh and Rafesky*, 1980, 1983] to model stresses and displacements in a large volcano and in the crust and mantle beneath and around the volcano. TECTON's capability for modeling a viscoelastic rheology in the mantle allows us to model the time-dependent flexural response of an elastic lithosphere to each major increment of load. The program first calculates the elastic (i.e., "instantaneous") response to a load. The stresses and displacements arising from load-induced viscoelastic flow in the mantle are then calculated for a specified number of time steps. The Maxwell time (τ_M) of the mantle, defined as the ratio of viscosity η to shear modulus μ, is used as a convenient reference time scale (in subsequent discussion the term "Maxwell time" will refer to the mantle Maxwell time). Complete

descriptions of stresses and displacements were obtained at 5, 10, 15, 20, 30, 40, 70, 100, 200, 400, 700 and 1000 Maxwell times after emplacement of each load increment.

We assume that the problem is axisymmetric, with cylindrical coordinates r, θ, and z. Out-of-plane shear stresses $\sigma_{r\theta}$ and $\sigma_{\theta z}$ are then zero. We solve for r and z displacements and stress components σ_{rr}, $\sigma_{\theta\theta}$, σ_{zz}, and σ_{rz}. In axial symmetry, two principal stresses are confined to the rz plane, and $\sigma_{\theta\theta}$, the stress normal to this plane, is also a principal stress. An example of the finite element grid used for this study is shown in Figure 6. The displacement boundary conditions are that nodes on the side walls ($r = 0$ and $r = r_{max}$) are fixed in r but free to move in z, and that nodes on the bottom boundary ($z = -820$ km in the example shown) are fixed in z but free to move in r. The lower corners of the box are fixed in both directions. The volcano in the example has a radius of 200 km and is 25 km in height, the approximate present dimensions of Ascraeus Mons. In Figure 6 the volcano is the triangular region in the upper left-hand corner. The volcano rests on top of an elastic lithospheric plate of thickness T_e. All elements in the volcanic edifice and the plate have a high viscosity appropriate to the lithosphere. These elements behave essentially elastically over the time scales considered here. All elements below the elastic lithosphere have a lower viscosity value, appropriate for an asthenosphere. These elements experience viscous relaxation over the time modeled. Material property values adopted in our calculations are listed in Table 2. Parameters such as density and Young's modulus differ for the crust and mantle. Elements above depth t_c are assigned crustal values for these parameters; below this depth mantle values are assigned. For most of the models discussed here, we have chosen $T_e = t_c$. We do not mean to imply that thicknesses of the Martian lithosphere and crust coincide; this choice serves only to simplify the models. We have performed additional calculations with $T_e > t_c$ to explore the effect of a strong upper mantle on the flexural solutions. We take T_e to be variously 20, 40, and 60 km. These values fall within the range obtained by *Comer et al.* [1985] for the Tharsis Montes and Olympus Mons. The outer radial boundary of the grid is taken as $r_{max} = 1200$ km.

As a check on the use of TECTON for plate flexure calculations, we have compared the stresses and displacements calculated by the code to those from an analytic solution for thick plate

flexure in axisymmetric geometry [*Comer*, 1983]. We constructed a model of the plate only, without the volcano elements, similar to analytic models. This was done to avoid local stiffening of the plate due to the added thickness of the volcano near r = 0, which would change the resulting flexural profile. The load of the volcano was simulated by applying appropriate axisymmetric forces to the nodes on the top surface of the plate. The surface elevation of the plate at the final time step, relative to its value at the right boundary $r = r_{max}$, is shown in Figure 7a; also plotted is the analytic thick-plate solution. The difference between the two solutions is plotted in Figure 7b. The TECTON solution closely matches the analytic solution except for errors of less than 1% near $r = 0$ and about 1.5% near the flexural arch.

We note that for cases in which the volcano is solidly attached to the lithosphere, the deflection given by TECTON at the final time step is less than that of the analytic solution near $r = 0$. Radial distances of the zero crossing and flexural bulge are also greater than those for the analytic solution. These effects result from a stiffening of the plate by the volcanic load itself. Near $r = 0$, the elements that make up the volcano take up some of the horizontal compressive flexural stresses that would otherwise be taken up by the top half of the plate. This effect may be important when analytic thin-plate flexure models are compared to topography in order to estimate elastic plate thicknesses, in that for welded volcanoes, T_e would be overestimated.

An important limitation of analytic models of lithospheric loading is that the load is emplaced instantaneously. This assumption implies a growth time t_g much less than the mantle Maxwell time τ_M. For Mars, if $\eta \sim 10^{21}$ Pa-s and $\mu \sim 10^{11}$ Pa, $\tau_M \sim 10^{10}$ s or 300 yr. A more realistic model would allow the volcano to grow incrementally with time, simulating the way in which many discrete lava flows are superposed to form an edifice. We have implemented a modification to the finite element code that allows us to specify the properties of a given element as a function of time. The finite element grid is set up exactly as in Figure 6a, except that volcano elements are initially given a density of zero and a low but finite value of Young's modulus (the latter to prevent a singularity in the stiffness matrix used to calculate displacements). These elements are considered "off;" that is, for the purposes of the simulation, such elements are considered initially unoccupied

by volcano material. At the beginning of an appropriate time step, an element can be turned "on" by changing the values of the density and Young's modulus to normal crustal values. Here we have simulated the incremental growth of a volcano by switching on elements in the volcanic edifice in three stages (Figure 6b), at time zero, at 1000 Maxwell times, and at 2000 Maxwell times. We note here that our attempt to model a growing load is necessarily a coarse one. A typical terrestrial volcanic shield will consist of thousands of units emplaced over about 10^5 to 10^6 years (this timescale may be 10^8 to 10^9 years on Mars). Such units are much lower in volume than those we model. Further, our increments are separated by only 1000 Maxwell times (about 30,000 years for the parameters adopted here). This value was selected to be long enough to complete the flexural response to a given increment, abut is not meant to imply that units are emplaced that rapidly.

In order to explore the hypothesis that volcanoes on Earth and Mars may have similar tectonic structures, we have used special features in the TECTON code to simulate the effect of a detachment between volcano and lithosphere as described by *Lipman et al.* [1985] and others. The effects of fault slip along such a detachment on the stresses and deformation can be modeled using the slippery node method implemented in TECTON by *Melosh and Williams* [1989]. We apply slippery nodes to all the nodes originally on the line $z = 0$, i.e., along the interface between the volcano and the lithosphere. This modification allows the volcano to thrust outward over the flexed lithosphere.

The evolution of the stress field within and beneath the volcanic edifice in a model is depicted by means of symbols for the principal stresses within each element (Figure 8, symbols after *Melosh and Williams* [1989]). The first and second symbols denote situations where the azimuthal or hoop stress is the intermediate principal stress σ_2. The third and fourth symbols represent cases where the hoop stress is the greatest extensional stress σ_3. The fifth and sixth symbols represent cases where the hoop stress is the greatest compressive stress σ_1.

Given stress values, we use the Mohr-Coulomb failure criterion to estimate regions where faulting would occur. The Mohr-Coulomb failure equation relates shear stress τ at failure to normal stress σ_n

$$\tau_{failure} = c + \sigma_n \tan \phi \tag{1}$$

where c is the cohesive strength of the rock and ϕ is the angle of internal friction. We adopt values for c (3.8×10^7 Pa) and ϕ ($49°$) appropriate for basalt [*Handin*, 1966]. Elements where the shear stress has exceeded the Mohr-Coulomb criterion are shaded to indicate failure. Once we have found where failure is expected, the orientations of principal stresses are used to determine the style and orientation of faulting, according to the criteria of *Anderson* [1951]. Given the principal stress directions, the type of faulting (normal, thrust, or strike-slip) and the orientation (radial or circumferential) can be determined. Figure 8 gives types and orientations of faulting in elements with the given orientations of the stress symbols. This classification scheme holds if the principal stresses approximately correspond to the horizontal (σ_{rr}, $\sigma_{\theta\theta}$) and vertical stresses (σ_{zz}) listed here. If the stresses are not aligned in this way, fault geometry may be less simply described. Strike-slip faults do not quite fit the usual definitions of radial and circumferential, because such faults are expected generally to strike obliquely to the principal stress directions. For most situations, strike-slip faults make smaller angles with the σ_1 direction than with the σ_3 direction. Thus, when $\sigma_1 = \sigma_{\theta\theta}$ we will consider the resulting faults approximately circumferentially oriented, and when $\sigma_1 = \sigma_{rr}$ we consider them approximately radial. Care must be taken when applying these results to regions at depth, or where principal stresses are oblique to the surface.

For a general state of stress in a plane layer constrained laterally and subjected to self-loading (before the volcanic load is applied), the orientation of the stress symbol will be as in the first line of Figure 8: maximum compression vertical and maximum extension horizontal. The magnitude of the deviatoric stress will increase with depth. This result can be derived from the equations for uniaxial strain (compaction) in the z-direction [e.g., *Turcotte and Schubert*, 1982, p. 108]:

$$\sigma_{rr} = \sigma_{\theta\theta} = \left(\frac{v}{1-v}\right)\sigma_{zz} \tag{2}$$

For Poisson's ratio $v = 0.25$, the factor $v/(1 - v)$ is 1/3. Thus, the vertical stress will be three times as great as the horizontal stress, and with vertical stress equal to the overburden pressure ($\sigma_{zz} = \rho_c gz$, where ρ_c is the density of crustal material and g is the gravitational acceleration), the stress difference will increase with depth. The state of stress in the terrestrial crust is still a matter of debate. *McGarr* [1989] argues that a stress state in which all principal stresses are equal to the overburden load is a better reference stress state than the "Poisson" stress state described by equation (2). However, it seems likely that the state of stress lies somewhere between the two extremes. In general, the stress state described by equation (2) is the initial state in the lithosphere for most of our models. We consider additional models, however, to determine the effects of an isotropic lithospheric prestress (with $\sigma_{rr} = \sigma_{\theta\theta} = \sigma_{zz} = \rho_c gz$). For all models, the prestress in the asthenospheric mantle is taken to be isotropic.

When applying the results of these calculations to actual geologic and tectonic features seen on Martian volcanoes, one must keep in mind the model limitations. The simplest calculations that we perform here start with the instantaneous placement, at time $t = 0$, of a significant portion of a volcanic edifice, equivalent to the condition $t_g \ll \tau_M$. This assumption is valid only for individual flows constituting at most a minor mass fraction of the volcano. While we have modified the finite element code to accommodate changes in element properties with time, as noted above the individual load increments are large fractions of the volcano mass. Other limitations are also noteworthy. It is difficult to determine the geometry of a given volcano load, even at the end of the last major shield-building eruptions, because of subsequent flexure and deformation that may have significantly modified the volcano's characteristics. These calculations are performed under the assumption of axial symmetry; possible effects of nonaxisymmetric loading (such as regional stress) and complex three-dimensional geometry are not incorporated. The effects of magma pressure, transport, and evacuation are not addressed in these models; these processes likely have important influences for caldera and flank tectonic evolution [*Thomas et al.*, 1990; *Zuber and Mouginis-Mark*, 1992]. Further, lateral variations in material properties (due to

horizontal temperature gradients, for example) are not included. Our choice that $T_e = t_c$, while made for convenience, is not necessarily valid for the Tharsis region. Finally, it must be remembered that a viscoelastic model cannot account for relief of stress due to faulting (except for faults modeled *a priori* such as in the detached volcano models). Once faulting occurs, the stress fields calculated are no longer strictly valid, since faulting would relieve stresses locally and could thus alter the predictions for failure at subsequent times. As discussed below, some of these limitations can be relaxed in future modeling efforts.

NUMERICAL RESULTS: STRESS, DEFORMATION, AND FAULTING

Models with Growing Loads

An illustrative model for the evolution of volcano-related stresses is shown in Figure 9, which depicts the case of an incrementally grown volcano on a lithosphere with $T_e = 40$ km. At $t = 0$ (Figure 9a) deviatoric stresses display the orientations and magnitudes expected from simple self-loading of horizontal layers everywhere but along the top layer of volcano elements, where the stresses are rotated such that the compressive axis is almost horizontal. As the effects of flexure manifest themselves with time, this rotation propagates deeper into the volcano, eventually reaching the upper part of the underlying plate (Figures 9b-f). These figures also show predicted locations and types of faulting as functions of time. For the initial volcano of 120 km radius, faulting is initiated in two areas by about 20 Maxwell times (Figure 9b). A subsurface region of normal faulting at a depth of 35-40 km (at the base of the elastic lithosphere) appears beneath the center of the volcanic load. Faulting also starts at the plate surface just outward of the volcano. In this region, all elements but one are predicted to experience circumferentially oriented normal faulting (the innermost element is predicted to fail by strike-slip). By 100 Maxwell times (Figure 9c), both regions have expanded radially and vertically, and a new zone of faulting appears along the upper volcano flanks. The predicted fault style and orientation on the flanks is predominantly circumferential thrusting. Mostly radial normal faults are predicted for the subsurface failure region. By 1000 Maxwell times (Figure 9d), the area of circumferential normal faulting extends up to 300 km radius (not shown in figure) and up to 10 km depth. The area of strike-slip faulting has

grown in radial extent at the expense of the region of circumferential normal faulting, but each of the elements in this zone has already been predicted to fail by a circumferential normal mechanism at an earlier time step (see Figures 9b, 9c). The upper flanks of the volcano are predicted to fail by circumferential thrust faulting, and the lowermost element on the flank by radial thrust faulting. The failure region at the bottom of the plate now extends slightly beyond the radius of the volcano itself. Near $r = 0$, this region includes the entire bottom half of the plate (20 to 40 km below the original surface).

In Figures 9e and 9f we see the effect of the next increment of volcano growth. Notice that most elements on the volcano flank predicted to fail in Figure 9d are no longer predicted to be in failure in Figure 9e, but some of them are predicted to fail again by the time depicted in Figure 9f. No failure is predicted, however, in the layer of elements constituting the new surface of the volcano. In Figure 9g, the effects of the final load increment can be seen. Only two elements in the entire edifice have deviatoric stresses sufficiently great to cause failure.

The magnitude of the maximum deviatoric stress (the difference between the principal stresses of greatest and least magnitude) in the vicinity of the volcano is shown versus time in Figure 10. A comparison with the stress orientation symbols of Figure 9 indicates the principal stresses used to calculate the maximum deviatoric stress at a given point. Figure 10a shows the state of deviatoric stress of the elastic solution. The stress difference increases with depth, as discussed above. At a given depth, the deviatoric stress is higher beneath the initial volcano load increment than outward of the volcano. In Figure 10b (at $t = 1000\ \tau_M$) concentrations of high deviatoric stresses have developed in the three characteristic regions of failure from Figure 9. Deviatoric stresses exceed 150 MPa near the volcano summit and in a wide area near the bottom of the plate beneath the volcano. Failure is predicted in both areas. Deviatoric stresses are not quite so high in the near-surface region immediately surrounding the volcano, but faulting is predicted there because of the low confining pressure. There are two important regions of relatively low deviatoric stress; directly beneath the volcano summit near $z = -4$ to -14 km, and far from the volcano (at both the top and bottom of the plate). In Figure 10c (at $t = 2000\ \tau_M$) the region of high stress in the edifice

has intensified, but remains centered at about the same position as before, at the top of the first load increment. The second load increment, emplaced atop the first, shows a much lower level of deviatoric stress than evident below. The deviatoric stress low beneath the volcano has shrunk in size and lowered its mean level to about $z = -10$ km. By the time subsidence is nearly complete (Figure 10d), most of the region near the volcano experiences deviatoric stress in excess of 200 MPa. The regions of high deviatoric stress have expanded to maximum size, and the deviatoric stress minimum below the volcano center has again shrunk slightly.

Changing the plate thickness can affect the evolution of regions of failure. For $T_e = t_c = 20$ km , the entire flank is predicted to fail by thrust faulting after 1000 τ_M (Figure 11a). Circumferential thrust faults on the upper flanks will be surrounded by a small annulus of radially oriented thrusts on the lower flanks. The region of failure outward of the volcano is smaller in radial extent than for the case with $T_e = 40$ km (Fig. 10b). While strike-slip faulting in the inner portion of this region, initial predicted failure for most of these elements occurs by circumferential normal faulting. In any case, this inner annulus will be covered by volcanic material later in the growth of the volcano. At the final stage (Figure 11b, $t = 3000$ τ_M), the subsurface region of failure reaches through almost the entire thickness of the plate to the base of the volcano. At the radially distal edge of this region, stresses are rotated such that strike-slip faulting is expected, and the region merges with the failure region outside the volcano to form a continuous zone predicted to be faulting. More elements (5 vs. 2) in the edifice retain stresses large enough to cause failure than for the case with $T_e = 40$ km.

The evolution of maximum deviatoric stress for this case (Figure 12) follows a course similar to that for $T_e = 40$ km. The regions of high deviatoric stress on the volcano flanks and at the bottom of the plate closely surround a stress minimum whose center lies at about $z = -3$ km. After the first load increment is accommodated (Figure 12a), peak stresses in the edifice are nearly twice as large as for the case with $T_e = 40$ km. A comparison of the late-stage stresses for these two cases (Figures 10d and 12b) shows that the deviatoric stresses near the base of the plate are similar

in magnitude, although the vertical gradient of stress is greater for the thinner plate. Peak deviatoric stresses in the volcanic edifice are significantly higher for the thinner plate.

Results for a model with a thicker elastic lithosphere and crust ($T_e = t_c = 60$ km) also reveal interesting changes from the first model. After the first loading increment ($t = 1000\ \tau_M$, Fig. 13a), faulting has initiated at the lithosphere base and outside the volcano, but not in the edifice itself. In the outer faulting region we again observe elements where predicted failure evolves from initial normal to later strike-slip. The area of predicted strike-slip faulting is much larger in extent than for the cases with thinner lithospheres. After the final load increment (Figure 13b) the region of predicted near-surface normal faulting expands outward to 590 km from the center (Table 3), as well as down to a maximum depth of 20 km. The region of failure beneath the volcano is found at a deeper level (30-60 km depth), because of the greater plate thickness. Faulting of any type is absent from the edifice throughout the period modeled.

Maximum deviatoric stresses for this case are shown in Figure 14. Compared to the case with $T_e = 40$ km (Figure 10), there are several differences. At the final time steps shown (Figures 10d and 14b), the region of high stress near the base of the lithosphere (as defined by, say, the 300 MPa contour) is greater in vertical and lateral extent for the case with $T_e = 60$ km, even though the maximum stress deviator is about the same. The deviatoric stress minimum, beneath the volcano, is also larger in extent and centered more deeply (about -14 km) than its counterpart for $T_e = 40$ km. Deviatoric stresses within the volcanic edifice are significantly lower for this case compared with the other two.

To investigate the effects of different crustal and lithospheric thicknesses, we performed a calculation with a 40-km-thick crust and a 60-km-thick elastic lithosphere. The upper mantle lithosphere has a higher value of Young's modulus and should cause the plate to behave more stiffly than if the plate consisted entirely of crustal material. Figure 15 shows plots of stress orientation and failure for this case; compare with Figure 9 for a case with crust and lithosphere both 40 km thick and with Figure 13 for a case with crust and lithosphere both 60 km thick. The evolution of the stress field and zones of predicted failure is qualitatively similar to those discussed

above. One effect of the stiff upper-mantle lithospheric layer is to concentrate into a narrower depth interval the zone of failure beneath the volcano, seemingly shielding the less rigid crust above from failure. In Figure 13, this zone extends from 30 to 60 km depth, whereas in Figure 15 only elements in the mantle portion of the lithosphere (40 to 60 km depth) show stresses that satisfy the failure criterion. We also observe that the size of the zone of near-surface failure outward of the volcano, and the amount of strike-slip faulting within it, are both greater for the plate with a strong upper mantle lithospheric layer (Table 3). Contours of maximum deviatoric stress after the final load increment for this model (Fig 16) are broadly similar to Figure 14, except that the deviatoric stress level is much higher at the base of the lithosphere, revealing a concentration of stress in the strong mantle lithosphere. Also, the deviatoric stress minimum beneath the load occurs at a slightly shallower depth.

Models with Instantaneous Loads

It is instructive to consider a model with an instantaneously emplaced load, both as a comparison with analytic models and as a reference to study the effects that incremental volcano growth has on the evolution of stresses in volcanoes. Figure 17 shows stress orientations and failure for this case at the conclusion of flexure ($t = 1000 \, \tau_M$). These are qualitatively similar to those for the case with incremental loading (Figure 9g) except for the volcano flanks, which are predicted to have failed along the entire surface and to 15 km depth near the summit. Circumferential thrust faults are predicted on the upper flanks, and an annulus of radially oriented thrusts is predicted on the lower flanks. This state is similar to that predicted for the first load increment of a growing volcano (Figures 9d, 11a). The maximum deviatoric stresses for this case (Figure 18) resemble those for the incrementally loaded case (Figure 10d) except for the concentration of stresses at the top of the edifice. In this respect the model behaves like an analytic plate flexure model, in which deviatoric stresses are a maximum at the top and bottom of the plate, with a minimum at mid-plate. The volcano serves effectively to stiffen the plate near $r = 0$, thus elevating the mid-plane from $z = -20$ km (for a 40-km-thick plate) to $z = -8$ (for a plate effectively 65 km thick at $r = 0$).

Models with Detached Loads

The evolution of stress orientations for an incrementally grown volcano detached from the lithosphere is shown in Figure 19. Immediately after loading, stresses in almost the entire edifice are oriented with maximum compression vertical and maximum extension out of the plane (Figure 19a). This geometry may be compared with that in Figure 9a, where both the maximum and minimum principal stresses are in the r-z plane in the upper flanks of the volcano, and the maximum compressional direction has rotated toward the horizontal. In Figure 19a the onset of faulting is predicted in two areas; at the plate surface just outside the volcano (as observed in most of the other models) and near the base of the volcano near $r = 0$. Radial normal faulting is predicted for this second region; the entire lower part of the volcano (near the detachment) exhibits horizontal extensional stress and vertical compressive stress, in contrast to the environment of generally horizontal compression in the models with welded volcanoes. This environment persists as the calculation proceeds (Figure 19 b-c). In Figure 19b, after 1000 Maxwell times, the area of radial normal faulting reaches outward through the edifice, above the detachment, to the surface at the volcano edge. Also note that stresses near the summit of the volcano have rotated to a state of horizontal compression. By the time the flexural response is complete (Figure 19c, 3000 Maxwell times), an annulus (with inner radius 170 km and outer radius 200 km) of radial normal faulting has formed on the lower flanks. Elsewhere, the stress state depicted in Figure 19c is similar to the final result of the welded case (Figure 9g), except that the area of predicted faulting outside the volcano is deeper, and the faulted area beneath the volcano does not extend as far vertically. These effects may be related to local stiffening of the plate by the welded volcano, which would raise the midplane of the plate.

A plot of maximum deviatoric stress for this case (Figure 20) shows how the distribution of stresses is changed by the detachment. After first load increment, deviatoric stresses in the volcano tend to increase from top to bottom, the reverse of the pattern for the welded volcano (Figure 10b). A region of high deviatoric stress forms beneath the detachment (with approximately the same magnitude as the high stress region at the top of the edifice in Figure 10b). Figure 20b shows

stresses after completion of loading; stresses in the edifice are greatest at the bottom, directly above the detachment. The upper parts of the edifice have low levels of stress, except for a small area of slightly elevated stresses near the summit. The stress maximum beneath the detachment has grown in magnitude and area.

In order to address the role of the initial stress state of the lithosphere in determining the time-dependent evolution of stresses and displacements, we consider a lithosphere with an isotropic prestress equal to the overburden pressure. For a model otherwise similar to that of Figure 9, the first faulting in the region outside the volcano (Figure 21a) is predicted to occur by strike-slip, in contrast to the prediction of circumferential normal faulting for the model of Figure 9. Notice that the onset of faulting in this region occurs at a later time, and the onset of faulting in the region below the volcano is delayed until about 400 τ_M (compared with 20 τ_M for the model in Figure 9). These delays are to be expected, since deviatoric stresses must build up from zero, as opposed to cases which start with a sizeable deviatoric stress. The extent of faulting at the final time step (Figure 21c) is similar (to 470 km radius, Table 3), and so is the predicted geometry of faulting in the region beneath the volcano (radial normal). In the early stages of flexure, however, strike-slip faulting is predicted for a greater proportion of the near-surface region than for the model of Figure 9 (Table 3). After the flexure following the final load increment the proportional area of predicted strike-slip to circumferential normal faulting at the surface is still about 10% greater than that of the model of Figure 9 (Table 3). Thus we conclude that the initial stress state of the lithosphere prior to volcanism can affect the distribution of near-surface faulting surrounding the volcano. Maximum deviatoric stresses (Figure 23) far from $r = 0$ are small, as might be expected in a plate which starts out with isotropic prestress. However, the stresses near the base of the plate beneath the volcano and in the volcanic edifice are qualitatively similar to those for cases with Poisson prestress.

DISCUSSION: IMPLICATIONS FOR VOLCANO EVOLUTION

The time-dependent displacement and stress fields calculated in our models can be used to predict the type and orientation of tectonic features that would result from loading of the lithosphere

by a volcanic edifice. We may compare these predictions to observed tectonic features on and around the Tharsis volcanoes. The evolution of tectonic deformation is also constrained by the model results, an advantage of the finite element method over analytical flexure and other lithospheric loading models which consider an instantaneously emplaced load. We may then evaluate the validity of each model and the applicability of terrestrial analogues for some tectonic and volcanic features.

Flank Tectonics: Circumferential Graben and Predicted Strike-Slip Faulting

As noted earlier, circumferential graben are observed on the lower flanks and the surrounding plains for all three of the Tharsis Montes (Figures 2-5). Formation of these circumferential graben requires an environment of radial horizontal extension at the top of the crust surrounding the volcano and in the near-surface region of the volcano flank. Almost every model predicts circumferential normal faulting in an annulus around the volcano. Models in which the volcano is welded to the underlying plate give near-surface horizontal compression in the edifice after lithospheric flexure, while models which include a detachment between volcano and plate show horizontal extension in the lower volcano flanks. At the base of the detached volcano, the hoop stress $\sigma_{\theta\theta}$ is extensional, and the radial normal stress σ_{rr} is compressional but small compared with the vertical normal stress σ_{zz}. In order for circumferential extensional features to form, σ_{rr} should be the least compressive stress. However, since the magnitudes of σ_{rr} and $\sigma_{\theta\theta}$ are small in this region, a small perturbation due to local or regional nonaxisymmetric stresses may determine the orientation of failure features [Nakamura, 1977]. The Tharsis Montes are located slightly below the crest of the Tharsis Rise, on a broad slope to the northwest [U. S. Geological Survey 1989]. This long-wavelength slope of Tharsis, in the presence of a detachment, would be expected to add a northwest-southeast extensional stress; superposition with the axisymmetric model stress field would result in radial extensional features in the northeastern and southwestern quadrants (and, at sufficiently high strains, a NE-SW trending rift), and circumferential graben on the northwestern and southeastern flanks.

On Arsia Mons, graben are prominent on the half of the volcano centered on the northwestern azimuth (all the way up the flank to the caldera rim, Figures 2, 5), but are generally absent on the upper southeastern-centered half. Several graben appear at the southeastern edge of the edifice, however. These graben are likely to be related to extensional stresses at the surface of the lithosphere surrounding the volcano, as described above, and thus not related to stresses in the edifice per se. The graben on the northwestern half terminate near the northeast-southwest-trending rift that bisects the volcano. We suggest that a portion of the northwestern half of the volcano was able to slide down the slope of the Tharsis rise, creating a stress state that led to the formation of the numerous graben. In the southeastern half, however, buttressed by the rising slope in that direction and thus unable to move, the stress state remained stable (horizontal compression at the surface, as in Figure 9f). This scenario would account for the dramatic difference in faulting character on the two "halves" of the volcano. Of course, stresses resulting from caldera formation and magma chamber formation may have had a strong effect on the stress field near the summit as well [*Zuber and Mouginis-Mark* 1992].

We can apply the above arguments to the remaining Tharsis Montes. Graben on the flanks of Pavonis Mons are in general narrower than those on the northwestern flank of Arsia Mons, but more widely distributed in azimuth relative to Arsia Mons [*Zimbleman and Edgett*, 1991]. The widest graben are on the west and northwest flanks, analogous to the situation on the flanks of Arsia Mons. The graben on the north, northeast, and east flanks of Pavonis Mons, however, indicate that the stress state in the edifice is too complex to be described solely by the above scenario for Arsia Mons. Ascraeus Mons shows the least amount of normal faulting on its flanks; the few concentrations of graben lie on the lower slopes, far from the summit caldera. Thus Ascraeus Mons shows the least evidence of tectonic modification due to the effects of a detachment. Perhaps the detachment is smaller in extent there because of inherent differences in crustal properties, or because it has had less time to develop. The latter scenario is consistent with the conclusion of *Crumpler and Aubele* [1978] that Ascraeus Mons is at an earlier stage in its development than the other two volcanoes.

Stresses from both analytic flexure models and our models with instantaneous volcano loads predict strike-slip faulting at the surface of the plate, immediately outside the load Evidence for strike-slip faulting around any of the Tharsis volcanoes, however, is lacking. The absence of such features has been discussed by *Golombek* [1985] and *Schultz and Zuber* [1992], in the general context of large axisymmetric loads on planetary lithospheres. Examination of the plots of stress orientation and failure from our models (Figures 11, 13, 15) however, reveals that the predicted failure modes for elements in the region surrounding the volcano can change with time. In this region, every element that eventually fails (except the innermost) is predicted to do so first by concentric normal faulting. This can be seen more clearly in a Mohr diagram of the stresses in a typical element in this area (Figure 22). The Mohr circles grow in size as flexure proceeds, until the failure envelope is exceeded at about 70 τ_M after first loading. The largest circle shows stresses at the conclusion of flexure. This stress state corresponds to that given by analytic plate models (in which flexure occurs instantaneously). Applying a failure criterion simply to the final stress state can be misleading. Consideration of the stress history in our models indicates that at the time of first failure, the shear failure criterion is satisfied in the surface elements immediately outside the volcano, and the principal stress directions predict circumferential normal faulting. These first-formed faults would tend to relieve extensional stresses in their vicinity and would serve as preferred planes of weakness for the relief of stresses accumulated later. Strike-slip features would thus tend to be prevented from forming. We also note that for the lower range of values of lithosphere thickness considered here (20-40 km), the zone of strike-slip faulting predicted from the late-stage stress models lies at the edge of the volcanic construct, which has the lowest surface elevation (Figure 7). This topographic low could accumulate lava flows and erosional deposits which would tend to cover deformational features (circumferential graben as well as strike-slip features).

Horizontal Compression in the Edifice

Circumferential terraces high on the flanks of Olympus have been interpreted as concentric thrust faults by *Thomas et al.* [1990], who applied elastic finite element models to investigate

edifice stresses and deformation. Our simplest model (a welded, instantaneously emplaced volcano) predicts a similar stress state, with circumferential thrust faulting on the upper flank and radial thrusts on the lower flank (Figure 17). Plate flexure models also predict large horizontal compressive stresses in the area of the load, which increase with height above the mid-plane of the plate, reaching a maximum at the surface, where thrust faulting is predicted. Models with growing loads, however, display a different distribution of stress. The maximum horizontal stress occurs in the lowest (first) load increment and decreases upward with each later load increment (Figures 9-14). Each successive load increment "feels" tectonic stresses from itself and all later load increments. The last units emplaced are sensitive only to the effects of their own loading and therefore exhibit a low degree of horizontal compression. Thus, thrust faults (predicted by simpler models) associated with such stresses would be expected to occur either early in the evolution of the volcano or not at all and, if formed, would be covered by later units which remain unfaulted because the failure criterion is not satisfied (Figures 9, 11). We note, however, that stresses in these elements are close to failure. Local stress perturbations and/or variations in internal friction ϕ could result in some failure visible at the surface. On the other hand, if loading increments are smaller than those adopted here (which is likely), then the degree of horizontal compression from such elements would be smaller than those shown here, and faulting would not be expected.

The presence of graben high on the flanks of the Tharsis Montes is not consistent with the state of horizontal compression in the edifice found in the welded volcano models. Other factors, such as a basal detachment, lithospheric rifting, or caldera stresses must be invoked to explain the presence of these faults on the upper flanks.

Magma Transport

The volcanic edifice stress fields calculated here have important implications for magma transport and eruption. Magma propagates through the lithosphere along fractures that form perpendicular to the direction of least compressive stress. Immediately following emplacement, the stresses in a given load increment are characterized by σ_3 horizontal (e.g., Figure 9a). Thus show that magma can propagate vertically to the summit region. As a result of flexure, however, the

principal stress directions in that load increment rotate such that σ_1 is horizontal and σ_3 is vertical. Magma propagation should tend to be horizontal in such a layer, leading outward from the summit to the flanks. Stresses in earlier load increments remain in horizontal compression as volcano growth proceeds. This behavior results in a maximum in horizontal stress near the core of the volcano, with lessening horizontal compression at higher (later) load increments. This stress pattern contrasts with that from analytic flexure calculations, where stresses increase linearly with distance from the plate midplane. Thus an implication of the models treated here is that within an interval of shield building there should be an evolution in favored eruption location from summit to lower flank. Such an evolution is consistent with the first two stages in the sequence of major events for the Tharsis Montes determined by *Crumpler and Aubele* [1978].

The stress evolution of a growing volcano may affect the location of magma collection zones or chambers. The maximum horizontal compression is achieved within the earliest load increments, near the bottom of the load. Such a region of high compressive stress at lower levels in the edifice could inhibit ascending magma from reaching the summit, and could thus lead to the pooling of magma. Since magma will propagate perpendicular to the direction of least compressive stress, radial propagation of magma in sheet dikes or sills might also occur. On the other hand, high stresses in this region will be relieved by faulting, until the failure criterion is no longer satisfied. This region may thus be the most pervasively faulted and fractured zone, and thus perhaps a favored location for magma to collect.

The issue of compressional versus extensional horizontal stresses in the volcanic edifice is critically important when considering volcano growth. In order for the volcano to grow, there must be a path for magma to reach the surface (or near the surface in the case of growth by intrusion). Large horizontal compressive stresses within the edifice may cut off summit eruptions unless there is sufficient magma overpressure. Thus, the route from a central magma chamber to the summit may be cut off, and flank eruptions would be favored, as noted above. After sufficient flank eruption, however, loading on the flanks might then lead to relief of compressive stresses near the summit, re-opening the path to the summit caldera. When the effects of time-dependent

loading during volcano growth are included, the magnitude of horizontal stresses in the later stages of evolution are greatly reduced compared with stresses at the equivalent level in instantaneously loaded models. When both time-dependent loading and a basal detachment are included, horizontal compressive stresses in the edifice are reduced further, and a state of extensional hoop stress is reached in the lower part of the edifice, adjacent to the detachment (Figure 19). Summit eruptions are then more easily accommodated. The stress state in the lower edifice resembles that determined seismically for western Hawaii by *Gillard et al.* [1992], with σ_1 vertical (or nearly so), and both σ_2 and σ_3 horizontal and similar in magnitude. The model stress state also resembles that of a tectonic model for the base of Hawaii proposed in Figure 3 of *Wyss and Koyanagi* [1992] (based in part on the results of *Gillard et al.* [1992]). The model of *Wyss and Koyanagi* [1992] has σ_3 parallel to the direction of slip along the basal detachment, whereas our model has σ_3 perpendicular to the basal slip. However, since σ_2 and σ_3 are similar in magnitude [*Gillard et al.* 1992], local perturbations and departures from axisymmetry may determine the orientations of these stresses in actual volcanoes.

Flank Tectonics: Aureoles, Lobes and Scarps

Results of our models also help us to understand the flank tectonics of the Tharsis volcanoes, in particular the large downslope motions of material in the form of large slides or slumps. As noted above, the Olympus Mons aureole has been interpreted as a large landslide deposit resulting from slip along large-offset listric normal faults [*Francis and Wadge*, 1983], the upper reaches of which are postulated to coincide with the basal scarp. Aureole material is most prominent to the north and west; there is an aureole lobe to the southeast, however, suggesting that the Tharsis rise did not fully buttress the southeastern flank of Olympus. Evidence for similar mass movement activity on a smaller scale is seen on the northwestern flanks of Ascraeus and Arsia Montes [*Zimbleman and Edgett*, 1991].

As discussed above, the interaction between the axisymmetric stress field from the volcano loading and regional stresses due to topography may influence the location, orientation and extent of scarps and of landslides triggered by fault slip on the Tharsis volcanoes. The Olympus Mons

aureole deposits are of greatest extent to the north and west, but also there is a significant aureole lobe to the southeast. The basal scarp has greatest relief on the northwestern and southeastern flanks. Models with a detachment predict that at the edge of the edifice $\sigma_3 = \sigma_{\theta\theta}$ and is extensional. This can account for radial normal faulting but not for the scarps and aureole deposits, which in the above scenario require that $\sigma_3 = \sigma_{rr}$. The addition of a regional northwest-southeast extensional stress, induced by the regional gradient in elevation, however, would provided the necessary orientation of stresses in the northwestern and southeastern quadrants of the volcano, where the aureole and scarp are most prominent. The aureole deposits to the north and west of Olympus Mons could then be a result of large landslides analogous to those off the Hawaiian chain but on a larger scale. The basal scarp would then consist of the coalesced head scarps of these landslides. The lobate features to the northwest of Arsia and Pavonis Montes would then be similar in origin but on a smaller scale, without prominent basal scarp formation. This scenario also explains why the deposits are always more prominent on the northwestern side of these volcanoes, since this is the regional downslope direction. Note that the above scenario postulates a consistent stress field (of NW-SE extension) throughout the evolution of the volcano. This contrasts with the view of *Francis and Wadge* [1983], who suggest that proto-Olympus Mons was elongate to the northwest due to an early NE-SW extensional regime, which allowed preferential effusion along a NW-SE axis.

Large landslides and slumps, triggered by extension on the flanks, may be a second important mode of volcano growth, in that mass movement clears the way for more volcanic material to be emplaced behind it [*Lipman et al.*, 1985]. The model of Lipman and others emphasizes the role of dike intrusion at the rift zones, with the subvolcano detachment passively taking up the resulting strain. Our results suggest that without such a detachment, the rift zones may not be able to form, due to a predicted environment of horizontal compression. As a welded volcano grows, an ever increasing horizontal compressive stress near the base of the edifice would eventually choke off magma supply to the summit. Thus, the Hawaiian rift zones may owe their existence to the presence of the detachment, and volcanoes lacking such a detachment may exhibit important

structural and evolutionary differences from Hawaiian volcanoes. For example, *Nakamura* [1980] has suggested that the lack of rift zones in the Galapagos shields is attributable to a paucity of oceanic sediments on the young ocean floor beneath the volcanoes.

Linear Rift Zones

Linear symmetries observed in all the Tharsis Montes volcanoes may be indirect evidence for failure in the sub-volcano region. The second stage in the *Crumpler and Aubele* [1978] sequence of volcano evolution involves the development of a linear rift bisecting the volcanoes, with eruptions emanating from this rift. Radially oriented normal faulting under a volcano might be thought at first to tend to divide the volcano into radial sections, much like pie slices. The existence of the linear rifts on the Tharsis Montes, however, suggests that this mode of failure may be concentrated into one large linear feature that bisects the volcano. This feature may owe its orientation to regional stress fields or to pre-existing zones of weakness. Our calculations predict radially oriented normal faulting in a broad zone beneath a volcano. For the case with $T_e = 20$ km (Figure 11), this zone extends beyond the volcano radius and reaches quite close to the surface. Such a zone, if concentrated into a linear feature and if continued to the surface by sustained faulting, may give rise to the linear rifts and bilateral symmetry observed on the Tharsis Montes. Stresses due to topography of Tharsis might be expected to add a component of northwest-southeast extension (the direction of greatest slope). This would concentrate the radial faulting into a rift zone striking northeast-southwest, as is observed on the Tharsis Montes. The rift zones would form orthogonal to the regional topographic gradient, as is observed. A problem with this model is that the rifting has to propagate upward somehow to the surface of the lower volcano flanks. The prediction of radially oriented normal faulting on the lower flanks for the model with a sub-volcanic detachment (Figure 20) suggests another mechanism for forming the observed rifts. This explanation has the advantage that rift formation would occur early, almost immediately after volcano creation, a timing more consistent with the chronology of *Crumpler and Aubele* [1978]. If the detachment model is applicable to Mars, it may help explain the existence of the rifts.

The evolution of Pacific hotspot volcanoes may provide some insight into the formation and influence of a bisecting rift zone. For instance, *Holcomb* [1985] has suggested that the island of Molokai in the Hawaiian chain resembles a volcano cut almost exactly in half, with one part transported downslope in one or more massive submarine slides, and the other part remaining to form the present island. Bathymetry of the ocean floor north of Molokai [*Moore*, 1964] supports this conclusion. We have earlier conjectured that a similar but less extreme mechanism could explain the presence of graben on the upper slopes of Arsia Mons and Pavonis Mons, in that as the volcano halves slide apart from each other, an extensional environment is created near the summit. To investigate this possibility quantitatively, a fully three dimensional model, or an axisymmetric model with non-axisymmetric loading, is required.

Detachment Tectonics

The flank tectonic characteristics of the Tharsis volcanoes, combined with the observations of and modeling results for terrestrial volcanoes with detachments, strongly suggests that detachments analogous to those of Hawaii-type volcanoes [*Lipman et al.*, 1985] exist on Mars. Such a detachment cannot arise from the presence of a thick oceanic sediment layer as for Hawaii. It has nonetheless been demonstrated that liquid water existed in moderate quantities at the Martian surface earlier in the history of the planet [e.g., *Carr*, 1987]. While liquid water is now unstable at the surface, large quantities of water are believed to be buried as ground-ice. *Tanaka* [1985] proposed that gravity sliding and spreading could account for the Olympus Mons aureole (and basal scarp) providing that a basal detachment zone of material with low shear strength was present. He calculated that a layer of material with about 10% interstitial or interbedded ice could provide the necessary detachment. The pre-volcanic upper crustal layer may have consisted dominantly of an impact breccia regolith produced by repeated impacts. Such a heavily fractured material is likely to be porous and thus may contain interstitial ice. Even in the absence of an excess ice content, the mechanical weakness of such a layer could contribute to the formation of a detachment between a strong lower crust and a volcanic edifice. *Tanaka* [1985] states that such a structure is unique to Olympus Mons. However, *Zimbleman and Edgett* [1991] have mapped

lobate deposits on the northwestern flanks of all three Tharsis Montes that may be smaller-scale analogues to the Olympus Mons aureoles, so some form of detachment beneath all four constructs appears to be indicated.

Plate Thickness and Volcano Size

The ratio of elastic plate thickness to volcano diameter is observed to have significant effects on the evolution of the subsidence, stress, and regions of predicted failure in our computations. We note several trends as plate thickness increases relative to volcano diameter. Study of the patterns of stress orientations and predicted failure in Figures 9, 11, and 13, shows that the outer region of failure, at a given time, increases in horizontal (and vertical) extent, and a greater proportion of the inner part of this region is predicted to fail at later stages by strike-slip faulting, with increasing plate thickness (Table 3). The deviatoric stress plots of Figures 10, 12, and 14 show that the average depth and volume of the region of low deviatoric stress beneath the volcano also increase with increasing plate thickness. The magnitude of deviatoric stress within the volcanic edifice, and in particular the magnitude of maximum horizontal compressive stress, decreases with increasing plate thickness. As noted above, a zone of large horizontal compressive stress may affect the propagation of magma from its mantle sources to the volcanic edifice. Elastic plate thickness may thus play a role in determining the location of magma storage areas. For the largest plate thickness considered here, stresses in the edifice never exceed the failure limit (Figure 13).

The relative timing of events in our models is generally consistent with the chronology set forth by *Crumpler and Aubele* [1978] for the Tharsis Montes. After construction of the main shield, rift formation and flank eruptions along this rift occur in the second stage of evolution. Figure 9b shows that, after 10 Maxwell times, the principal model result is the beginning of rotation of the stress axes in the edifice (which is expected to favor flank eruptions). After a few tens of Maxwell times the failure zone beneath the volcano (which could favor formation of the rift) has begun to grow. The third stage involves summit subsidence and formation of concentric fractures and graben. After 100 Maxwell times, our computations show increased subsidence as

well as the growth of the region of normal faulting outward of the volcano (Figure 9c-g). The fourth stage of *Crumpler and Aubele* [1978] involves further eruption along the rift, flooding the summit and flanks. Late stage flank eruptions are consistent with the stress fields in our calculations. Summit eruptions, however, would not be favored by the computed stress fields. It is likely that the stress field is influenced by the effects of previous stages of the evolution. Flank eruptions result in an added flank load, not modelled here, to which the lithosphere will respond with additional flexure. Subsidence and additional flexure near the flanks of the volcano may at least partially relieve the compressional stresses near the summit, thus enhancing the possibility of additional summit eruptions. By this scenario, the preferred site for eruptions could alternate between summit and flank, on time scales on the order of 100-1000 τ_M. Also, the effect of sections of the volcano sliding away from the bisecting rift may result in an extensional environment near the summit, once again favoring summit eruptions.

Future Directions

Because of the limitations of these calculations in accurately modeling the behavior of large volcanoes, we hope to be able to relax some of these limitations in future models. In our models, assume that the crust and mantle are perfectly viscoelastic; within an element, no provision is made for stresses that exceed reasonable failure limits (such as in all the shaded elements in Figures 9, 11, and 13). The inclusion of localized yielding in a volcano model can be presumed to have important effects on the geometry and magnitudes of the calculated stress and deformation fields. A finite element code that incorporates plastic yielding will allow us to account more realistically for the effects that failure will have on predicted fault locations and styles. Further, the effect of thermal stresses has been ignored. Thermal stresses can play an important role in the evolution of the volcano, both through stresses accumulated by cooling after emplacement of each layer, and through the time-dependent thermal stresses in regions reheated by the later passage or storage of magma.

CONCLUSIONS

In this paper we have used finite element calculations to simulate the deformational and stress response of the lithosphere to a volcano load. The results of these calculations are compared with observed tectonic features and inferred eruption characteristics of large Martian volcanoes. Some of the zones of failure and faulting predicted in our models have direct analogues in observed features; others may be indirectly related to observed structures. Three regions of failure with characteristic stress regimes are identified in our calculations. Flexural stresses in the lithosphere immediately surrounding the volcano can result in circumferential graben. Flexurally induced failure in a wide zone beneath the center of a large volcano may play a major role in the development and modification of the edifice. Given that magma ascending through the lithosphere propagates along fractures oriented perpendicular to the direction of least compressive stress, a rotation in the principal stress orientations during lithospheric flexure in the models tends to favor eruption sites shifting from the volcano summit to the flanks as flexure proceeds. We conclude that time-dependent lithospheric flexure is important in determining the location and style of faulting within and surrounding large volcanoes as well as regulating the timing and location of volcanic eruptions.

Horizontal compressive stresses caused by flexure and subsidence may lead to thrust faulting on the flanks of large volcanoes. Incremental volcano growth, however, results in a less extreme environment of horizontal compression on the upper flanks at late stages of development. Late load increments on the flanks are not stressed from earlier flexure, and horizontal stresses are no longer great enough to cause flank thrusting. The most highly stressed area of the edifice is near the top of the earliest load increment. Inclusion of a detachment between volcano and lithosphere results in an environment of horizontal extension in the part of the volcano that overthrusts the lithosphere. Without effects such as these, which reduce the extreme magnitude of horizontal compression in our model volcanoes, it would be very difficult for a volcano to continue growth via summit eruptions.

A mass movement origin has been suggested for the vast aureole deposits surrounding Olympus Mons [*Harris*, 1977; *Lopes et al.*, 1980; *Francis and Wadge*, 1983] as well as smaller lobate deposits to the northwest of each of the Tharsis Montes [*Zimbleman and Edgett*, 1991]. Analogy with large slumps and slides off of the Hawaiian islands [*Moore et al.*, 1989; *Lipman et al.*, 1985] suggests that a detachment between volcano and lithosphere may play a role in the evolution of volcanoes on Mars as well as Earth. Models that include such a detachment, in contrast with models with welded volcanoes, predict a state of horizontal extension in the edifice (and eventually radial normal faulting on the lower flanks). When the effects of non-axisymmetric stresses due to regional topography are considered, predicted patterns of faulting match well observed structures on the Tharsis Montes.

REFERENCES

Albee, A. L., R. E. Arvidson, and F. D. Palluconi, Mars Observer mission, *J. Geophys. Res.*, *97*, 7665-7680, 1992.

Anderson, E. M., *The Dynamics of Faulting and Dyke Formation with Applications to Britain*, 2nd ed., Oliver and Boyd, Edinburgh, 206 pp., 1951.

Blasius, K. R., and J. A. Cutts, Shield volcanism and lithospheric structure beneath the Tharsis Plateau, Mars, *Proc. Lunar Planet. Sci. Conf. 7th*, 3561-3573, 1976.

Blasius, K. R., and J. A. Cutts, Topography of Martian central volcanoes, *Icarus, 45*, 87-112, 1981.

Borgia, A., J. Burr, W. Montero, G. E. Alvarado, L. D. Morales, and G. E. Alvarado, Fault-propagation folds induced by gravitational failure and slumping of the Central Costa Rica volcanic range: Implications for large terrestrial and Martian volcanic edifices, *J. Geophys. Res., 95*, 14357-14382, 1990.

Chevallier, L., and W. J. Verwoerd, A numerical model for the mechanical behavior of intraplate volcanoes, *J. Geophys. Res., 93*, 4182-4198, 1988.

Comer, R. P., Thick plate flexure, *Geophys. J. R. Astron. Soc., 72*, 101-113, 1983.

Comer, R. P., S. C. Solomon, and J. W. Head, Mars: Thickness of the lithosphere from the tectonic response to volcanic loads, *Rev. Geophys., 23*, 61-92, 1985.

Crumpler, L. S., and J. C. Aubele, Structural evolution of Arsia Mons, Pavonis Mons, and Ascraeus Mons: Tharsis region of Mars, *Icarus, 34*, 496-511, 1978.

Dieterich J. H., Growth and persistence of Hawaiian volcanic rift zones, *J. Geophys. Res., 93*, 4258-4270, 1988.

Eliason, E., R. Batson, and A. Manley, Mars Mosiacked Image Model (MDIM) and Digital Terrain Model (DTM), U. S. Geol. Surv., Flagstaff, Az., 1991.

Francis, P. W., and G. Wadge, The Olympus Mons aureole: Formation by gravitational spreading, *J. Geophys. Res., 88*, 8333-8344, 1983.

Gillard, D., M. Wyss, and J. S. Nakata, A seismotectonic model for western Hawaii based on stress tensor inversion from fault plane solutions, *J. Geophys. Res.*, *97*, 6629-6641, 1992.

Golombek, M. P., Fault type predictions from stress distribution of planetary surfaces: Importance of fault initiation depth, *J. Geophys. Res.*, *90*, 3065-3074, 1985.

Greeley, R., and P.D. Spudis, Volcanism on Mars, *Rev. Geophys. Space Phys.*, *19*, 13-41, 1981.

Handin, J., Strength and ductility, in *Handbook of Physical Constants*, edited by S.P. Clark, Jr., *Memoir 97*, Geol. Soc. Amer., Boulder, Colo., pp. 223-289, 1966.

Harris, S. A., The aureole of Olympus Mons, Mars, *J. Geophys. Res.*, *82*, 3099-3107, 1977.

Holcomb, R. T., The caldera of East Molokai volcano, Hawaiian Islands, in *National Geographic Society Research Reports (for 1980-1983)*, *21*, 81-87, 1985.

Lipman, P. W., J. P. Lockwood, R. T. Okamura, D. A. Swanson, and K. M. Yamashita, Ground deformation associated with the 1975 magnitude-7.2 earthquake and resulting changes in activity of Kilauea volcano, Hawaii, *U. S. Geol. Survey Prof. Paper 1276*, 45 pp., 1985.

Lopes, R. M. C., J. E. Guest, and C. J. Wilson, Origin of the Olympus Mons aureole and perimeter scarp, *Moon Planets*, *22*, 221-234, 1980.

McGarr A., On the state of lithospheric stress in the absence of applied tectonic forces, *J. Geophys. Res.*, *93*, 13,609-13,617, 1988.

McNutt, M. K., Lithospheric flexure and thermal anomalies, *J. Geophys. Res.*, *89*, 11,180-11,194, 1984.

Melosh, H. J., and A. Rafesky, The dynamical origin of subduction zone topography, *Geophys. J. R. Astron. Soc.*, *60*, 333-354, 1980.

Melosh, H. J., and A. Rafesky, Anelastic response of the Earth to a dip slip earthquake, *J. Geophys. Res.*, *88*, 515-526, 1983.

Melosh, H. J., and C. A. Williams, Jr., Mechanics of graben formation in crustal rocks: A finite element analysis, *J. Geophys. Res.*, *94*, 13,961-13,973, 1989.

Moore, J. G., Giant submarine landslides on the Hawaiian Ridge, *U. S. Geol. Survey Prof. Paper 501-D*, pp. D95-D98, 1964.

Moore, J. G., D. A. Clague, R. T. Holcomb, P. W. Lipman, W. R. Normark, and M. E. Torresan, Prodigious submarine landslides on the Hawaiian ridge, *J. Geophys. Res., 94*, 17,465-17,484, 1989.

Morris, E. C., The basal scarp of Olympus Mons (abstract), *Reports of the Planetary Geology Program-1988, NASA TM 84211*, 389-390, 1981.

Nakamura, K., Volcanoes as possible indicators of tectonic stress orientation - principle and proposal, *J. Volcanol. Geotherm. Res., 2*, 1-16, 1977.

Nakamura, K., Why do long rift zones develop in Hawaiian volcanoes - a possible role of thick oceanic sediments, *Bull. Volcanol. Soc. Japan, 25*, 255-269, 1980.

Peterson, D. W., and R. B. Moore, Geologic history and evolution of geologic concepts, island of Hawaii, *U. S. Geol. Survey Prof. Paper 1350*, 149-189, 1987.

Ryan M. P., The mechanics and three-dimensional internal structure of active magmatic systems: Kilauea volcano, Hawaii, *J. Geophys. Res., 93*, 4213-4248, 1988.

Schultz, R. A., and M. T. Zuber, Why are strike-slip faults that are "predicted" by lithospheric deformation models rarely observed on planetary surfaces?, *Lunar Planet. Sci. , 23*, 1247-1248, Lunar and Planetary Institute, Houston, 1992.

Scott, D. H., and K. L. Tanaka, Map showing lava flows in the northeast part of the Phoenicis Lacus quadrangle of Mars, Map I-1277, U. S. Geol. Surv., Reston, Va., 1981.

Scott, D. H., G. G. Schaber, K. C. Horstmann, A. L. Dial Jr., and K. L. Tanaka, Map showing lava flows in the southwest part of the Tharsis quadrangle of Mars, Map I-1268, U.S. Geol. Surv., Reston, Va., 1981a.

Scott, D. H., G. G. Schaber, and K. L. Tanaka, Map showing lava flows in the southeast part of the Tharsis quadrangle of Mars, Map I-1269, U. S. Geol. Surv., Reston, Va., 1981b.

Scott D. H., G. G. Schaber, K. C. Horstmann, A. L. Dial Jr., and K. L. Tanaka, Map showing lava flows in the northwest part of the Phoenicis Lacus quadrangle of Mars, Map I-1272, U. S. Geol. Surv., Reston, Va, 1981c.

Solomon, S. C., and J. W. Head, Heterogeneities in the thickness of the elastic lithosphere of Mars: Constraints on heat flow and internal dynamics, *J. Geophys. Res., 95*, 11,073-11,083, 1990.

ten Brink, U. S., and T. M. Brocher, Multichannel seismic evidence for a subcrustal intrusive complex under Oahu and a model for Hawaiian volcanism, *J. Geophys. Res., 92*, 13,687-13,707, 1987.

Tanaka, K. L., Ice-lubricated gravity spreading of the Olympus Mons aureole deposits, *Icarus, 62*, 191-206, 1985.

Tanaka, K. L., The stratigraphy of Mars, *Proc. Lunar Planet. Sci. Conf. 17th, J. Geophys. Res., 91*, E139-E158, 1986.

Thomas, P. J., S. W. Squyres, and M. H. Carr, Flank tectonics of Martian volcanoes, *J. Geophys. Res., 95*, 14,345-14,355, 1990.

Thurber, C. H., and A. E. Gripp, Flexure and seismicity beneath the south flank of Kilauea volcano and tectonic implications, *J. Geophys. Res., 93*, 4271-4278, 1988.

Turcotte, D. L., and G. Schubert, *Geodynamics*, Wiley, New York. 450 pp, 1982.

U. S. Geological Survey, Topographic maps of the western, eastern equatorial and polar regions of Mars, Map I-2030, U. S. Geol. Surv., Washington, D.C., 1989.

Wu, S. S. C., Mars synthetic topographic mapping, *Icarus, 33*, 417-440, 1978.

Wu, S. S. C., P. A. Garcia, R. Jordan, F. J. Schafer, and B. A. Skiff, Topography of the shield volcano, Olympus Mons on Mars, *Nature, 309*, 432-435, 1984.

Wyss, M. and R. Y. Koyanagi, Seismic gaps in Hawaii, *Bull. Seismol. Soc. Am., 82*, 1373-1387, 1992.

Zimbleman, J. R., and K. S. Edgett, The Tharsis Montes, Mars: Comparison of volcanic and modified landforms, *Proc. Lunar Planet. Sci., 22*, 31-44, 1992.

Zuber, M. T., and P. J. Mouginis-Mark, Caldera subsidence and magma chamber depth of the Olympus Mons volcano, Mars, *J. Geophys. Res., 97*, 18,295-18,307, 1992.

P.J. McGovern, Building 54-521, Department of Earth, Atmospheric, and Planetary Sciences, Massachusetts Institute of Technology, Cambridge MA 02139.

S. C. Solomon, Department of Terrestrial Magnetism, Carnegie Institution of Washington, 5241 Broad Branch Road, N. W., Washington, DC 20015.

FIGURE CAPTIONS

Figure 1. Viking Orbiter view of Olympus Mons. The multiple-pit caldera and basal scarp (at bottom) are the main tectonic features visible. No graben are seen on the flanks of the volcano or on the volcanic plains immediately surrounding the structure. Frame VO641A52; width of image is 440 km.

Figure 2. (a) Viking Orbiter view of western Ascraeus Mons. The complex caldera is seen at the summit, and graben with a predominantly circumferential orientation are seen along the western and southwestern margins. Graben are located on Ascraeus Mons itself and in surrounding flows (unit as, Figure 3); some graben grade into collapse pits or sinuous channels formed by magma withdrawal and downslope flow. Frame VO643A78; width of image is 420 km. (b) Viking Orbiter mosaic of the western flank of Arsia Mons [Eliason et al. 1991]. Note that graben extend all the way up the flank to the edge of the summit caldera. (c) Viking Orbiter mosaic of the eastern flank of Arsia Mons [Eliason et al. 1991]. Note the lack of graben and the radial texture of flows on the upper flank. Graben are evident near the boundary between the edifice and the surrounding plain.

Figure 3. Geologic map of Ascraeus Mons and surroundings, simplified from Scott et al. [1981b] by Comer et al. [1985]. Volcanic units shown include relatively young Ascraeus Mons flows (as), intermediate-age Tharsis Montes flows (tm), and volcanic material undivided by age (vu). Also shown as a distinct unit is slide material (s), interpreted by Scott and coworkers as landslides and debris flows. Dashed lines show approximate elevation contours, in kilometers, relative to a fourth-degree, fourth-order equipotential [Wu, 1978]. The summit caldera complex is indicated by inward hatched lines. Extensional faults and graben are shown as heavy lines.

Figure 4. Geologic map of Pavonis Mons and surroundings, simplified from Scott et al. [1981a, b, c] and Scott and Tanaka [1981] by Comer et al. [1985]. Units shown, in addition to those described in Figure 3, are relatively young volcanic flows from Pavonis Mons (pm) and Arsia Mons (am). Other information follows the format of Figure 3. Circumferential graben reach

quite far up the slopes, and an approximate bilateral symmetry can be seen about an axis trending approximately NNE-SSW.

Figure 5. Geologic map of Arsia Mons and surroundings, simplified form *Scott et al.* [1981c] by *Comer et al.* [1985]. See Figures 3 and 4 for further explanation of symbols. Circumferential graben extend almost up to the summit caldera complex.

Figure 6. (a) The finite element grid used for the calculations shown in later figures. The volcano is the small triangular area in the upper left-hand corner. (b) Plot of element types for models with incremental volcano loading, implemented by means of time-dependent element properties. Elements marked with a "3" are "on" from the start of the calculation; those with a "4" are switched "on" after 1000 Maxwell times, and those with a "5" are switched "on" after 2000 Maxwell times.

Figure 7. Comparisons of the TECTON solution and analytic thick-plate flexure [*Comer*, 1983] for vertical displacements resulting from an axisymmetric load simulating a conical volcano. For both cases, $T_e = t_c = 40$ km. (a) surface elevation relative to that at $r = r_{max}$ after essentially complete viscoelastic relaxation in the asthenosphere; (b) difference between the two solutions.

Figure 8. Key for stress symbols in models. These symbols denote the principal stress directions under axisymmetry. The hourglass shapes are oriented along the direction of greatest compressive stress, the bars along the direction of least compressive stress. Magma is expected to ascend locally along the plane orthogonal to the least compressive stress, that is, perpendicular to the bar.

Figure 9. Principal stress orientations and predicted failure in the vicinity of an incrementally grown volcano load on a 40-km-thick elastic lithosphere. See Figure 8 for the meaning of the stress orientation symbols. Elements in which stresses satisfy the Mohr-Coulomb failure criterion are shaded. Given the orientation of the stress symbol in a shaded element, the style and orientation of faulting can be inferred. (a) The elastic solution. (b-d) 20, 100, and 1000 Maxwell times after the first load increment is added; (e-f) 20 and 1000 Maxwell times after the

second load increment is added; and (g) 1000 Maxwell times after the third load increment is added.

Figure 10. Contours of maximum deviatoric stress in the vicinity of the volcano, for the model of Figure 9. Contour interval is 50 MPa. (a) The elastic solution. (b-d) 1000 Maxwell times after the first, second, and third load increments are added, respectively.

Figure 11. Principal stress orientations and predicted failure for an incrementally grown volcano load on a lithosphere with $T_e = 20$ km. (a) 1000 Maxwell times after the first load increment is added; (b) 1000 Maxwell times after the third load increment is added.

Figure 12. Contours of maximum deviatoric stress for the model of Figure 11. (a) 1000 Maxwell times after the first load increment is added; (b) 1000 Maxwell times after the third load increment is added.

Figure 13. Principal stress orientations and predicted failure for an incrementally grown volcano load on a lithosphere with $T_e = 60$ km, 1000 Maxwell times after the third load increment is added.

Figure 14. Contours of maximum deviatoric stress for the model of Figure 13, 1000 Maxwell times after the third load increment is added.

Figure 15. Principal stress orientations and predicted failure for an incrementally grown volcano load on a crust 40 km thick and on an elastic lithosphere 60 km thick, 1000 Maxwell times after the third load increment is added.

Figure 16. Contours of maximum deviatoric stress for the model of Figure 15, 1000 Maxwell times after the third load increment is added.

Figure 17. Principal stress orientations and predicted failure for an instantaneous volcano load on a lithosphere with $T_e = 40$ km, after 1000 Maxwell times.

Figure 18. Contours of maximum deviatoric stress for the model of Figure 17, after 1000 Maxwell times.

Figure 19. Principal stress orientations and predicted failure for a model with a growing volcano load, a basal detachment between lithosphere and volcano, and crust and elastic lithosphere 40

km thick. (a-b) 10 and 1000 Maxwell times after the first load increment is added; (c) 1000 Maxwell times after the third load increment is added.

Figure 20. Contours of maximum deviatoric stress for the model of Figure 19. (a) 1000 Maxwell times after the first load increment is added; (b) 1000 Maxwell times after the third load increment is added.

Figure 21. Principal stress orientations and predicted failure for a growing volcano load with isotropic prestress in the lithosphere. Crust and elastic lithosphere are 40 km thick. (a-b) 40 and 1000 Maxwell times after the first load increment is added; (c) 1000 Maxwell times after the third load increment is added.

Figure 22. Mohr diagrams for typical elements in regions of predicted failure. Diagonal line is the Mohr-Coulomb failure envelope for basalt [*Handin*, 1966] with an angle of internal friction $\phi =$ 49° and cohesion $c = 38$ MPa. (a) Mohr diagram for an element at the top of the lithosphere (stresses calculated at element center: $r = 265$ km, $z = -2.5$ km). In order of increasing radius, the circles represent the stress state at $t = 0$ (elastic solution), 20, 100, 1000, 2000, and 3000 τ_M. When the failure envelope is first exceeded ($t = 70 \tau_m$), $\sigma_3 = \sigma_{rr}$ and $\sigma_1 = \sigma_{zz}$. At the final time shown, $\sigma_3 = \sigma_{rr}$ and $\sigma_1 = \sigma_{\theta\theta}$. See Figure 9 for the principal stresses used to calculate circles.

TABLE 1. Dimensions of Tharsis Volcanoes

Volcano	Diameter, km	Relief, km
Olympus Mons	600[a]	24[a]
Ascraeus Mons	400[b]	18[b]
Pavonis Mons	320[b]	14[b]
Arsia Mons	420[b]	19[c]

[a] *Wu et al.* (1984).

[b] *Blasius and Cutts* (1976).

[c] *Blasius and Cutts* (1981).

TABLE 2. Adopted Parameter Values

Parameter	Crust	Mantle
E, Pa	1×10^{11}	3×10^{11}
ρ, kg/m^3	3000	3500
ν	0.25	0.25

	Lithosphere	Asthenosphere
η, Pa s	1×10^{27}	1×10^{21}

TABLE 3. Characteristics of Predicted Near-surface Failure for Each Model.

Model[1] / increment		Inner radius[2], km	Outer radius[2], strike-slip faulting, km	Outer radius[2], normal faulting, km	First observed failure (time, radius, type)
GW40	1	140	230	380	$20\ \tau_M$
	2	150^3	270	440	130-170 km
	3	170^3	300	490	mixed
GW20	1	120	170	280	$30\ \tau_M$
	2	120^3	190	320	120-140 km
	3	140^3	220	360	radial normal
GW60	1	180	270	410	$40\ \tau_M$
	2	180	330	520	170-220 km
	3	190^3	360	590	mixed
GW40/60	1	200	300	430	$40\ \tau_M$
	2	200	350	550	200-220 km
	3	210	390	630	radial normal
IW 40	1	190^3	290	490	$10\ \tau_M$ 200-250 km radial normal
GD40	1	120	240	380	$20\ \tau_M$
	2	130^3	280	440	120-150 km
	3	150^3	310	500	mixed
GWPS40	1	150	290	340	$40\ \tau_M$
	2	160	310	410	140-190 km
	3	170^3	320	470	mixed

[1] Model key:

G = growing volcano,

W = welded volcano,

I = instantaneously emplaced volcano,

D = detached volcano,

PS = isotropic pre-stress applied to lithosphere, integer = elastic lithosphere thickness.

[2] Radius values given at $t = 1000\ \tau_M$ after application of given load increment.

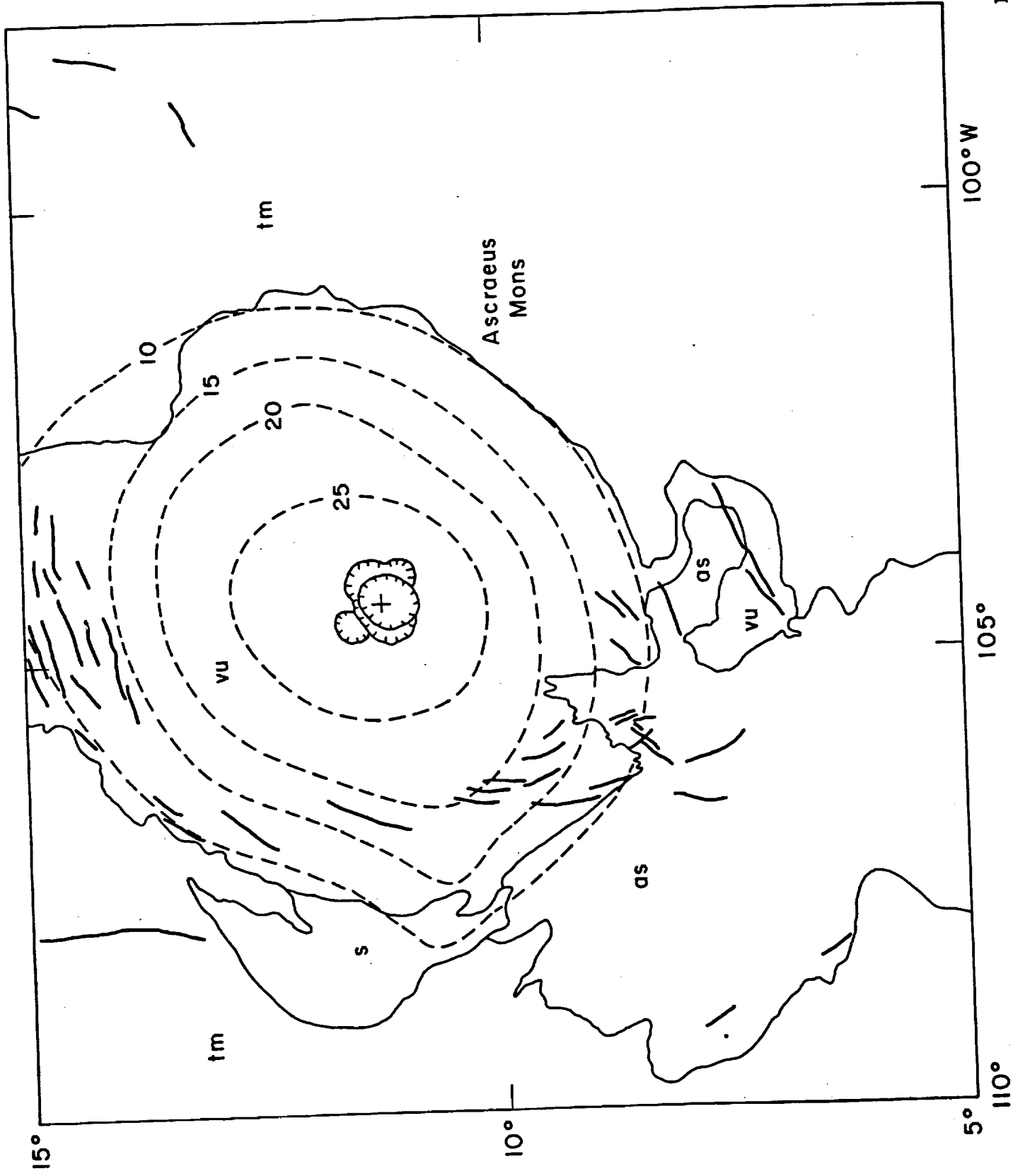[3] Value less than the maximum radius of the volcano at a given load increment
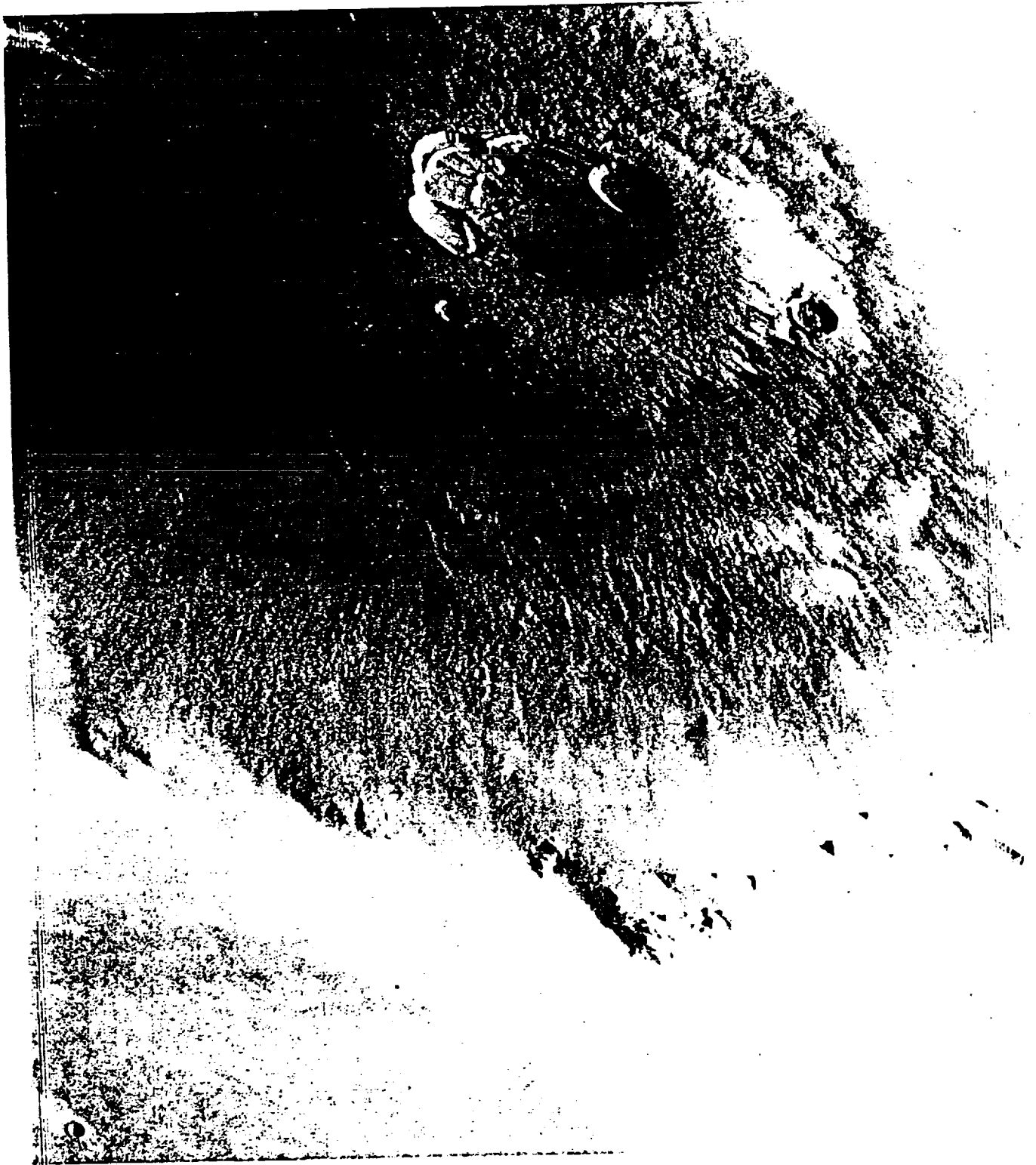
Figure 1
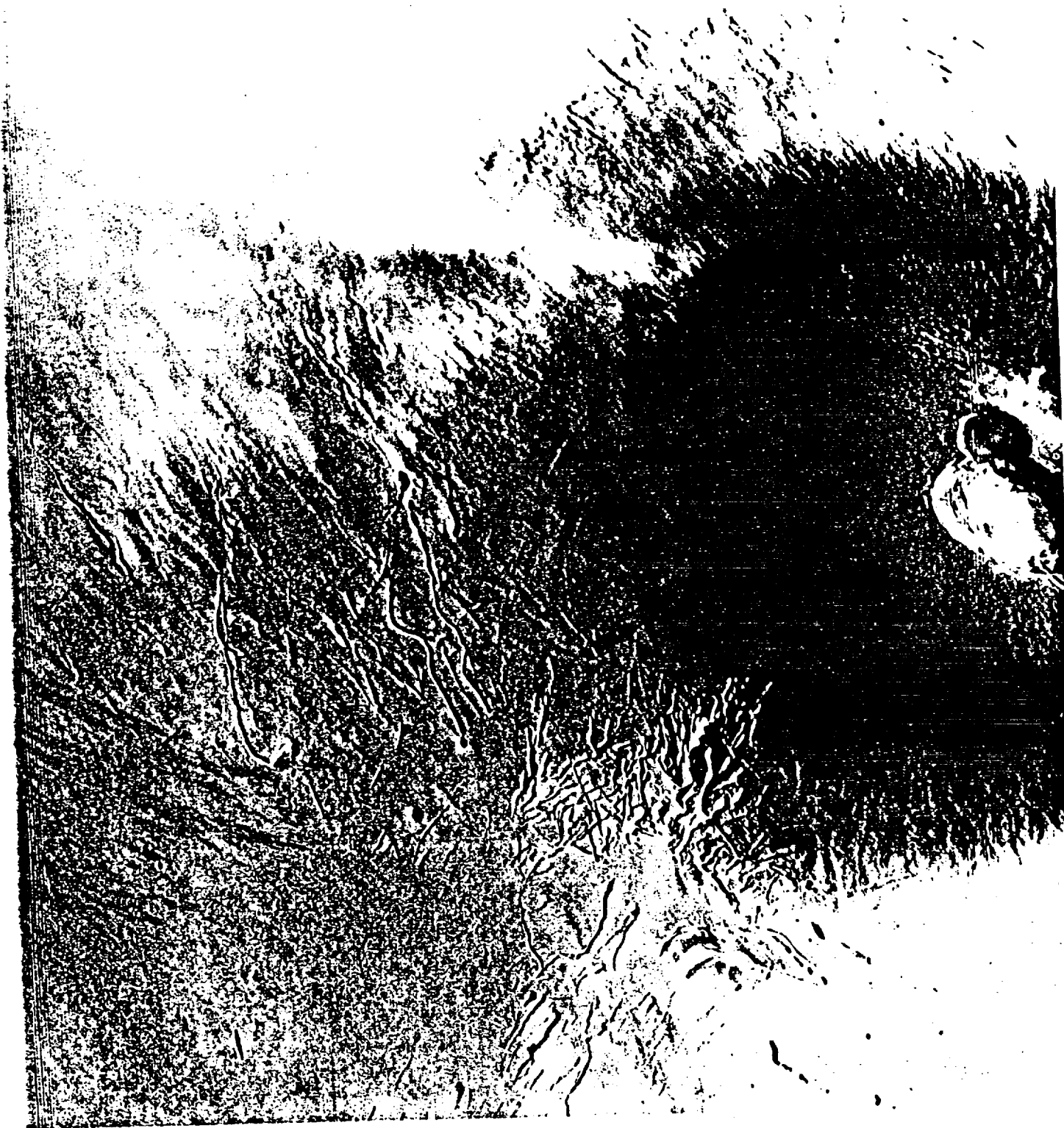
Figure 2a
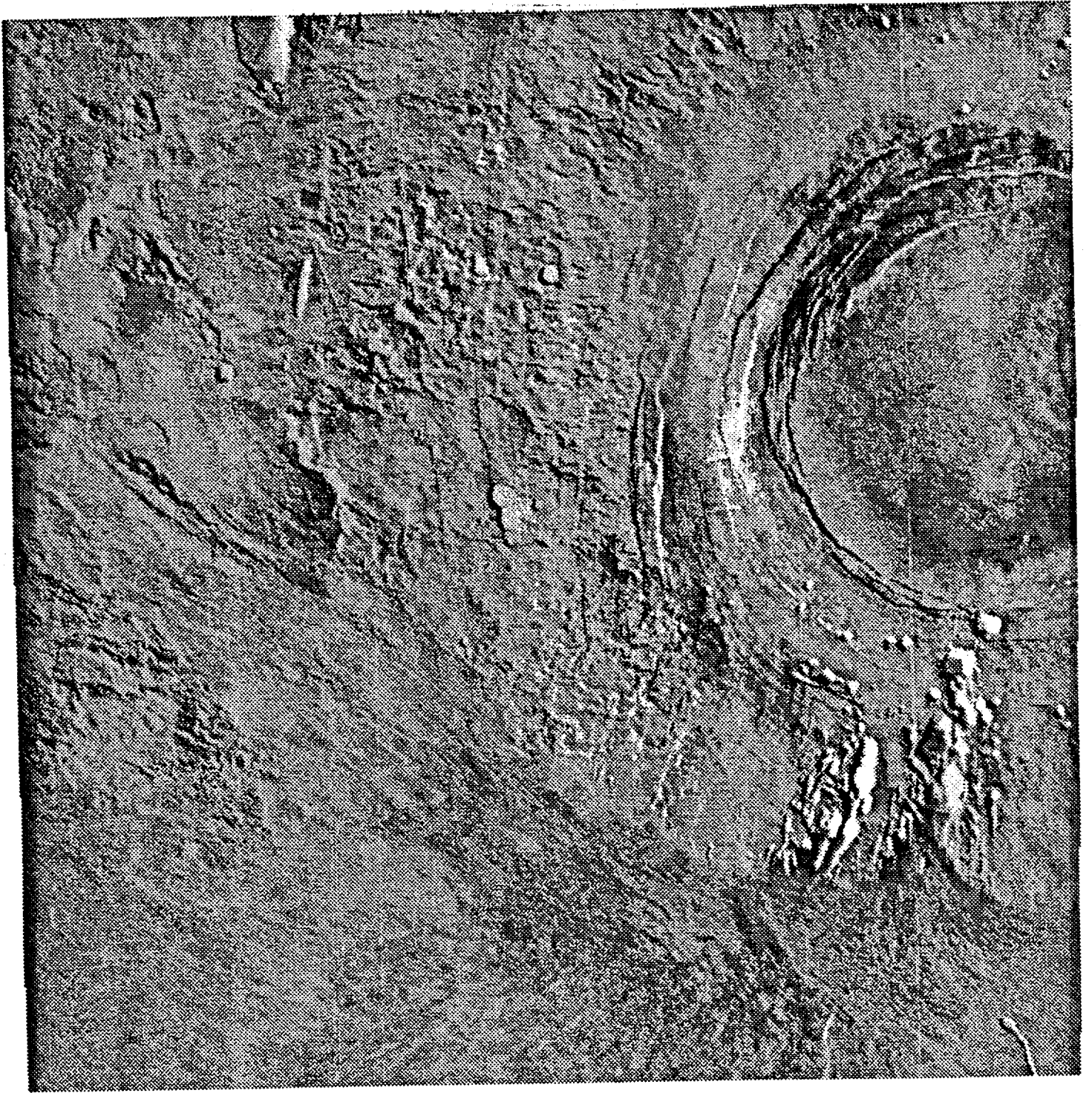
Fig. 2b
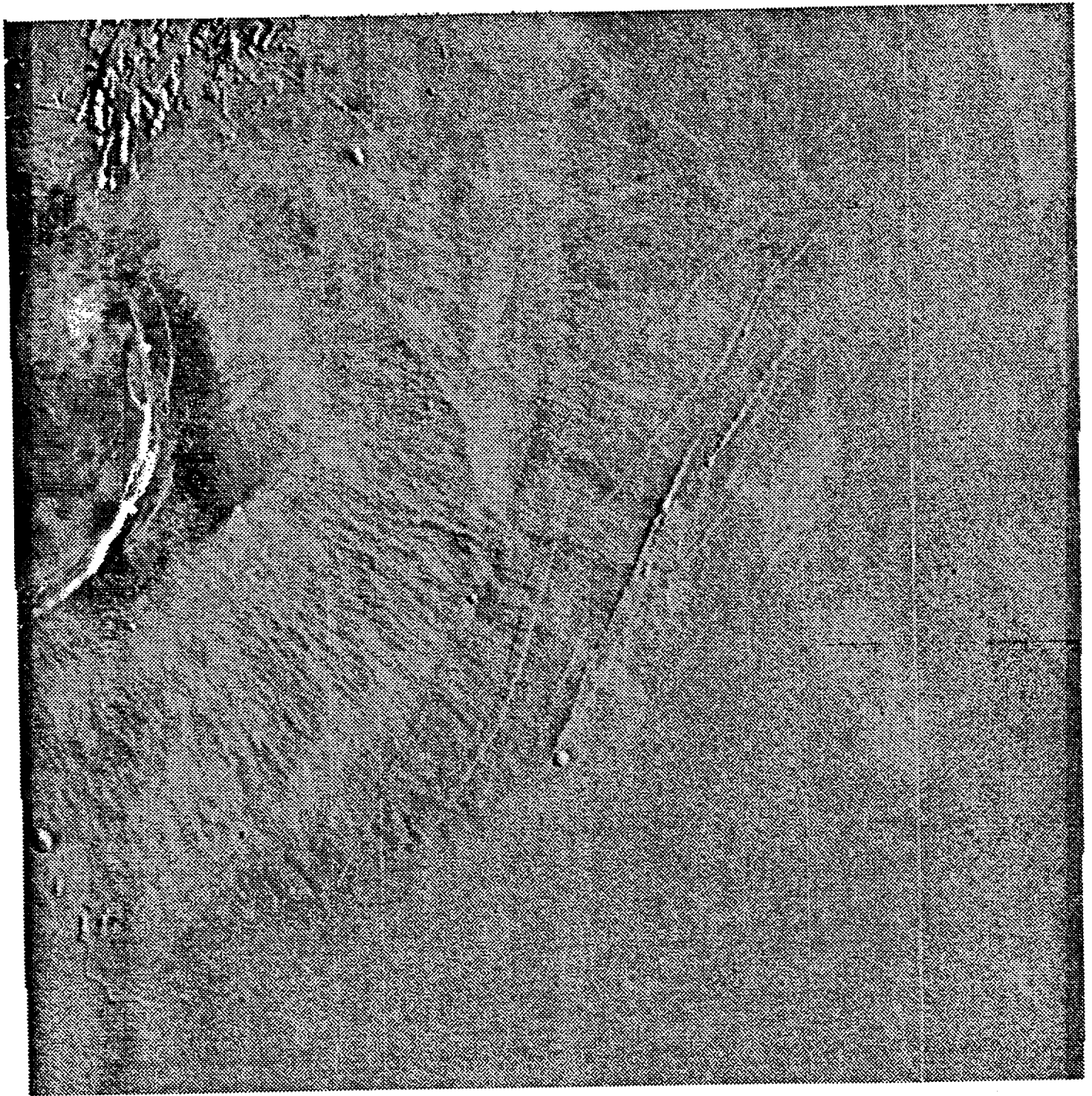
Figure 2c

Figure 3

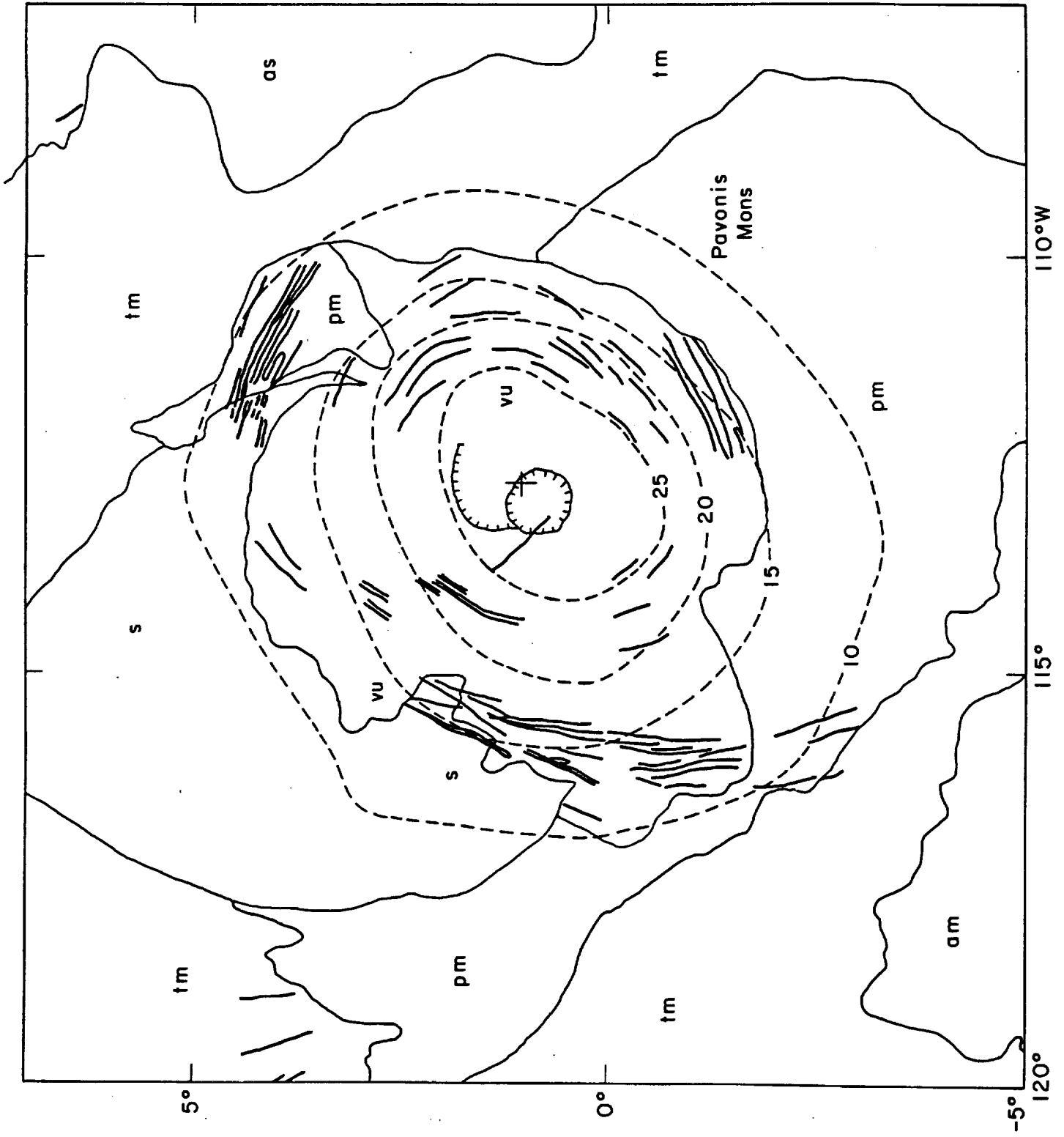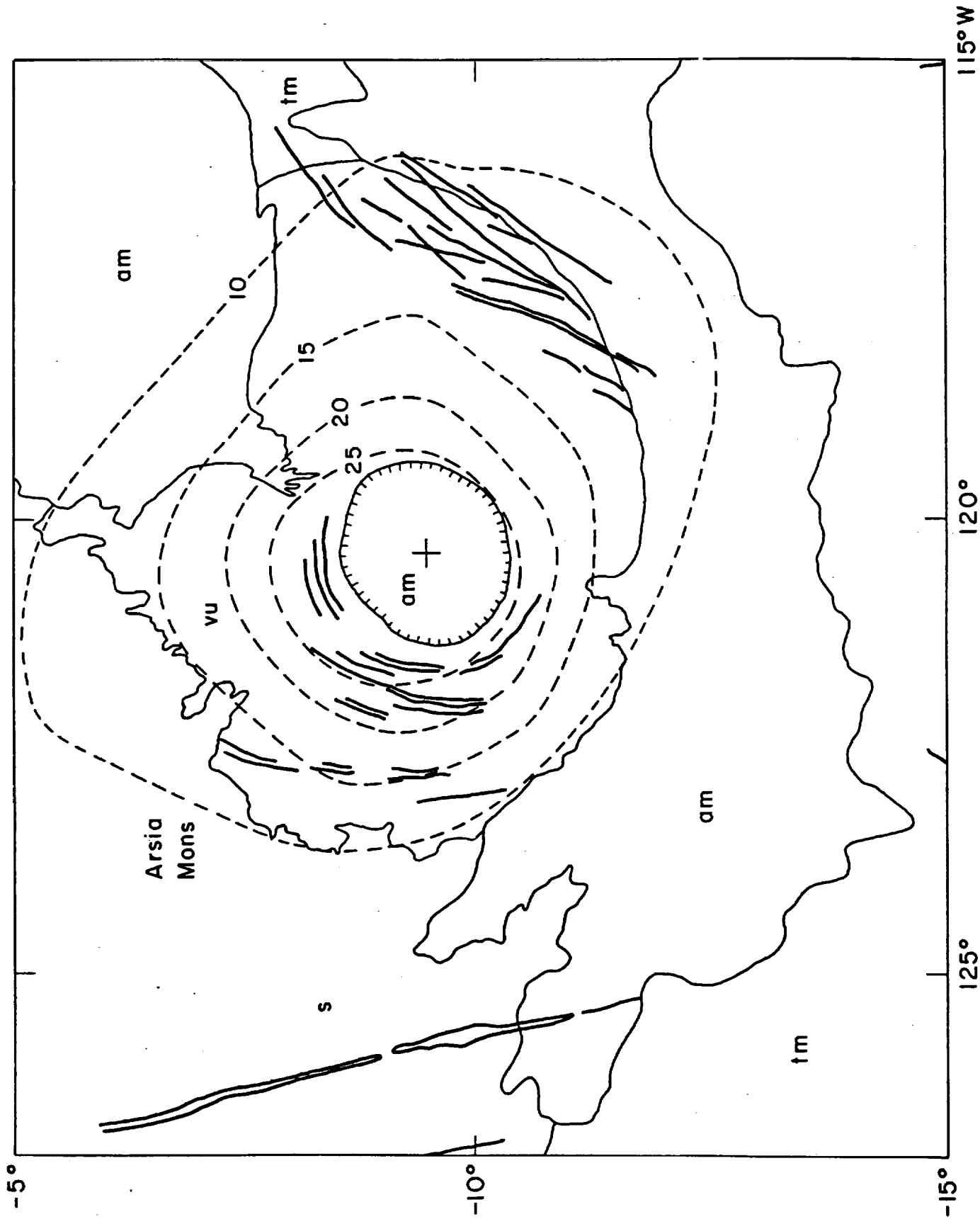Figure 4

Pavonis Mons

as

tm

tm

pm

vu

25

20

15

pm

10

s

vu

s

tm

pm

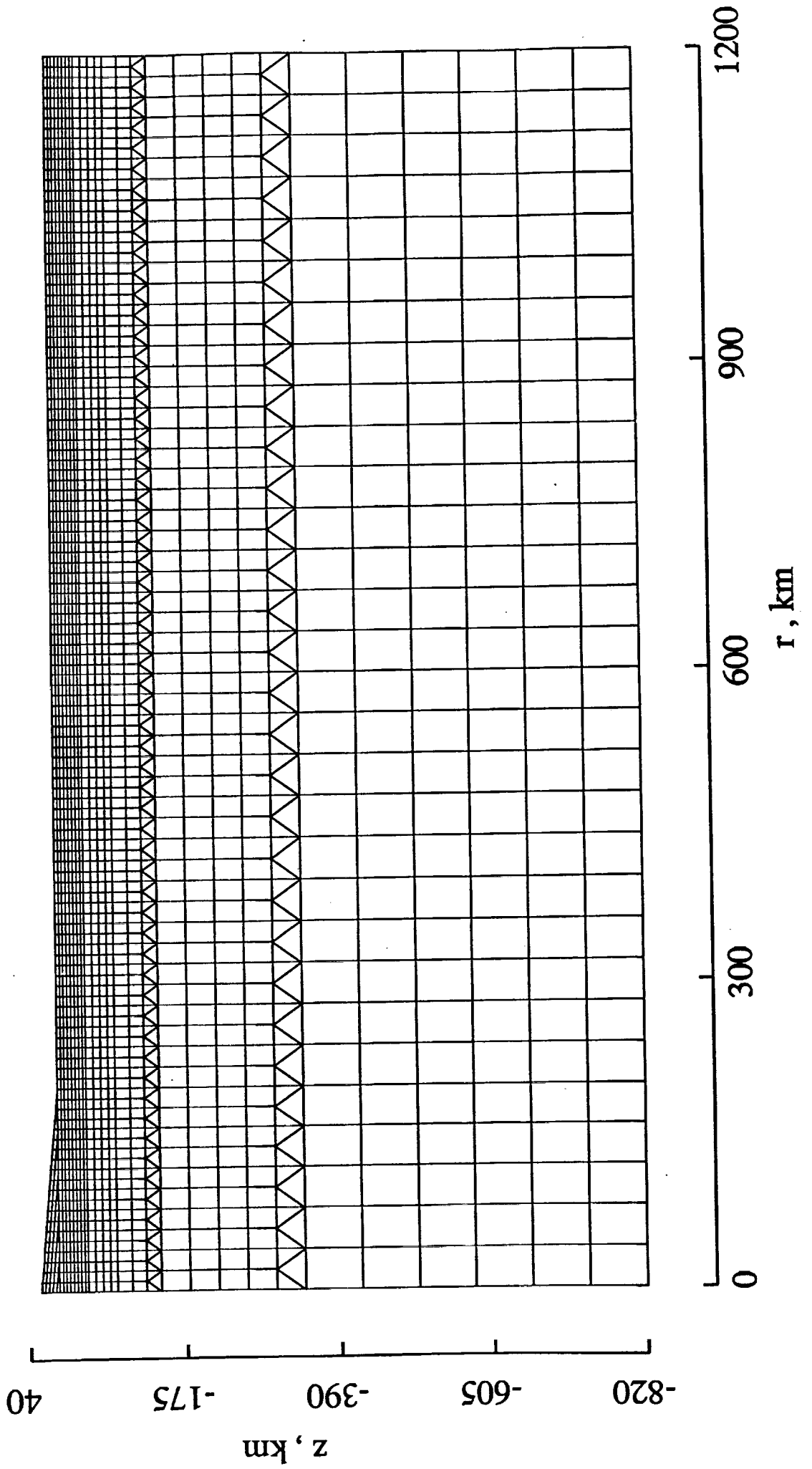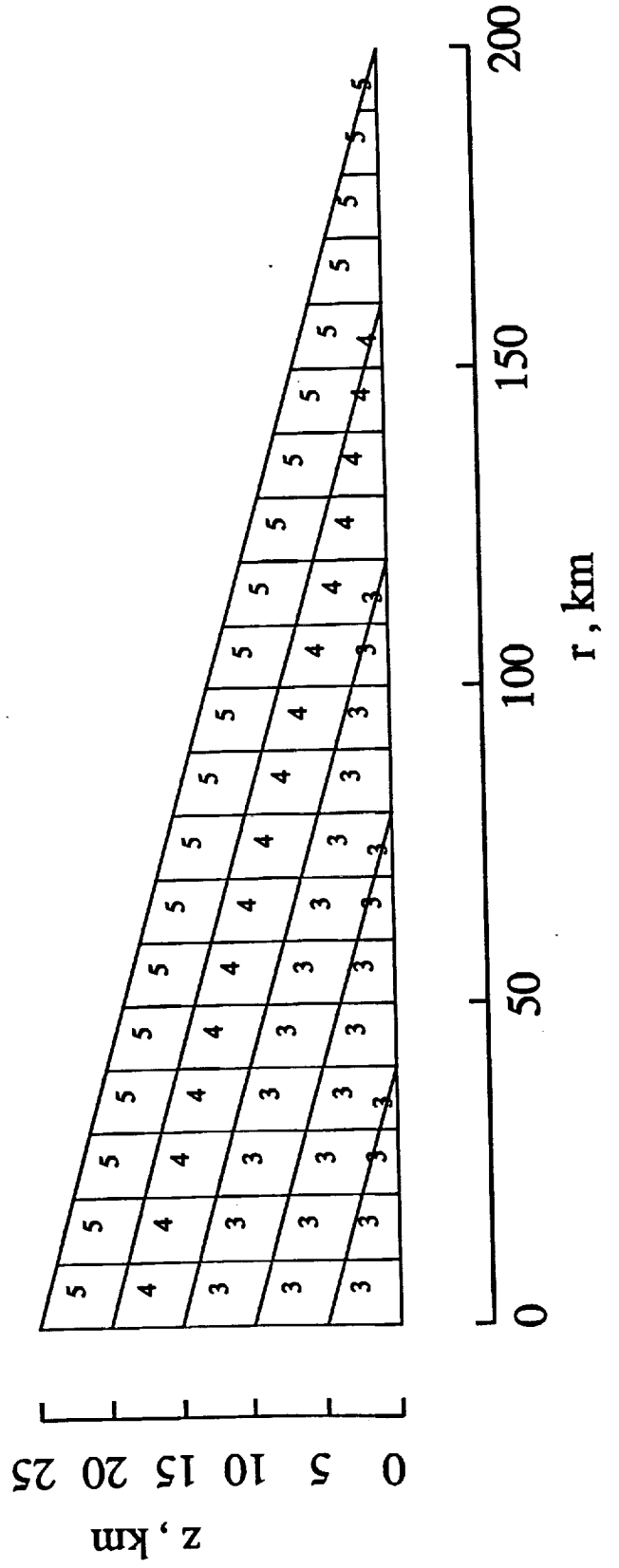tm

am

-5°

0°

-5°

120°

115°

110°W

Figure 5
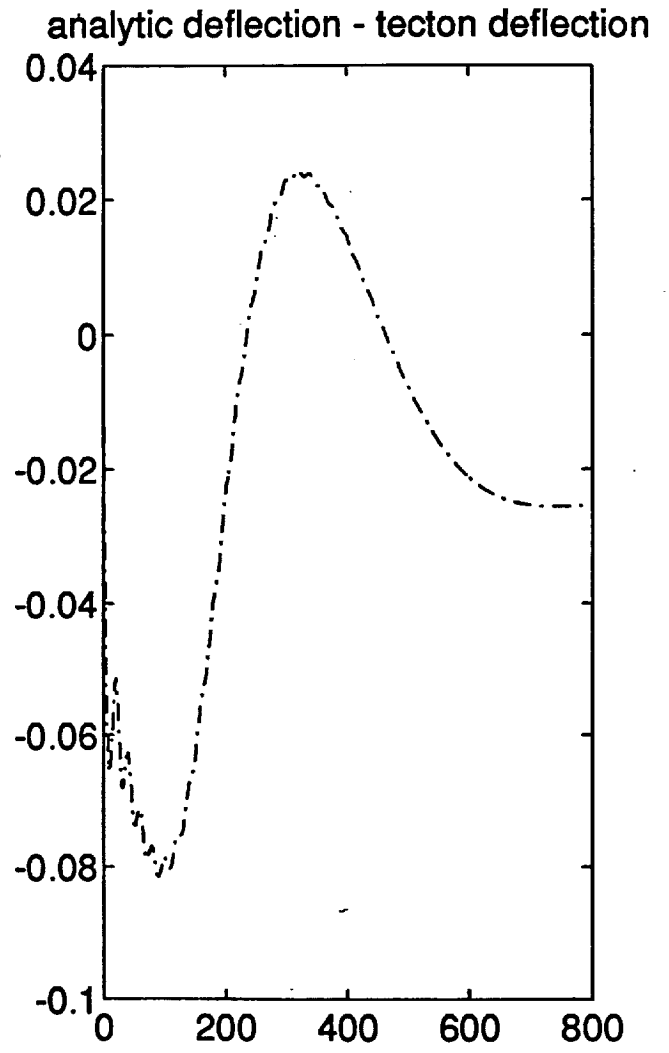
Arsia 2.2 l3 40km
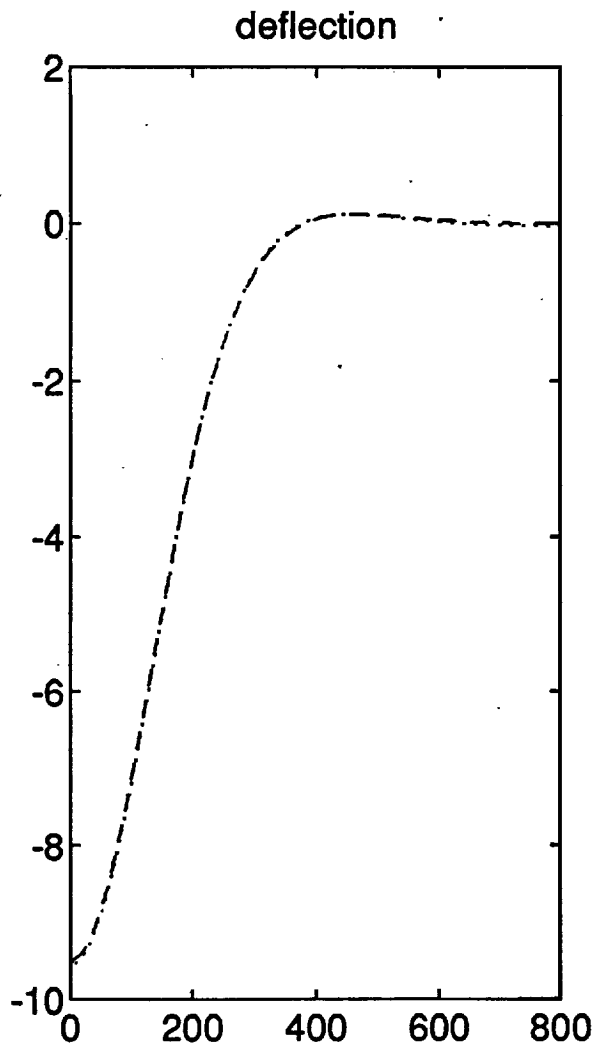
Figure 6a

Arsia 2.2 l3 40km

Figure 6b .

Figure 7

Maximum Stress:

Symbol	Compressive	Extensional	"Predicted" Fault Type
⊠	vertical	horizontal	circumferential normal
⋈	horizonal	vertical	circumferential thrust
⊠	vertical	out of plane	radial normal
⋈	horizontal	out of plane	strike-slip
⊖	out of plane	horizontal	strike-slip
⊕	out of plane	vertical	radial thrust

Figure 8

Figure 8

Arsia 2.2 I3 40km

stress orientation/failure plot

cohesion = 3.50000E+07 pa; phi = 49.0000degrees

time = 0. seconds

full output timestep # 0

Figure 9a

Arsia 2.2 l3 40km

stress orientation/failure plot

cohesion = 3.50000E+07 pa; phi = 49.0000degrees

time = 1.66700E+11 seconds

full output timestep # 4

Figure 9b

Arsia 2.2 l3 40km

stress orientation/failure plot
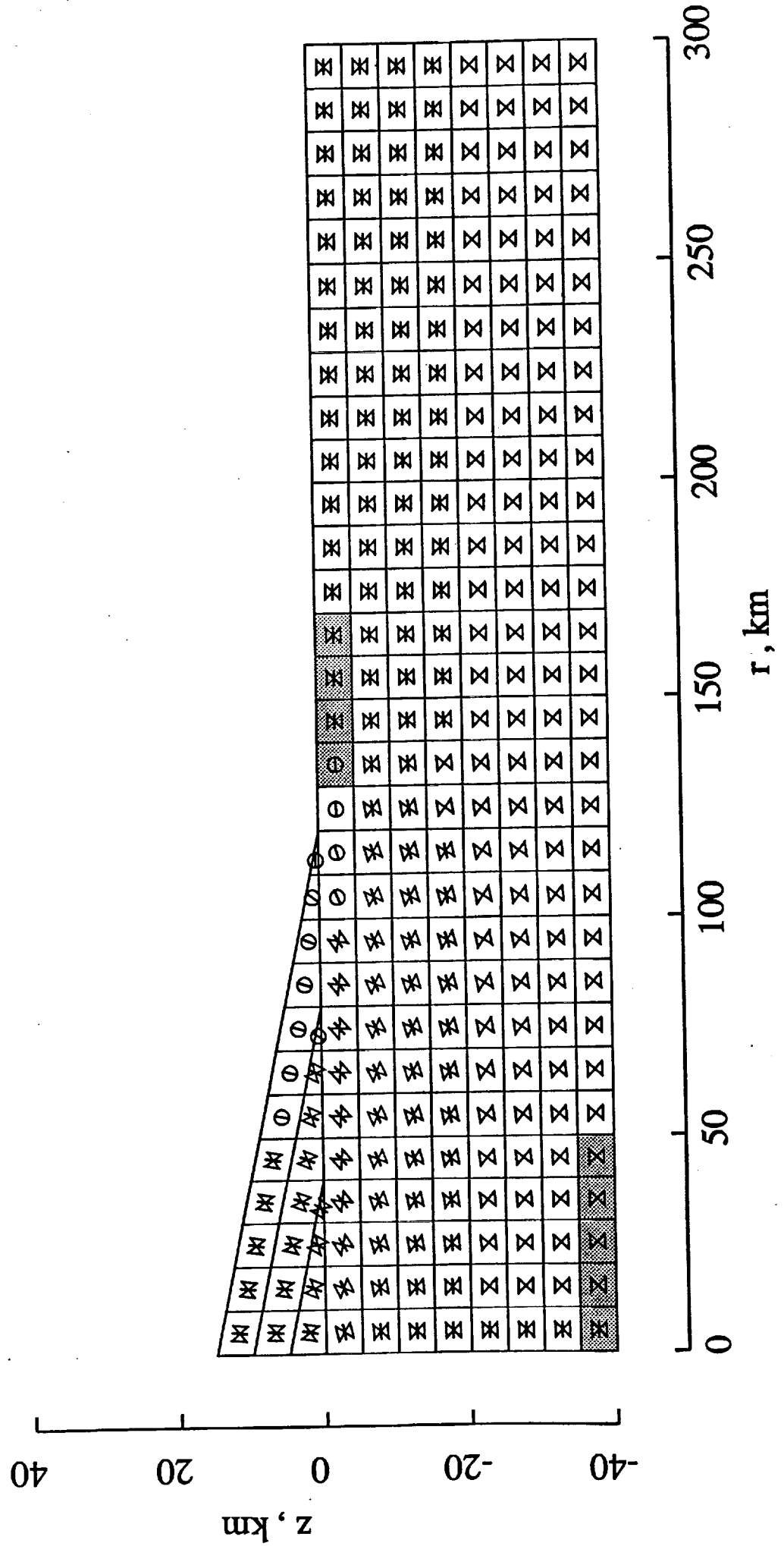
cohesion = 3.50000E+07 pa; phi = 49.0000degrees

time = 8.33400E+11 seconds

full output timestep # 8

Figure 9c

Arsia 2.2 l3 40km

stress orientation/failure plot
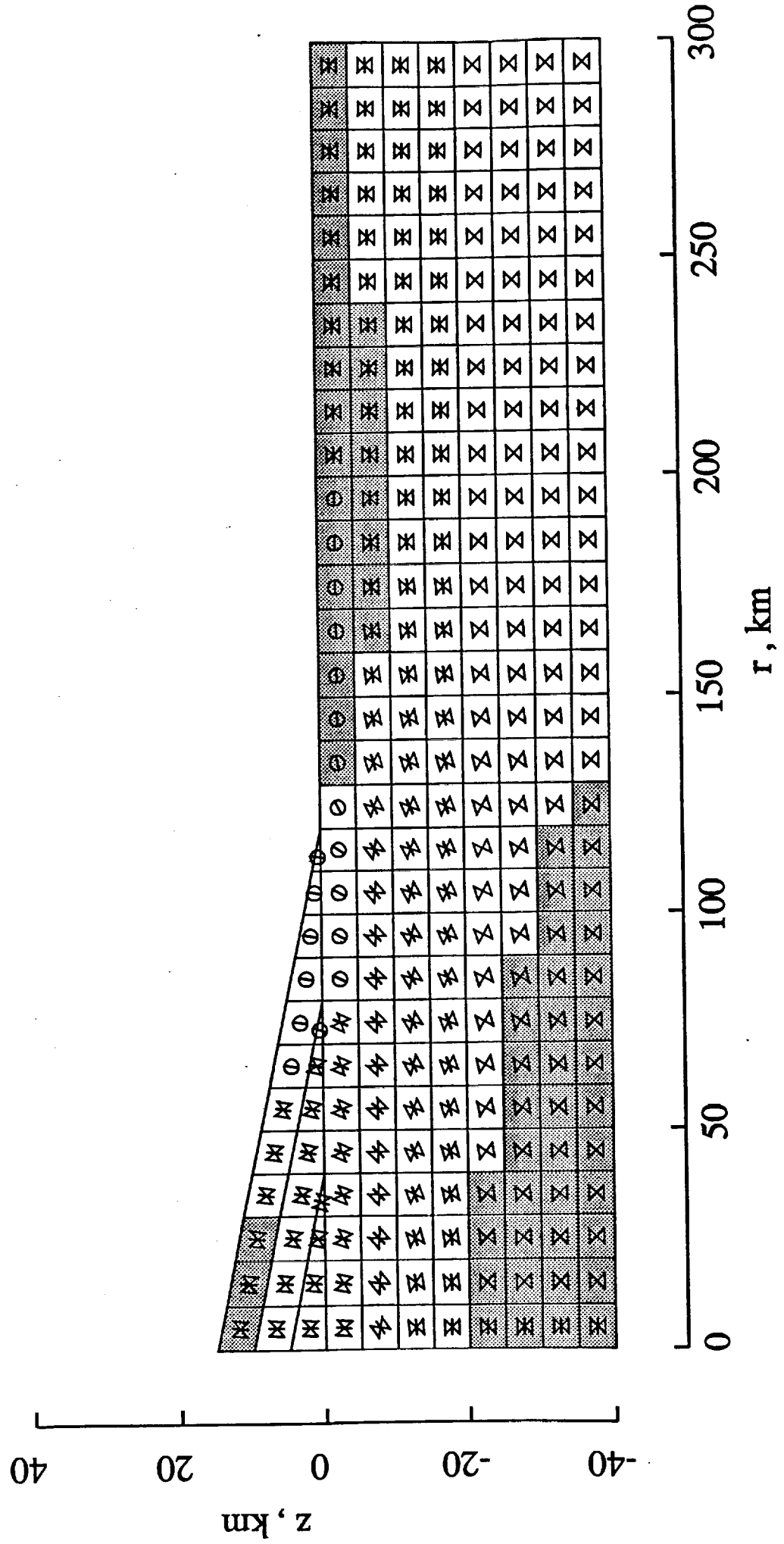
cohesion =   3.50000E+07 pa; phi =   49.0000degrees

time =   8.33300E+12 seconds

full output timestep # 12

Figure 9d

Arsia 2.2 l3 40km

stress orientation/failure plot
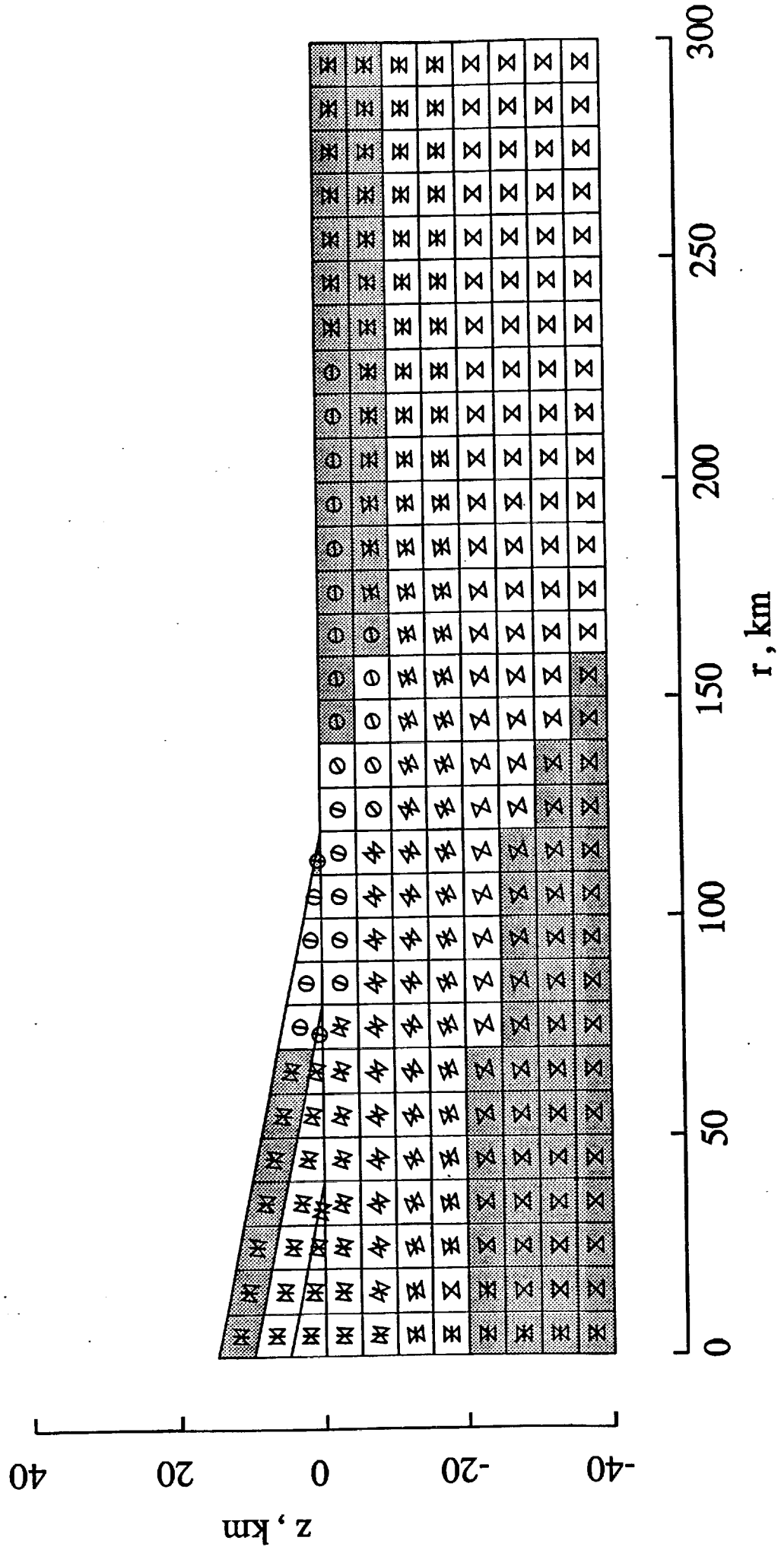
cohesion =   3.50000E+07 pa; phi =   49.0000degrees

time =   8.50000E+12 seconds

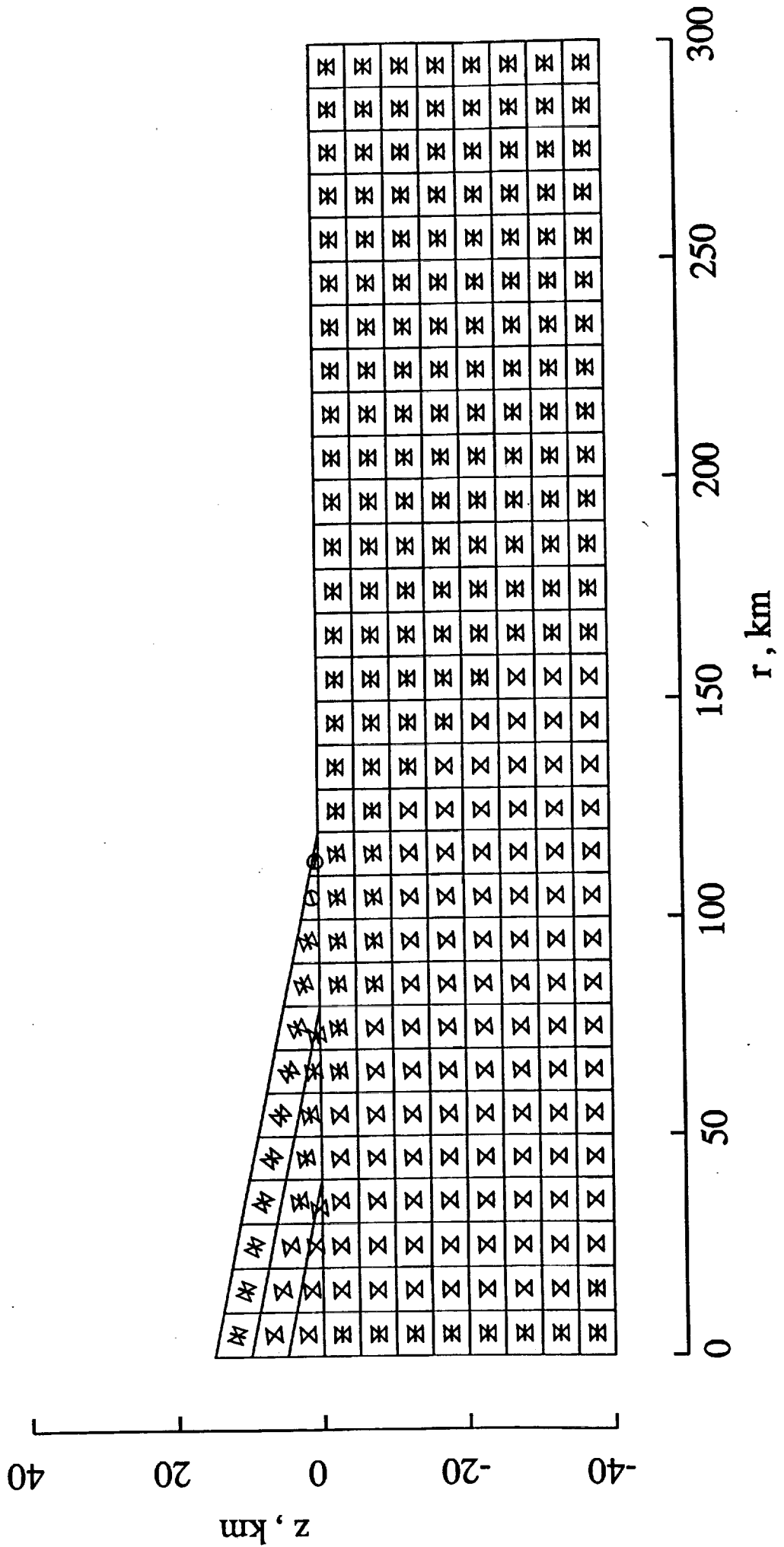full output timestep # 14

Figure 9e

Arsia 2.2 l3 40km

stress orientation/failure plot

cohesion = 3.50000E+07 pa; phi = 49.0000degrees
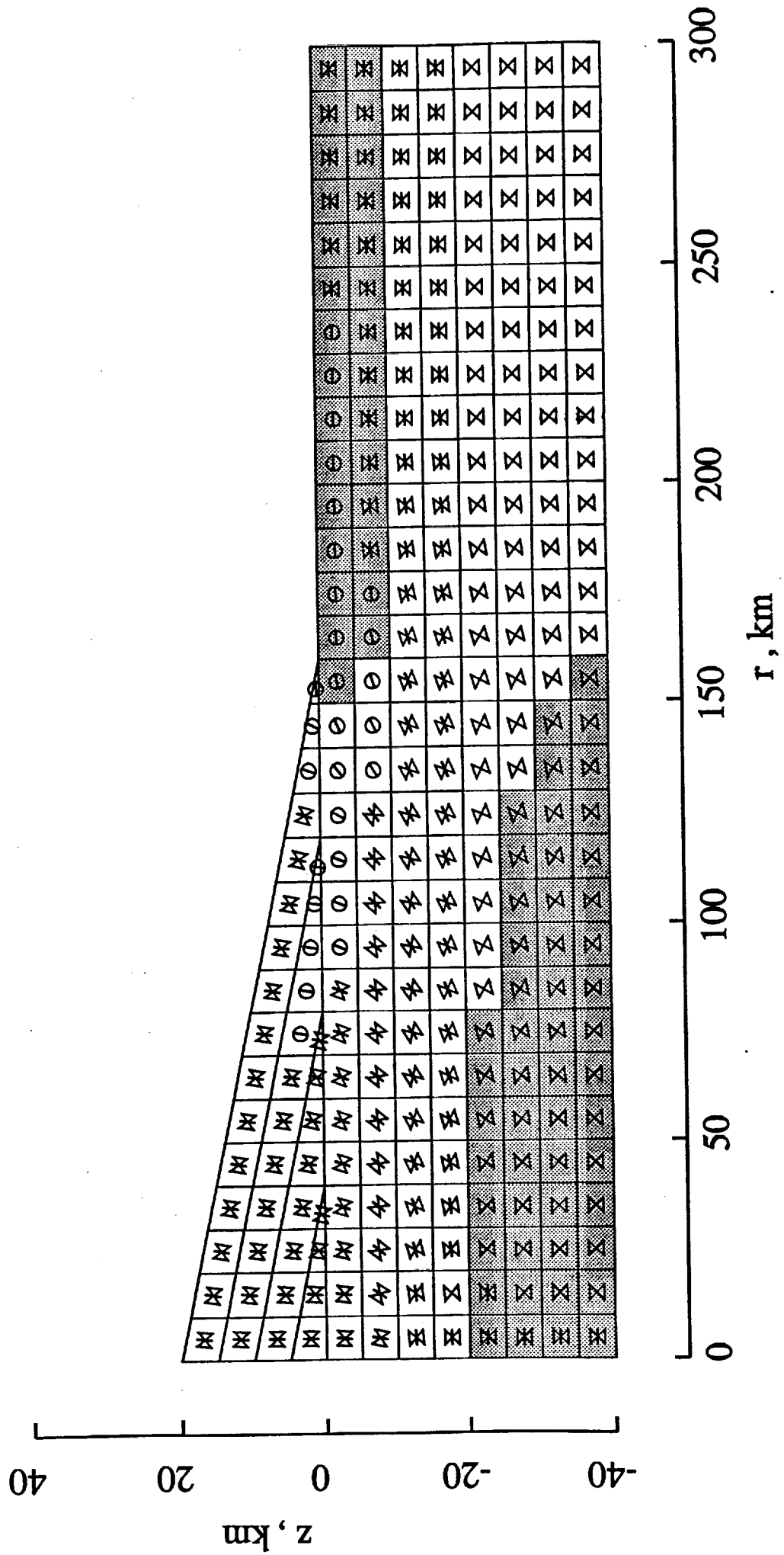
time = 1.66700E+13 seconds

full output timestep # 22

Figure 9f

Arsia 2.2 13 40km

stress orientation/failure plot

cohesion = 3.50000E+07 pa; phi = 49.0000degrees

time = 2.50000E+13 seconds

full output timestep # 32

Figure 9g

Figure 10a

Figure 10b

Figure 10c

Figure 10d

Arsia 2.2 l3 20km

stress orientation/failure plot

cohesion = 3.50000E+07 pa; phi = 49.0000degrees

time = 8.33300E+12 seconds

full output timestep # 12

Figure 11a

Arsia 2.2 13 20km

stress orientation/failure plot

cohesion = 3.50000E+07 pa; phi = 49.0000degrees

time = 2.50000E+13 seconds

full output timestep # 32

Figure 11b

Figure 12a

Figure 12b

Arsia 2.2 l3 60km

stress orientation/failure plot

cohesion = 3.50000E+07 pa; phi = 49.0000degrees

time = 8.33300E+12 seconds

full output timestep # 12

Figure 13a

Arsia 2.2 13 60km

stress orientation/failure plot
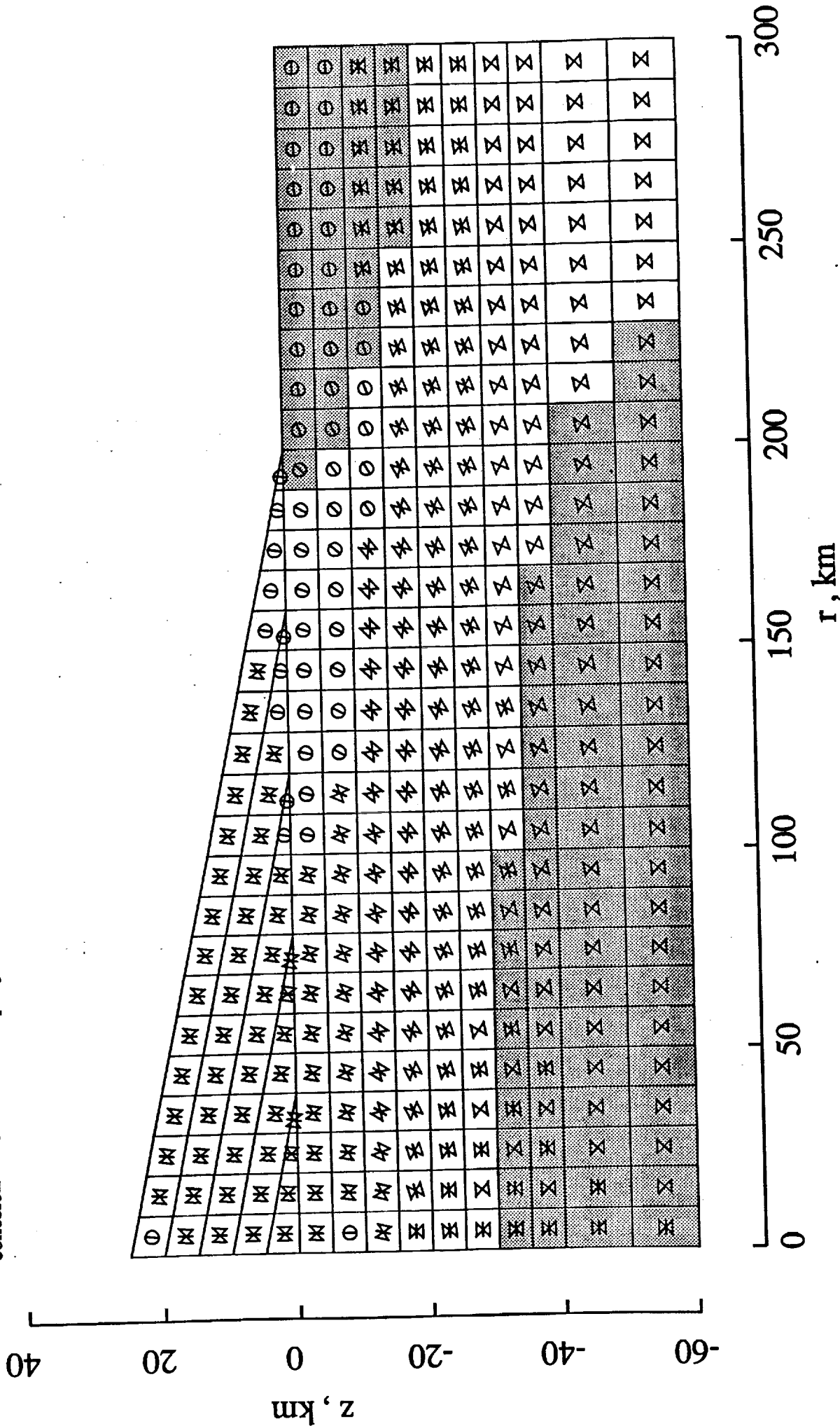
cohesion = 3.50000E+07 pa; phi = 49.0000degrees

time = 2.50000E+13 seconds

full output timestep # 32
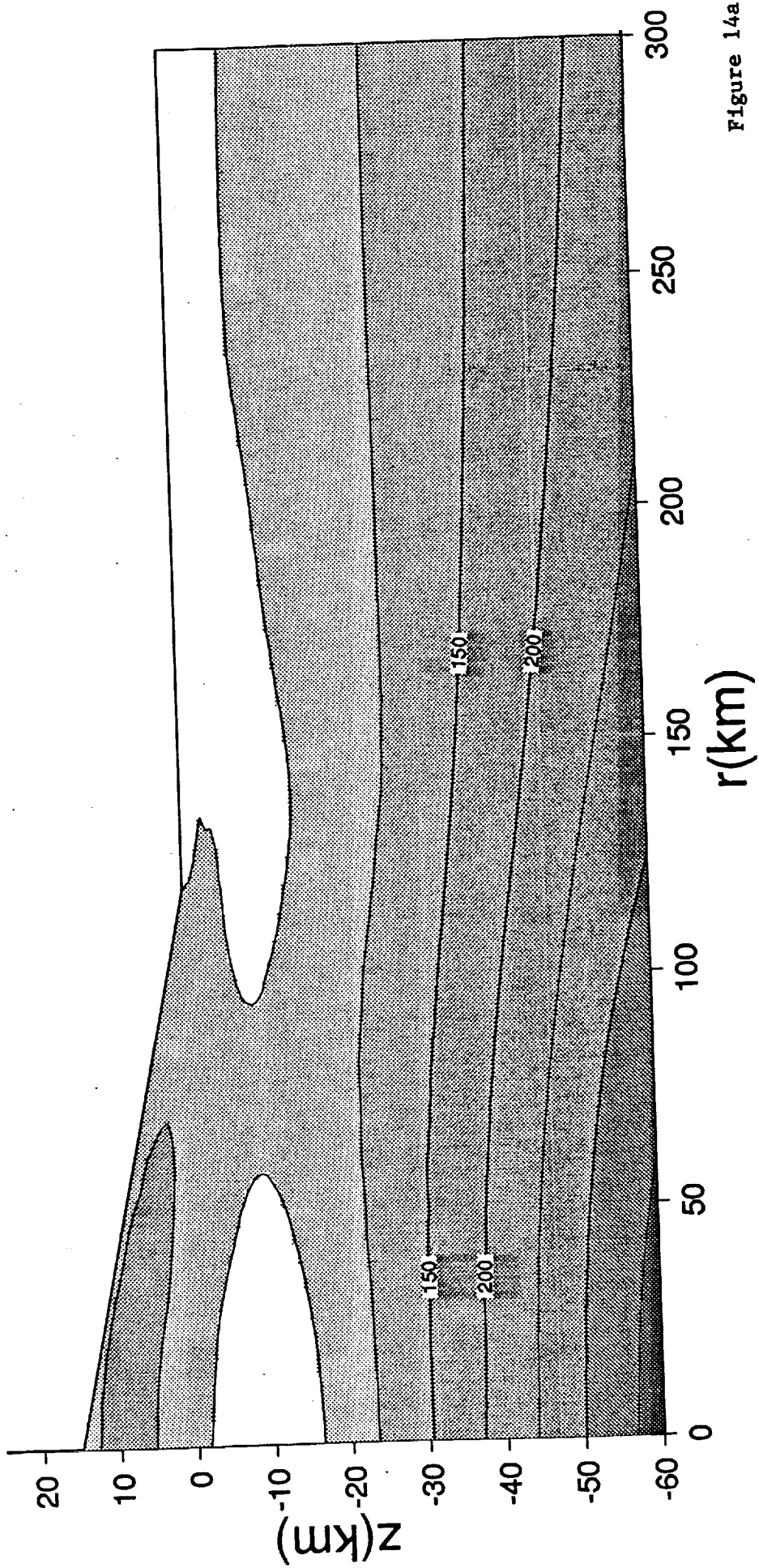
Figure 13b

Figure 14a
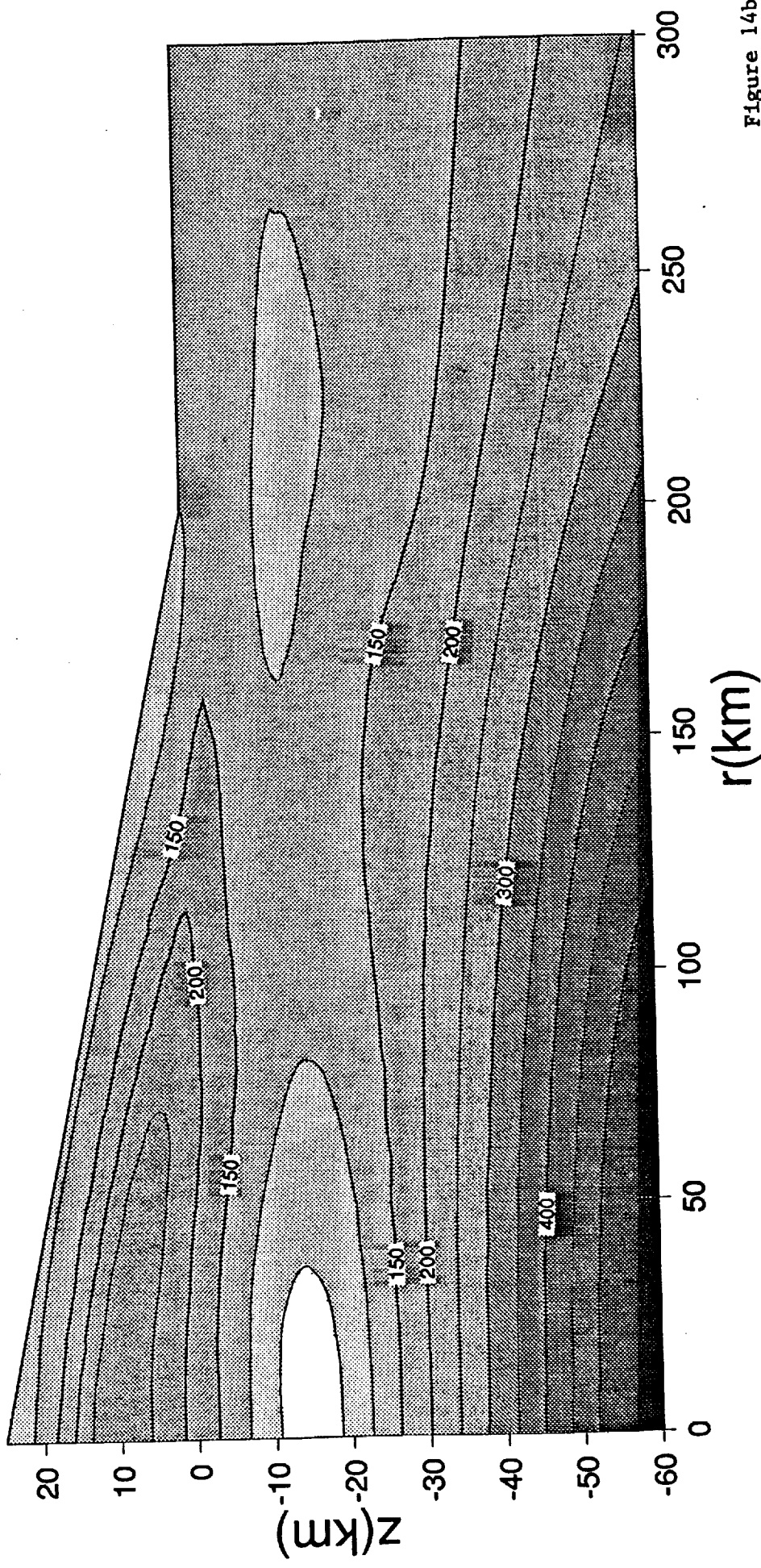
Figure 14b

Arsia 2.2 l3 crust=40km lith=60km

stress orientation/failure plot

cohesion = 3.50000E+07 pa; phi = 49.0000degrees

time = 2.50000E+13 seconds
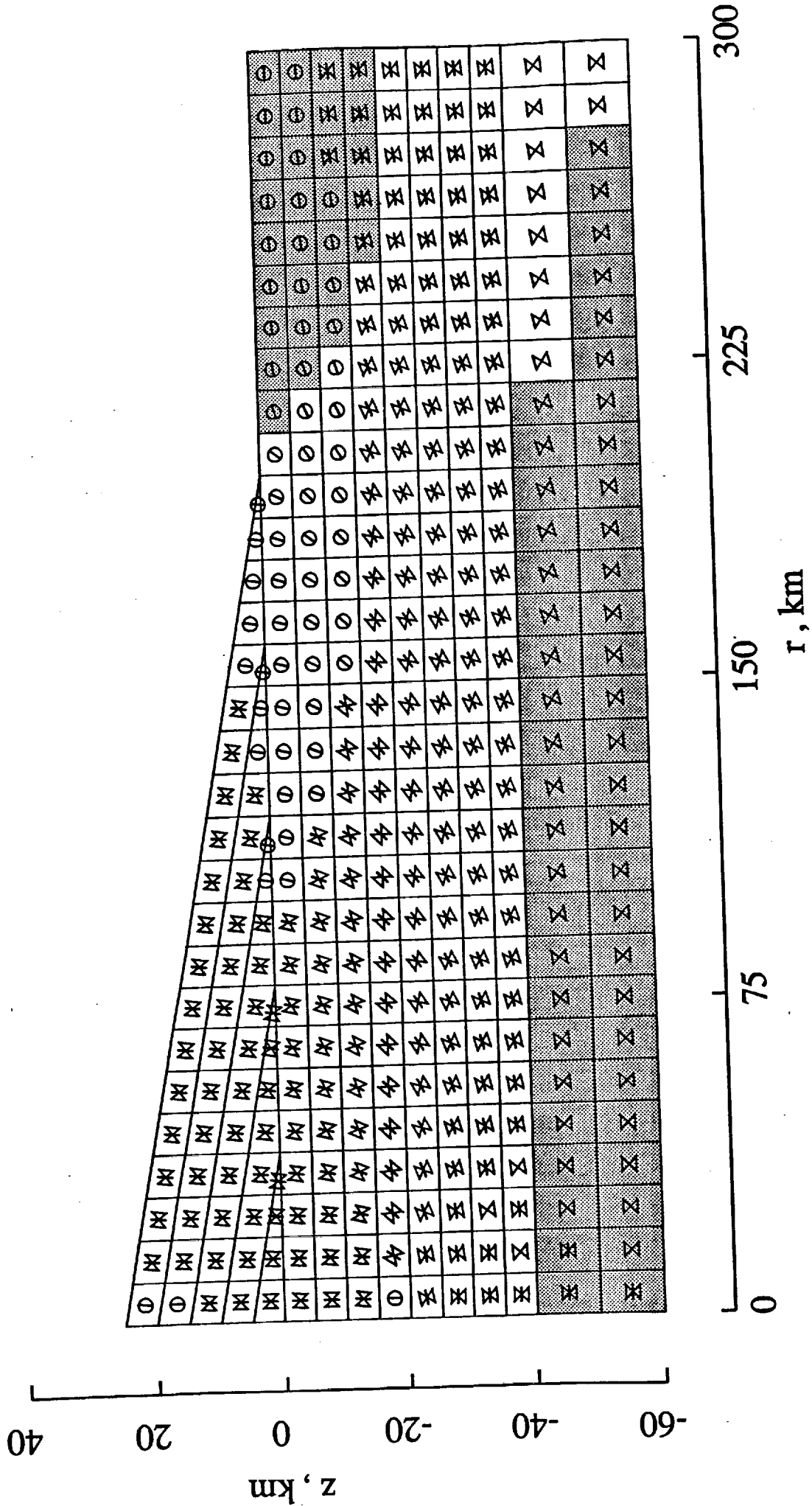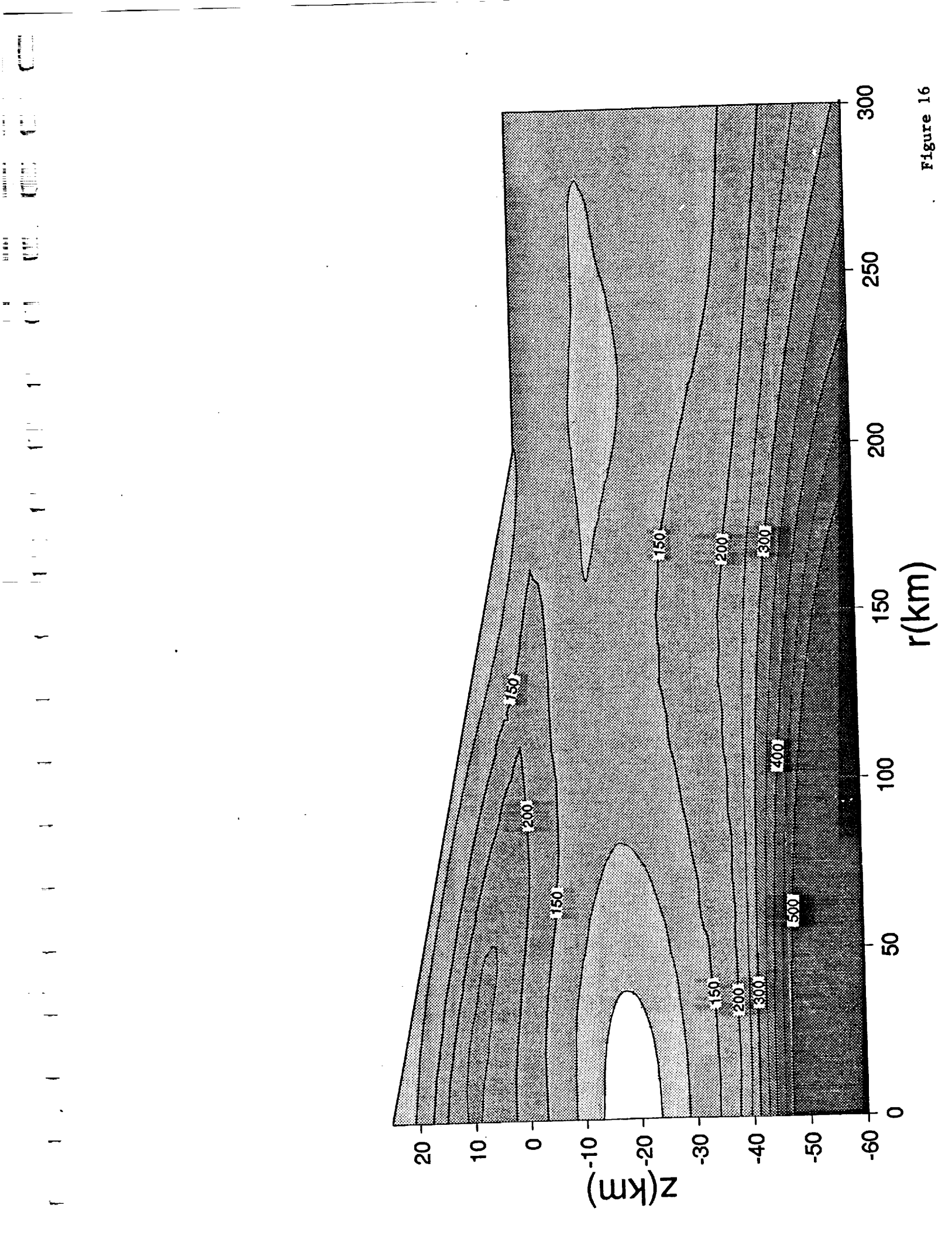
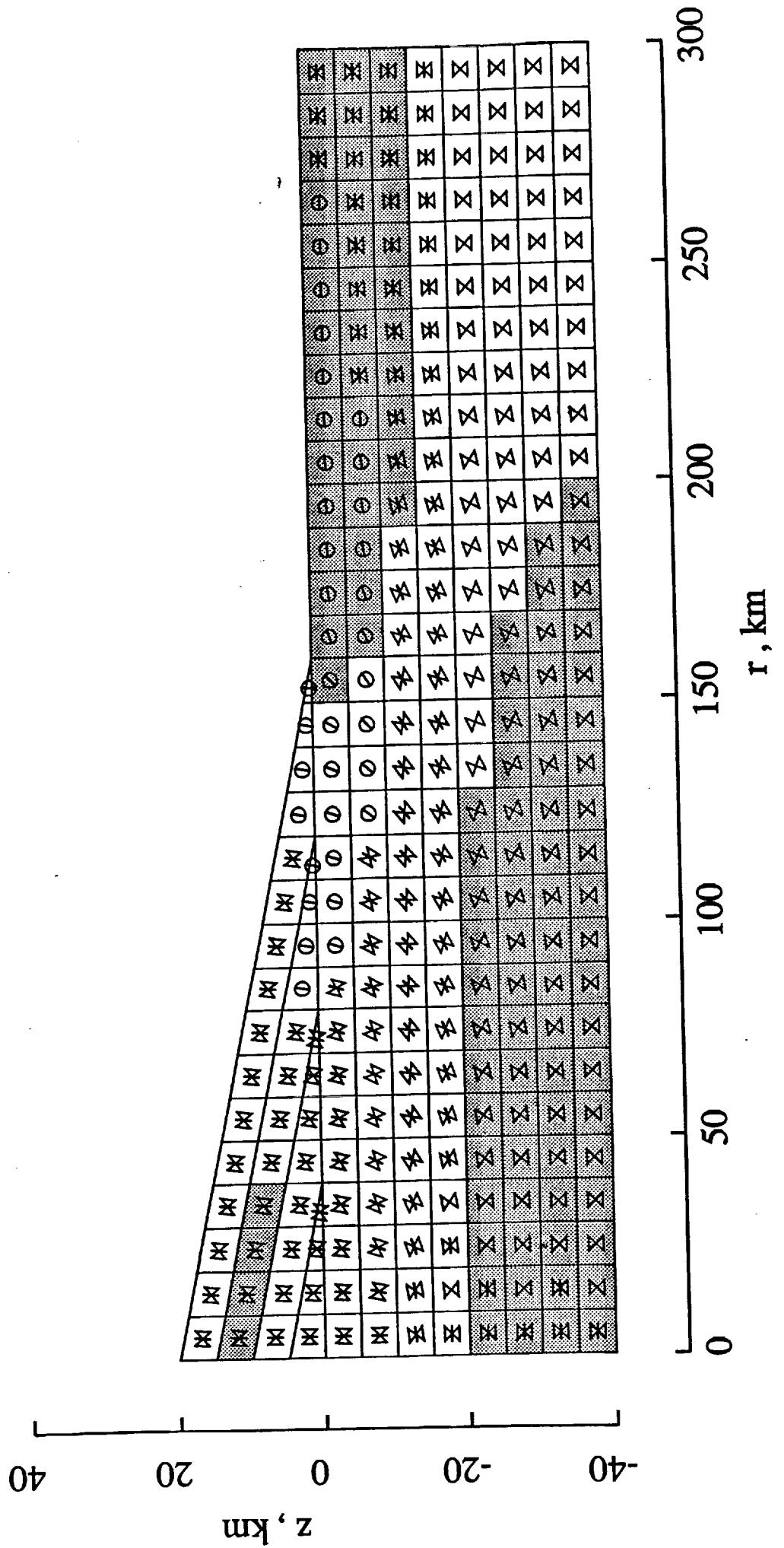full output timestep # 32

Figure 15

Figure 16

Arsia 2.2 11 40km

stress orientation/failure plot

cohesion = 3.50000E+07 pa; phi = 49.0000degrees

time = 8.33300E+12 seconds

full output timestep # 12

Figure 17

Figure 18

Arsia 2.2 l3 slip 40km

stress orientation/failure plot

cohesion =   3.50000E+07 pa; phi =   49.0000degrees
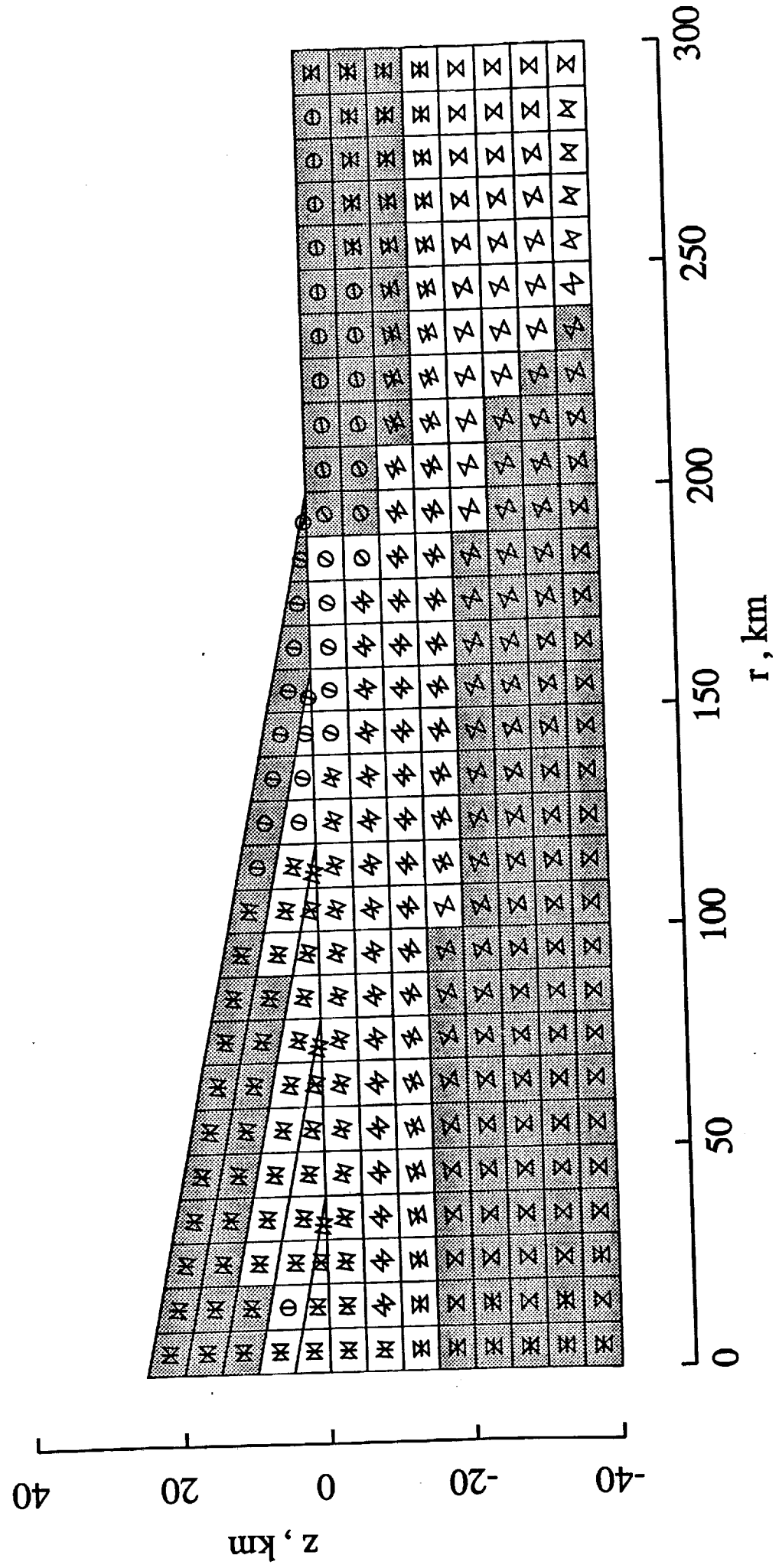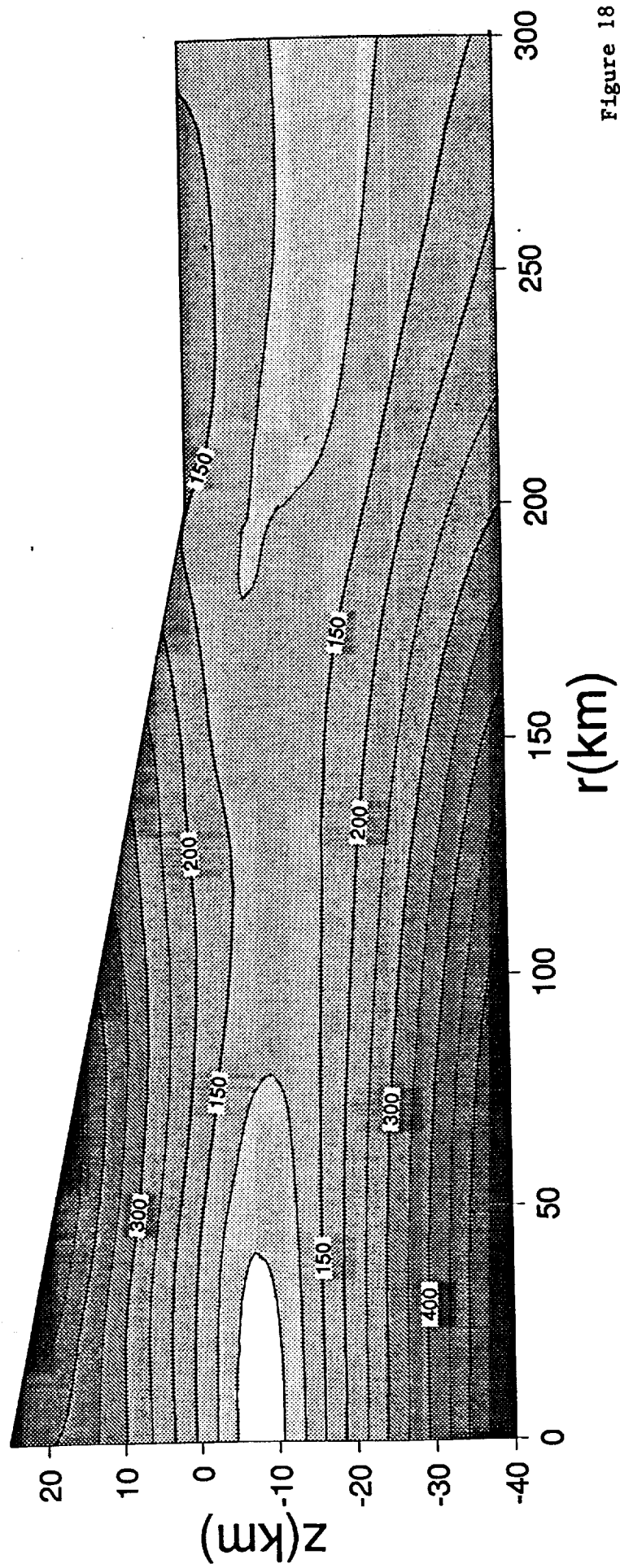
time =   8.33300E+10 seconds

full output timestep # 2

Figure 19a

C-2.

Arsia 2.2 l3 slip 40km

stress orientation/failure plot

cohesion =   3.50000E+07 pa; phi =   49.0000degrees

time =   8.33300E+12 seconds

full output timestep # 12

Figure 19b

Arsia 2.2 13 slip 40km

stress orientation/failure plot

cohesion = $3.50000E+07$ pa; phi = 49.0000 degrees
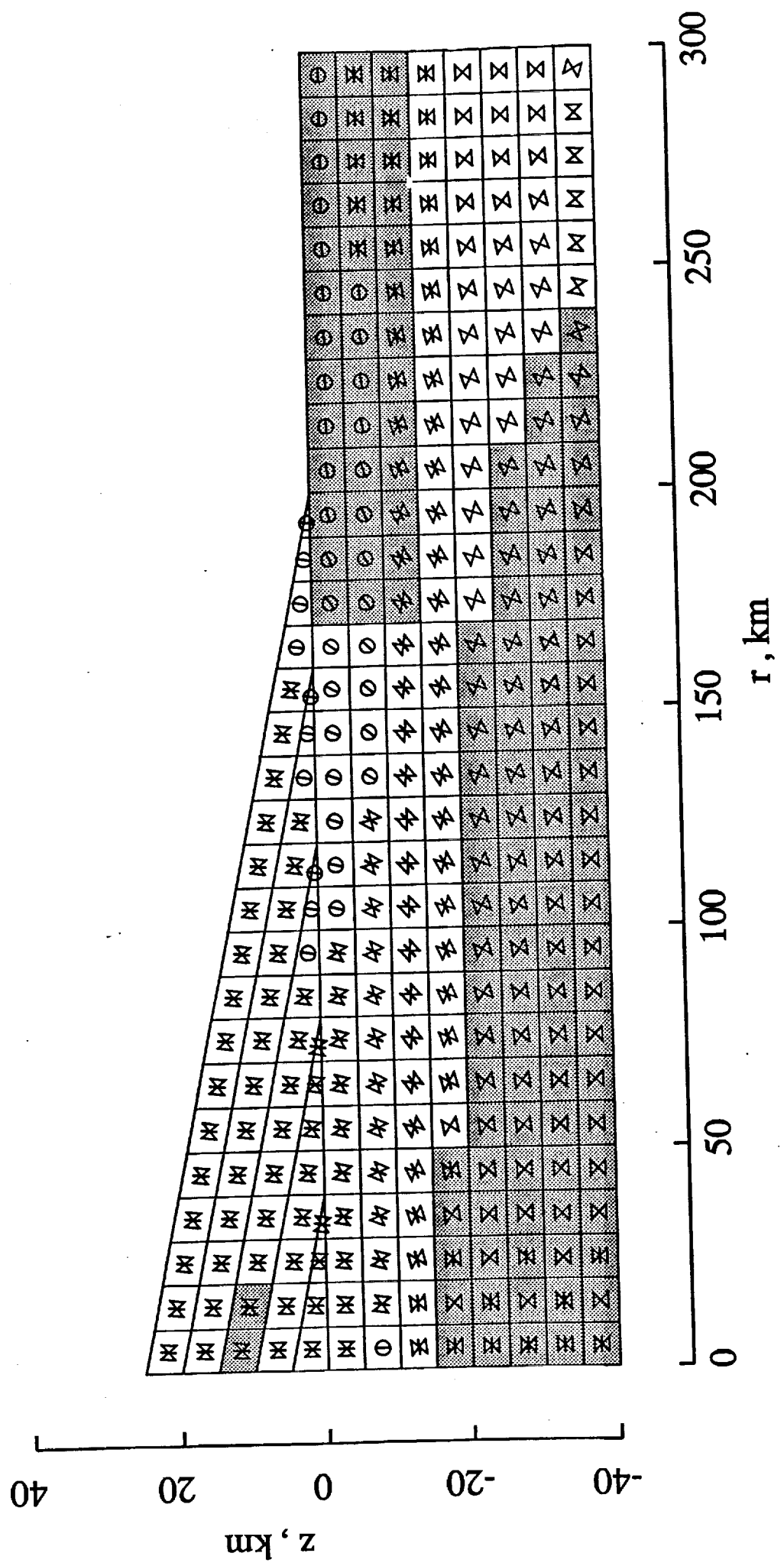
time = $2.50000E+13$ seconds

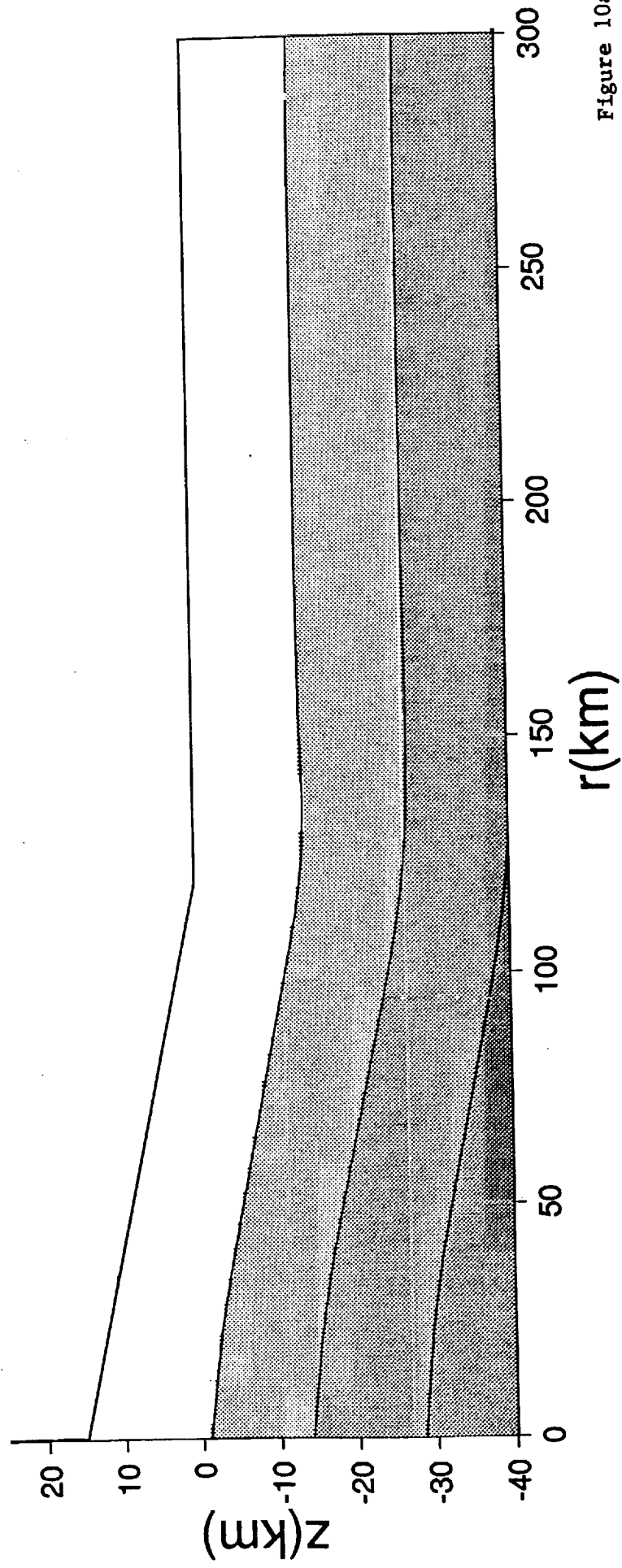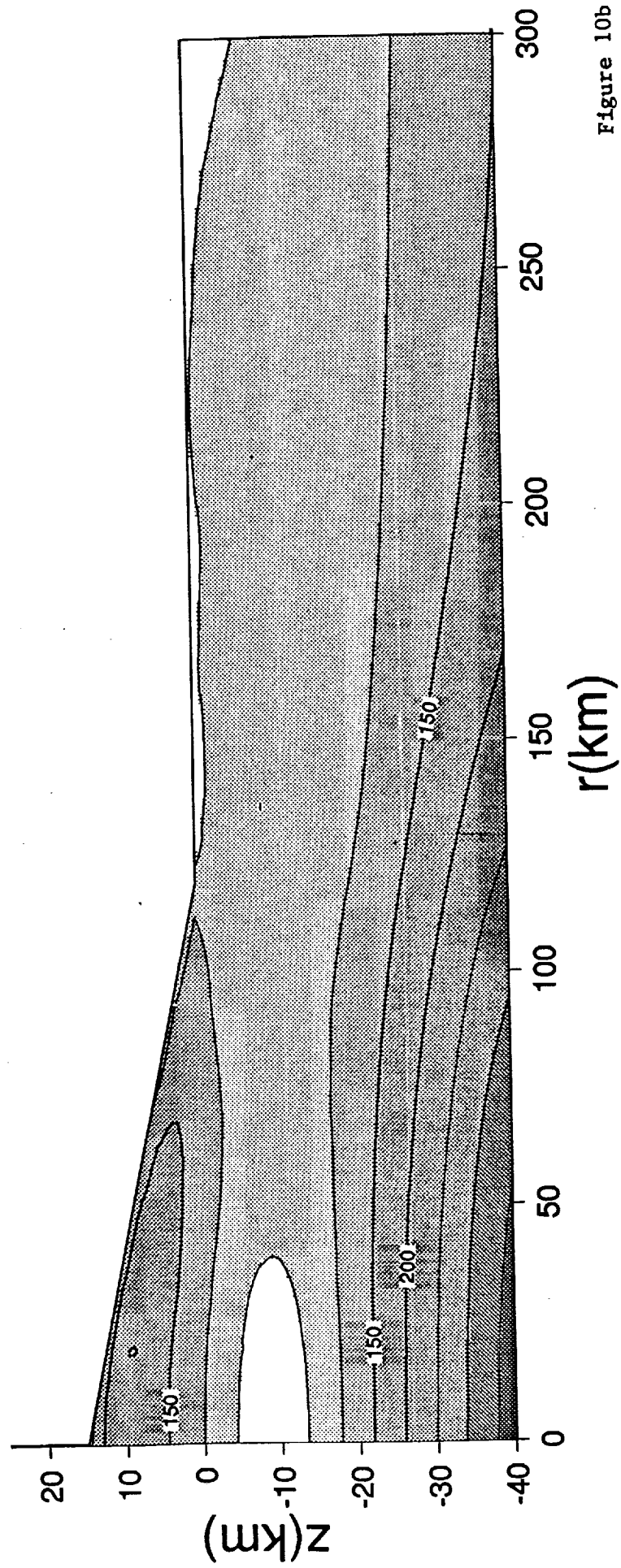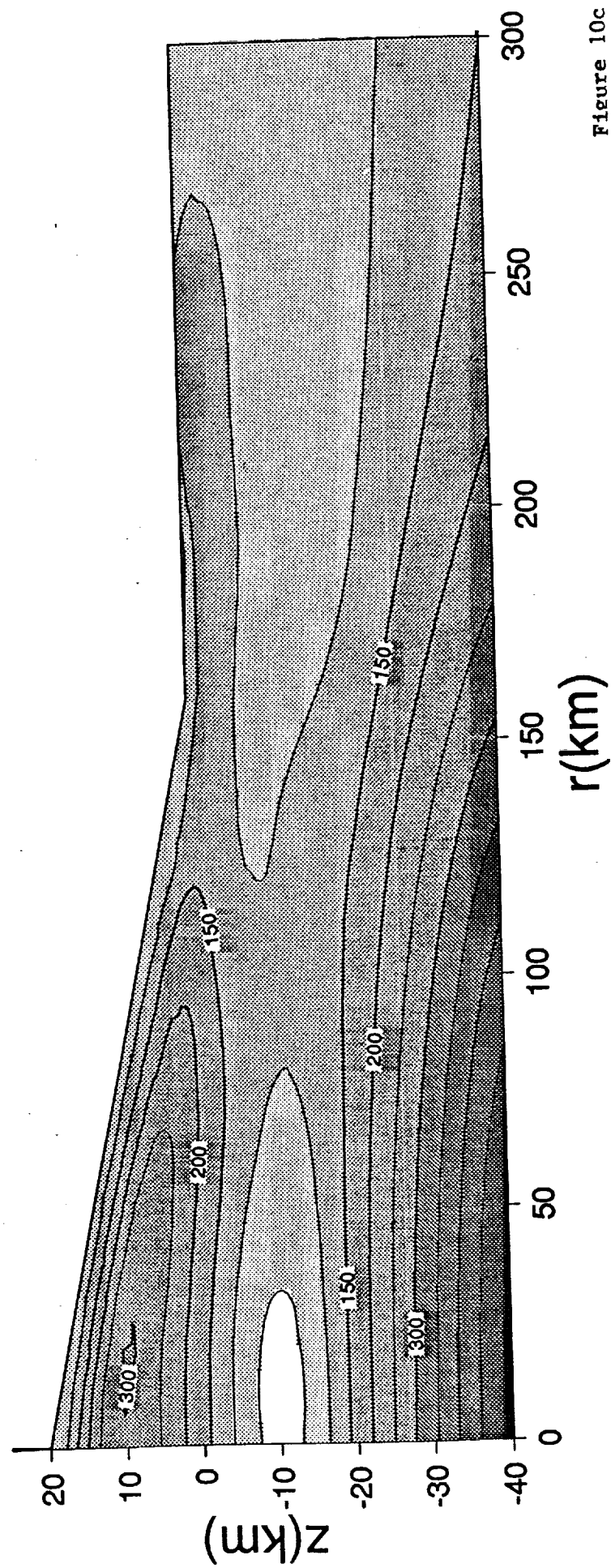full output timestep # 32
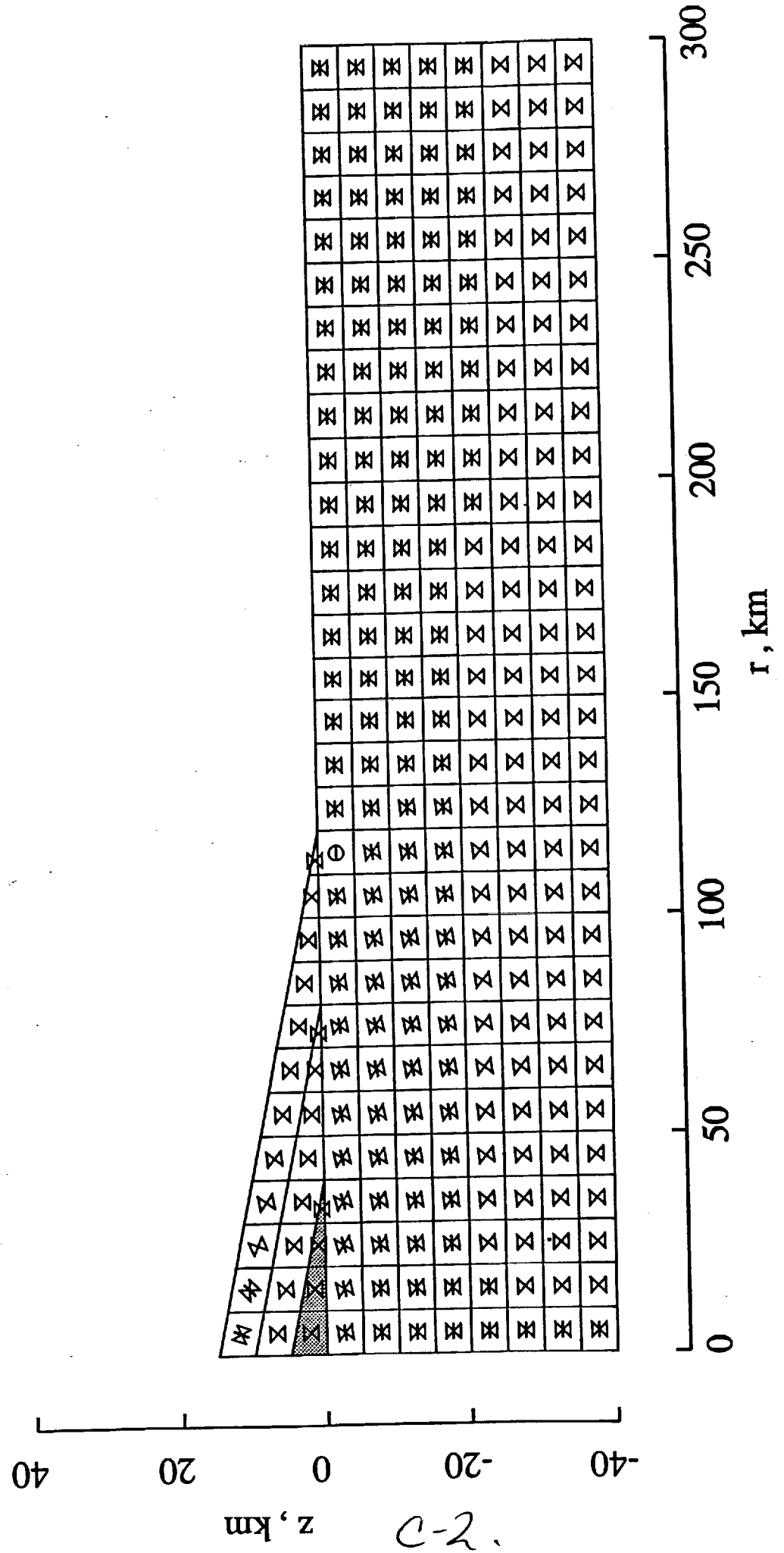
Figure 19c
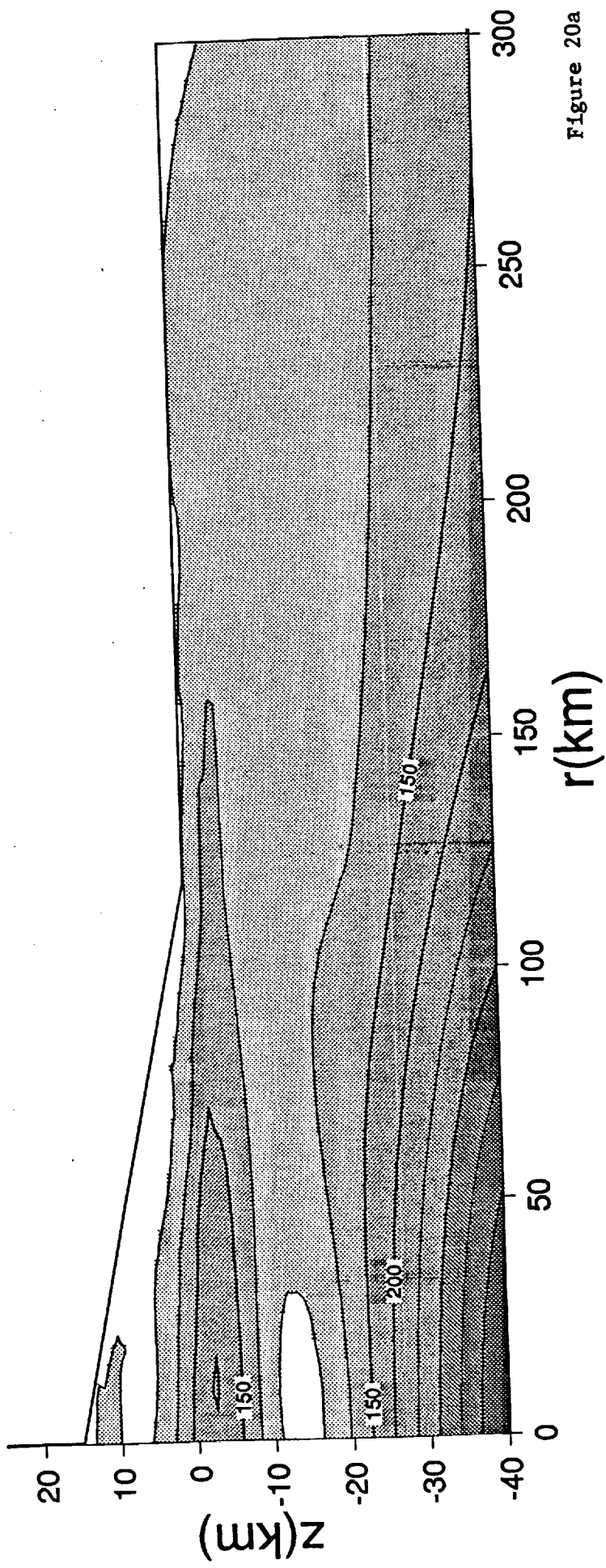
Figure 20a

Figure 20b

Arsia 2.2 l3 40km ps1

stress orientation/failure plot

cohesion = 3.50000E+07 pa; phi = 49.0000degrees
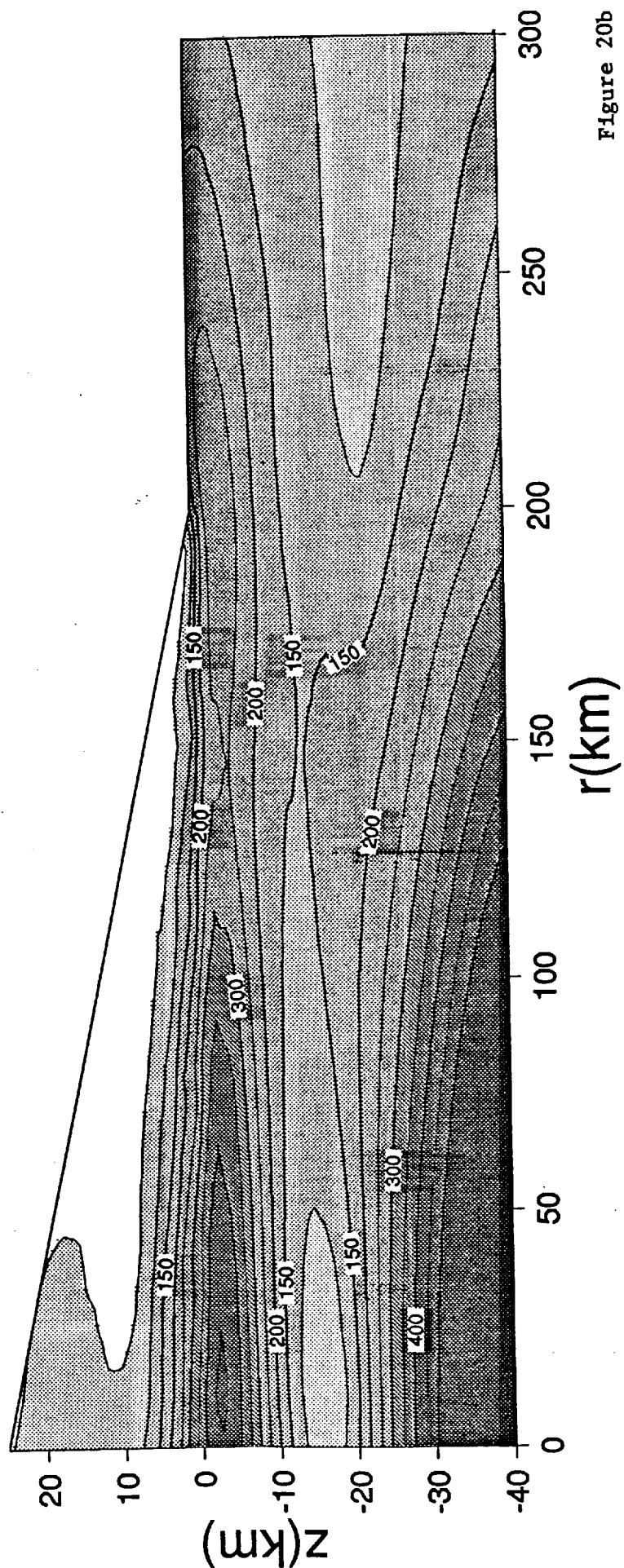
time = 3.33300E+11 seconds

full output timestep # 6

Figure 21a

Arsia 2.2 l3 40km ps1

stress orientation/failure plot

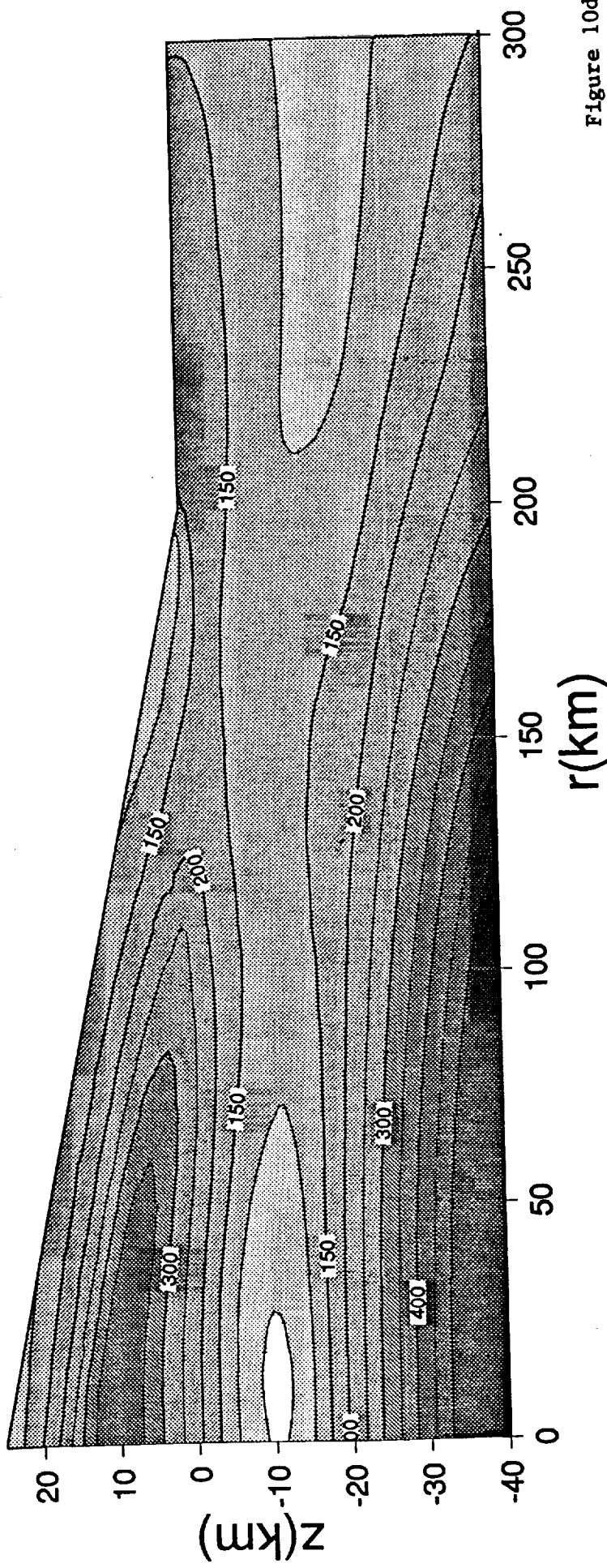cohesion = 3.50000E+07 pa; phi = 49.0000degrees

time = 8.33300E+12 seconds

full output timestep # 12

Figure 21b

Arsia 2.2 l3 40km ps1

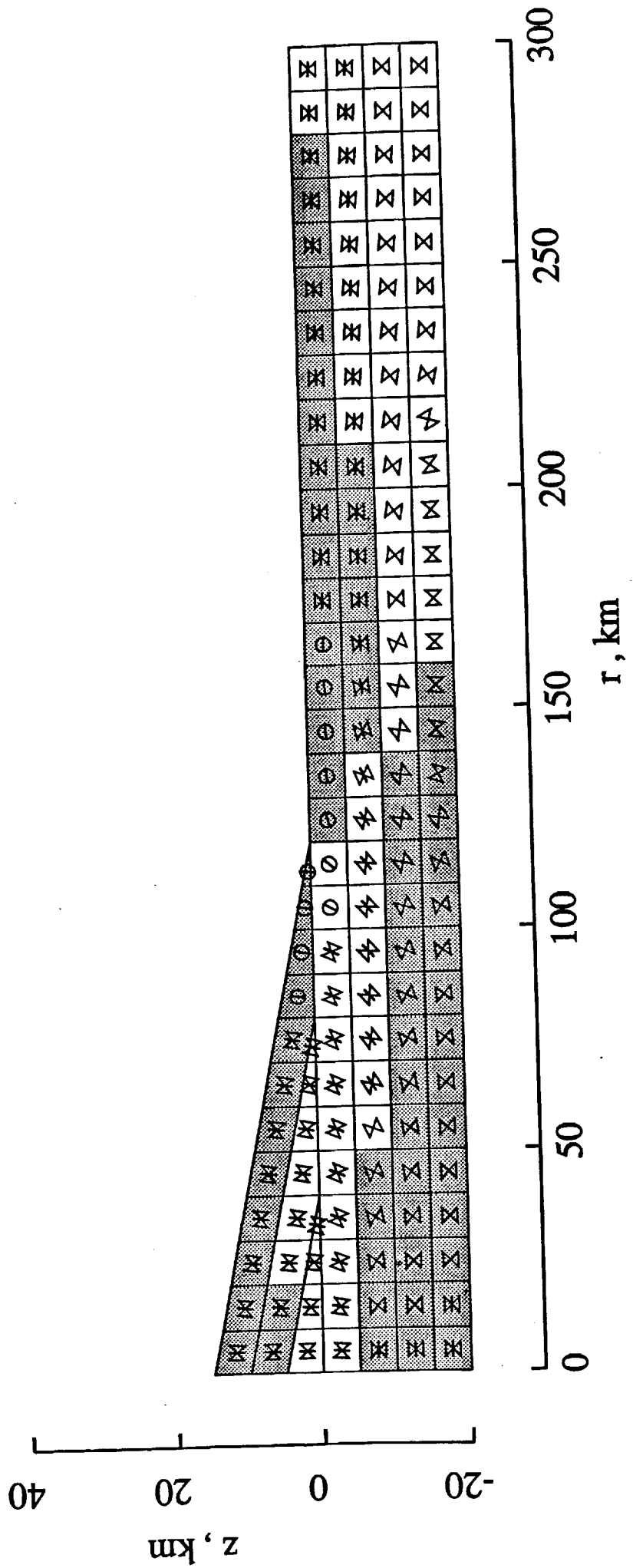stress orientation/failure plot

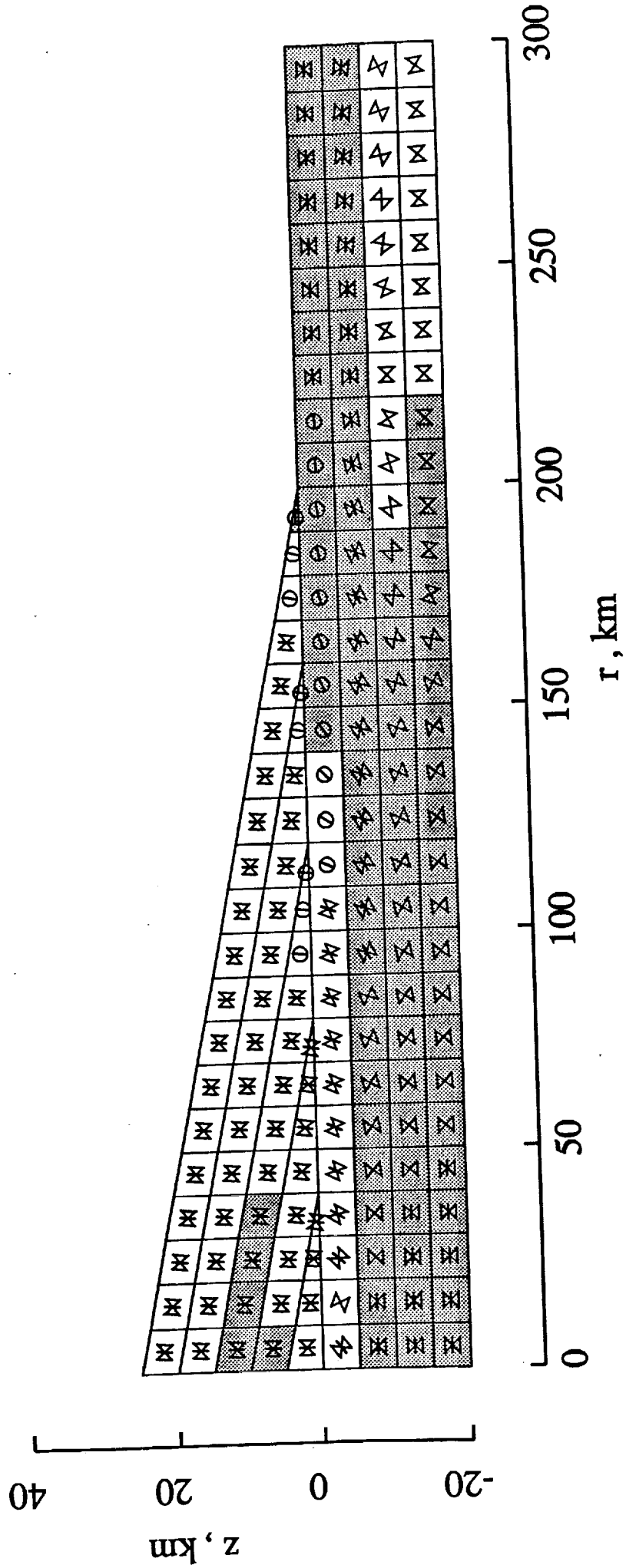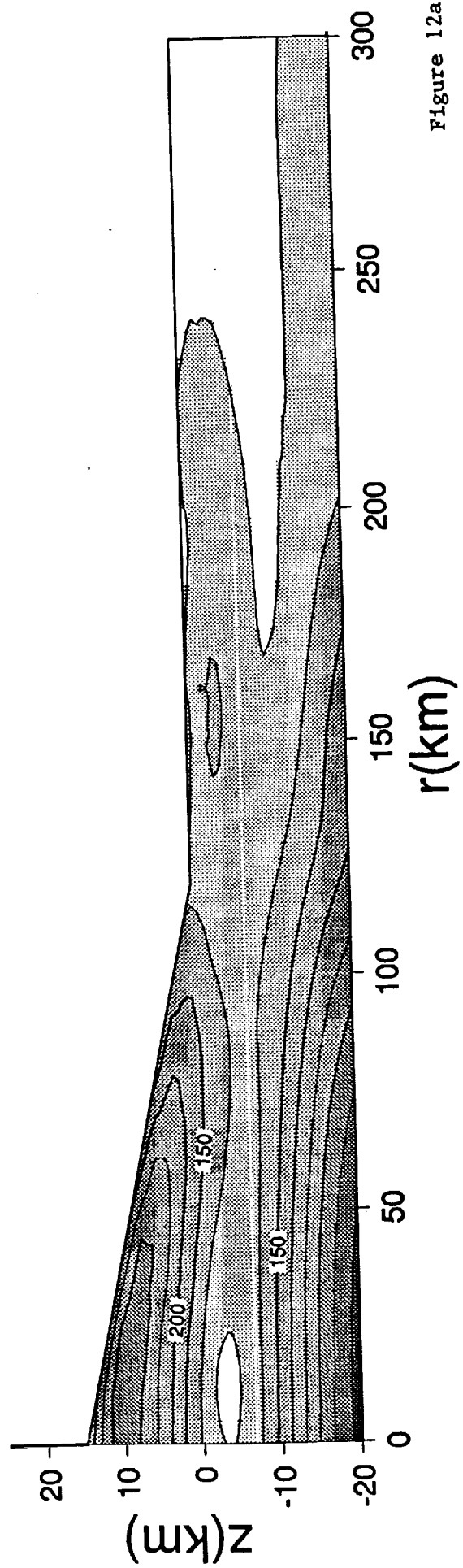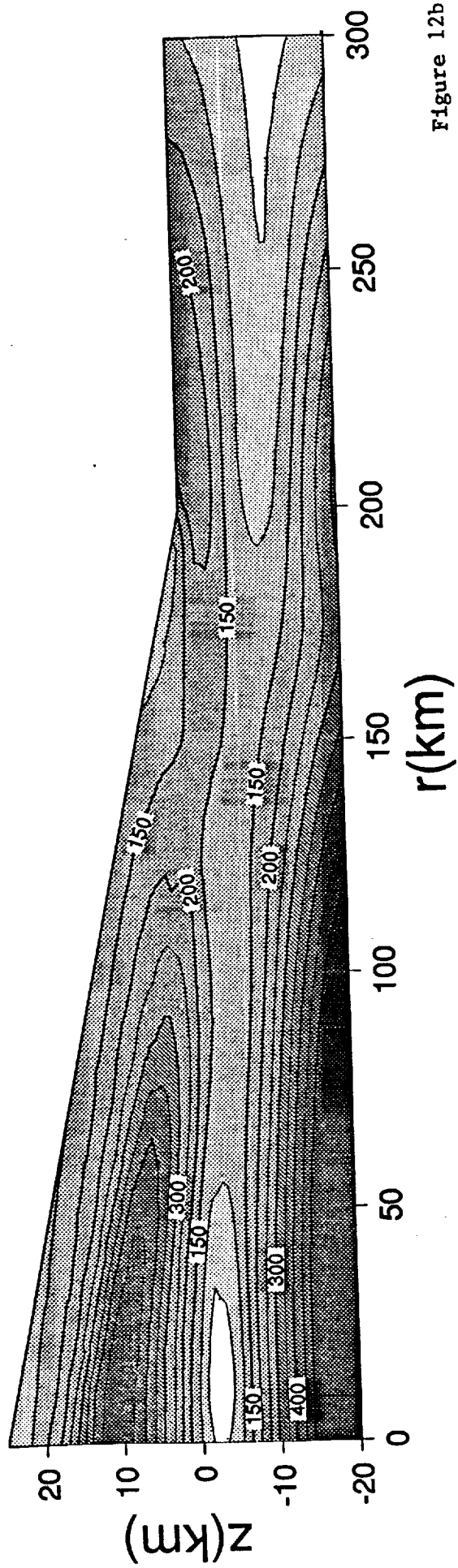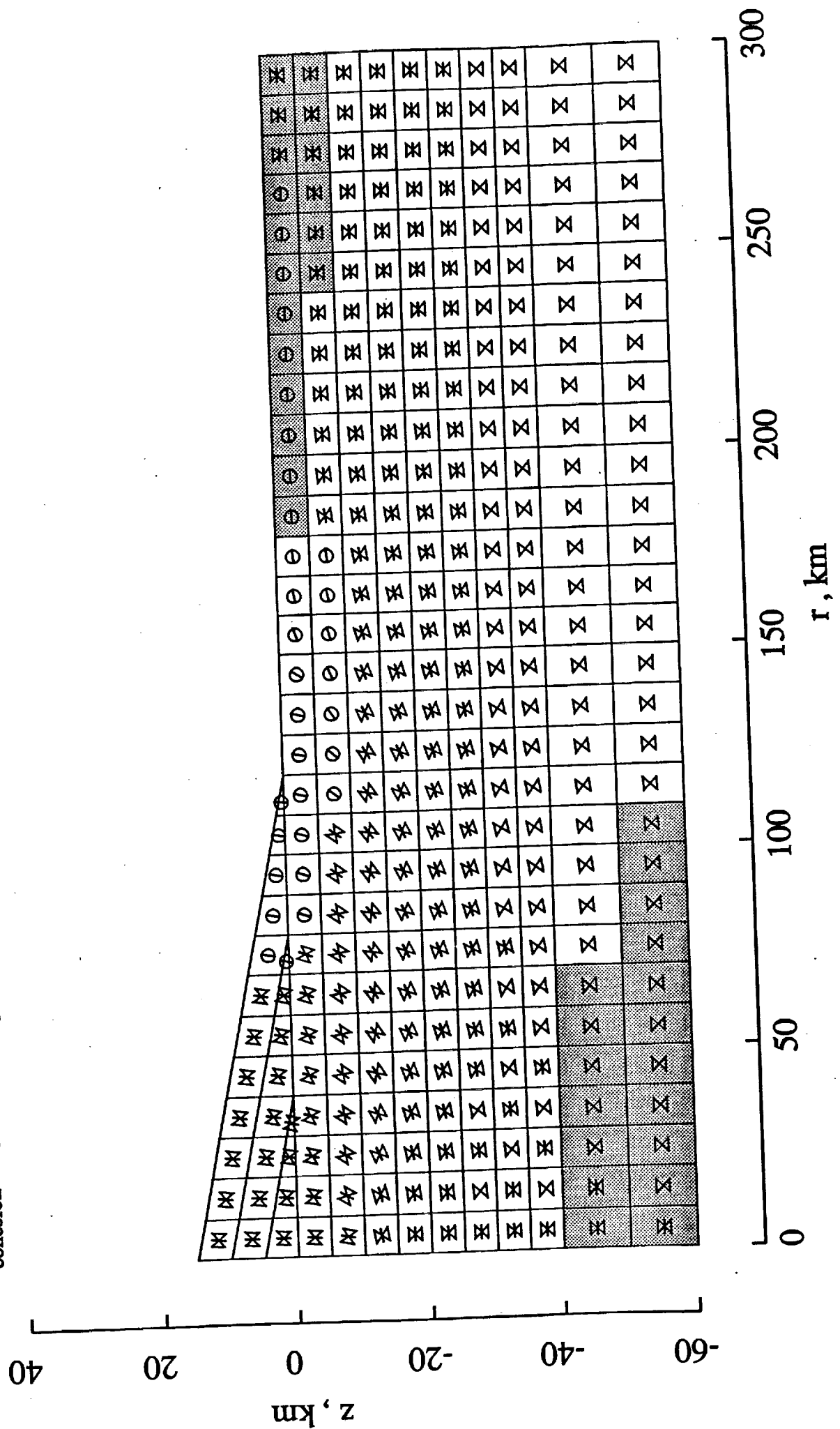cohesion =   3.50000E+07 pa; phi =   49.0000degrees

time =   2.50000E+13 seconds

full output timestep # 32

Figure 21c

Mohr Circle for element number 2277
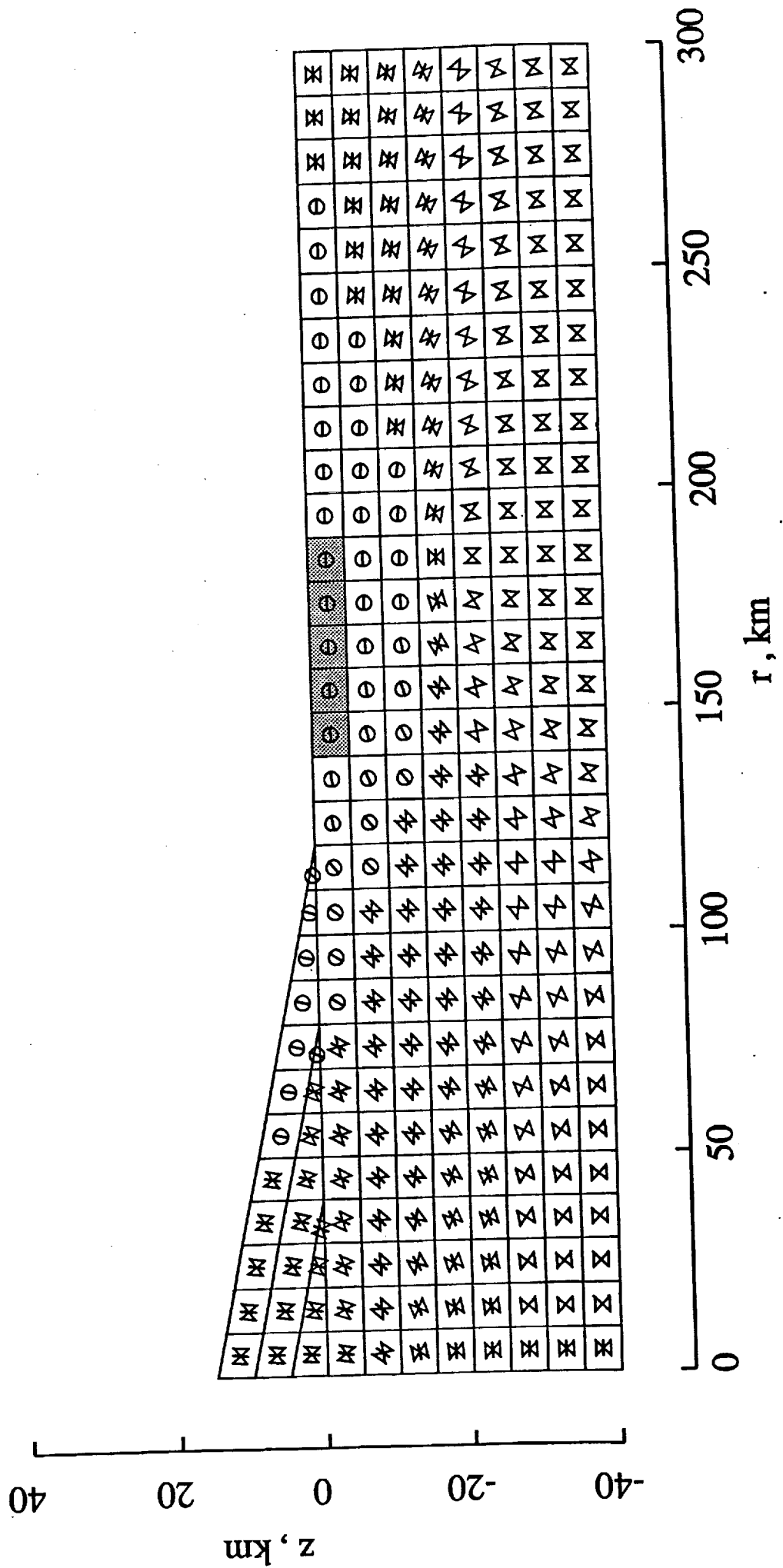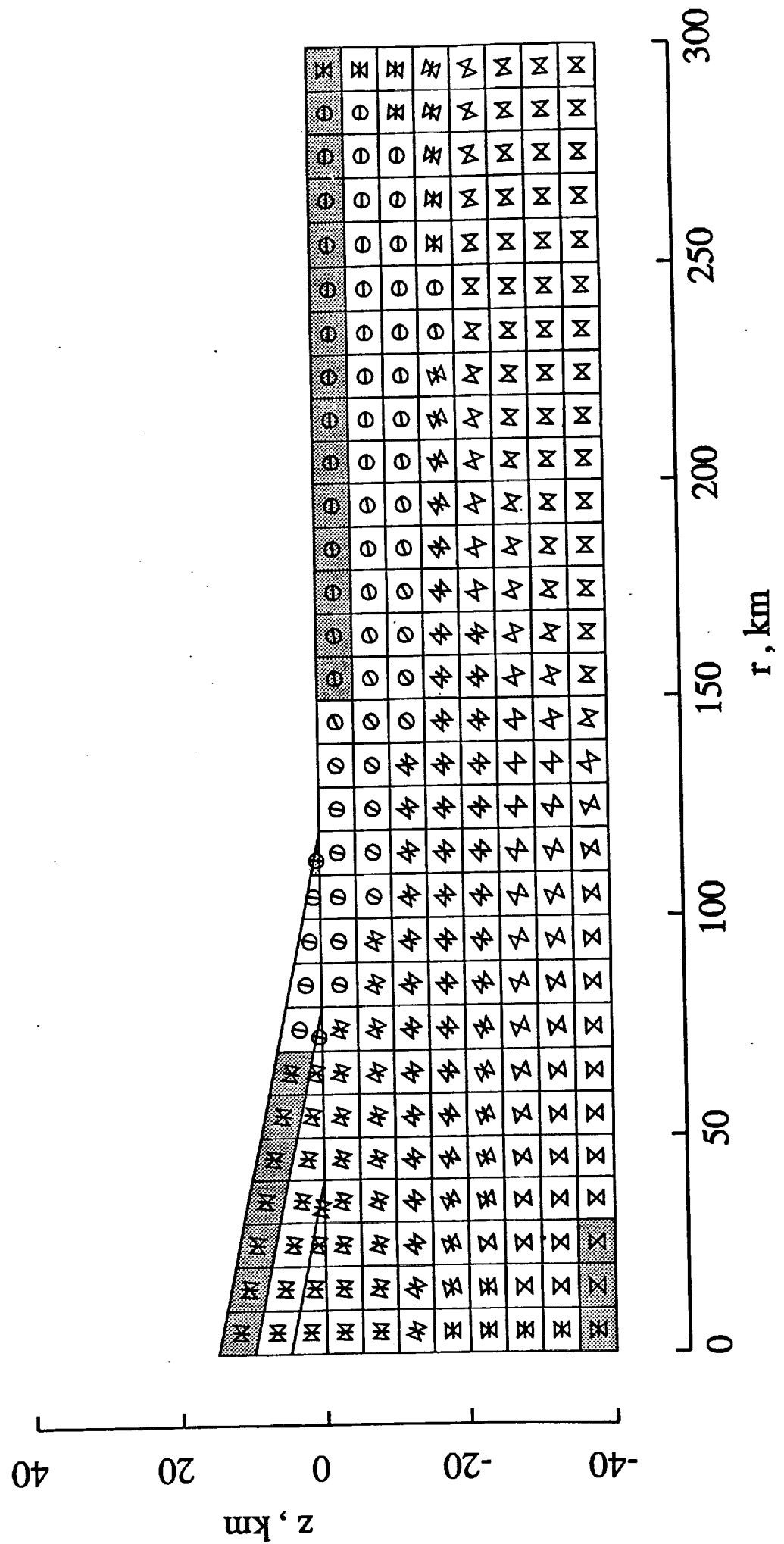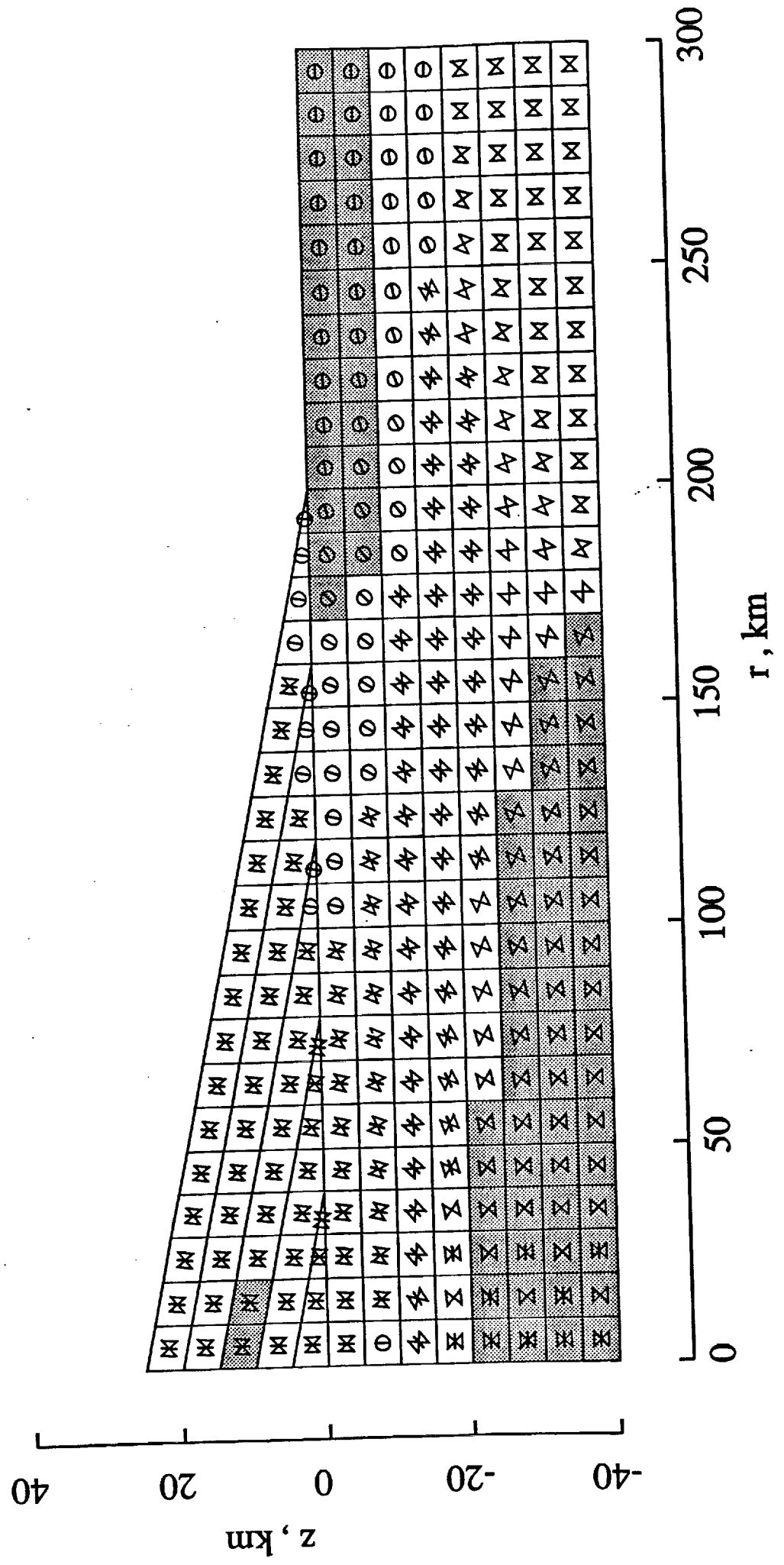
Figure 22
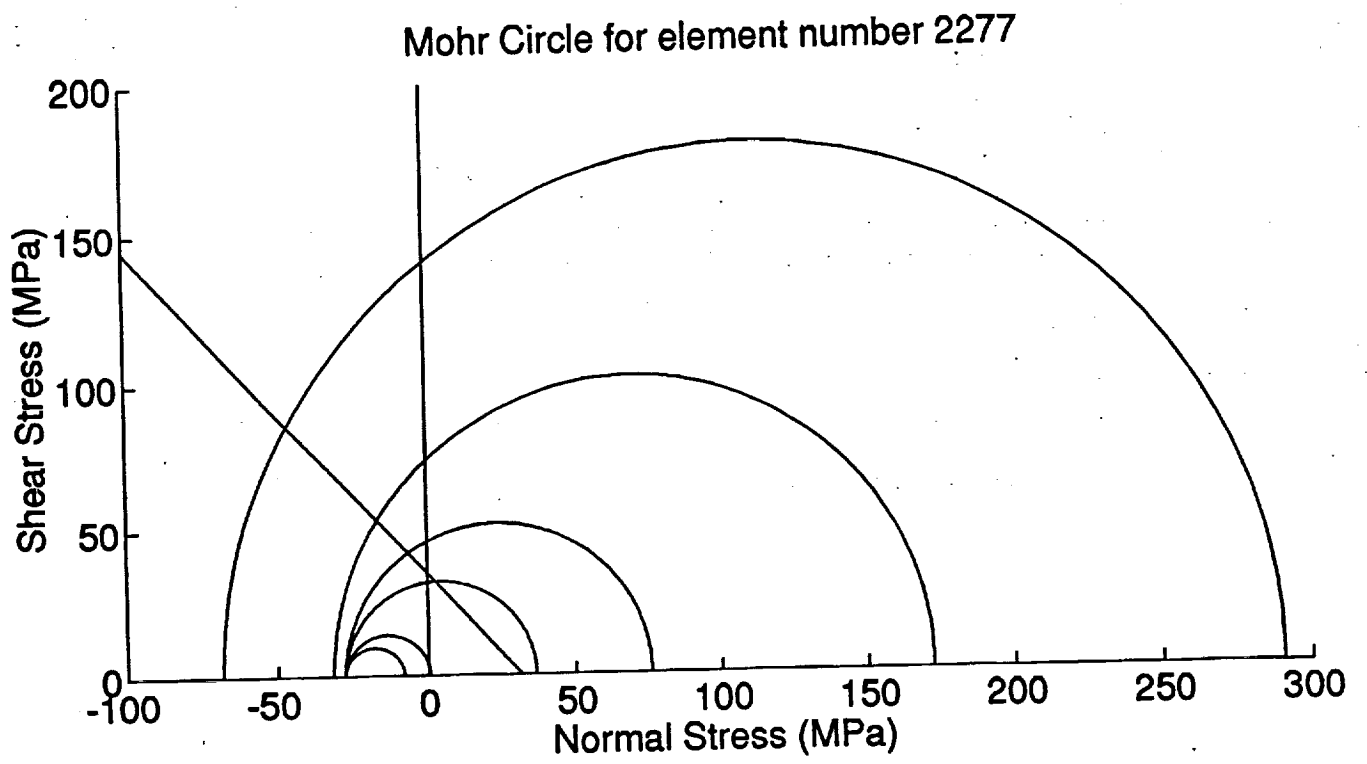
Features on Venus Generated by Plate Boundary Processes

Dan McKenzie (Bullard Laboratories, Madingley Road, Cambridge, CB3 0EZ, U.K.; ph. 44-223-337177; fax. 44-223-60779; e-mail dpm1@phx.cam.ac.uk); Peter G. Ford (Center for Space Research, MIT, Cambridge, MA 02139); Catherine Johnson and David Sandwell (Scripps Institution of Oceanography, La Jolla, CA 92093); Barry Parsons (Department of Earth Sciences, Oxford University, Oxford OX1 3PR, U.K.); Stephen Saunders (Jet Propulsion Laboratory, 4800 Oak Grove Drive, Pasadena, CA 91109); Sean C. Solomon (Dept. of Earth, Atmospheric and Planetary Sciences, MIT, Cambridge, MA 02139)

SAR images of Venus, taken with a radar whose wavelength is 12.6 cm, are compared with GLORIA images of active plate boundaries, obtained with a sound source whose wavelength is 23 cm. Features similar to transform faults and to abyssal hills on slow and fast spreading ridges can be recognized within the Artemis region of Venus, but are not clearly visible elsewhere. The composition of the basalts measured by the Venera 13 and 14 and the Vega 2 spacecraft corresponds to that expected from adiabatic decompression, like that which occurs beneath spreading ridges on the Earth. Structures that resemble trenches are widespread on Venus, and show the same curvature and asymmetry as they do on Earth. These observations suggest that the same simple geophysical models that have been so successfully used to understand the tectonics of the Earth can also be applied to Venus.

THE GABBRO - ECLOGITE PHASE TRANSITION AND THE ELEVATION OF MOUNTAIN BELTS ON VENUS;

Noriyuki Namiki and Sean C. Solomon, Department of Earth, Atmospheric, and Planetary Sciences, Massachusetts Institute of Technology, Cambridge, MA 02139.

Introduction. The linear mountain belts of Ishtar Terra on Venus are notable for their topographic relief and slope and for the intensity of surface deformation [1,2]. The mountains surround the highland plain Lakshmi Planum. Volcanism is rare to absent in Maxwell, Freyja, and Akna Montes, but a number of magmatic features are evident in Danu Montes [2,3], the mountain range least elevated above Lakshmi Planum. Whether western Ishtar Terra is a site of mantle upwelling and consequent hot spot volcanism [4-6] or of mantle downwelling and consequent convergence of lithospheric blocks [7,8] is currently a matter of debate. However, the mountains are generally regarded as products of large-scale compression of the crust and lithosphere [2,9].

Among the four mountain belts surrounding Lakshmi Planum, Maxwell Montes is the highest and stands up to 11 km above the mean planetary radius and 7 km above Lakshmi Planum. The bulk composition and radioactive heat production of the crust on Venus, where measured, are similar to those of terrestrial tholeiitic basalt [10]. Because the thickness of the low-density crust may be limited by the gabbro - garnet granulite - eclogite phase transitions (Fig. 1), the 7-11 km maximum elevation of Maxwell Montes is difficult to understand except in the unlikely situation that the crust contains a large volume of magma [11]. A possible explanation is that the base of the crust is not in phase equilibrium. It has been suggested that under completely dry conditions, the gabbro - eclogite phase transition takes place by solid state diffusion and may require a geologically significant time to run to completion [12]. Solid state diffusion is a strongly temperature-dependent process. In this paper we solve the thermal evolution of the mountain belt to attempt to constrain the depth of the gabbro - eclogite transition and thus to assess this hypothesis quantitatively.

Thermal Model. The one-dimensional heat equation is solved numerically by a finite difference approximation. The deformation of the horizontally shortening crustal and mantle portions of the thermal boundary layer is assumed to occur by pure shear, and therefore the vertical velocity is given by the product of the horizontal strain rate $\dot{\gamma}$ and depth z. The thermal diffusivity is assumed to be $1.0 \times 10^{-6} m^2 s^{-1}$ in both crust and mantle. Crustal heat production is assumed to equal $1.4 \times 10^{-13} K s^{-1}$. The initial temperature profile is determined by the assumption of steady-state conditions with zero velocity. Temperature at the surface and the bottom of the thermal boundary layer are fixed at 750 K and at a value T_{bl} taken as free parameter.

The phase diagram is assumed to be that of tholeiitic basalt [13], and the densities of gabbro and eclogite are taken to be 2900 and $3500 kg m^{-3}$. The density of garnet-granulite is assumed to increase linearly from that of gabbro to that of eclogite as pressure increases at a given temperature. The density of the mantle is assumed to be $3400 kg m^{-3}$. The micromechanism of the gabbro - eclogite transition is not well understood. In this study we assume that the volume diffusion of cations is the most likely rate-limiting process of the transformation, which involves chemical as well as phase changes. The volume fraction of reacted component, ψ, is given by,

$$\psi = D/r^2$$

where r is the grain radius and D is the diffusion coefficient [12]. Since the slowest-moving cation limits the reaction rate and Al^{3+} is likely to be this cation, we adopt as a minimum value for D the lower end of the range of estimates of the diffusion rate of Al^{3+} in orthopyroxene [14]:

$$D = D_{Al, Opx} = 1.1 \times 10^{-5} exp \left(-400 \ kJ/RT\right)$$

where R is the gas constant and T is the absolute temperature. The diffusion rate, however, is experimentally uncertain because Al^{3+} diffusion is extremely sluggish, particularly at low temperature. In order to bound D from above, we use the diffusion rate of Fe in garnet ($D_{Fe,Gt} = 6.4 \times 10^{-8} exp \left[-\left(270 \ kJ + 5.7 \times 10^{-5} P\right)/RT\right]$), where P is in Pa. For each parcel of shortening lithosphere, ψ is obtained by integration over time. The density at a given depth is determined from the volume fractions of unreacted and reacted components.

Numerical Results. Temperatures in the thickening crust and mantle are calculated for rates of

horizontal convergence of 10^{-15} (Fig. 1a) and 10^{-16} s^{-1} (Fig. 1b). For all models discussed here (Table 1), thicknesses of crust and thermal boundary layer are assumed to be initially 20 and 50 km, respectively, and to increase to 100 and 250 km, respectively. Temperature profiles for the strain rate of 10^{-15} s^{-1} are vertically stretched as the crust and lithospheric mantle are thickened (Fig. 1a). Temperatures do not increase significantly from initial values because heat is mainly transferred by advection and the contribution of crustal heat production is minor. Hence gabbro remains metastable for 50 My or more, and the elevation of shortened lithosphere can increase as much as 12 km above the surrounding plains in that time interval (Fig. 2a). The phase transition proceeds, i.e., elevation is limited, only if grains are small and diffusion is fast (Model 3).

For $\dot{\gamma}=10^{-16}$ s^{-1}, crustal heat production dominates advective heat transfer after the crust becomes as thick as 60-80 km (Fig. 1b). The resulting increase in temperature hastens the phase transition. The slower strain rate also lengthens the formation time of the mountains relative to the characteristic reaction time, which depends on r, D, and temperature at the base of the crust. For larger grains (r=10 mm), the elevation reaches 11 km or more if the initial temperature at the base of the crust, T_c, is 1150 K (Model 6 in Fig. 2b). For the same value of T_c the elevation is at most 6 km for grains of 1 mm radius (Model 7). This result constitutes an upper bound on T_c for small grain size. If $D=D_{Fe,Gt}$ is assumed, that upper bound is lowered to 1050 K (Model 8).

Discussion. Because at long wavelengths the topography of western Ishtar Terra is correlated with the gravity field, dynamical support of the broad 4-km elevation of the region is likely [e.g., 15]. Therefore the 7-km elevation of Maxwell Montes above the adjacent plateau is a more meaningful constraint on maximum relief than the 11-km elevation above mean planetary radius. The results are insensitive to the assumed initial thickness of crust but are sensitive to the density difference between crust and mantle. If densities of 3000 and 3300 kg m^{-3} for crust and mantle are assumed, elevations are ~40% lower than the values presented here. Such changes constrain the models of thermal structure and phase transition depth more severely at low strain rate than the density values adopted above.

Two diffusion rates have been assumed in this study so as to represent a wide range of diffusion data. We should note, however, that under wet conditions, i.e., in the presence of either water [16] or melt [17], grain-boundary diffusion becomes much more efficient than volume diffusion. This is potentially noteworthy for understanding the contrast between Maxwell and Danu Montes. Despite the fact that Danu Montes display compressional deformation as extensive as the other mountain belts, the maximum elevation is as little as 0 km above the bounding plateau. Such comparatively modest elevation may be related to the presence of magmatic features within Danu Montes, if elevation is limited by an enhanced diffusion rate because of the melt at grain boundaries. Assessing the cause of higher temperatures beneath Danu Montes requires more detailed thermal models than the simple one-dimensional model considered here.

Conclusions. Taking into account the temperature-dependent reaction rate of the gabbro - eclogite phase transition, horizontal strain rates of 10^{-15} and 10^{-16} result in significant differences in the of maximum elevation of mountains, not only because of the difference in the formation time for relief, but also because of the difference in the thermal regime from advection-dominanted to crustal-heat-production dominated. For $\dot{\gamma}=10^{-15}$ s^{-1}, the observed maximum elevation of mountain belts can be explained as a consequence of disequilibrium phase boundary depth for a wide range of physical parameters, although a comparatively young age for Maxwell Montes (50 My) is implied. For the lesser horizontal strain rate of 10^{-16} s^{-1}, only limited parameter values for thermal models are allowed.

References. [1] V.L. Barsukov et al., *JGR, 91*, D378, 1986; [2] S.C. Solomon et al., *Science, 252,* 297, 1991; [3] J.W. Head et al., *Science, 252,* 276, 1991; [4] A. A. Pronin, *Geotectonics, 20,* 271, 1986; [5] A. T. Basilevsky, *Geotectonics, 20,* 282, 1986; [6] R. E. Grimm and R. J. Phillips, *GRL, 17,* 1349, 1990; [7] K.M. Roberts and J.W. Head, *GRL, 17,* 1341, 1990; [8] D.L. Bindschadler and E.M. Parmentier, *JGR, 95,* 21329, 1990; [9] L.S. Crumpler et al., *Geology, 14,* 1031, 1986; [10] Yu.A. Surkov et al., *JGR, 92,* E537, 1987; [11] R.W. Vorder Bruegge and J.W. Head, *Geology, 19,* 885, 1991; [12] T.J. Ahrens and G.

Schubert, *Rev. Geophys. Space Phys., 13*, 383, 1975; [13] K. Ito and G.C. Kennedy, in *Geophys. Mon.,14*, AGU, 303, 1971; [14] D. Smith and B.R. Barron, *Am. Mineral., 76*, 1950, 1991; [15] R.E. Grimm and R.J. Phillips, *JGR, 96*, 8305, 1991; [16] R. Joesten, in *Diffusion, Atomic Ordering and Mass Transport*, Springer-Verlag, 345, 1991; [17] R.H. Condit et al., in *Geophys. Mon., 31*, AGU, 97, 1985.

Table 1. Model parameters.

Models	r, mm	$\dot{\gamma}$, s^{-1}	D	T_c, K	T_{bl}, K
1	1	10^{-15}	$D_{Al,Opx}$	1050	1321
2	10	10^{-15}	$D_{Al,Opx}$	1050	1321
3	1	10^{-15}	$D_{Fe,Gt}$	1050	1321
4	1	10^{-16}	$D_{Al,Opx}$	1050	1321
5	10	10^{-16}	$D_{Al,Opx}$	1050	1321
6	10	10^{-16}	$D_{Al,Opx}$	1350	1521
7	1	10^{-16}	$D_{Al,Opx}$	1150	1521
8	10	10^{-16}	$D_{Fe,Gt}$	1050	1321
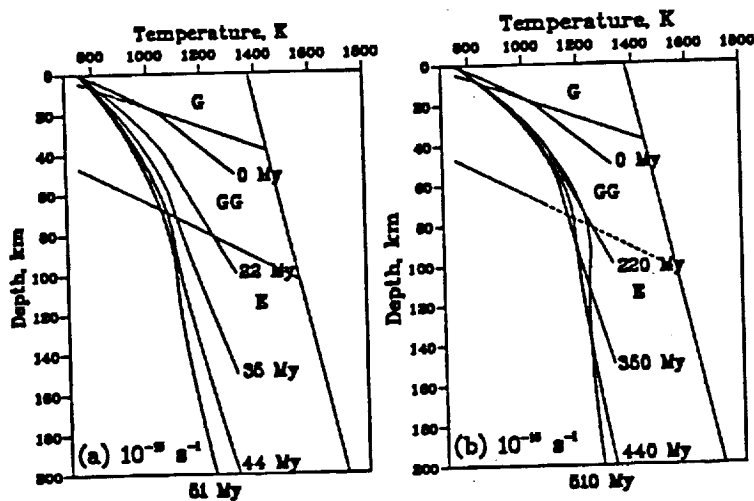
Figure 1. Thermal evolution of crust and mantle thickened by a uniform horizontal strain rate of (a) 10^{-15} and (b) 10^{-16} s^{-1}. The phase diagram of the gabbro (G) - garnet granulite (GG) - eclogite (E) transition [13] is also shown. The models shown correspond to models (a) 1, 2 and 3, and (b) 4, 5 and 8 in Table 1.
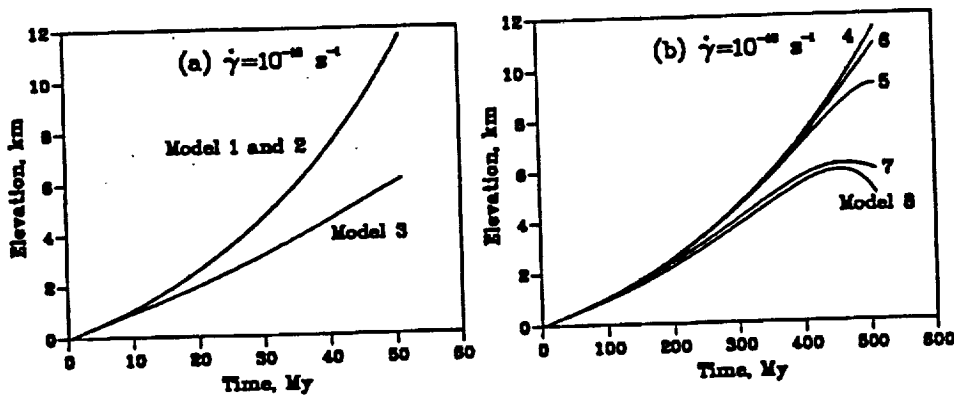
Figure 2. Temporal variation of elevation for the models in Table 1.

The Gabbro - Eclogite Phase Transition and The Elevation of Mountain Belts on Venus

NORIYUKI NAMIKI

Department of Earth, Atmospheric, and Planetary Sciences, Massachusetts Institute of

Technology, Cambridge

SEAN C. SOLOMON

Department of Terrestrial Magnetism, Carnegie Institution of Washington, Washington, D.C.

ABSTRACT

Maxwell Montes, standing up to 7 km above the adjacent highland plateaus, constitute the highest mountain belt on Venus. Because the thickness of the crust is likely to be limited by the gabbro - garnet granulite - eclogite phase transitions, this relief is difficult to reconcile with the assumption of thermodynamic equilibrium and a standard Airy isostatic model. We explore the hypothesis that the crust-mantle boundary is not in phase equilibrium, but rather is rate-limited by the temperature-dependent diffusion of the slowest ionic species. Under the simplifying assumption that the mountains formed by uniform horizontal shortening of the crust and lithospheric mantle at a constant rate, we solve the one-dimensional thermal evolution problem. The time-dependent density structure and surface elevation are calculated by assuming a temperature-dependent reaction rate and local Airy isostatic compensation. For a rate of horizontal strain of 10^{-15} s^{-1} or greater, the rise in temperature at the base of the crust during mountain formation is modest to negligible, the deepening lower crust is metastable, and surface elevation increases as the crust is thickened. For strain rates less than 10^{-16} s^{-1}, in contrast, crustal temperature increases with time because of internal heat production, and the lower crust is more readily transformed to the dense eclogite assemblage. For such models a maximum elevation is reached during crustal shortening. While this maximum relief is 7 km or more for some models, a smaller density contrast between crust and mantle than assumed here (500 kg m^{-3}) and incorporation of horizontal heat transport would lessen this value. We therefore favor formation of the mountain belt at a strain rate at least of order 10^{-15} s^{-1}. By this reasoning, Maxwell Montes must be comparatively young, of order 50 My.

INTRODUCTION

The linear mountain belts of western Ishtar Terra on Venus are notable for their topographic relief and slope and for the intensity of surface deformation [*Barsukov et al.*, 1986; *Solomon et al.*, 1991, 1992]. These four mountain belts, including Akna, Freyja, Maxwell, and Danu Montes (Figure 1), are generally regarded as products of large-scale compression and horizontal shortening of the crust and lithosphere [*Crumpler et al.*, 1986; *Solomon et al.*, 1991, 1992; *Kaula et al.*, 1992]. Among these mountain belts, Maxwell Montes is the highest and stands up to 11 km above mean planetary radius and 7 km above the highland plain Lakshmi Planum (Figure 1). Volcanism is rare to absent in Maxwell, Freyja, and Akna Montes, but a number of magmatic features are evident in Danu Montes [*Solomon et al.*, 1991; *Head et al.*, 1991; *Kaula et al.*, 1992], the mountain range least elevated above Lakshmi Planum.

The bulk composition and radioactive heat production of the crust on Venus, where measured, are similar to those of terrestrial basalts [*Surkov et al.*, 1984, 1987]. Because basalt transforms to eclogite at high pressure and because eclogite is likely to be denser than mantle material, the thickness of the crust may be limited by the gabbro - garnet granulite - eclogite phase transitions [*Anderson*, 1981; *Turcotte*, 1989]. The phase transition depth depends on the temperature structure of the crust beneath the mountains. If the thermal gradient is low and thermodynamic equilibrium is assumed, the phase changes would take place at shallow depth, and simple isostatic models underpredict the relief [*Vorder Bruegge and Head*, 1991]. If the thermal gradient is high, in contrast, the base of the crust is predicted to undergo melting before a sufficiently deep root can form to support the mountains. Thus the 7-11 km maximum elevation of Maxwell Montes is difficult to understand under the assumptions of local isostasy and thermodynamic equilibrium except in the unlikely situation that the crust beneath the mountains contains a large volume of magma [*Vorder Bruegge and Head*, 1991].

A possible explanation for the great relief of Maxwell Montes is that the base of the crust is not in phase equilibrium. Because of the high surface temperature on Venus (750 K) and the very low

water abundance of the lower atmosphere [*von Zahn et al.*, 1983], the Venus crust is thought to contain negligible water [*Kaula*, 1990]. It has been suggested that under anhydrous conditions, the gabbro - eclogite phase transition takes place by solid-state diffusion and may require a geologically significant time to run to completion [*Ahrens and Schubert*, 1975]. Solid-state diffusion is a strongly temperature-dependent process, so that quantifying this suggestion for application to Venus requires the solution of a heat transport problem. In this paper we develop simple models for the thermal evolution of the crust beneath mountain belts on Venus in an attempt to constrain the time-dependent depth of the gabbro - eclogite transition and thus to assess this hypothesis.

Because at long wavelengths the topography of western Ishtar Terra is correlated with the gravity field, at least partial dynamical support of the regional elevation of about 4 km is likely [e.g., *Grimm and Phillips*, 1991]. We therefore adopt the 7-km elevation of Maxwell Montes above the adjacent plateau as a conservative estimate of the relief attributable to local isostasy.

THERMAL MODEL

We assume that the crustal and mantle portions of the thermal boundary layer shorten horizontally and thicken vertically with time in the manner of pure shear. The thermal structure is then governed by the one-dimensional heat equation,

$$\frac{\partial T}{\partial t} + \dot{\gamma} \, z \, \frac{\partial T}{\partial z} = \kappa \frac{\partial^2 T}{\partial z^2} + \frac{A}{C_P} \tag{1}$$

where T is temperature, t is time, $\dot{\gamma}$ is the horizontal strain rate, z is depth, κ is the thermal diffusivity, A is the crustal heat production, and C_P is the specific heat. Under the assumption that deformation is by pure shear, $\dot{\gamma}$ is constant and the vertical velocity is given by the product of $\dot{\gamma}$ and z. We solve equation (1) numerically by an explicit finite difference approximation.

Model Parameters

The thermal diffusivity is assumed to be 1.0×10^{-6} m^2 s^{-1} in both crust and mantle. The crustal

heat production is assumed to equal 1.0×10^{-10} W kg^{-1}, on the basis of the K, U, and Th concentrations determined by gamma ray spectrometry by Venera and Vega landers [*Surkov et al.*, 1987]. The specific heat is assumed to be 850 kJ kg^{-1} K^{-1}. The other physical properties of crustal and mantle materials are assumed to be those, respectively, of tholeiitic basalt and peridotite [*Basaltic Volcanism Study Project*, 1981]. Temperature at the surface and the bottom of the thermal boundary layer are fixed, respectively, at 750 K and at a value T_{bl}, a free parameter in numerical models. The initial temperature profile is determined by the assumption of steady-state conditions with zero strain rate. The increase in temperature with depth due to adiabatic compression is not considered here, because compressional heating is negligible compared with crustal heat production.

T_{bl} is interpreted as the temperature in an isothermal core of a thermal convection cell [*Turcotte and Schubert*, 1982] and is, thus, fixed at a constant. For a given T_{bl}, an initial temperature T_c at the base of the crust is determined. Since temperature at the base of the crust controls the elevation of the mountains, T_c has more importance than T_{bl}. *Zuber* [1987] analyzed wavelengths of tectonic features on Venus and found that the crustal thickness is less than about 15 km if the average vertical thermal gradient in the crust dT/dz is 25 K km^{-1}, and less than about 30 km if dT/dz is 10 K km^{-1}. The absence of significant viscous relaxation of impact crater relief also limits the crustal thickness in plains regions to be less than 10 km for dT/dz = 20 K km^{-1} and 20 km for dT/dz = 10 K km^{-1} [*Grimm and Solomon*, 1988]. These results give a maximum temperature difference across the crust of about 400 K. Therefore T_{bl} is given initially so that T_c satisfies this upper bound.

The phase diagram is assumed to be that of tholeiitic basalt [*Ito and Kennedy*, 1971], and the densities of gabbro and eclogite are taken to be 2900 and 3500 kg m^{-3}. The density of garnet granulite is assumed to increase linearly from that of gabbro to that of eclogite as pressure increases at a given temperature. The density of the mantle is assumed to be 3400 kg m^{-3}. The elevations calculated by an assumption of local Airy isostatic compensation are sensitive to the density difference between crust and mantle. We have adopted a relatively large value of 500 kg m^{-3}.

Because a large density difference results in a higher elevation for a given root thickness, this assumption permits a conservative lower bound on horizontal strain rate. We discuss later the consequence of a lesser density contrast.

Diffusion Rates

The micromechanism of the gabbro - eclogite transition is not well understood. In this study we assume that volume diffusion of cations is the process most likely to limit the rate of the transformation, which involves chemical as well as phase changes. The volume fraction of reacted components, ψ, is given by,

$$\dot{\psi}\psi = D/r^2 \tag{2}$$

where r is the typical grain radius and D is the diffusion coefficient [*Ahrens and Schubert*, 1975]. For each parcel of shortening thermal lithosphere, ψ is obtained by integration over time. The density at a given depth is determined from the volume fractions of reacted and unreacted components.

There are several reactions occurring among constituent minerals in the garnet granulite stability field [*Ringwood*, 1975]. The rate of each reaction is difficult to assess, because of a paucity of experimental data. We focus on the diffusion rates of ionic species in pyroxene, garnet, and olivine, because those minerals characterize the phase assemblages and therefore play important roles in the phase transitions. Plagioclase is possibly another important mineral for this assessment, but no data for self diffusion in plagioclase are available. The data for volume diffusion in silicates show that silicon and oxygen diffuse much more slowly than divalent and trivalent cations. Thus the Si-O groups provide a static framework through which the cations diffuse [*Freer*, 1981]. We examine the diffusion rates of four major cations, Mg^{2+}, Fe^{2+}, Ca^{2+}, and Al^{3+} (Figure 2). The slowest diffusion rate is likely to limit the reaction rate.

Diffusion rates of Fe^{2+} and Mg^{2+} in garnet and olivine [*Chakraborty and Ganguly*, 1991; *Morioka and Nagasawa*, 1991], of Mg^{2+} in pyroxene [*Cygan and Lasaga*, 1985], and of Ca^{2+} in olivine [*Morioka and Nagasawa*, 1991] have been experimentally determined (Figure 2). Of these

the diffusion rate of Mg^{2+} in garnet ($D_{Mg,Gt}$) is the lowest. Of course, if the diffusion rate of any unmeasured major species is slower than that of Mg^{2+} in garnet, then the phase change rate will be limited by this slower cation. We therefore take the diffusion coefficient $D_{Mg,Gt}$ for this process as an upper bound on D in equation (2).

Other diffusion rates, while not well-determined experimentally, have been estimated, either from measurements at a single temperature, or from observed compositional gradients. While all such estimates include large uncertainties, we take the minimum value of these estimates as a lower bound on D in equation (2). This minimum is for diffusion of Al in orthopyroxene (Figure 2), estimated from an analysis of compositional gradients in natural assemblages [Smith and Barron, 1991]. The estimated rate depends on assumptions of cooling rate and pressure. While neither data nor estimates are available for the diffusion coefficients of Al^{3+} in olivine and garnet, cation diffusion in olivine and garnet is generally faster than in pyroxene [Freer, 1981; Smith and Brown, 1988], and thus is not likely to be rate-limiting. The diffusion of Ca^{2+} in garnet has been estimated by numerical simulation only at 1200°C [Chakraborty and Ganguly, 1991] and is faster than that of Al^{3+} in orthopyroxene at that temperature (Figure 2). The mobilities of Ca^{2+} and Fe^{2+} are held to be comparable in garnet and pyroxene, because neither garnet nor pyroxene in natural assemblages is consistently homogeneous in those elements [Smith and Barron, 1991]. These considerations reinforce the view that $D_{Al,Opx}$ gives a reasonable lower bound on D in equation (2). The two bounds on D are

$$D \leq D_{Mg,Gt} = 2.8 \times 10^{-8} \exp \left[- (270 \text{ kJ} + 3.2 \times 10^{-6} \text{ P}) / (\text{RT}) \right] \quad (3a)$$
$$D \geq D_{Al, Opx} = 1.1 \times 10^{-5} \exp \left[-400 \text{ kJ} / (\text{RT}) \right] \quad (3b)$$

where P is in Pa [Morioka and Nagasawa, 1991; Smith and Barron, 1991].

There is some possibility that the assumed lower bound on D is too large. Sauter et al. [1988] and Sauter and Harte [1990] reported a diffusion rate of Al^{3+} in clinopyroxene less than the lower bound given above (Figure 2), while Freer et al. [1988] experimentally obtained a maximum diffusion rate as great as the upper bound given above (Figure 2). Further, the diffusion rates in

plagioclase are generally less than in pyroxene [*Smith and Brown*, 1988], and interdiffusion of CaAl-NaSi in plagioclase is several orders of magnitude slower than the lower bound on D [*Grove et al.*, 1984]. If D is as low as suggested by these last results, no phase transition is expected to occur during the formation of mountains on Venus. However, the reaction rate is unlikely to be much slower than as given by the lower bound on D, because if volume diffusion is too slow, the reaction rate will be limited by grain-boundary diffusion.

Grain-boundary diffusion, in fact, has been proposed as a possible governing process in metamorphic reactions, because grain-boundary diffusion coefficients can be several orders of magnitude greater than those for volume diffusion [*Joesten*, 1991]. Whether the phase change proceeds by volume diffusion or grain-boundary diffusion will be governed by the process that is most efficient for mass transport. Grain-boundary diffusion coefficients can be misleading, however, because mass transport by such a process is confined to a thin layer, i.e., the grain boundary. Unfortunately, grain-boundary diffusion data for the minerals involved in the gabbro - garnet granulite - eclogite reactions are few and generally not well determined [*Joesten*, 1991]. Reliable experimental data for grain-boundary diffusion of oxygen in forsterite, for instance, have been reported only at two temperatures [*Condit et al.*, 1985]. These measurements suggest that grain-boundary diffusion for grain sizes of 1-10 mm is no more efficient for bulk transport than the lower bound on volume diffusion adopted above (Figure 2).

NUMERICAL RESULTS

Temperatures in the thickening crust and mantle are calculated for rates of horizontal convergence of 10^{-15} (Figure 3a) and 10^{-16} s^{-1} (Figure 3b). For all models discussed here (Table 1), thicknesses of crust and thermal boundary layer are assumed to be initially 20 and 50 km, respectively, and to increase to 100 and 250 km, respectively. Temperature profiles for the strain rate of 10^{-15} s^{-1} are vertically stretched as the crust and mantle portion of thermal boundary layer are thickened (Figure 3a). Temperatures do not increase significantly from initial values because heat is transferred mainly by advection and the contribution of crustal heat production is minor.

Hence gabbro remains metastable for 50 My or more, and the elevation of shortened lithosphere can increase as much as 12 km above the surrounding area of undeformed lithosphere in that time interval (Model 1 in Figure 4a). Equation (2) shows that the reaction runs to completion in a shorter time for small grains than for larger grains. Also it is clear from equation (3) that a higher temperature increases the diffusion rate and promotes the reaction. For the slower diffusion rate ($D_{Al,Gt}$), however, a strain rate of 10^{-15} s^{-1} is sufficiently fast to suppress these effects (Model 2). The phase transition proceeds, i.e., elevation is limited, only if grains are small, diffusion is rapid, and temperature is high (Model 3).

For a strain rate of 10^{-16} s^{-1}, crustal heat production dominates advective heat transfer after the crust becomes as thick as 60-80 km (Figure 3b). The resulting increase in temperature hastens the phase transition, and the slower strain rate lengthens the formation time of the mountains. For larger grains (r=10 mm) and a diffusion constant given by equation (3a) the elevation reaches 11 km or more even if T_c is as great as 1120 K (Model 4 in Figure 4b). For the same value of T_c the elevation is at most 7 km for grains of 1 mm radius (Model 5). If T_c is greater than 1120 K, the model gives a maximum elevation lower than 7 km, that is, the model fails to explain the observed relief of Maxwell Montes. Therefore this result provides an upper bound on T_c for small grain size. If D is given by equation (3b), that upper bound is lowered to 1030 K (Model 6). Thus the combination of the longer formation time due to the lesser value of $\dot{\gamma}$ and the faster reaction due to higher temperature yields constraints on the range of parameters controlling the phase change if the elevation of the mountains is to reach 7 km or more above the adjacent plateaus.

DISCUSSION

The thermal model described above is simple, but significant constraints on the strain rate governing mountain building and the temperature at the base of the crust are nonetheless obtained. In this section, we first consider how the results would differ if key parameters were varied or the models were modified. We then discuss some implications of the numerical results given above.

The thermal evolution results are insensitive to the assumed initial thickness of the crust. At a

strain rate of 10^{-15} s^{-1}, the advection-dominated thermal profile indicates that the temperature of each parcel of crust changes little as the parcel deepens. For a given value of T_c, the thermal structure at a given crustal thickness is not affected by initial crustal thickness, or, equivalently, initial thermal gradient. Only the time required for the crust to reach that thickness depends on the initial thickness. At a strain rate of 10^{-16} s^{-1}, in contrast, the thermal profile is close to steady state, that is, the geotherm is nearly the same as that for zero strain rate and thus does not depend on the initial crustal thickness. The initial crustal thickness is still important for the maximum relief, however, because by assumption it is identical to the crustal thickness beneath surrounding areas, taken here to be undergoing negligible rates of horizontal strain. By the assumption of Airy isostasy, at a given crustal thickness beneath the mountains a difference of 10 km in the thickness of the crust beneath surrounding areas results in a 1.5 km difference in relief.

Also important is the density difference between crust and mantle. If densities of 3000 and 3300 kg m^{-3} for crust and mantle are assumed, relative elevations are ~40% lower than the values presented here. At a strain rate of 10^{-15} s^{-1}, gabbroic lower crust remains metastable during the formation of mountains in most cases, as shown by models 1 and 2. Therefore a smaller density contrast simply requires thicker crust, i.e., greater duration of shortening, and does not otherwise constrain the model parameters. In contrast, at a strain rate of 10^{-16} s^{-1}, maximum elevations are limited in most cases by the gabbro - eclogite phase transition because of the high temperature at the base of the crust, as shown by models 5 and 6. The lower relief resulting from a smaller density contrast lessens the upper bound on T_c. Thus such a lower density contrast constrains the models of thermal structure and phase transition depth more severely at low strain rates than do the density values adopted above.

At a strain rate of 10^{-16} s^{-1}, the thermal regime is dominated by crustal heat production and diffusion of heat. Horizontal heat transfer within the shortening thermal lithosphere therefore is probably not negligible. The maximum increase in temperature at the bottom of the crust due to horizontal heat transfer can be estimated from the solution for the instantaneous heating of a semi-infinite half-space [*Turcotte and Schubert*, 1982],

$$\delta T = \Delta T \, \text{erfc} \left(\frac{L}{2\sqrt{\kappa t}} \right) \qquad \qquad (4)$$

where δT is the increase in temperature, ΔT is the temperature difference beneath the crust and an isothermal core which surrounds the shortening lithosphere, L is the horizontal scale of the mountains, and t is the formation time. In our problem, ΔT is given by T_{bl} - T_c, and L is ~100 km. Formation times of 50 My at a strain rate of 10^{-15} s^{-1} and of 500 My at a strain rate of 10^{-16} s^{-1} result in δT of 2×10^{-2} and 60 K, respectively. The assumption of one-dimensional heat transfer is therefore reasonable at the higher strain rate, but horizontal diffusion of heat increases temperature significantly at the lower strain rate. If horizontal heat transport were included in the thermal models at the lower strain rate, the reaction rate of the phase change would be faster, the maximum elevation would be less, and the corresponding upper bound on T_c would be lower.

These considerations favor the formation of Maxwell Montes at horizontal strain rates on the order of 10^{-15} s^{-1}. The implied age of the mountains is of order 50 My or less. Such an age is young compared with the average crater retention age of the surface of Venus of about 500 My [*Phillips et al.*, 1991]. An important question is whether such a young age is consistent with the presence of the 100-km diameter Cleopatra crater [*Basilevsky et al.*, 1987] (Figure 1) in Maxwell Montes. The age of a single crater, of course, even a large one, is difficult to specify. The rate of formation of impact craters larger than 20 km in diameter on Venus has been estimated as $3.3 \pm 1.8 \times 10^{-15}$ km^{-2} yr^{-1} from the statistics of Earth-crossing and Venus-crossing asteroids and an assumed set of scaling laws [*Shoemaker et al.*, 1991]. If Maxwell Montes, 1000 km long and 500 km wide, formed in 50 My, the expected number of craters larger than 20 km in diameter is ~0.08. The probability that one and only one crater larger than 20 km diameter formed in Maxwell Montes in 50 My is thus ~8 %. This value indicates that the presence of a large impact crater is not likely if the mountains formed in only 50 My, but the figure is not so low as to reject the hypothesis at high confidence.

Although Danu Montes display compressional deformational features as extensive as the other mountain belts of Ishtar Terra, their maximum relief with respect to Lakshmi Planum is as little as 1 km (Figure 1). The presence of magmatic features within Danu Montes [*Solomon et al.*, 1991,

1992; *Head et al.*, 1991; *Kaula et al.*, 1992] indicates that temperature beneath the mountains exceeded the solidus of crustal or shallow mantle material at least locally. Given such evidence for relatively high temperature in the lower lithosphere, the reaction of sufficiently deep lower crustal material has probably gone nearly to completion, which may account for the comparatively modest topographic relief of these mountains. It is also noteworthy that even a small amount of melting can greatly enhance grain-boundary diffusion [*Condit et al.*, 1985; *Watson*, 1991]. Assessing the cause of higher temperatures beneath Danu Montes requires more detailed thermal models than the simple one-dimensional ones considered here.

CONCLUSIONS

Taking into account the temperature-dependent reaction rate of the gabbro - eclogite phase transition, horizontal strain rates of 10^{-15} and 10^{-16} s^{-1} result in significant differences in the maximum elevation of mountains on Venus, not only because of the difference in the formation time for relief, but also because of the difference in the thermal regime from advection-dominated to crustal-heat-production dominated. For a strain rate of 10^{-15} s^{-1}, the observed maximum elevation of Maxwell Montes can be explained as a consequence of local isostasy and disequilibrium phase boundary depth for a wide range of physical parameters. For the lesser horizontal strain rate of 10^{-16} s^{-1}, only limited parameter values for thermal models are allowed, and this limitation becomes more difficult to satisfy when a smaller density contrast between the crust and mantle is assumed or when horizontal heat transport is considered. We favor the formation of Maxwell Montes at a strain rate of 10^{-15} s^{-1} or greater, although the likelihood that Cleopatra crater is younger than the implied age for Maxwell Montes (~50 My) is low. Magmatism within Danu Montes indicates higher temperatures in the crust or shallow mantle beneath those mountains than beneath the other mountains. The modest elevation of Danu Montes relative to the other mountain belts of Ishtar Terra can be understood as a consequence of near completion of the phase transition.

REFERENCES

Ahrens, T. J., and G. Schubert, Gabbro - eclogite reaction rate and its geophysical significance, *Rev. Geophys. Space Phys., 13*, 383-400, 1975.

Anderson, D. L., Plate tectonics on Venus, *Geophys. Res. Lett., 8*, 309-311, 1981.

Barsukov, V. L., et al., The geology and geomorphology of the Venus surface as revealed by the radar images obtained by Venera 15 and 16, *Proc. Lunar Planet. Sci. Conf. 16th, J. Geophys. Res., 91*, D378-D398, 1986.

Basaltic Volcanism Study Project, *Basaltic Volcanism on the Terrestrial Planets*, 1286 pp., Pergamon, New York, 1981.

Basilevsky, A. T., Structure of central and eastern areas of Ishtar Terra and some problems of Venusian tectonics, *Geotectonics, 20*, 282-288, 1986.

Basilevsky, A. T., B. A. Ivanov, G. A. Burba, I. M. Chernaya, V. P. Kryuchkov, O. V. Nikolaeva, D. B. Campbell, and L. B. Ronca, Impact cratering of Venus: A continuation of the analysis of data from Venera 15 and 16 spacecraft, *J. Geophys. Res., 92*, 12,869-12,901, 1987.

Bindschadler, D. L., and E. M. Parmentier, Mantle flow tectonics: The influence of ductile lower crust and implications for the formation of topographic uplands on Venus, *J. Geophys. Res., 95*, 21,329-21,344, 1990.

Chakraborty, S., and J. Ganguly, Compositional zoning and cation diffusion in garnets, in *Diffusion, Atomic Ordering, and Mass Transport*, edited by J. Ganguly, pp. 120-175, Springer-Verlag, New York, 1991.

Condit, R. H., H. C. Weed, and A. J. Piwinskii, A technique for observing oxygen diffusion along grain boundary regions in synthetic forsterite, in *Point Defects in Minerals*, edited by R. N. Schrock, *Geophysical Monograph, 31*, 97-105, Am. Geophys. Union, Washington, D. C., 1985.

Crumpler, L. S., J. W. Head, and D. B. Campbell, Orogenic belts on Venus, *Geology, 14*, 1031-1034, 1986.

Cygan, R. T., and A. C. Lasaga, Self - diffusion of magnesium in garnet at 750°C to 900°C, *Am. J. Sci.*, *285*, 328-350, 1985.

Freer, R., Diffusion in silicate minerals and glasses: A data digest and guide to the literature, *Contrib. Mineral. Petrol.*, *76*, 440-454, 1981.

Freer, R., M. A. Carpenter, J. V. P. Long, and S. J. B. Reed, "Null result" diffusion experiments with diopside: Implications for pyroxene equilibria, *Earth Planet. Sci. Lett.*, *58*, 285-292, 1982.

Grimm, R. E., and R. J. Phillips, Tectonics of Lakshmi Planum, Venus: Tests for Magellan, *Geophys. Res. Lett.*, *17*, 1349-1352, 1990.

Grimm, R. E., and R. J. Phillips, Gravity anomalies, compensation mechanisms, and the geodynamics of western Ishtar Terra, Venus, *J. Geophys. Res.*, *96*, 8305-8324, 1991.

Grimm, R. E., and S. C. Solomon, Viscous relaxation of impact crater relief on Venus: Constraints on crustal thickness and thermal gradient, *J. Geophys. Res.*, *93*, 11,911-11,929, 1988.

Grove, T. L., M. B. Baker, and R. J. Kinzler, Coupled CaAl-NaSi diffusion in plagioclase feldspar: Experiments and application to cooling rate speedometry, *Geochim. Cosmochim. Acta*, *48*, 2113-2121, 1984.

Head, J. W., III, D. B. Campbell, C. Elachi, J. E. Guest, D. P. McKenzie, R. S. Saunders, G. G. Schaber, and G. Schubert, Venus volcanism: Initial analysis from Magellan data, *Science*, *252*, 276-288, 1991.

Ito, K., and G. C. Kennedy, An experimental study of the basalt - garnet granulite - eclogite transition, in *The Structure and Physical Properties of the Earth's Crust*, edited by J. G. Heacock, *Geophysical Monograph*, *14*, 303-314, Am. Geophys. Union, Washington, D. C., 1971.

Joesten, R., Grain-boundary diffusion kinetics in silicate and oxide minerals, in *Diffusion, Atomic Ordering, and Mass Transport*, edited by J. Ganguly, pp. 345-395, Springer-Verlag, New York, 1991.

Kaula, W. M., Venus: A contrast in evolution to Earth, *Science*, *247*, 1191-1196, 1990.

Kaula, W. M., D. L. Bindschadler, R. E. Grimm, V. L. Hansen, K. M. Roberts, and S. E. Smrekar, Styles of deformation in Ishtar Terra and their implications, *J. Geophys. Res, 97*, 16,085-16,120, 1992.

Morioka, M., Cation diffusion in olivine—II. Ni-Mg, Mn-Mg, Mg, and Ca, *Geochim. Cosmochim. Acta, 45*, 1573-1580, 1981.

Morioka, M., and H. Nagasawa, Ionic diffusion in olivine, in *Diffusion, Atomic Ordering, and Mass Transport*, edited by J. Ganguly, pp. 176-197, Springer-Verlag, New York, 1991.

Phillips, R. J., R. E. Arvidson, J. M. Boyce, D. B. Campbell, J. E. Guest, G. G. Schaber, and L. A. Soderblem, Impact craters on Venus: Initial analysis from Magellan, *Science, 252*, 288-297, 1991.

Pronin, A. A., The structure of Lakshmi Planum, an indication of horizontal asthenospheric flow on Venus, *Geotectonics, 20*, 271-281, 1986.

Ringwood, A. E., *Composition and Petrology of the Earth's Mantle*, 618 pp., McGraw-Hill, New York, 1975.

Roberts, K. M., and J. W. Head, Western Ishtar Terra and Lakshmi Planum, Venus: Models of formation and evolution, *Geophys. Res. Lett., 17*, 1341-1344, 1990.

Sautter, V., and B. Harte, Diffusion gradients in an eclogite xenolith from the Roberts Victor kimberlite pipe: (2) kinetics and implications for petrogenesis, *Contrib. Mineral. Petrol., 105*, 637-649, 1990.

Sautter, V., O. Jaoul, and F. Abel, Aluminum diffusion in diopside using the $^{27}Al(p,r)^{28}Si$ nuclear reaction: Preliminary results, *Earth Planet. Sci. Lett., 89*, 109-114, 1988.

Shoemaker, E. M., R. F. Wolfe, and C. S. Shoemaker, Asteroid flux and impact cratering rate on Venus (abstract), *Lunar Planet. Sci., 22*, 1253-1254, 1991.

Smith, D., and B. Barron, Pyroxene - garnet equilibration during cooling in the mantle, *Am. Mineral., 76*, 1950-1963, 1991.

Smith, J. V., and W. L. Brown, *Feldspar Minerals*, 828 pp., Springer-Verlag, Berlin, 1988.

Solomon, S. C., J. W. Head, W. M. Kaula, D. McKenzie, B. Parsons, R. J. Phillips, G.

Schubert, and M. Talwani, Venus tectonics: Initial analysis from Magellan, *Science*, *252*, 297-312, 1991.

Solomon, S. C., et al., Venus tectonics: An overview of Magellan observation, *J. Geophys. Res.*, *97*, 13,199-13,255, 1992.

Surkov, Y. A., V. L. Barsukov, L. P. Moskalyeva, V. P. Kharyukova, and A. L. Kemurdzhian, New data on the composition, structure, and properties of Venus rock obtained by Venera 13 and Venera 14, *Proc. Lunar Planet. Sci. Conf. 14th, J. Geophys. Res.*, *89*, B393-B402, 1984.

Surkov, Y. A., F. F. Kirnozov, V. N. Glazov, A. G. Dunchenko, L. P. Tatsy, and O. P. Sobornov, Uranium, thorium, and potassium in the Venusian rocks at the landing sites of Vega 1 and 2, *Proc. Lunar Planet. Sci. Conf. 17th, J. Geophys. Res.*, *92*, E537-E540, 1987.

Turcotte, D. L., A heat pipe mechanism for volcanism and tectonics on Venus, *J. Geophys. Res.*, *94*, 2779-2785, 1989.

Turcotte, D. L., and G. Schubert, *Geodynamics: Applications of Continuum Physics to Geological Problems*, 450 pp., Wiley, New York, 1982.

von Zahn, U., S. Kumar, H. Niemann, and R. Prinn, Composition of the Venus atmosphere, in *Venus*, edited by D. M. Hunten, L. Colin, T. M. Donahue, and V. I. Moroz, pp. 299-430, University of Arizona Press, Tucson, 1983.

Vorder Bruegge, R. W., and J. W. Head, Processes of formation and evolution of mountain belts on Venus, *Geology*, *19*, 885-888, 1991.

Watson, E. B., Diffusion in fluid-bearing and slightly-melted rocks: Experimental and numerical approaches illustrated by iron transport in dunite, *Contrib. Mineral. Petrol.*, *107*, 417-434, 1991.

Zuber, M. T., Constraints on lithospheric structure of Venus from mechanical models and tectonic surface features, *Proc. Lunar Planet. Sci. 17th, J. Geophys. Res.*, *92*, E541-E551, 1987.

N. Namiki, Building 54-521, Department of Earth, Atmospheric, and Planetary Sciences, Massachusetts Institute of Technology, Cambridge, MA 02139.

S. C. Solomon, Department of Terrestrial Magnetism, Carnegie Institution of Washington, 5241 Broad Branch Road, N.W., Washington, DC 20015.

FIGURE CAPTIONS

Figure 1. Topographic map of western Ishtar Terra. Contour map of Magellan altimetry data gridded at 0.5° intervals of latitude and longitude; 1-km contour interval; polar stereographic projection. Cross symbol shows the location of Cleopatra crater (65.9°N 7.0°E).

Figure 2. Diffusion constants for ionic species in olivine, pyroxene, and garnet. Solid lines show diffusion constants that were experimentally determined (1 is for Fe in garnet [*Chakraborty and Ganguly*, 1991]; 2 is for Mg in garnet [*Chakraborty and Ganguly*, 1991]; 3 is for Fe in olivine [*Morioka and Nagasawa*, 1991]; 4 is for Mg in olivine [*Morioka and Nagasawa*, 1991]; 5 is for Mg in clinopyroxene [*Cygan and Lasaga*, 1985]; and 6 is for Ca in olivine [*Morioka and Nagasawa*, 1991]). The shaded area shows the range of estimates for $D_{Al,Opx}$, including maximum and minimum (7) values [*Smith and Barron*, 1991]. Cross symbols show the values determined at a single temperature (8 is for Ca in garnet [*Chakraborty and Ganguly*, 1991]; 9 is an upper bound on the diffusion constant of Al in clinopyroxene [*Freer et al.*, 1988]; 10 and 11 are values for Al in clinopyroxene from *Sautter et al.* [1988] and *Sautter and Harte* [1990], respectively). The constants for grain-boundary diffusion of O in forsterite [*Condit et al.*, 1985] are converted to equivalent volume diffusion by multiplying by the ratio of grain boundary width to grain diameter (12); the grain boundary width was taken to be 3 μm [*Condit et al.*, 1985], and the grain diameters were taken to be 1-10 mm.

Figure 3. Thermal evolution of crust (solid) and mantle (dashed) thickened at a uniform horizontal strain rate of (a) 10^{-15} and (b) 10^{-16} s^{-1}. The phase boundary of the gabbro (G), garnet granulite (GG), and eclogite (E) assemblages and the solidus (S) [*Ito and Kennedy*, 1971] are shown by dotted lines. The models shown correspond to models (a) 1 and (b) 4 and 5 in Table 1.

Figure 4. Temporal variation of elevation for the thermal models in Table 1.

TABLE 1. Parameters for Thermal Models

Model	r, mm	$\dot{\gamma}$, s^{-1}	D	T_c, K	T_{bl}, K
1	10	10^{-15}	$D_{Al,Opx}$	1050	1321
2	1	10^{-15}	$D_{Al,Opx}$	1120	1461
3	1	10^{-15}	$D_{Mg,Gt}$	1130	1481
4	10	10^{-16}	$D_{Al,Opx}$	1120	1461
5	1	10^{-16}	$D_{Al,Opx}$	1120	1461
6	10	10^{-16}	$D_{Mg,Gt}$	1030	1281

Fig. 1

Fig. 2

Fig. 3

Fig. 4

(a) $\dot{\gamma} = 10^{-15}$ s^{-1}

Model 1 Model 2 Model 3

(b) $\dot{\gamma} = 10^{-16}$ s^{-1}

Model 4 Model 5 Model 6

Elevation, km

Time, My
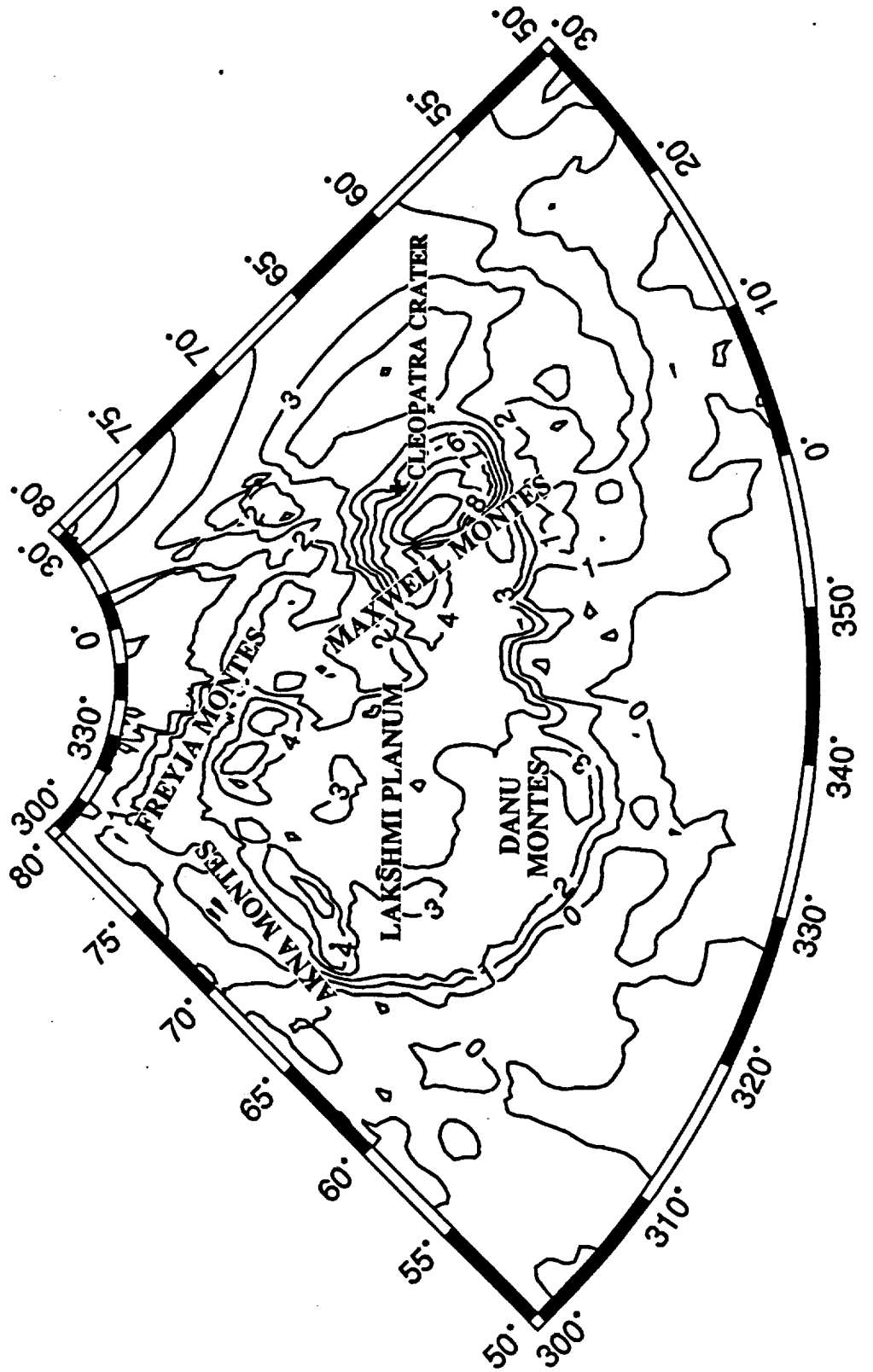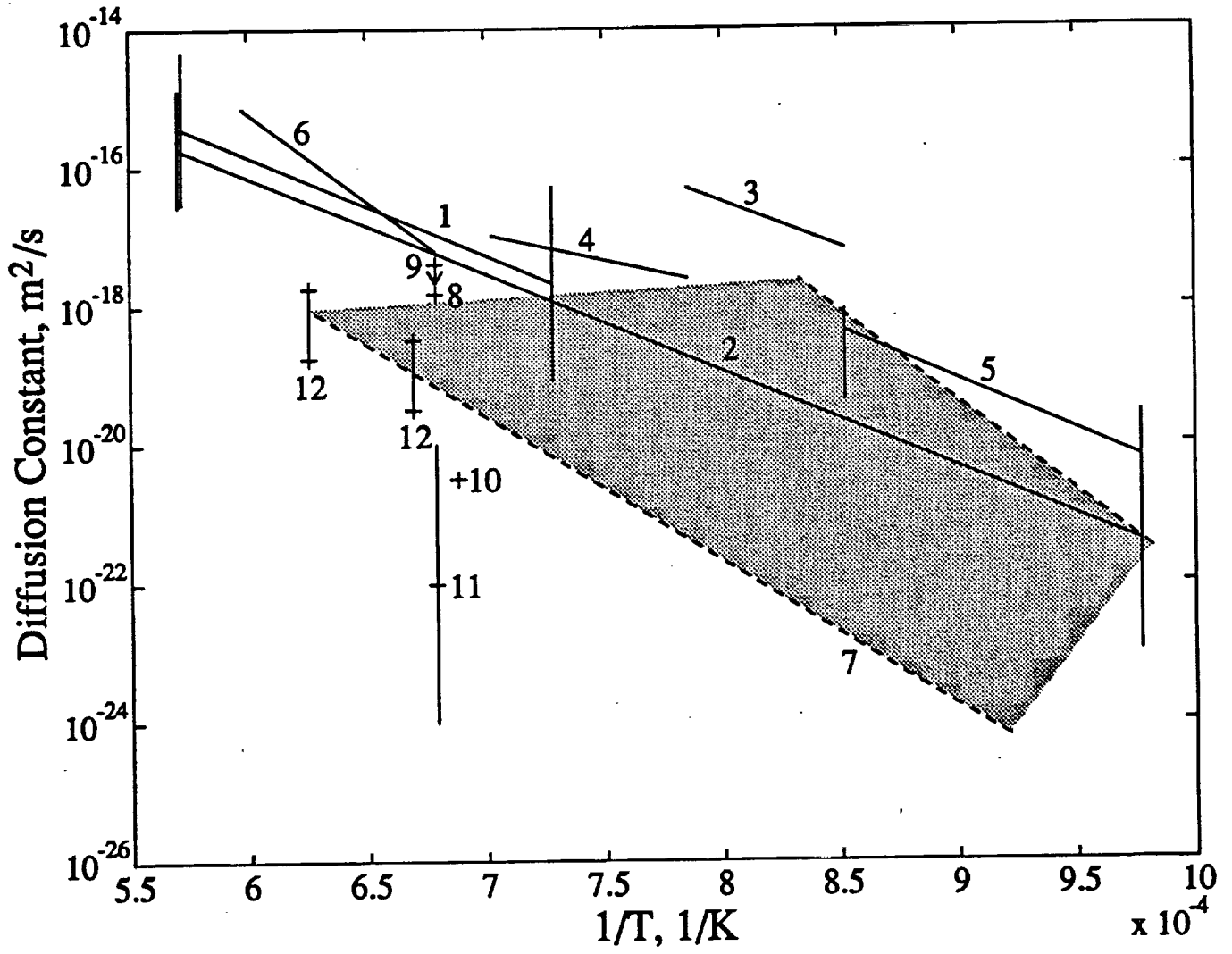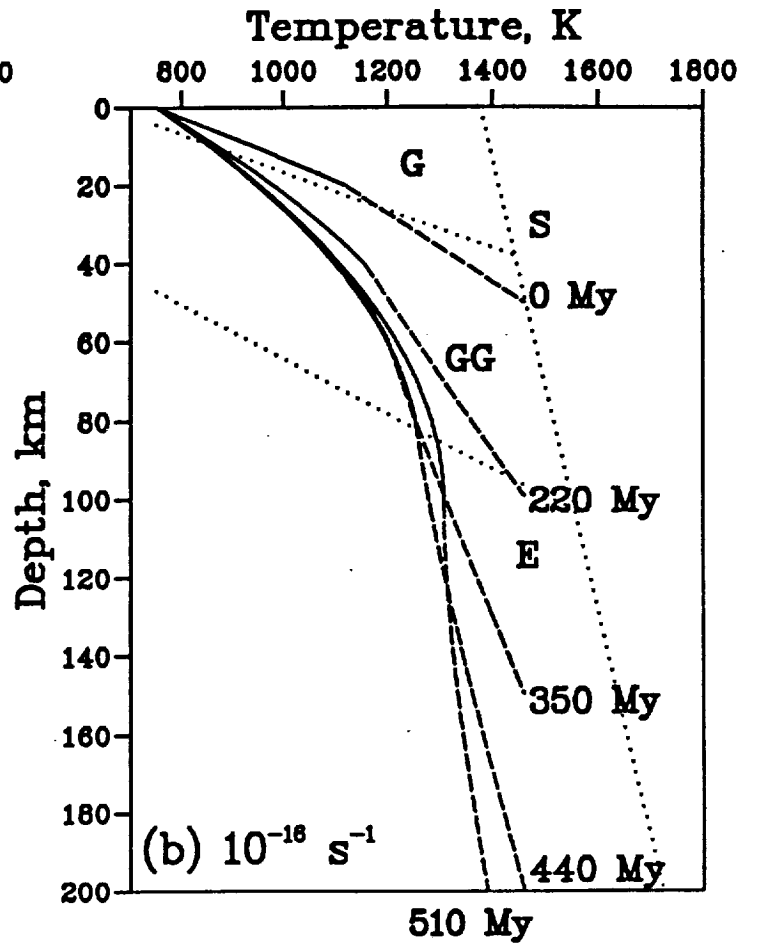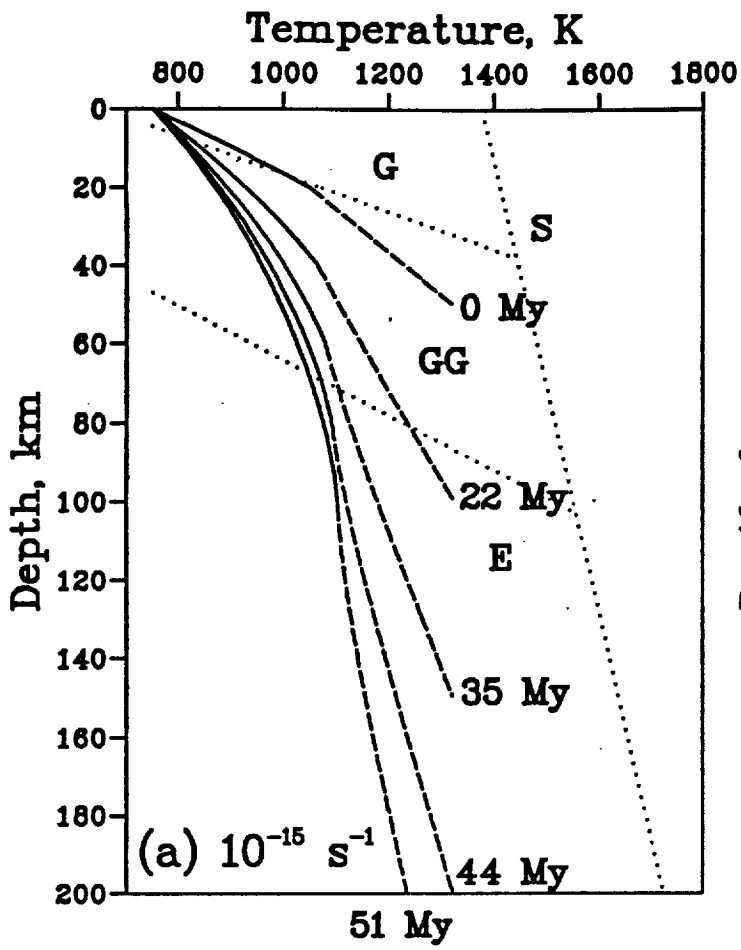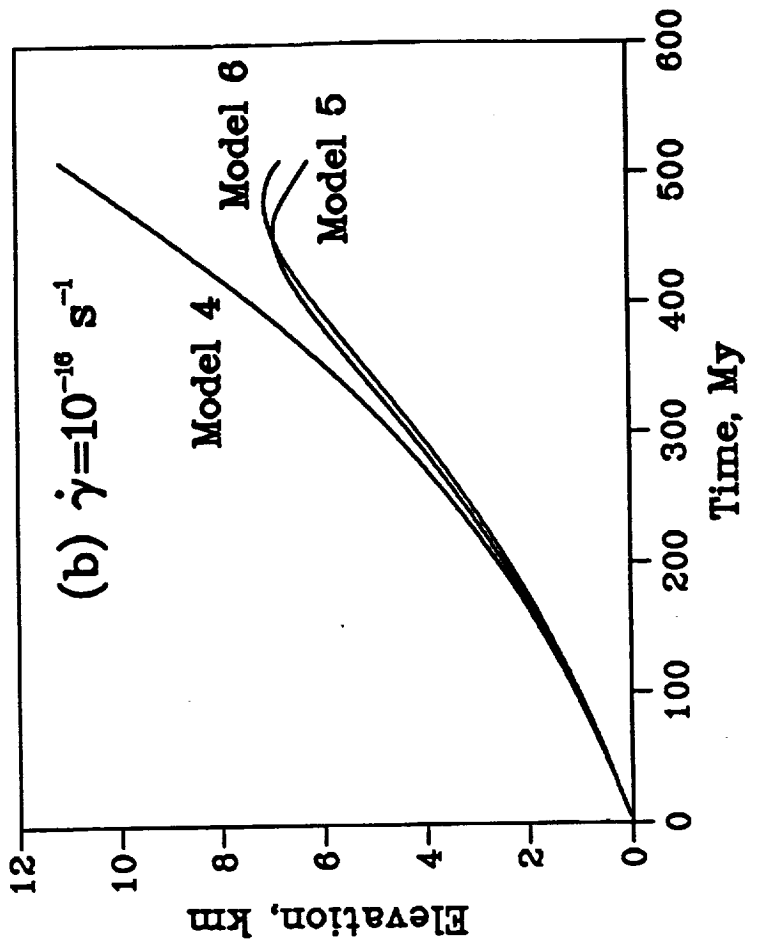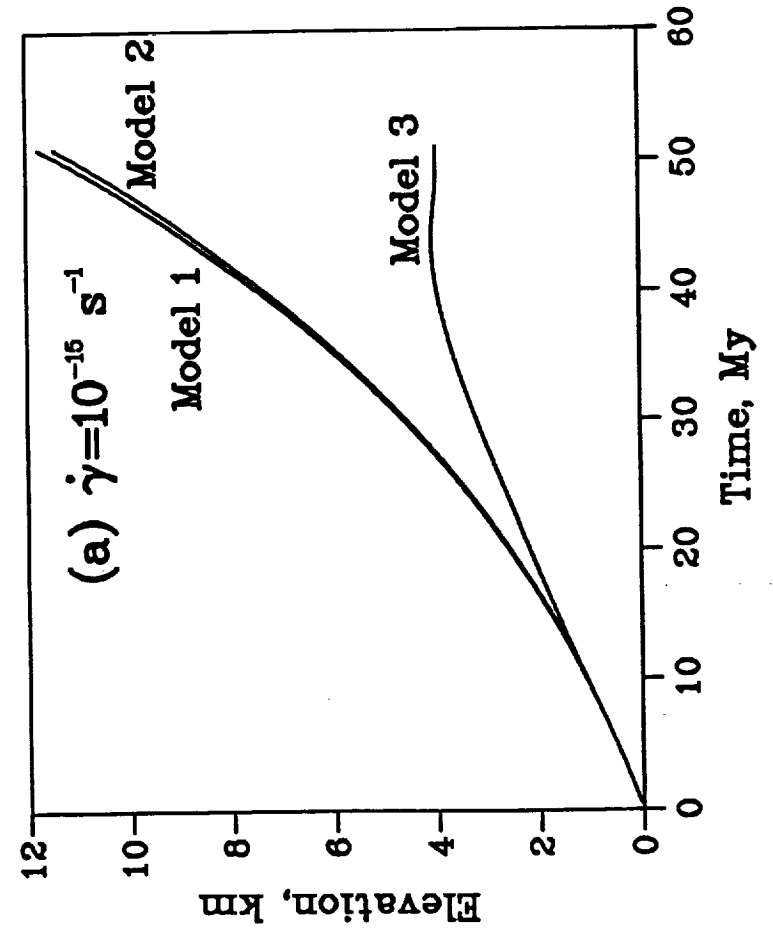
5. ORIGIN AND THERMAL EVOLUTION OF MARS

G. SCHUBERT
University of California, Los Angeles

S. C. SOLOMON
Massachusetts Institute of Technology

D. L. TURCOTTE
Cornell University

M. J. DRAKE
University of Arizona

and

N. H. SLEEP
Stanford University

The thermal evolution of Mars is governed by subsolidus mantle convection beneath a thick lithosphere. Models of the interior evolution are developed by parameterizing mantle convective heat transport in terms of mantle viscosity, the superadiabatic temperature rise across the mantle and mantle heat production. Geological, geophysical and geochemical observations of the composition and structure of the interior and of the timing of major events in Martian evolution, such as global differentiation, atmospheric outgassing and the formation of the hemispherical dichotomy and Tharsis, are used to constrain the model computations. Isotope systematics of SNC meteorites suggest core formation essentially contemporaneously with the completion of accretion. Ancient fluvial landforms and a high atmospheric D/H ratio imply substantial degassing and

atmosphere formation early in the history of Mars. Accretional considerations also favor initial melting of much of the outer portions of the planet. Initial conditions assumed for the thermal history calculations thus include full differentiation of a silicate mantle and metal-sulfide core and a mantle at a high, near-solidus temperature. The subsequent thermal evolution involves cooling of the mantle and core, differentiation of a crust and thickening of a rigid lithosphere. As a result of the removal of much of the initial interior heat by vigorous mantle convection, perhaps augmented by an upward concentration of heat-producing elements into the crust, the rate of decrease of mantle temperature and surface heat flow was much more rapid during the first 1 Gyr of Martian history than subsequent to that era. Crustal production rates were also much higher in the first 1 Gyr of Martian evolution than later in the planet's history. This temporal behavior is consistent with geologic evidence for a general decrease with time in the Martian volcanic flux and, following a brief initial period of massive crustal formation, early global contraction recorded in the widespread formation of wrinkle ridges on geologically ancient surface units. The thermal evolution models predict a present lithosphere several 100 km thick, in agreement with estimates of elastic lithosphere thickness inferred from the response to major surface loads. Numerical calculations of fully three-dimensional, spherical convection in a shell the size of the Martian mantle are carried out to explore plausible patterns of Martian mantle convection and to relate convective features, such as plumes, to surface features, such as Tharsis. The models have upwellings in the form of cylindrical-like plumes and down-wellings in the form of interconnected sheets. There is no single dominant plume. Therefore, if Tharsis is associated with one or more mantle plumes, then the lithosphere beneath Tharsis must be thinned or cracked either to promote plume concentration in the region or to facilitate magma migration through the lithosphere. Thermal history models for Mars admit present core states similar to the Earth, but they also allow completely fluid cores and cores closer to complete freezing. The key parameter distinguishing among these possibilities is the weight fraction of sulfur in the core. If this fraction is ~ 15% or more, then the present Martian core is completely fluid and there is no thermal convective dynamo. The unambiguous determination of the presence or absence of an intrinsic Martian magnetic field by future spacecraft missions will provide an essential constraint on interior structure and thermal evolution models. The eventual measurement of the natural magnetic remanence of rock samples on Mars with ages > 3.5 Gyr will also provide an essential test of thermal history and core dynamo models.

I. INTRODUCTION

The acceptance of Mars as the parent body of the SNC meteorites (McSween 1984; Bogard et al. 1984; Becker and Pepin 1984; chapter 4) has profoundly changed our view of the planet's evolution. Martian thermal history models of the late 1970s and early 1980s were largely dominated by the idea that the core of Mars formed subsequent to its accretion, after radioactive heating had raised the temperatures in the planet's interior sufficiently above the relatively cold initial temperatures to initiate melting and gravitational separation of Fe-FeS (Johnston et al. 1974; Solomon et al. 1976; Johnston and Toksöz 1977; Toksöz and Johnston 1977; Toksöz et al. 1978;

Toksöz and Hsui 1978; Solomon 1978,1979; Arvidson et al. 1980; Davies and Arvidson 1981). Core formation in these models occurred as late as a few Gyr after Mars accreted, and the segregation of the core lasted for up to 1 Gyr. Late core formation was supported by the notion that Martian surface geology was dominated by extensional tectonics, requiring global heating and planetary expansion until late in the planet's evolution (Solomon and Chaiken 1976; Solomon 1978,1979). However, the U/Pb isotopic composition of SNC meteorites requires core formation at about 4.6 Gyr ago (Chen and Wasserburg 1986), either contemporaneous with accretion or within a few 100 Myr of the end of accretion. We must therefore abandon thermal evolution scenarios of Mars with cold initial temperatures and late core formation and instead adopt the view that accretional heating raised temperatures inside Mars sufficiently high that the core formed early, prior to the end of accretion or within a few 100 Myr thereof, and that Mars began its post-accretional evolution fully differentiated and hot. In this new view of Martian thermal history, early Mars was similar to the larger terrestrial planets Venus and Earth, whose cores formed early as a consequence of high accretional temperatures (see, e.g., Kaula 1979b; Wetherill 1985). The post-accretional evolution of Mars, like that of Venus and Earth, is one of secular cooling.

In the following, we discuss the case for a hot initial Mars and early core formation in greater detail. Numerous lines of evidence, in addition to the U-Pb isotopic composition of SNC meteorites, support an early hot, differentiated planet. The structure of the Martian interior is a major factor in determining the post-accretional thermal history of Mars, and we briefly discuss interior structural models inferred from geophysical and geochemical data (see also chapter 7). In accordance with the model of early core and crust formation, we assume that the major radial structure of Mars has been little changed since the end of accretion (except for the lithosphere, which has thickened with time).

The principal characteristics of Mars, i.e., the north-south crustal dichotomy, the Tharsis Rise, the center of mass-center of figure offset, global tectonic patterns and the possible absence of a magnetic field, must all be understood in terms of the thermal history, and we discuss how these characteristics might be accommodated in a model in which Mars steadily cools from a hot, differentiated start. We present quantitative models of Martian cooling history that parameterize heat transport by subsolidus mantle convection. These models allow us to estimate properties of Mars for which no direct measurements presently exist, such as the cooling rate of the planet, its present lithosphere thickness and surface heat flux, and the present extent of inner core solidification. Finally, we use the results of numerical calculations of fully three-dimensional, spherical convection to discuss convective patterns in the Martian mantle. These computations place constraints on possible convective models for the formation of the hemispheric crustal asymmetry and Tharsis.

II. INTERNAL STRUCTURE

Although the seismic experiment on Viking Lander 2 provided no direct information on Mars' internal structure (Anderson et al. 1977; Goins and Lazarewicz 1979; Toksöz 1979), it is likely that Mars is divided into a crust, mantle and core. However, the thicknesses, densities and compositions of these regions are uncertain (see chapter 7).

A. Core

Geophysical and geochemical data constrain the size and composition of the Martian core. The geophysical data include the mean density of Mars (3933 kg m⁻³; Bills and Ferrari 1978) and its dimensionless axial moment of inertia (0.365, according to Reasenberg [1977] and Kaula [1979a]). The dimensionless axial moment of inertia C/MR^2, where C is the principal moment of inertia about the rotation axis, M is the mass of Mars (6.42×10^{23} kg) and R is the radius of Mars (3390 km) is obtained from the inferred value of J_2 (the second-degree zonal coefficient in the spherical harmonic representation of the hydrostatic part of the gravitational potential of Mars). To determine C/MR^2 it is necessary first to remove the relatively large nonhydrostatic contribution J_2 to the observed J_2 ($J_2 = J_2 + J_{2H}$). Estimation of J_2 is model dependent and, as a result, the axial moment of inertia of Mars is uncertain. According to Reasenberg (1977) and Kaula (1979a), J_2 is principally due to Tharsis (see also Binder and Davis 1973). Under the assumption that the nonhydrostatic contributions to the moments of inertia are symmetric about an equatorial axis through the center of Tharsis, it can be shown that $C/MR^2 = 0.365$ (Reasenberg 1977; Kaula 1979a). Bills (1989a) has recently suggested that the nonhydrostatic component of J_2 is more likely to be a maximally triaxial ellipsoid, i.e., with the intermediate moment of inertia exactly midway between the greatest and least moments. This assumption leads to a value of C/MR^2 equal to 0.345. Kaula et al. (1989) have argued that the larger value of C/MR^2 is more physically plausible: (1) because the rotation axis of Mars adjusts sufficiently rapidly compared to changes in nonhydrostatic density anomalies that it is the axis of maximum moment of inertia for the nonhydrostatic density field; (2) because the gravity and topography of Mars are dominated by Tharsis; and (3) because tectonic models of Tharsis require generation and support that are almost axisymmetric about a line from the center of Mars through Tharsis.

Goettel (1981) has explored the consequences of the mean density and moment of inertia I of Mars for the radius of the Martian core and the densities of the planet's core and mantle ($I = (C + B + A)/3$, where A and B are principal moments of inertia about two orthogonal axes in the equatorial plane; $I/MR^2 = C/MR^2 - 2J_3/3$; $J_3 = 1.96 \times 10^{-3}$). His results, based on $I/MR^2 = 0.365$, are summarized in Table I. (Spherically symmetric compositional models can only be constrained by I/MR^2 and other spherically aver-

aged observables.) Mars could possess either a small, iron-rich core of high density (a pure Fe core would have a density of 8090 kg m⁻³ and constitute 14.8% of the mass of Mars), or a large, low-density core with substantial S (or other light element). An FeS core would have a density of 5770 kg m⁻³ and comprise 26.3% of the mass of Mars. The core mass increases with its size despite the density decrease (Fig. 1). Goettel's (1981) results for core properties consistent with the mean density and the mean moment of inertia of Mars are in general agreement with the predictions of other models (Johnston and Toksöz 1977; Okal and Anderson 1978; Basaltic Volcanism Study Project 1981). On the basis of all these models, the probable radius of the Martian core lies in the range 1500 to 2000 km, and the fractional mass of the core is likely to be between 15 and 30%.

Independent geochemical evidence on the mass of the Martian core is provided by the SNC meteorites. Treiman et al. (1987) have determined the

TABLE I

Ranges In Properties of the Martian Core Allowed by the Mean Density and Dimensionless Mean Moment of Inertia[a]

Property	Range
Radius	1300-1900 km
Fractional mass	13-26%
Central pressure	45-37 GPa
Density	8900-5800 kg m⁻³

[a] $I/MR^2 = 0.365$ assumed. Table after Goettel 1981.

Density, kg m⁻³ — Core Density — Mantle Density — Mass Core/Mass Mars — Percent — Core Radius/Mars Radius

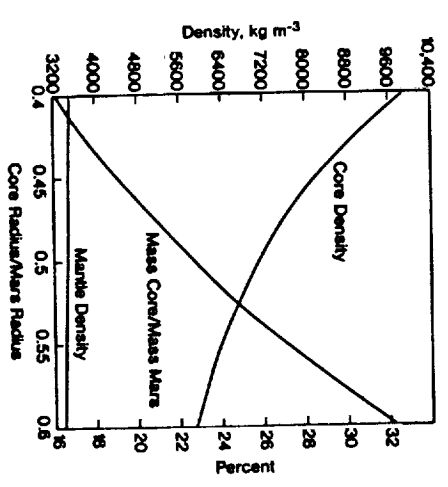Fig. 1. Core density ρ_c, mantle density ρ_m, and fractional core mass vs normalized core radius x for a two-layer model of Mars consistent with the mean density (3393 kg m⁻³) and dimensionless moment of inertia (0.365). The curves are simultaneous solutions of the equations 3933 kg m⁻³ = $\rho_m + (\rho_c - \rho_m)x^3$ and (0.365)(3933)(2.5) kg m⁻³ = $\rho_m + (\rho_c - \rho_m)x^5$.

abundances of siderophile and chalcophile elements in the mantle of Mars from SNC meteoritic abundances (using an element correlation method); they have modeled these abundances in terms of segregation of metal into the core. The abundances of siderophile and chalcophile elements may be substantially matched if Mars accreted homogeneously and a metallic core constituting 25 to 35 wt% of the planet formed in chemical equilibrium with the mantle. Best fits are achieved if the core material during differentiation consisted of ~ 50% solid Fe-Ni metal and 50% liquid Fe-Ni metal containing ~ 25 wt% S. The S content of such a core would be ~ 12.5 wt%. The ratio of Fe to Ni is poorly known, and the relative fractions of the solid and liquid components of both the early and modern core are unconstrained.

Laul et al. (1986) have also calculated the mass and composition of the core by assuming C I abundances of Fe and Ni and a $0.35 \times$ C I abundance of S. From mass balance, and abundances of these elements inferred for the Martian mantle from the compositions of the SNC meteorites, they obtained a core comprising 21.7 wt% of the planet, with an S abundance of 14 wt%. Laul et al. (1986) also conclude that Mars accreted homogeneously and that the core is in equilibrium with the mantle. However, the low core mass that they compute does not yield as good a fit to the depletions of siderophile and chalcophile elements as the larger core masses of Treiman et al. (1987).

We will see in Sec. IV.A that the abundance of S in the core of Mars is a crucial parameter determining the extent to which the core solidifies as the planet cools through geologic time. Unfortunately, the S content of the Martian core must still be considered as uncertain. The agreement between the estimates of Laul et al. (1986) and Treiman et al. (1987) of the wt% S in the Martian core, while encouraging, may only reflect the use of the same limited geochemical data set by both groups.

B. Mantle

Consistent with the core properties summarized in Table I, the thickness of the Martian mantle ranges between ~ 1500 and 2100 km. The zero pressure density of the mantle, for $I/MR^2 = 0.365$, is between ~ 3400 and 3470 kg m^{-3} (Goettel 1981). If the olivine-spinel phase transition occurs in the Martian mantle, it would be found at depths greater than approximately 1000 km (Basaltic Volcanism Study Project 1981; see chapter 7). Still higher-pressure phase changes involving the formation of perovskite and magnesiowustite might occur in the deep lower mantle of Mars depending on the size of the Martian core (chapter 7).

C. Crust

Mars has a distinct low-density crust of variable thickness, as indicated by the partial to complete isostatic compensation of surface topography (Phillips et al. 1973; Phillips and Saunders 1975). The mean thickness of the crust, however, is poorly constrained. A minimum value for the average crustal

thickness of 28 ± 4 km (depending on choice of crust-mantle density difference) was obtained by Bills and Ferrari (1978) by fitting a model crust of uniform density and variable thickness overlying a uniform mantle to topography and gravity expressed in spherical harmonics to degree and order 10; for this minimum mean thickness, the crust is of zero thickness beneath the Hellas basin. For a crustal thickness of 15 km at the Viking 2 Lander site, a value derived from arrival times of seismic phases of a possible Marsquake interpreted as waves reflected off the crust-mantle boundary (Anderson et al. 1977), Bills and Ferrari (1978) obtained a mean crustal thickness of 37 ± 3 km. The crustal thickness beneath the Hellas basin in this model is 9 ± 1 km while beneath Tharsis it is 69 ± 8 km. In all the models of Bills and Ferrari (1978), maximum crustal thickness occurs beneath Tharsis and minimum crustal thickness is found beneath the Hellas basin. Sjogren and Wimberly (1981) used topography and gravity data to infer that the Hellas basin is isostatistically compensated at a best-fitting compensation depth of 130 ± 30 km. From the models of Bills and Ferrari (1978), this value corresponds to a globally averaged crustal thickness of ~ 150 km.

The approximately hemispherical division of the Martian surface between the topographically lower and stratigraphically younger northern plains and the heavily cratered southern uplands, often termed the crustal dichotomy, is associated with thicker crust in the southern hemisphere (see, e.g., Janle 1983). The hemispheric crustal dichotomy contributes to the Martian center of mass-center of figure offset, as does the Tharsis bulge. The Martian center of figure is displaced from the center of mass by ~ 2.5 km toward a direction approximately midway between the centers of the southern highlands and the Tharsis bulge (see chapter 7).

III. CONSTRAINTS ON THERMAL EVOLUTION

Among the major constraints on thermal history models of Mars is the origin of the present internal structure of the planet. Viable thermal evolution models must account for the timing and formation of the core, the hemispheric crustal dichotomy, and the Tharsis Rise. Models should provide an explanation for the lack of magnetic field at present, or, if future observations should prove the existence of a small Martian magnetic field, the models should allow for the generation of that field. Thermal history models should be consistent with the evolution of surface stresses and strains as revealed by global tectonic patterns.

A. Core Formation

U-Pb data for several SNC meteorites intercept the concordia curve at about 4.5 Gyr as well as at a younger age variously thought to represent the crystallization age of the shergottites (Jones 1986) or the impact event that resulted in ejection of SNC material from the parent body (Chen and Wasser-

burg 1986). The 4.5 Gyr "age" indicated by U-Pb data, as well as whole-rock Rb-Sr model ages for SNC meteorites of about 4.6 Gyr (Shih et al. 1982), suggest early global differentiation, including formation of the core essentially contemporaneously with the completion of accretion. Differentiation of a core would heat Mars on average by as much as 300 K (Solomon 1979). A hot initial state for the planet is indicated by these results. Other indicators of a hot early Mars include: (1) the old age (≥4 Gyr) of the southern hemisphere highlands, suggesting early crustal differentiation (see below); (2) geologic (ancient, large flood features and valley networks; Carr 1987) and isotopic (high-atmospheric D/H ratio; Owen et al. 1988) evidence of early outgassing and an early atmosphere; and (3) tectonic evidence of global compression associated with planetary cooling over geologic time (see below). The interpretation of D/H in terms of early loss of water is not unique. Yung et al. (1988) and Jakosky (1990a) suggest loss of water over geologic time, while Zahnle et al. (1990a) argue for loss of water upon accretion.

Early core formation is made possible by the high accretional temperatures achieved through the burial of heat by large impacts (Kaula 1979b; Wetherill 1985). An example of accretional temperature profiles for Mars is shown in Fig. 2 (Coradini et al. 1983). In this example, there is a power-law distribution of impacting planetesimals by size, 30% of the impact kinetic energy is retained as heat, and a 100-Myr time scale of accretion is assumed. For this particular model, melting of a 360-km-thick shell occurs at the end of accretion. Models with higher temperatures and larger degrees of melting
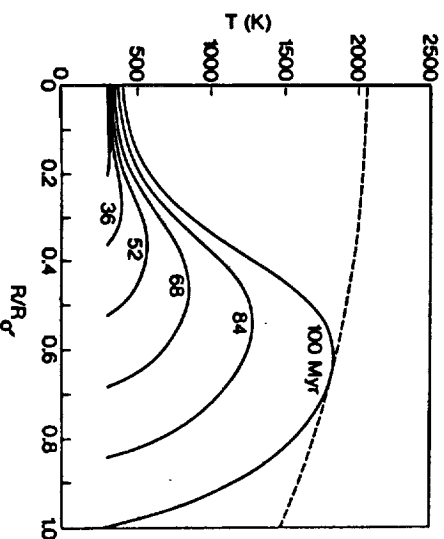

Fig. 2. Model accretional temperature profiles for Mars (figure after Coradini et al. 1983). The calculations are based on a 100 Myr accretion time scale and the assumption that 30% of the impact kinetic energy is retained as heat in the growing planet. The dashed curve is a model solidus temperature profile.

are possible, for example, by adoption of a larger value for the percent of impact kinetic energy retained as heat.

The importance of large impacts in the formation of the terrestrial planets and the validity of the 100-Myr accretional time scale are demonstrated by the planetary accumulation models of Wetherill (1985,1986). The spin and orbital properties of Mars and the other planets, especially their obliquities, are plausibly explained as consequences of impacts with large bodies during the process of planetary formation (Harris and Ward 1982; Hartmann and Vail 1986). A major problem in understanding the growth of Mars according to present models of planetary accretion is that the calculations typically result in objects that are several times more massive than Mars (Wetherill 1985,1986). The size of Mars may have been limited by disturbances to the planetesimal source population for Mars associated with outer-planet secular resonance regions, assuming of course that the formation of the outer planets preceded the growth of Mars (Wetherill 1986).

B. Magnetic Field

Mars may have a weak magnetic field, though this hypothesis is presently a matter of dispute (Russell et al. 1984; Dolginov 1987; see chapter 31). A fit of a dipole to the available Soviet magnetic field data gives a moment of 2×10^{12} Tesla-m^3 (2×10^{22} gauss-cm^3), or 3×10^{-4} times the Earth's moment, tilted ~ 15° with respect to the rotation axis and oriented in the opposite sense to the Earth's dipole moment (Dolginov et al. 1973,1976). A re-evaluation by Russell (1978b) leads only to an upper bound on the moment of 2×10^{11} Tesla-m^3, an order of magnitude less than the value of Dolginov and co-workers. Recent Phobos observations of the Martian magnetotail give no indication of an intrinsic planetary magnetic field (Riedler et al. 1989b; Ong et al. 1989). Magnetic field measurements in the close vicinity of Mars are needed to resolve this issue.

Several SNC meteorites display natural remanent magnetization (NRM) consistent with a magnetizing field of less than ~ 8 A/m (0.1 oe; Cisowski 1986). The timing and acquisition mechanism of the NRM are not well established, but it has been inferred that the magnetizing event was shock metamorphism during impact (Cisowski 1986). Whether an internal magnetic field on Mars is indicated at the time the SNC meteorites were ejected from the planet is unclear.

C. Crustal Dichotomy

The relative chronology of the various large-scale surface units on Mars is reasonably well established from stratigraphic and crater density relationships (see, e.g., Carr et al. 1973; Tanaka et al. 1988; also see chapters 11 and 12). The oldest units are the cratered terrain, an upland region as heavily cratered as the lunar highlands and occupying approximately the hemisphere south of a great circle inclined 35° to the equator (Mutch and Saunders 1976).

to the formation of the Martian ridged plains) ~3 to 3.5 Gyr ago (Tanaka 1986). In the synthesis of Tanaka et al. (1988), the early Hesperian "peak" is quite modest; a monotonic or nearly monotonic decrease of flux with time is implied. Greeley (1987) has suggested that the volume of volcanic material may be estimated by multiplying the area by an average thickness of ~1 km. A volume of 2×10^8 km^3 is equivalent to a global layer of volcanic material 1.5 km thick. Because the volume of igneous intrusions accompanying each eruption is generally larger than the volume of volcanic material (by a factor of 10 in continental regions on Earth [Crisp 1984] and perhaps even larger on Mars), a significant fraction of the Martian crust may have been added by igneous activity since the end of heavy bombardment.

E. Global Tectonic Deformation

Large-scale patterns of tectonic deformation on a planetary surface can be direct signatures of global thermal evolution (see chapter 8). For a planet with a globally continuous lithosphere, such as Mars, warming or cooling of the interior will give rise to net global expansion or contraction and thus, respectively, to extensional or compressional horizontal stress and strain near the planetary surface. The magnitude σ_t of thermal stress accumulated in any time interval is given by

$$\sigma_t = [E/(1 - \nu)]\Delta R/R \qquad (1)$$

where E and ν are the Young's modulus and Poisson's ratio of near-surface material and $\Delta R/R$ is the fractional change in radius during that time interval (Solomon 1986). The fractional radius change is related to the radial distribution of temperature change $\Delta T(r)$ by

$$\Delta R/R = (1/R) \int_0^R 2\alpha(r)\Delta T(r)dr \qquad (2)$$

where α is the volumetric coefficient of thermal expansion. For $\alpha = 3 \times 10^{-5}$K^{-1}, a change ΔT in average interior temperature of 100 K yields $\Delta R/R = 10^{-3}$ or $\Delta R = 3$ km. From Eq. (1), with $E = 80$ GPa and $\nu = 0.25$, such a radius change corresponds to $\sigma_t = 100$ MPa (1 kbar). Sufficiently large thermal stress and strain should be visible in globally distributed tectonic features whose timing and sense of deformation yield strong constraints on the history of internal temperatures (see, e.g., Solomon and Chaiken 1976). Large-scale tectonic features confined to a regional, rather than global, scale are also important indicators of thermal evolution, particularly of the characteristics of heat and strain imparted to the lithosphere by mantle dynamic processes.

The view of Martian tectonics that followed the Mariner 9 mission was that the planet experienced a prolonged period of lithospheric extension which gave rise to the extensive systems of graben mostly centered on the

While the absolute chronology of the Martian surface is a matter of debate (see, e.g., Hartmann 1973b,1977; Soderblom et al. 1974; Neukum and Wise 1976; Neukum and Hiller 1981; see chapter 12), most workers are in agreement that the heavily cratered southern uplands probably record the terminal phase of heavy bombardment of the inner solar system, dated for the Moon at 3.9 to 4.0 Gyr ago. The bulk of crustal formation must have occurred prior to this time.

The approximately hemispherical dichotomy between the ancient southern highlands and the younger northern plains is generally held to be an ancient first-order feature of the Martian crust. The dichotomy has been ascribed variously to a very long-wavelength mantle convective planform (Lingenfelter and Schubert 1973; Wise et al. 1979a), to post-accretional core formation (Davies and Arvidson 1981), and to a giant impact (Wilhelms and Squyres 1984). In view of the evidence from SNC meteorites discussed above, that core separation occurred essentially contemporaneously with accretion, that the crustal dichotomy involving late scenarios for the formation of the crustal dichotomy (Wise et al. 1979a: Davies and Arvidson 1981) may core-mantle segregation (Wise et al. 1979a: Davies and Arvidson 1981) may be discounted. Whether the dichotomy was the result of endogenic or exogenic processes, however, remains unresolved despite considerable ongoing photogeological analysis of the dichotomy boundary region (see, e.g., McGill 1988; Wilhelms and Baldwin 1989a).

D. Volcanic Flux

Mars shows abundant evidence of surface volcanic activity spanning a wide range of relative geologic ages (see chapter 13). There are numerous volcanic constructs, including the large volcanoes of the Tharsis province, and extensive volcanic plains with apparent flow fronts and other features associated with volcanic units (Carr 1973,1974; Malin 1977; Carr et al. 1977). There are relatively old and relatively young examples of both plains and shields. While the stratigraphic sequence of major volcanic units has been reasonably well established from crater density and superposition relationships (Tanaka et al. 1988), estimates of the absolute ages of volcanic units depend upon knowledge of the scaling of cratering flux and impacting-object size vs crater size from the Moon to Mars, knowledge that is, at best, incomplete (see, e.g., Chapman 1974; Wetherill 1974; Hartmann et al. 1981). Published ages for the stratigraphically young surfaces of the Tharsis shields, for instance, range from 2.5 Gyr (Neukum and Wise 1976) to on the order of 0.1 Gyr (see, e.g., Hartmann 1977).

An important constraint on global thermal evolution is the volcanic flux through time. Estimates of the surface area of volcanic material at each major stratigraphic stage, including corrections for later burial, have been given by Greeley (1987) and Tanaka et al. (1988). Both find 2×10^8 km^2 of volcanic material, though the two analyses differ in detail, particularly in the relative strength of a "peak" in the flux curve at early Hesperian times (corresponding

Tharsis region (Hartmann 1973c; Carr 1974b), the Valles Marineris canyon system (Sharp 1973) and the pervasive volcanism (Carr 1973). Thermal history models consistent with this view of tectonic evolution involved net warming and global expansion over much of the Martian history. The net warming was attributed variously to late core formation (Solomon and Chaiken 1976), to radioactive heating of the mantle following low-temperature differentiation of a sulfur-rich core (Toksöz and Hsui 1978), or to degassing of the interior and a consequent stiffening of the mantle rheology (Tozer 1985). As noted above, a hot initial state is now indicated for Mars from lead isotope data and planetary accretion considerations, so scenarios involving an initially cool interior (see, e.g., Solomon and Chaiken 1976; Toksöz and Hsui 1978) are not viable. Further, thermal history calculations explicitly including interior degassing and the consequent effect on mantle viscosity (McGovern and Schubert 1989) do not show a secular warming of the mantle as suggested by Tozer (1985).

Much of the evidence for lithospheric extension on Mars is provided from tectonic features in and near the Tharsis area. Although the extensional fractures radiating from the center of Tharsis span a region more than 8000 km across, Tharsis may nonetheless be regarded as a regional feature rather than part of a response to global stress. Further, there are important compressional features located in the ridged plains of Tharsis and oriented approximately circumferential to the center of activity (Wise et al. 1979b). Considerable effort has gone into understanding the evolution of the Tharsis province from this regional perspective. The long-wavelength gravity and topography of the region are not consistent with complete isostatic compensation by a single mechanism, such as crustal thickness variations (Phillips and Saunders 1975). Complete local isostasy is possible, however, if a combination of Airy (crustal thickness variations) and Pratt (mantle density variations) mechanisms act in concert; but this is possible only if the crust is relatively thin (or is pervasively intruded by high-density plutonic material) beneath the Tharsis Rise and substantial density anomalies persist to at least 300 to 400 km depth (Sleep and Phillips 1979,1985; Finnerty et al. 1988). Alternatively, a portion of the high topography of Tharsis can be supported by membrane stresses in the elastic lithosphere (Banerdt et al. 1982; Willemann and Turcotte 1982).

These compensation models have been used to predict lithospheric stresses for comparison with the observed distribution of tectonic features. The isostatic model for Tharsis predicts stresses in approximate agreement with the distribution and orientation of extensional fractures in the central Tharsis region and of compressive wrinkle ridges, while the model involving lithospheric support of a topographic load predicts stresses consistent with the more distal extensional features in regions adjacent to the Tharsis Rise (Banerdt et al. 1982; Sleep and Phillips 1985). An evolution in the nature of the support of Tharsis topography has been suggested (Banerdt et al. 1982; Solomon and Head 1982), though the sequence depends upon the relative

ages of distal and proximal tectonic features. If the distal features are older, then viscoelastic relaxation of stresses associated with an early episode of lithospheric loading may have led to an essentially isostatic state at present; if the distal features are younger, then a progression from local isostasy to lithospheric support as the Tharsis Rise was constructed may have been the natural consequence of global interior cooling and lithospheric thickening (Sleep and Phillips 1985). This distinction is complicated by the fact that superimposed global thermal stress is apparently required to account for the formation of many of the graben and wrinkle ridges, particularly in regions where both types of features are present.

Recent work on Martian tectonics may sharpen the constraints on global thermal stress. Chicarro et al. (1985) have utilized Viking images to map the global distribution of wrinkle ridges on Mars, including regions distant from Tharsis. They find that ridges occur commonly throughout ancient terrain. In volcanic plains, however, the distribution is highly uneven, with ridges strongly concentrated in the ridged plains units and in spotty occurrences in other regions. The lower Hesperian age (approximately 3 to 3.5 Gyr ago) for most major ridged plains units (Tanaka 1986) and the contrast in ridge density between cratered uplands and young volcanic plains (Chicarro et al. 1985) suggest that ridge formation may have been concentrated in a comparatively early state in Martian evolution (Watters and Maxwell 1986). Examining of crosscutting relations between ridges and graben also supports the view that most ridge formation in the Tharsis region was restricted to an early time period (Watters and Maxwell 1983).

The Martian tectonic history most consistent with all of these findings is one in which Tharsis evolved after the end of heavy bombardment from a primarily isostatic state to one with long-term lithospheric support. Superimposed on the stresses associated with the Tharsis Rise was a globally compressive stress produced by significant interior cooling in the interval 3 to 4 Gyr ago. Any additional cooling (or warming) in the last 3 Gyr has been sufficiently modest so that further changes in planetary volume have not led to widespread development of young compressive (or extensional) features.

F. Lithospheric Thickness

Estimates of lithospheric thickness on Mars provide important constraints on near-surface thermal gradients and thus on heat flux. The thickness of the thermal lithosphere may be inferred approximately from the heights of volcanic constructs, and the thickness of the elastic lithosphere may be inferred from the response to volcanic loads.

Volcanic constructs on Mars show a tendency to increase in height with time of formation, in that the oldest such features are a few kilometers high and the youngest shields are approximately 20 km high with respect to surrounding terrain (Carr 1974b; Blasius and Cutts 1976). This relationship has been ascribed to an increase in the hydrostatic head of the magma with time

because of a progressive deepening of the source region (Vogt 1974; Carr 1976). Assuming a relative density contrast of 10% between magma and average overburden, and ignoring viscous head loss, these heights give depths to magma chambers varying from perhaps as little as a few tens of km to somewhat over 200 km over the history of Martian shield formation.

The thickness T_e of the elastic lithosphere of Mars has been estimated from the tectonic response to individual loads (Thurber and Toksöz 1978; Comer et al. 1985) and from the global response to the long-wavelength load of the Tharsis Rise (Banerdt et al. 1982; Willemann and Turcotte 1982). The spacing of graben circumferential to the major volcanoes Ascraeus Mons, Pavonis Mons, Arsia Mons, Alba Patera and Elysium Mons indicate values for T_e of 20 to 50 km—equivalently, values of flexural rigidity D of 10^{23} to 10^{24} N-m (10^{30} to 10^{31} dyn cm) at the times of graben formation (Comer et al. 1985). For the Isidis basin region, the elastic lithosphere thickness is inferred to have exceeded 120 km ($D > 10^{25}$ N-m) at the time of mascon loading and graben formation (Comer et al. 1985). The absence of circumferential graben around Olympus Mons requires the elastic lithosphere to have been at least 150 km thick ($D > 3 \times 10^{25}$ N-m) at the time of loading (Thurber and Toksöz 1978; Comer et al. 1985; Janle and Jannsen 1986). Models of the response of Mars to the long-wavelength topography of the Tharsis Rise provide a reasonable fit to the geoid and to the distribution of tectonic features in the Tharsis province if the elastic lithosphere of Mars is globally ~ 100 to 400-km thick, corresponding to $D = 10^{25}$ to 7×10^{26} N-m (Banerdt et al. 1982; Willemann and Turcotte 1982).

The values for T_e, derived for individual loads are not consistent with a simple progressive increase with time in the thickness of the elastic lithosphere of Mars. The largest estimates of T_e, for instance, are for perhaps the oldest (Isidis mascon) and youngest (Olympus Mons) features considered (Tanaka et al. 1988). Spatial variations in elastic lithosphere thickness must have been at least as important as temporal variations (Comer et al. 1985). In particular, there appears to have been a dichotomy in lithosphere thickness that spanned a significant interval of time, with comparatively thin elastic lithosphere (T_e = 20 to 50 km) beneath the central regions of major volcanic provinces and substantially thicker elastic lithosphere (T_e in excess of 100 km) beneath regions more distant from volcanic province centers and appropriate for the planet as a whole.

The values of T_e may be converted to estimates of the lithospheric thermal gradient and heat flow, given a representative strain rate and a flow law for ductile deformation of material in the lower lithosphere and estimates of lithospheric thermal conductivity. Under the assumption that the large-values of elastic lithosphere thickness determined from the local response to the Tharsis Isidis mascon and Olympus Mons and from the global response to the Tharsis Rise exceed the thickness of the Martian crust, the depth to the base of the

mechanical lithosphere is determined by the ductile strength of the mantle. The minimum values of T_e, for the Isidis mascon and Olympus Mons correspond, by this line of reasoning, to mean lithospheric thermal gradients of no greater than 5 to 6 K km^{-1} and heat flow values < 17 to 24 mW m^{-2} (Solomon and Head 1990). For the Tharsis Montes and Alba Patera, the mechanical lithosphere thickness is likely governed by the strength of crustal material. The mean thermal gradients consistent with the values of T_e for these loads under this assumption fall in the range 10 to 14 K km^{-1} and heat flow values in the range 25 to 35 mW m^{-2} (Solomon and Head 1989). Essentially contemporaneous temperature differences of at least 300 K at 30 to 40 km depth are implied at a late stage in the development of the Tharsis province. Such temperature differences are too large to be solely the effect of large impacts that occurred some Gyr earlier (Bratt et al. 1985), but they are broadly similar to the temperature variations associated with lithospheric reheating beneath hot-spot volcanic centers on Earth (McNutt 1987). The temperature and heat-flow anomalies beneath the central regions of major volcanic provinces on Mars are presumably also related to mantle dynamic processes, such as convective upwelling plumes and magmatism. Lithospheric thinning beneath the central regions of major volcanic provinces by hot, upwelling mantle plumes can account for the different estimates of elastic lithosphere thickness in these regions as compared with the global average.

G. Mantle Heat Sources

Of particular importance to the thermal evolution of Mars are the concentrations of the radiogenic heat-producing elements K, Th and U in the Martian mantle. Estimates of the abundances of these elements have been made by Taylor (1986), Treiman et al. (1986) and Laul et al. (1986) using SNC meteorites. Taylor (1986) plots analyses of the meteorites on a K/U vs K diagram and shows that the SNC meteorite data are consistent with terrestrial data. The K/U ratio in Mars is not distinguishable from the Earth's, but this analysis does not yield information on the bulk K abundance in Mars.

Treiman et al. (1986) and Laul et al. (1986) have estimated abundances of K, Th and U using their correlation with other refractory lithophile elements. The database used by the two sets of authors is substantially the same. Correlations of K with La show that the mantle of Mars has a K/La ratio of ~ 0.3 of the C I ratio. The corresponding Th/La and U/La ratios are ~ 1.7 and 2 times the C I ratio, respectively (Treiman et al. 1986). Uncertainties in each estimate are factors of 2, 1.7 and 2, respectively. The abundances of K, Th and U, assuming that the Martian mantle has C I abundances of La, are summarized in Table II. If the Martian mantle has higher abundances of La, the abundance of K, Th and U must be scaled upward accordingly. The bulk Martian abundances must be reduced in proportion to the mass of the core, assuming that these elements are excluded from the core. The ratios of K/U

TABLE II

Radiogenic Element Abundance Estimates for the Mantles of Mars and Earth

	K (ppm)	Th (ppb)	U (ppb)	K/U	Th/U
Mars[a]	170	48	16	10^4	3
Mars[b]	315	56	16	2×10^4	3.5
Earth[c]	257	102.8	25.7	10^4	4

[a]Treiman et al. 1986.
[b]Laul et al. 1986.
[c]Turcotte and Schubert 1982.

and Th/U are ~ 10^4 and 3, respectively, the former being indistinguishable from the Earth's ratio while the latter is lower than the terrestrial value of ~ 4. There is uncertainty in each ratio of about a factor of 2 based on the scatter in the raw data and the lack of knowledge of the absolute values of refractory-element abundances such as La in Mars relative to C I chondrites. Given the uncertainties in these values, we conclude that radiogenic element abundances in the mantles of Mars and Earth are broadly similar.

IV. THERMAL HISTORY MODELS

On the basis of the constraints discussed in the previous section, we present quantitative simulations of Martian thermal history. In its initial state, Mars is hot and completely differentiated into a core and mantle. The mantle temperature is essentially at the solidus and the core is superliquidus. Radiogenic heat sources are assumed to be distributed uniformly through the mantle, although upward concentration of radioactive elements could accompany differentiation of an early crust. The subsequent evolution consists of a simple cooling, with monotonic decreases in temperature, heat flux and convective vigor and a monotonic increase in the viscosity of the mantle. We parameterize convective heat transport through the mantle by a simple Nusselt number-Rayleigh number relationship. The parameterization approach is well established as a way of investigating the thermal evolution of the planets (see, e.g., Schubert et al. 1979; Sharpe and Peltier 1979; Stevenson and Turner 1979; Cook and Turcotte 1981). We employ two different parameterization schemes. With the parameterization model of Stevenson et al. (1983) we focus on the cooling of the core, the extent of core solidification and the generation of a planetary magnetic field by a core dynamo. With the parameterization model of Turcotte et al. (1979), we emphasize crustal differentiation.

A. Coupled Core-Mantle Evolution

The planetary thermal history model of Stevenson et al. (1983) is employed in this section to study the consequences of core cooling for the thermal and physical state of the Martian core and the generation of a magnetic field by thermal or chemical compositional convection in the core. The model includes: (1) mantle radiogenic heat production; (2) a mantle viscosity directly proportional to $\exp(H/RT)$, where H is a constant activation enthalpy, T is a mantle temperature and R is the gas constant; (3) heat transfer by whole-mantle subsolidus convection parameterized by a Nusselt number-Rayleigh number relation; (4) coupled energy balance equations for the mantle and core; (5) possible inner core freezeout with exclusion of a light-alloying element (most likely sulfur) which then mixes uniformly through the outer core; and (6) realistic pressure- and composition-dependent freezing curves for the core. More detailed information about the model equations and parameter values can be found in Stevenson et al. (1983) and Schubert and Spohn (1990), who have recently extended the Mars model to include lithospheric growth and the magnetic dipole moment. The solutions we discuss below are actually new calculations, based on the Mars model of Schubert and Spohn (1990), of cases that are almost identical to ones presented in Stevenson et al. (1983). Parameter values are given in Stevenson et al. (1983) and Schubert and Spohn (1990).

Model cooling histories of Mars are typified by the results in Fig. 3, which shows mantle heat flow vs time for models with initial core sulfur concentrations x_s of 10 and 25 wt% (sulfur is assumed to be the light-alloying element in the core in these models). The models with $x_s = 10\%$ and 25%
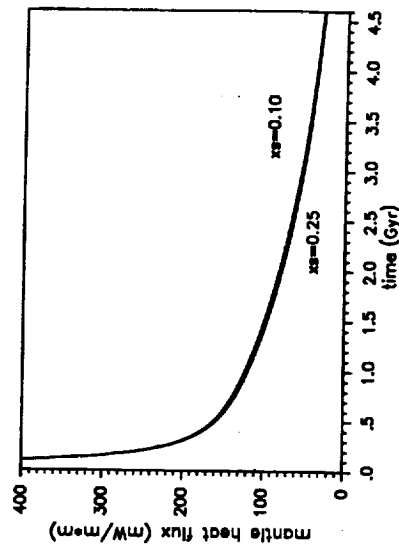

Fig. 3. Heat flow from the mantle vs time for two models of Martian thermal history. Details of the models are given in Stevenson et al. (1983). The models have initial core sulfur concentrations x_s of 10 and 25 wt%, respectively.

are essentially identical to models M1 and M2, respectively, of Stevenson et al. (1983). During the first few 100 Myr of evolution, when the planet is hot and its mantle is convecting particularly vigorously, there is a dramatic decrease in heat flow. Following this early period of rapid cooling is a phase of gradual, slow cooling lasting most of the geologic life of the planet. The present heat flow in these models is ~ 30 mW m⁻².

The decrease of mantle temperature with time in these models (Fig. 4) occurs, like the mantle heat flow, in an early period of short and dramatic temperature reduction followed by a decrease of only 200 to 300 K over the last 4 Gyr of the planet's history. The lithospheres in these models grow to thicknesses of ~ 100 km at the present (Fig. 5). Lithosphere thickness and mantle heat flow and temperature are largely independent of the sulfur concentration in the core. The models have thermal boundary layers at the base of the mantle that at present are ~ 100 km thick. Relatively small temperature increases across these bottom boundary layers raise the present core-mantle boundary temperatures of the models ~ 100 K above the mantle temperatures.

The present lithosphere thicknesses in the models of Fig. 5 are smaller, by perhaps a factor of 2 or more, than what would be expected based on our discussion of lithospheric thickness in the previous section. The lithosphere thickness calculated in the models is the thickness of the rheological lithosphere. It is assumed in the models of Fig. 5 that a temperature of 1073 K marks the base of this rheological lithosphere. At temperatures higher than 1073 K, the Martian mantle is taken to be readily deformable on a geologic time scale. Lithosphere thickness is strongly dependent on the concentration of radiogenic heat sources in the mantle. If the mantle heat-source density were half the value assumed in the models of Fig. 5, consistent with the
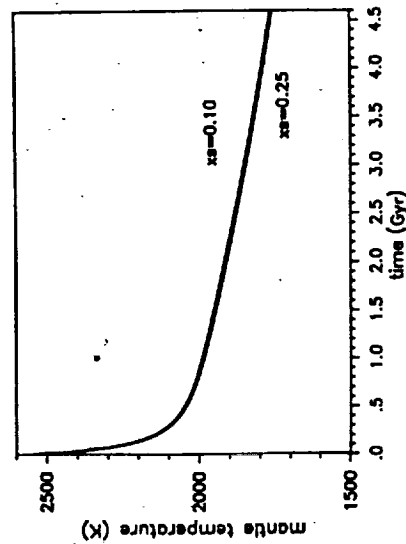
Fig. 4. The decrease of characteristic mantle temperature with time in the Martian thermal history models of Fig. 3.
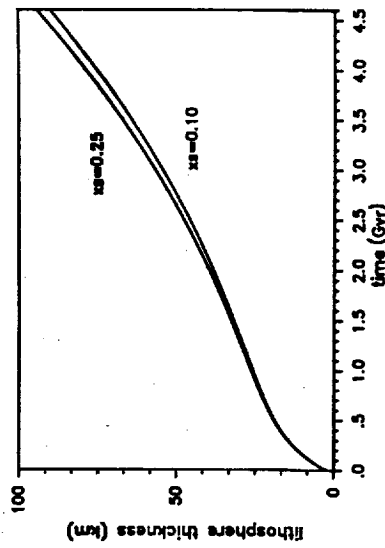
Fig. 5. Thickening of the Martian lithosphere with time in the cooling models of Fig. 3.

estimates of mantle heat-source densities from SNC meteorite data (refer to our discussion in the previous section), then the present lithosphere thickness would be about 200 km (Spohn 1990). Lithosphere thickness would also be increased by magmatic heat transfer (Spohn 1990) and by upward differentiation of radiogenic heat sources from the mantle into the crust. Thermal history models discussed later in this chapter (Sec. IV.B) demonstrate that depletion of mantle heat sources with time as a consequence of crustal differentiation results in a thicker lithosphere at present. The present lithosphere thicknesses calculated in the models of Schubert et al. (1979) are representative of maximum thicknesses as those models contained no mantle heat sources.

The decrease with time in the heat flow from the core is shown in Fig. 6
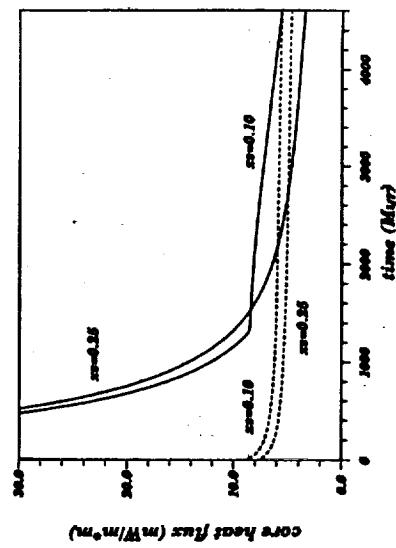
Fig. 6. Core heat flux as a function of time in the Martian thermal evolution models of Fig. 3. The dashed line marks the conductive heat flux along an adiabat in the liquid outer core. The sharp bend in the curve for the model with $x_s = 0.10$ denotes the onset of inner-core solidification.

for models with x_s = 10% and 25%. Inner-core growth in the x_s = 10% model is marked by the sudden change in the rate of core cooling at ~ 1.3 Gyr after core cooling begins. After 4.5 Gyr, the inner core in this model is about 920 km in radius, leaving an outer liquid core ~ 670-km thick. When inner-core growth in this model begins, the core heat flow is above the estimated value of heat flow conducted along the core adiabat (the upper dashed curve in Fig. 6). Convection in the outer core after ~ 1.3 Gyr is maintained by both thermal and chemical buoyancy, the latter arising from the release of gravitational potential energy upon concentration of the light-alloying element into the outer core. The slow decline in core heat flow after ~ 1.3 Gyr is mainly a consequence of latent heat and gravitational energy release upon inner-core growth. Core heat flow in the x_s = 10% model falls below the heat flow conducted along the adiabat just after 4.5 Gyr. Core convection beyond 4.5 Gyr would still occur but it would be driven entirely by compositional buoyancy. Thermal convective transport after 4.5 Gyr would actually be downward in the core, but the compositional buoyancy would be adequate to offset the slightly stable thermal state. In the x_s = 10% model, a magnetic field would be generated by thermal convection prior to inner core solidification at ~ 1.3 Gyr. Both thermal and chemical convection would support a dynamo for times between 1.3 and 4.5 Gyr. Subsequent to 4.5 Gyr, a magnetic field would be produced by compositionally driven convection associated with inner-core growth.

The sulfur-rich model (x_s = 25%) does not nucleate an inner core. Thermal convection ceases in this model after ~ 2.7 Gyr, when the core heat flux falls below the heat flux conducted along the core adiabat (lower dashed curve in Fig. 6). There is no dynamo action in the core or planetary magnetic field subsequent to 2.7 Gyr. Stevenson et al. (1983) have used the results of the model calculation with x_s = 25% to estimate the smallest initial sulfur fraction for which no inner-core freezeout would occur after 4.5 Gyr; they obtain a value of ~ 15 wt% S.

Schubert and Spohn (1990) have carried out a number of additional Martian thermal history calculations with a view toward more carefully delineating conditions for no inner-core freezeout. Their results are shown in Fig. 7, which gives the dependence of present inner-core radius (as a fraction of total core radius) on both present mantle viscosity and initial wt% sulfur x_s in the core. Present inner-core radius increases with decreasing x_s or decreasing present mantle viscosity because the former increases the core melting temperature and cooling is more rapid with the latter; both result in earlier inner-core freezeout and a longer period of inner-core growth. Fifteen wt% is a good estimate of the minimum core sulfur concentration required for no core freezing through geologic time, unless the present mantle viscosity is $\lesssim 10^{16}$ m² s⁻¹ (or ~ 3.5 × 10¹⁹ Pa s for a mantle density of 3500 kg m⁻³).

Figure 8, after Schubert and Spohn (1990), shows inner-core radius vs time for three different initial S concentrations. Inner-core growth is very rapid once freezeout begins; the inner core is almost completely grown within 0.5 to 1 Gyr of initial freezeout. The depression of the melting temperature in the outer core as the sulfur concentrates there with progressive inner-core growth and the slowing of the cooling rate as the planet evolves both contribute to the reduction in inner-core growth rate with time. With increasing x_s, the time of initial core freezeout is delayed and the present inner-core radius decreases.

If the estimates of Laul et al. (1986) and Trieman et al. (1987) of 14 and 12.5 wt% S in the Martian core are taken to imply that x_s is $\lesssim$ 15 wt%, then
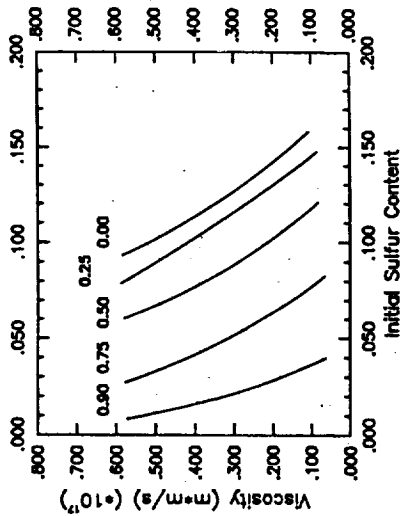
Fig. 7. Contours of fractional inner-core radius as a function of present mantle kinematic viscosity and initial weight fraction sulfur in the core (figure after Schubert and Spohn 1990).
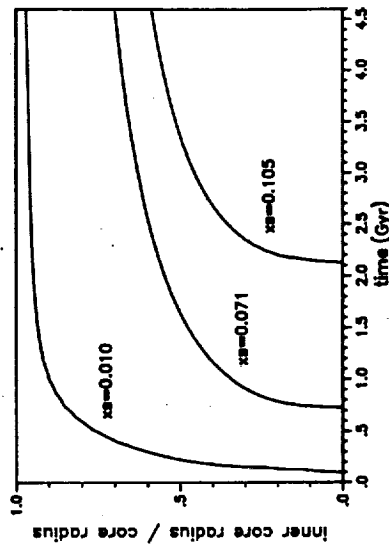
Fig. 8. Fractional inner-core radius vs time for model cooling histories of Mars with three different initial sulfur concentrations x_s in the core (figure after Schubert and Spohn 1990).

based on Fig. 7, it is likely that Mars has a solid inner core. If Mars has no magnetic field, the explanation may then lie in the nearly complete solidification of the core (Young and Schubert 1974). On the other hand, if the Laul et al. (1986) and Treiman et al. (1987) predictions of wt% S in the Martian core are underestimates, then according to Fig. 7, Mars would not have a solid inner core at present, and the explanation for lack of a present Martian magnetic field might lie in the absence of a drive (a growing inner core) for chemical convection in a core that had cooled too far to convect thermally at present (Stevenson et al. 1983). Our knowledge of Mars is inadequate to distinguish unambiguously between these alternative possibilities, although complete freezing of the Martian core probably requires an unreasonably low content of S in the core. The thermal history models are also consistent with a Mars that presently has a growing solid inner core, a dynamo in its liquid outer core driven by chemical compositional convection, and a planetary magnetic field, albeit a small one. Figure 7 shows that if x_s is ≤ 15 wt%, but not too small, then the core of Mars would only be partially solidified at present and a Martian dynamo and magnetic field would be likely.

This is illustrated in Fig. 9, which shows the results of a model calculation of the Martian magnetic dipole moment μ_M, normalized with respect to the Earth's present magnetic dipole moment, as a function of time for the Mars model with x_s = 10% and 25%. The calculation of μ_M follows Stevenson et al. (1983) and Schubert and Spohn (1990). The magnetic dipole moment decreases rapidly during the first several 100 Myr of evolution concomitant with the early rapid cooling of the planet and the rapid decline in core heat flow. With x_s = 10%, dynamo action occurs throughout the planet's evolution. Prior to 1.3 Gyr, the model Martian dynamo is driven by thermal convection in the core. There is a sudden increase in μ_M at ~ 1.25 Gyr coin-

cident with inner-core formation. Subsequent to 1.3 Gyr, the dynamo is driven by both thermal and chemical compositional convection as the inner core solidifies and releases latent heat and gravitational potential energy. With x_s = 25%, there is no inner-core solidification and the dynamo is driven solely by thermal convection until about t = 2.7 Gyr when dynamo action ceases because the core heat flux falls below the conductive heat flux along the core adiabat and thermal convection can no longer occur in the core. There is no present magnetic field in this model of Martian evolution because thermal convection is not possible in the present liquid core and there is no source of chemical convection in the core. Because of the uncertainty in the exact value of the conductive heat flux along the Martian core adiabat (Schubert and Spohn 1990), we cannot exclude the possibility that at present there is a weakly thermally convecting liquid core in Mars and a weak dynamo. If it should be determined that Mars has a small magnetic field, then such a model would provide a plausible explanation.

B. Crustal Differentiation

Magmatism in planetary interiors results in crustal formation and the removal of heat-producing radiogenic elements from the planetary mantle. The removal of heat sources reduces the vigor of mantle convection, allows the mantle to cool more rapidly, increases the lithosphere thickness, and reduces surface volcanism. In this section we provide quantitative estimates of the rate of crustal magmatism by extending the approach of Turcotte et al. (1979,1980) to the parameterization of convective cooling in the mantle of Mars. We refer the reader to Turcotte and Huang (1990) for the details of this approach and discuss here only the modifications necessary to simulate crustal production and the depletion of the mantle in radiogenic heat sources. A recent study of Martian thermal history with crustal differentiation has also been carried out by Spohn (1990).

In order to model the loss of heat-producing elements from the interior of Mars to its crust by magma transport, we take the rate of internal heat generation per unit mass H to be given by

$$\frac{dH}{dt} = -H\left(\lambda + \frac{\chi u}{R}\right) \tag{3}$$

where t is time, λ is the radioactive decay rate ($2.77 \times 10^{-10} yr^{-1}$; Turcotte and Schubert 1982), u is a mean convective velocity in the mantle, R is the radius of Mars and χ is a crustal fractionation parameter. The parameter χ is the ratio of the characteristic turnover time for mantle convection to the characteristic time for crustal fractionation. Based on the present rate of formation of the oceanic crust on the Earth, we show below that χ = 0.01 for the Earth. Of course, the crustal fractionation model developed here is not applicable to the Earth because crustal recycling through subduction is occurring.
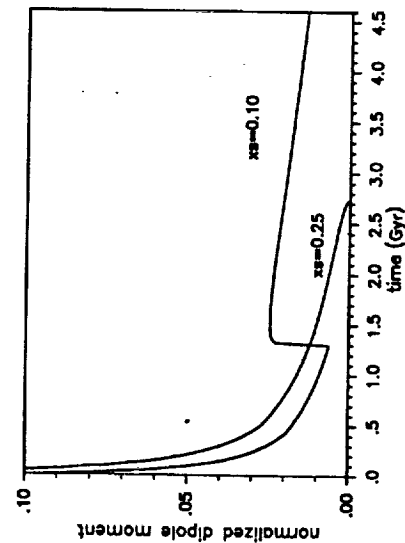

Fig. 9. Normalized magnetic dipole moment vs time for the models of Fig. 3. The dipole moment is normalized with respect to the value of the Earth's present magnetic dipole moment computed following the method presented in Schubert and Spohn (1990).

If the crustal fractionation parameter is sufficiently large then the planet will be fully differentiated. If f is the fraction of crustal material available, then the maximum thickness of crust D_{c0} that can be formed is

$$D_{c0} = \frac{f\rho_m R}{3\rho_c}. \quad (4)$$

In deriving Eq. (4) we have neglected the volume of the core. With $f = 0.1$, mantle density $\rho_m = 3940$ kg m^{-3}, crustal density $\rho_c = 2900$ kg m^{-3} and $R = 3398$ km, we find that $D_{c0} = 154$ km. The thickness of the evolving crust is assumed to be given by

$$D_c = D_{c0}\left(1 - \frac{H}{H_c}\right) \quad (5)$$

where H_e is the rate of heat generation in the interior without any crustal extraction given by

$$H_e = H_o e^{-\lambda t} \quad (6)$$

and $H_o = 2.47 \times 10^{-11}$ W kg^{-1} (based on estimates for the Earth; Turcotte and Schubert 1982).

Removal of radioactive elements from the mantle through crustal differentiation affects the growth of the lithosphere by reducing the heat flux from the mantle that must be conducted across the lithosphere. We assume that the heat-producing elements in the crust are sufficiently near the surface that they do not influence the conductive gradient; the base of the lithosphere is defined to lie at a temperature T_r. With these assumptions, the thickness of the conductive lithosphere is given by

$$D_L = (T_r - T_s)\left[\frac{R\rho_m H}{3}\left(\frac{1}{k} - \frac{1}{\kappa}\frac{dT}{dt}\right)\right]^{-1} \quad (7)$$

where k is the thermal conductivity, κ is the thermal diffusivity, T is the mean mantle temperature, and T_s is the surface temperature. The denominator is related to the heat flow through the lithosphere.

The volumetric rate V_v of addition of magma to the crust can be determined through its relation to the change in crustal thickness by

$$\dot{V}_v = 4\pi R^2 \frac{dD_c}{dt}. \quad (8)$$

The parameterized convection calculations can also be used to determine whether the radius of the planetary body is increasing or decreasing. The appropriate relation is

$$\frac{\delta R}{R} = -\frac{\alpha}{3}\left[T_o - T\left(1 - \frac{3}{2}\frac{D_L}{R}\right)\right] + \frac{\Delta\rho D_c}{3\rho_m D_{c0}}. \quad (9)$$

where T_o is the initial temperature of the planet, α is the volumetric coefficient of thermal expansion and $\Delta\rho$ is the decrease in density associated with crustal differentiation. The first term on the right of Eq. (9) follows from Eq. (2) and the second term represents the increase in volume associated with crustal formation.

We present results of planetary evolution calculations for the following parameter values: $\kappa = 10^{-6}$ m^2 s^{-1}, thermal conductivity $k = 4$ W m^{-1} K^{-1}, $T_r = 1000$ K, $T_s = 255$ K, $T_o = 2000$ K, $\alpha = 3 \times 10^{-5}$ K^{-1} and $\Delta\rho = 80$ kg m^{-3}. The mean mantle temperature, crustal thickness, rate of volcanism, lithosphere thickness, surface heat flow and fractional radius change are given in Figs. 10 through 15 as functions of time for various values of the crustal fractionation parameter χ in the range 0 to 10^{-2}.

The extraction of heat-producing elements into the crust can have important effects on the thermal evolution of Mars. The results for the mean mantle temperature given in Fig. 10 show a temperature reduction of about 250 K if the heat producing elements are removed. It is seen from Fig. 11
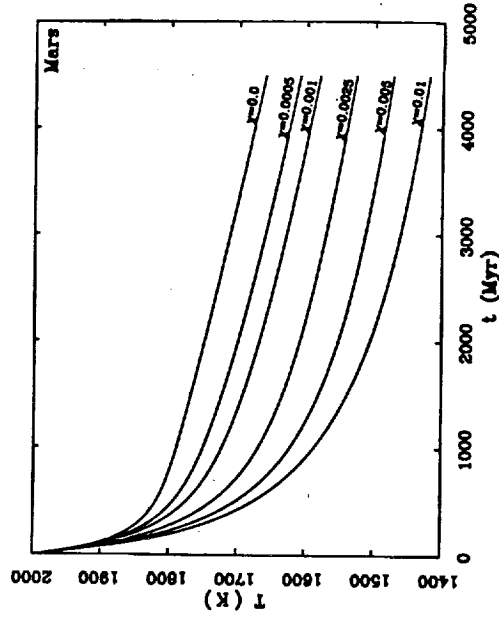
Fig. 10. Dependence of the mean mantle temperature T on time t for several values of the crustal fractionation parameter χ. See text for a discussion of the model used.
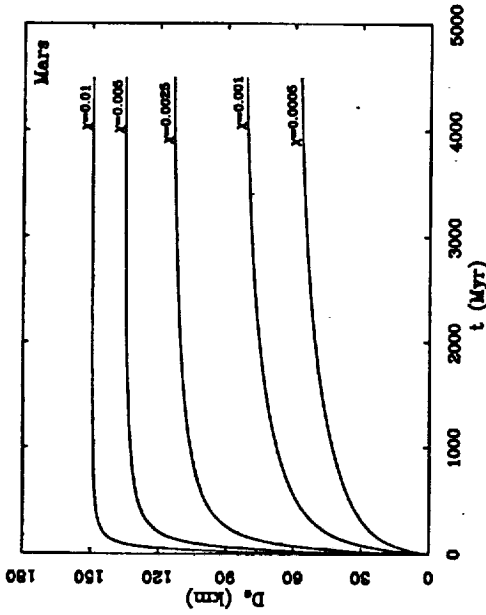
Fig. 11. Thickness of the crust D_c vs time t for a number of values of the crustal fractionation parameter χ. The crustal thickness for a fully differentiated Mars is $D_{ce} = 154$ km.

Fig. 12. Dependence of the volumetric flux of Martian volcanism $\dot{V}_v$ on time t for several values of the crustal fractionation parameter χ.

Fig. 13. Thickness of the Martian lithosphere D_L vs time t for several values of the crustal fractionation parameter χ.

that most of the crustal growth occurs early in the evolution of Mars, i.e., within several 100 Myr of the end of accretion. This is in accord with the evidence discussed earlier of an age ≥ 4 Gyr for the southern crustal highlands. The present mean crustal thickness depends on the choice of the crustal fractionation parameter χ. The volumetric flux of volcanics is given in Fig. 12. For a small crustal fractionation parameter ($\chi = 0.0005$) the volcanic flux decreases rapidly early in the evolution, but it continues throughout the history of the planet. For larger values of the parameter χ, the interior is completely depleted and the volcanic flux drops to low levels.

With the extraction of the heat producing elements the lithosphere becomes considerably thicker (Fig. 13) and the mantle heat flux is reduced (Fig. 14). The heat flux given in Fig. 14 is the heat flux into the base of the Martian crust. The expansion and contraction of the planet is given in Fig. 15. With no crustal extraction ($\chi = 0$), only thermal contraction occurs. As the rate of crustal extraction is increased (increasing χ), the initial expansion due to crustal formation increases and the rate of thermal contraction also increases.

We can estimate the value of the crustal fractionation parameter for the Earth. It is the ratio of the crustal fractionation time $V/\dot{V}_c$ to the characteristic mantle turnover time R/u ($\dot{V}_c$ is the volumetric fractionation rate of the mantle and V_c is the volume of the mantle). Taking the rate of formation of oceanic crust to be 2.8 km² yr⁻¹ and the depth processed to be 60 km, we have $\dot{V}_c = 168$ km³ yr⁻¹. With $V_c = 10^{12}$ km³, we find that the characteristic time for creation of the oceanic crust is $V/\dot{V}_c = 6$ Gyr. With $R = 5800$ km (approximately twice the mantle thickness) and $u = 0.1$ m yr⁻¹, we find that

G. SCHUBERT ET AL.
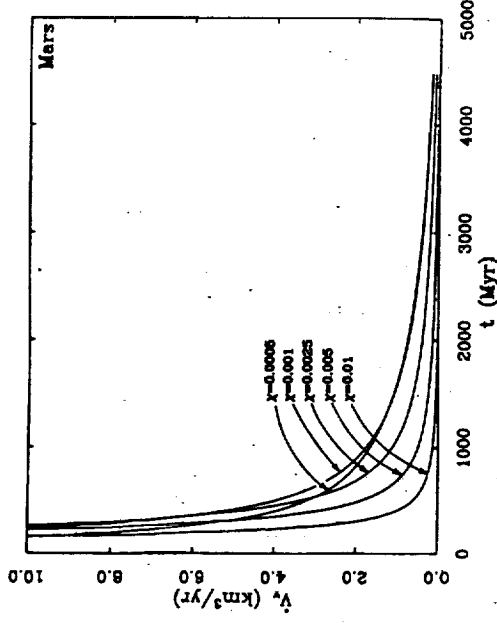
the characteristic mantle turnover time is $R/u = 58$ Myr. Thus we find that χ is about 0.01 for the Earth at the present time.

The crustal thickness on Mars has been estimated using gravity data and the assumption of Airy isostasy. For Hellas Planitia, as noted above, Sjogren and Wimberly (1981) estimated that the depth of compensation is 130 km. Using similar data and assumptions for the crater Antoniadi, Sjogren and Ritke (1982) found that the depth of compensation is 115 km. From gravity profiles across the highland-lowland escarpment, Janle (1983) found that the depth of compensation is also 115 km. Taking the crustal thickness to be $D_c = 120$ km, we find from Fig. 11 that the corresponding crustal fractionation factor is $\chi = 0.003$, about a factor of 3 less than for the Earth. This estimate of χ is uncertain because of the poorly constrained value of the mean crustal thickness on Mars.

Accepting, for purposes of discussion, that the crustal fractionation factor for Mars is $\chi = 0.003$, we can determine rates of crustal addition from Figs. 11 and 12. The average amount of crust added in the last 1 Gyr was 600 m, that added between 1 and 2 Gyr ago was 1.8 km, and that added between 2 and 3 Gyr ago was 2.9 km. The volumetric rate of crustal magmatism was much higher early in the evolution of Mars. The decline to the lower values of crustal production rate characteristic of most of Martian geologic history occurred with about a 100 Myr time scale.

The most recent volcanism on Mars during the Upper Amazonian period (Tanaka 1986) occurred in the Arcadia, Olympus Mons, Medusae Fossae and Tharsis Montes Formations, but the principal volcanics are flood basalts in the southern Elysium Planitia. These have an area of 10^6 km², but Tanaka (1986) suggests that the thickness is only a few 10 m. Taking a thickness of 50 m, this is only 0.03 m when averaged over the surface of Mars.

Greeley (1987) has estimated that 26×10^6 km³ of volcanics erupted during the Middle and Upper Amazonian. This corresponds to a mean thickness of 200 m when averaged over the entire surface of Mars. From the estimate of cratering rates given by Hartmann et al. (1981), the Upper Amazonian extended from 0 to 0.7 Gyr ago and the Middle Amazonian from 0.7 to 2.3 Gyr ago. Thus, the volume of young volcanics on Mars is broadly consistent with the model results above as volcanism represents only a part of crustal addition. It should be emphasized, however, that there are considerable uncertainties in the absolute ages and in the crustal fractionation parameter.

Other predictions of our calculations using $\chi = 0.003$ are a lithospheric thickness $D_L = 400$ km and a net global contraction corresponding to $\delta R/R = -0.001$. From Fig. 15 we see that a global expansion of $\delta R = 10$ km occurred in the first 200 Myr of the evolution of Mars. This expansion was caused by the density change associated with the generation of the early crust. For the remainder of the evolution of Mars, a nearly steady contraction occurred associated with the cooling of the interior. The total contraction sub-

Fig. 14. Dependence of the mantle heat flux Q_s on time t for different values of the crustal fractionation parameter χ.

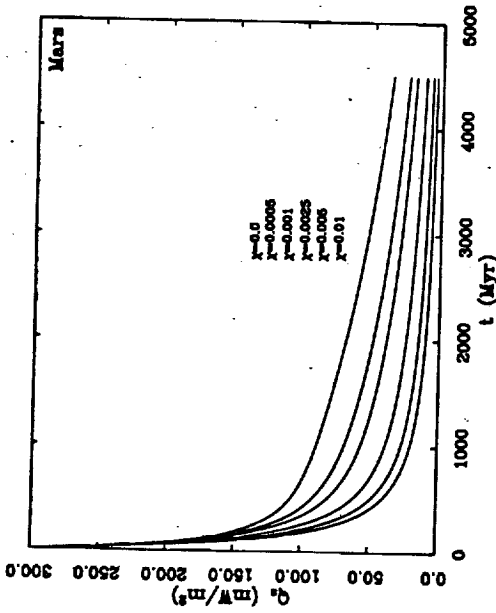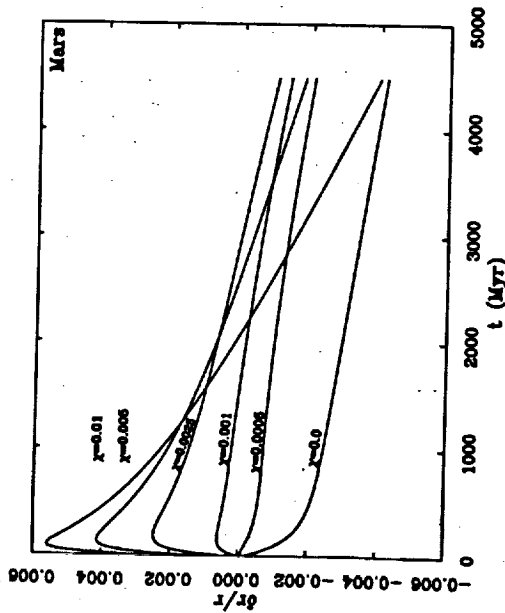Fig. 15. Radial expansion (contraction) $\delta R/R$ as a function of time t for several values of the crustal fractionation parameter χ.

sequent to the period of early crustal differentiation was $\delta R = -13$ km. All models in Fig. 15 with substantial crustal fractionation show an early period of planetary expansion followed by a larger amount of planetary contraction.

As noted earlier, large-scale surface tectonic features of Mars include both extensional and compressional structures. The graben systems in and near the Tharsis region are likely to be the result of stresses generated by the Tharsis load. Compressive wrinkle ridges occur commonly throughout ancient terrains. These can be attributed to the early phase of rapid thermal contraction illustrated in Fig. 15.

Models of the response of Mars to the long-wavelength topographic load of the Tharsis Rise provide a reasonable fit to the observed gravity if the elastic lithosphere of Mars was globally in the range 100 to 400 km when the Tharsis construct formed (Banerdt et al. 1982; Willemann and Turcotte 1982). As the elastic lithosphere is generally ~1/2 the thickness of the thermal lithosphere, these values are consistent with those given in Fig. 13. All models in Fig. 13 with large lithosphere thicknesses show substantial depletion in mantle radioactivity due to crustal differentiation. For no crustal differentiation, the lithosphere thickness from Fig. 13 is ~ 100 km, in agreement with the result previously obtained in Fig. 5.

V. PATTERNS OF MANTLE CONVECTION

Numerical calculations of fully three-dimensional convection in a spherical shell were recently carried out by Schubert et al. (1990) to simulate possible convective planforms in the Martian mantle. These results have important implications for proposed convective origins for major geologic features on Mars, such as the crustal dichotomy. The reader is referred to that work for more detailed information about the calculations than can be provided here.

The spherical shell model of the Martian mantle consists of a Boussinesq fluid that is heated both internally and from below to account for secular cooling, radiogenic heating and heat flow from the core. The lower boundary of the shell is assumed to be isothermal and stress-free, as appropriate to the interface between the mantle and a liquid outer core. The upper boundary of the shell is rigid and isothermal, as appropriate to the base of a thick, immobile lithosphere. The ratio of the inner radius of the shell to its outer radius is 0.55, in accordance with possible core radii in Mars. We present results for two different modes of heating. In one case, 20% of the surface heat flow originates in the core, and in the other case the percentage of heating from below is 94%. The Rayleigh numbers of both cases are approximately 100 times the critical Rayleigh numbers that characterize the onset of convection in the constant-viscosity spherical shells. These Rayleigh numbers may be an order of magnitude or more smaller than the Rayleigh number of the Martian mantle. However, the Rayleigh number of the Martian mantle is unknown

because of uncertainties in the thickness of the mantle and its material properties, viscosity in particular. The numerical approach is described in detail in Glatzmaier (1988) and Bercovici et al. (1989a). Table III lists the parameter values for the calculations discussed here.

The horizontal planforms of convection for both modes of heating are illustrated in Fig. 16 by contours of radial velocity on spherical surfaces midway through the shells. Meridional cross sections of entropy contours (equivalent to isotherms in these Boussinesq calculations) for both heating modes are shown in Fig. 17. The prominent form of upwelling in the Martian mantle is the cylindrical plume. The number of upwelling plumes is strongly influenced by the mode of heating; with only 20% heating from below, there are a dozen plumes, while 94% bottom heating produces only 6 plumes. There are fewer, stronger plumes as the proportion of bottom heating increases. Plumes carry the heat flow from the core and arise from instability of the lower thermal boundary layer at the core-mantle interface. In general, the fraction of mantle heating delivered from the core has probably decreased with time as the core cooled to temperatures not much greater than those of the lower mantle (see, e.g., Fig. 6). The isotherm cross sections of Fig. 17 show several plumes originating in the lower thermal boundary layer. Convective downwelling occurs in planar sheets that form an interconnected network surrounding the upwelling plumes. The downwellings also show cylindrical concentrations along the sheets and even distinct cylindrical downwellings.

The patterns of Fig. 16 have evolved through many overturns of the mantle and the solutions appear to be fundamentally time dependent. However, the basic nature of the convective planform, i.e., cylindrical upwelling plumes surrounded by planar downwelling sheets, does not change with time. Thus, we can expect major volcanic provinces on Mars, like Tharsis and Elysium, to reflect the cylindrical nature of upwelling mantle plumes, similar

TABLE III

Parameter Values for Three-Dimensional Spherical Convection Models of the Martian Mantle

Outer radius	3200 km
Inner radius	1762 km
Density	3450 kg m⁻³
Core mass	1490×10^{20} kg
Kinematic viscosity	10^{18} m² s⁻¹
Thermal diffusivity	10^{-6} m² s⁻¹
Specific heat at constant pressure	1.2 kJ kg⁻¹ K⁻¹
Thermal expansivity	2×10^{-5} K⁻¹
Temperature difference across the mantle	800 K
Internal heating rate (94% from below)	1.5×10^{-13} W kg⁻¹
Internal heating rate (20% from below)	5.3×10^{-12} W kg⁻¹
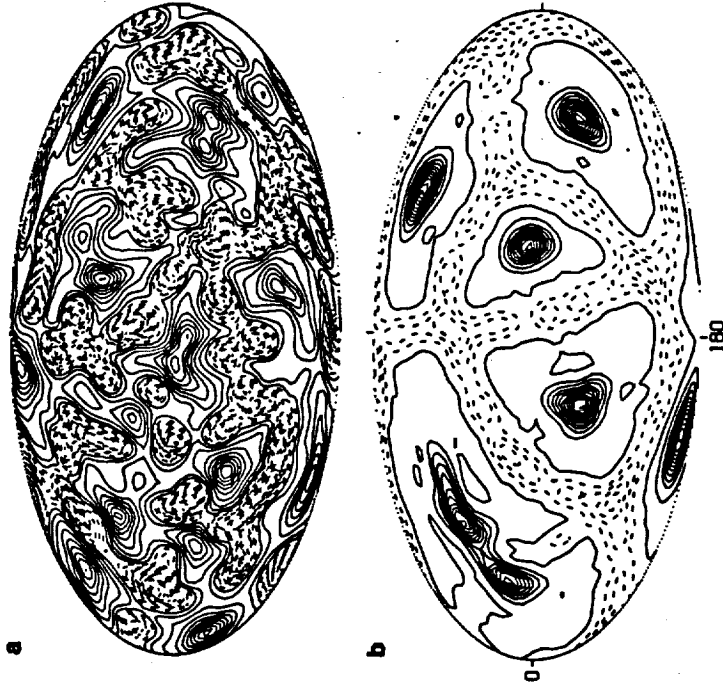
Fig. 16. Contours of radial velocity at mid-depth in the Martian mantle in numerical models of three-dimensional mantle convection with (a) 20% and (b) 94% heating from below. The projection is an equal-area projection extending 360° in longitude and over all latitudes. Model parameter values are listed in Table III (figure after Schubert et al. 1990). Solid contours indicate radially outward motion, dashed contours denote radially inward motion.

Fig. 17. Meridional cross sections of temperature in the numerical models of Fig. 13 for (a) 20% and (b) 94% heating from below.

to hot spots on the Earth. There are no sheet-like upwelling features in the Martian mantle to produce a pattern similar to the linear global system of mid-ocean ridges on the Earth. Even the mid-ocean ridges on the Earth are not connected to deep sheet-like upwellings in the Earth's mantle (Bercovici et al. 1989b). The deep upwellings in models of convection in the Earth's mantle are also cylindrical plumes. The Earth's mid-ocean ridges are shallow, passive upwellings occurring in response to the tearing of lithospheric plates by the pull of descending slabs (Bercovici et al. 1989b). The non-Newtonian rheology of the Earth's lithosphere is essential for the occurrence of plate tectonics. Mars is a one-plate planet with a thick lithosphere (Solomon 1978; Schubert et al. 1979) beneath which mantle upwellings are in the form of cylindrical plumes.

The results of the spherical convection models have implications for proposed explanations of the crustal dichotomy and the concentrations of volcanism at Tharsis and Elysium. If the crustal dichotomy was caused by a

Fig. 18. (a) and (b) are similar to Figs. 16 and 17 but for a small Martian core of radius 0.2 times the radius of Mars. In the model 90% of the heating is from below.

convective system dominated by spherical harmonic degree $\ell = 1$ (Schubert and Lingenfelter 1973; Lingenfelter and Schubert 1973; Wise et al. 1979a) with upwelling under the northern hemisphere, then the convection must have been driven strongly from below (while our models produced 6 to 12 plumes, the number of pl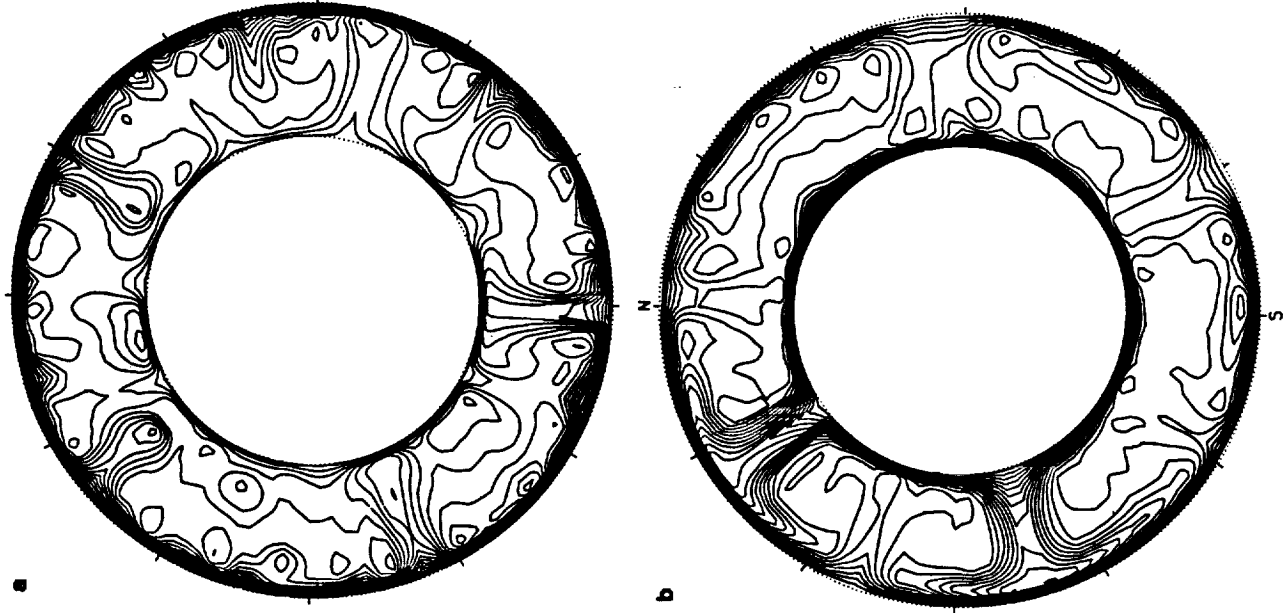umes decreases with increasing percentage of bottom heating). Such strong heating concentrated deep within Mars can arise from the heating pulse accompanying core formation or from the flow of heat from a hot core. Indeed, the overturning accompanying core formation could in itself be an $\ell = 1$ mode (Stevenson 1980), obviating the need for a thermally driven motion.

Core size is another important factor in determining the number of convective plumes. With smaller cores there is a tendency toward fewer upwelling plumes (Zebib et al. 1983). This is confirmed by the results of Fig. 18, which shows mid-depth radial velocity contours and isotherms in meridional cross section in the mantle of a Mars model with a core radius of 0.2 times the radius of Mars (Schubert et al. 1990). The model has settled into a predominantly $\ell = 2$ (not $\ell = 1$, however) convection pattern. During the early stages of core formation, the effective core radius would have been smaller than the radius at present, favoring a thermally forced convection with perhaps just one dominant upwelling. Since the Martian core formed contemporaneously with accretion or within a few 100 Myr of the end of accretion, conditions favoring $\ell = 1$ convection, i.e., a small core and a deep heat source, occur very early in the evolution of Mars. If a convective mechanism is responsible for the crustal dichotomy, then the dichotomy must also be a very ancient feature.

It is not obvious from the models why there should be only two major volcanic centers (Tharsis and Elysium) on Mars. The models predict several to ~ 10 major mantle plumes. Perhaps the models are not realistic enough to predict the actual number of major hot spots on Mars. On the other hand, there may be many plumes in the Martian mantle, but the properties of the lithosphere may select only one or two of them for prominent surface expression. Plume activity could be focused beneath Tharsis if fracturing or thinning of the lithosphere in this region has facilitated magma and heat transport across the lithosphere. The temperature dependence of mantle viscosity will strongly influence the structure of plumes and their number, through the control that variable viscosity exerts on the nature and vigor of small-scale convective activity in the lower thermal boundary layer (Olson et al. 1987).

The numerical solutions discussed above can be used to infer that several km of dynamic topography could be associated with plumes in the Martian mantle (Schubert et al. 1990). Dynamic uplift is insufficient to account for the 10 km of topography in the Tharsis region. This large topographic excess must be largely the result of other processes, such as volcanic construction, magmatic thickening of the crust, or depletion of the underlying mantle (see, e.g., Sleep and Phillips 1979,1985; Solomon and Head 1982). Nevertheless,
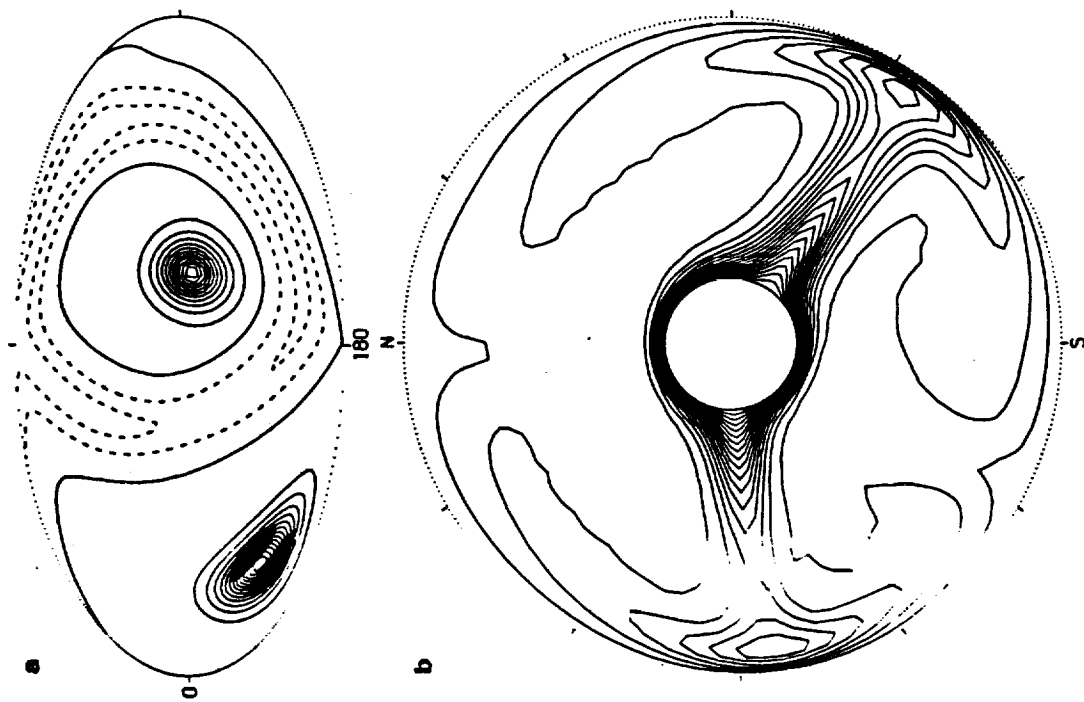
it is likely that the Tharsis Rise and its volcanic constructs are a consequence of a strong mantle plume (or grouping of plumes) beneath the region.

VI. CONCLUSIONS

Several themes emerge from this overview of the thermal history of Mars. The first is the hot initial state of the planetary interior and the sharp contrasts that can be drawn between the first 1 Gyr of Martian history and the subsequent 3.5 Gyr. As a result of accretional heating and core formation essentially contemporaneous with planetary formation, the early history of Mars was characterized by high internal temperatures, a vigorously convecting mantle, and high surface fluxes of heat and magma. Outgassing contributed to an early atmosphere, and widespread magmatism may have helped trigger the release of subsurface water and large-scale floods. Parameterized convection models indicate, however, that on a time scale of only a few 100 Myr the mantle convective engine slowed, as primordial interior heat was lost and as radioactive heat production decayed or was concentrated into the shallow crust. Rapid interior cooling led to a globally thick lithosphere and was accompanied by global contraction, recorded in the pervasive formation of wrinkle ridges now preserved on ancient geologic units. The last 3.5 Gyr of Martian history was marked, in contrast, by slow cooling and by the concentration of volcanic and tectonic activity in ever more limited regions.

The second theme of Martian thermal history is the strong role of plumes expected for mantle convection. As long as a significant fraction of mantle heating comes from the core, three-dimensional convection calculations indicate that plumes dominate the upwelling portions of the flow. At least some of those plumes would be expected to have strong signatures in the surface topography and volcanic flux. The Tharsis and Elysium volcanic provinces are probably the consequences of plume-delivered heat and magma. The number and characteristics of plumes depend on the relative contributions of radioactivity and core cooling to the mantle heat budget, as well as the size of the core. While current models do not predict as few as 2 dominant plumes or plume families, development of Tharsis and Elysium very early in Martian history, when core cooling occurred at its highest rate, is favored.

A third theme of this overview is the dominating influence of core sulfur concentration on the thermal evolution of the core and the history of the Martian magnetic field. A core with more than ~ 15 wt % S probably would not crystallize a solid inner core and probably would not be thermally convecting at present. This critical S concentration is tantalizingly close to estimates of the core sulfur content from elemental abundances of SNC meteorites. Therefore, a nearly completely fluid core that is nonconvecting or only weakly thermally or chemically convecting may provide an explanation for the lack of a present Martian magnetic field or the existence of a very weak one.

A final theme of this overview is the strong impact that new information from Mars would have on our understanding of the origin and thermal evolution of the planet. Detection of an internal magnetic field or evidence for a paleofield would strongly constrain the evolution of the Martian core. Seismic determination of the thickness of the crust would provide a crucial tie point to discussions of the planetary magmatic budget, and a seismic estimate of the radius and state of the core would enable a considerably more confident assessment of bulk composition. Measurement of surface heat flow would substantially constrain the present mantle heat production. Finally, the return of Martian igneous rocks to terrestrial laboratories would provide crucial knowledge of the detailed absolute time scale for the major events in the history of the planet.

Geoid, Topography, and Convection-Driven Crustal Deformation on Venus;

Mark Simons, Bradford H. Hager, and Sean C. Solomon, Department of Earth, Atmospheric, and Planetary Sciences, Massachusetts Institute of Technology, Cambridge, MA 02139.

Introduction. High-resolution Magellan images and altimetry of Venus reveal a wide range of styles and scales of surface deformation [1] that cannot readily be explained within the classical terrestrial plate tectonic paradigm. The high correlation of long-wavelength topography and gravity and the large apparent depths of compensation suggest that Venus lacks an upper-mantle low-viscosity zone [2-5]. A key difference between Earth and Venus may be the degree of coupling between the convecting mantle and the overlying lithosphere. Mantle flow should then have recognizable signatures in the relationships between surface topography, crustal deformation, and the observed gravity field [6,7].

Model. We explore the effects of this coupling by means of a finite element modelling technique. The crust and mantle in these models are treated as viscous fluids. We solve both the equations of motion and the heat equation at every time step using a modified version of the 2-D Cartesian finite-element program ConMan [8]. A passive marker chain tracks the crust-mantle interface and permits variation in the crustal buoyancy as well as specific crustal and mantle rheologies. These rheologies depend on composition, temperature and stress. In addition to the flow field, the stress field in the lithosphere, the surface topography, and the resulting geoid are readily calculated. The models presented here use an irregular finite-element mesh that is 50 elements high and 160 elements wide. Our maximum resolution is in the 40-km-thick top layer, where each element is 2 km high and 5 km wide. In all, the mesh is 800 km in the horizontal dimension and 400 km in the vertical dimension. We impose free-slip boundary conditions on the top and side walls, with no flow through these walls. Flow at the bottom boundary is constrained to be vertical with no horizontal flow permitted. This last boundary condition gives a virtual 800 km by 800 km box. The surface topography is calculated from the vertical stresses on the top wall of the box. Top and bottom temperatures are fixed at 500°C and 1250°C, respectively. Initially, we impose a linear temperature gradient across the lithosphere and set the rest of the mantle to be isothermal. We investigate two classes of models. Flow in the first class is initiated with a sinusoidal temperature perturbation throughout the box. This results in mantle flow that is dominated by concentrated downwelling (Figure 1b). In the second class of models, flow is driven by a hot patch at the side of the box, thereby driving flow by concentrated upwelling (Figure 1a).
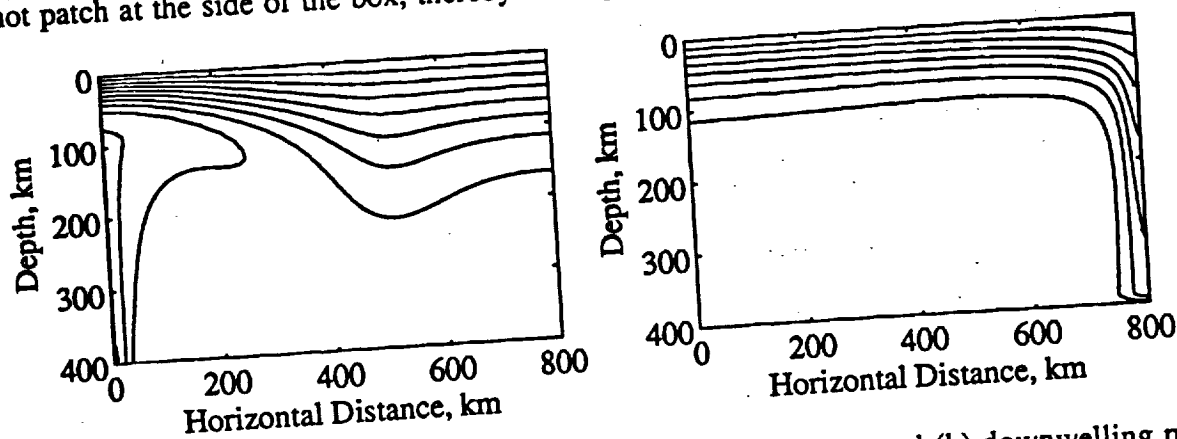

Figure 1. Temperature contours at 130 My for the (a) upwelling and (b) downwelling models. Contour interval is 100 °C; the top of the box is at 500 °C.

Results. In all our models, convection produces horizontal compressional stresses in lithosphere above downwelling mantle and extensional stresses in lithosphere above upwelling mantle. As the convective vigor increases so does the magnitude of the stress. In models with constant-viscosity mantle overlain by a constant-viscosity crust, stress in the crust reaches values in excess of 100 MPa in less than 100 My. We find that the rate of increase in compressive stress decreases with increasing crustal viscosity. This is because the stronger the crust, the more the development of the convective instability in the mantle driving the deformation is impeded. We also find that the magnitude of the peak compressive stress achieved above the downwelling increases with higher viscosities and/or with thinner initial crustal layers; the stronger the crustal lid, the more are tractions from mantle convection supported in the crust. Since force balance on the crust requires that shear traction integrated along the base be balanced by normal tractions integrated through its thickness, the thinner the crust, the larger the horizontal stresses.

Both analytical models [9,10] and our numerical models of convection-induced crustal flow indicate that the amplitude and sign of the topography are highly time- and rheology-dependent. In general, possible responses of the crust to mantle flow can be divided into three categories. The first involves little, if any, crustal flow, and topography results mainly from the transmission of normal tractions induced by density contrasts within the mantle. The second possible regime involves substantial crustal flow, with geologically rapid thickening over convective downwelling and thinning over convective upwelling. In this regime the effects of crustal thickness variations dominate the topography. A third possible regime lies between the first two, with "in phase" deformation on short time scales and crustal flow on longer time scales. A strong mantle lithosphere tends to shield the crust from convective shear tractions, and topography results mainly from the transmission of convective normal tractions. A relatively weak lower crust facilitates crustal deformation, and the isostatic effects of crustal thickness variations dominate the topography.

Consideration of geoid to topography ratios (GTRs) can restrict which regime of crustal response is appropriate for Venus. The distibution of estimated GTRs for several highland regions on Venus is bimodal with two clusters around 10 and 25 m/km [5]. The positive correlation of long-wavelength gravity and topography implies that there are no major regions that have negative GTRs. To keep the GTRs positive, the geoid must follow the surface topogaphy in sign at all times. Although the regime of negligible crustal flow can correctly predict both the sign and magnitude of the GTRs, it does not allow for the crustal deformation (i.e., flow) inferred from observations of tectonic features on Venus.

In contrast to the regime of negligible flow, that of time-dependent crustal flow generates topography that changes sign. Over a mantle downwelling, the topography is negative in the early stages of deformation and positive in the later stages of deformation; the converse holds over a mantle upwelling. During the transitional period the topography goes through zero, the geoid does not go through zero, and the GTR is unbounded; this singularity is not observed on Venus. An example of the evolution of the GTR for a model in the time-dependent regime is shown in Figure 2. Note that before 90 My both topography and geoid are negative, but at 90 My crustal thickening effects begin to dominate and the topography switches sign, causing the GTRs to first become unbounded and then negative.

In the absence of a mechanism by which the sign of the geoid anomaly mimics that of the topography over a given upwelling or downwelling, only the regime of rapid crustal flow is

plausible. In the case of mantle downwelling this would also require that the lower mantle be more viscous than the upper mantle in order to produce the required positive geoid anomalies. This has already been shown to be true for the Earth, where the observed geoid highs over regions of mantle upwelling and regions of mantle downwelling are best explained by the presence of a strong lower mantle [11,12]. The large positive GTRs and the presence of large shield volcanoes in certain highland regions on Venus, such as Beta Regio and Eistla Regio, are best explained as areas of mantle upwelling [5,13,14]. The regime of rapid crustal flow predicts crustal thinning over the upwelling. However, the extensive partial melt and ensuing volcanism expected over such regions of mantle may outweigh the effects of crustal thinning on the surface topography and thus also yield postive GTRs [15].
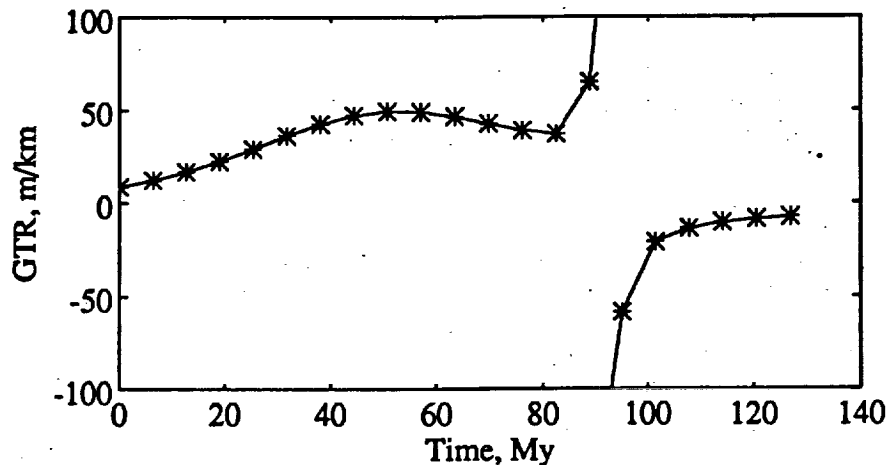
Figure 2. Evolution of GTR with time. At each time step, the GTR shown is the slope of the best fit line to the collection of geoid and topography values upward continued to 250 km above the surface nodes in the model. The result is for a downwelling model, with a crust of constant viscosity 50 times that of the mantle. In this model the sign of the topography is time-dependent, but that of the geoid is not. The singularity at about 90 My corresponds to the time when topography crosses the zero datum. Note that the GTRs for this model are neither always positive nor always bounded.

References: [1] S. C. Solomon et al., *Science,* 252, 297, 1991; [2] W. S. Kiefer et al., *Geophys. Res. Lett.,* 13, 14, 1986; [3] B. G. Bills et al., *J. Geophys. Res.,* 92, 10, 1987; [4] R. J. Phillips et al., *Science,* 252, 651, 1991; [5] S. E. Smrekar and R. J. Phillips, *Earth Planet. Sci. Lett.,* 107, 587, 1991; [6] R. J. Phillips, *Geophys. Res. Lett.,* 13, 1141, 1986; [7] R. J. Phillips, *J. Geophys. Res.,* 95, 1301, 1990; [8] S. D. King et al., *Phys. Earth Planet. Inter.,* 59, 195, 1990; [9] D. L. Bindschadler and E. M. Parmentier, *J. Geophys. Res* , 95, 21, 1990; [10] H. Schmeling and G. Marquart, *Geophys. Res. Lett* , 17, 2417, 1990; [11] M. A. Richards and B. H. Hager, *J. Geophys. Res* , 89, 5987, 1984; [12] B. H. Hager, *J. Geophys. Res* , 89, 6003, 1984; [13] R. E. Grimm and R. J. Phillips, *J. Geophys. Res.,* 96, 8305, 1991; [14] R. E. Grimm and R. J. Phillips, *J. Geophys. Res* , *in press,* 1991; [15] R. J. Phillips et al., *Science,* 252, 651, 1991.

Geoid, Topography, and Convection-Driven Crustal Deformation on Venus;

Mark Simons[1], Bradford H. Hager[1], and Sean C. Solomon[2], [1]Department of Earth, Atmospheric, and Planetary Sciences, Massachusetts Institute of Technology, Cambridge, MA 02139, [2]Department of Terrestrial Magnetism, Carnegie Institution of Washington, Washington, DC 20015.

Introduction. High-resolution Magellan images and altimetry of Venus reveal a wide range of styles and scales of surface deformation [1] that cannot readily be explained within the classical terrestrial plate tectonic paradigm. The high correlation of long-wavelength topography and gravity and the large apparent depths of compensation suggest that Venus lacks an upper-mantle low-viscosity zone [2-5]. A key difference between Earth and Venus may be the degree of coupling between the convecting mantle and the overlying lithosphere. Mantle flow should then have recognizable signatures in the relationships between the observed surface topography, crustal deformation, and the gravity field [6,7]. Therefore, comparison of model results with observational data can help to constrain such parameters as crustal and thermal boundary layer thicknesses as well as the character of mantle flow below different Venusian features. We explore in this paper the effects of this coupling by means of a finite element modelling technique.

Model. The crust and mantle in the models are treated as viscous fluids. We solve both the equations of motion and the heat equation at each time step using a modified version of the two-dimensional, Cartesian finite-element program ConMan [8]. Our formulation assigns material properties to each element and explicitly tracks the free surface topography and the crust-mantle interface by letting the grid deform with time in a semi-Lagrangian fashion. This procedure permits variation in the crustal buoyancy as well as specific crustal and mantle rheologies that can depend on composition, temperature and stress. In addition to the flow field, the stress field in the lithosphere, the surface topography, and the resulting geoid are readily calculated. The model domain is a square box. We impose free-slip boundary conditions on the bottom and side walls, with no flow through these walls. The top of the box is a true free surface, so there is no need to derive surface topography from vertical stresses on the top of the box. We investigate two classes of models. In the first class flow is dominated by concentrated upwelling (Figure 1a), and in the second class flow is dominated by concentrated downwelling (Figure 1b). We vary the initial crustal and thermal boundary layer thicknesses as well as the effect of crustal and mantle viscosities that are either constant, temperature-dependent, or fully non-Newtonian.

Results. In all of our models, convection produces horizontal compressional stresses in lithosphere above downwelling mantle and extensional stresses in lithosphere above upwelling mantle. As the convective vigor increases so does the magnitude of the stress. In models with constant-viscosity mantle overlain by a constant-viscosity crust, stress in the crust reaches values in excess of 100 MPa in less than 100 My. We find that the rate of increase in compressive stress decreases with increasing crustal viscosity. This is because the stronger the crust, the more the development of the convective instability in the mantle driving the deformation is impeded. We also find that the magnitude of the peak compressive stress achieved above the downwelling increases with higher viscosities and/or with thinner initial crustal layers; the stronger the crustal lid, the more are tractions from mantle convection supported in the crust. Since force balance on the crust requires that shear tractions integrated along the base be balanced by normal tractions integrated through its thickness, the thinner the crust, the larger the horizontal stresses.

Both analytical models [9,10] and our numerical models of convection-induced crustal flow indicate that the amplitude and sign of the topography are time- and rheology-dependent. In general, possible responses of the crust to mantle flow can be divided into three categories. The first involves little, if any, crustal flow, and topography results mainly from the transmission of normal tractions induced by density contrasts within the mantle. The second possible regime involves substantial crustal flow, with geologically rapid thickening over convective downwelling and thinning over convective upwelling. In this regime the effects of crustal thickness variations dominate the topography. A third possible regime lies between the first two, with "in phase" deformation on short time scales and crustal flow on longer time scales. A strong mantle lithosphere tends to shield the crust from convective shear tractions, and topography results mainly

from the transmission of convective normal tractions. A relatively weak lower crust facilitates crustal deformation, and the isostatic effects of crustal thickness variations dominate the topography.

Consideration of geoid-to-topography ratios (GTRs) can restrict the regime of crustal response appropriate for Venus. The distribution of estimated GTRs for several highland regions on Venus is bimodal with two clusters around 10 and 25 m/km [5]. The positive correlation of long-wavelength gravity and topography implies that there are no major regions that have negative GTRs. To keep the GTRs positive, the geoid must follow the surface topography in sign at all times. Although the regime of negligible crustal flow can correctly predict both the sign and magnitude of the GTRs, it does not account straightforwardly for the crustal deformation (i.e., flow) inferred from observations of tectonic features, and particularly areas of extensively deformed terrain, on Venus.

In contrast to the regime of negligible flow, that of time-dependent crustal flow generates topography that changes sign. Over a mantle downwelling, the topography is negative in the early stages of deformation and positive in the later stages of deformation; the converse holds over a mantle upwelling. During the transitional period the topography goes through zero, the geoid does not go through zero, and the GTR is unbounded; this singularity is not observed on Venus.

In the absence of a mechanism by which the sign of the geoid anomaly mimics that of the topography over a given upwelling or downwelling, only the regime of rapid crustal flow is plausible. In the case of mantle downwelling this would also require that the lower mantle be more viscous than the upper mantle in order to produce the required positive geoid anomalies. This layering of viscosity structure has already been shown to hold for the Earth, where the observed geoid highs over regions of mantle upwelling and regions of mantle downwelling are best explained by the presence of a strong lower mantle [11,12]. The large positive GTRs and the presence of large shield volcanoes in certain highland regions on Venus, such as Beta Regio and Eistla Regio, are best explained as areas of mantle upwelling [5,13,14]. The regime of rapid crustal flow predicts crustal thinning over the upwelling. However, the partial melting and ensuing volcanism and crustal plutonism expected over such regions may outweigh the effects of crustal thinning on the surface topography and thus also yield positive GTRs [15].

References. [1] S. C. Solomon et al., Science, 252, 297, 1991; [2] W. S. Kiefer et al., Geophys. Res. Lett., 13, 14, 1986; [3] B. G. Bills et al., J. Geophys. Res., 92, 10, 1987; [4] R. J. Phillips et al., Science, 252, 651, 1991; [5] S. E. Smrekar and R. J. Phillips, Earth Planet. Sci. Lett., 107, 587, 1991; [6] R. J. Phillips, Geophys. Res. Lett., 13, 1141, 1986; [7] R. J. Phillips, J. Geophys. Res., 95, 1301, 1990; [8] S. D. King et al., Phys. Earth Planet. Inter., 59, 195, 1990; [9] D. L. Bindschadler and E. M. Parmentier, J. Geophys. Res , 95, 21, 1990; [10] H. Schmeling and G. Marquart, Geophys. Res. Lett , 17, 2417, 1990; [11] M. A. Richards and B. H. Hager, J. Geophys. Res , 89, 5987, 1984; [12] B. H. Hager, J. Geophys. Res , 89, 6003, 1984; [13] R. E. Grimm and R. J. Phillips, J. Geophys. Res., 96, 8305, 1991; [14] R. E. Grimm and R. J. Phillips, J. Geophys. Res., 97, 16035, 1992; [15] R. J. Phillips et al., Science, 252, 651, 1991.
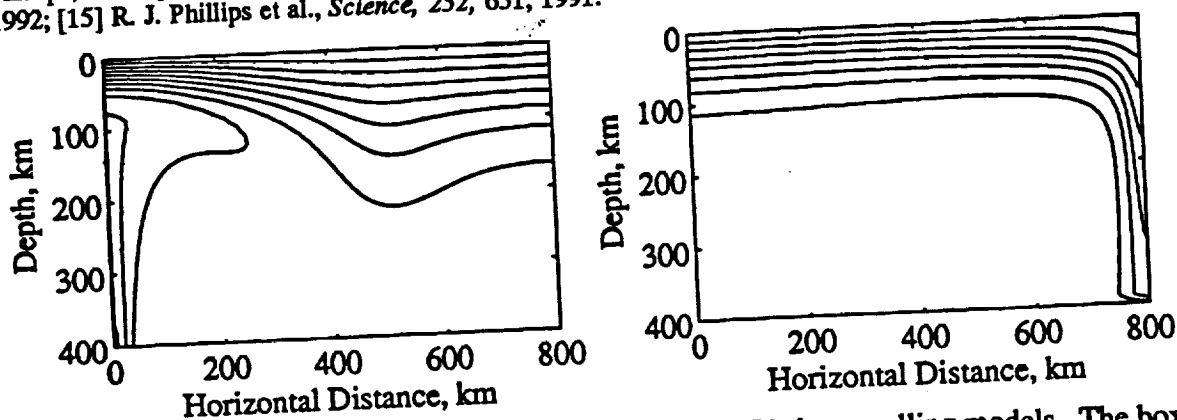

Figure 1. Temperature contours for the (a) upwelling and (b) downwelling models. The box is 800 km in the horizontal dimension and 400 km in the vertical. Top and bottom temperatures are fixed at 500 °C and 1250 °C, respectively. Contour interval is 100 °C.

Geoid - to - Topography Ratios on Venus: A Global Perspective

Mark Simons (Department of Earth, Atmospheric, and Planetary Sciences, Massachusetts Institute of Technology, Cambridge, MA 02139)

Sean C. Solomon (Department of Terrestrial Magnetism, Carnegie Institution of Washington, Washington DC 20015)

Recently available spherical harmonic solutions for the geoid and topography of Venus are of sufficiently high resolution (to degree and order 60) that they can be used to address questions concerning the relationship between geoid and topography on a regional scale. We have approached this question by mapping the geoid-to-topography ratio (GTR) on a systematic global basis. For a given a point on the surface, we consider the geoid and elevation values at all points on a gridded representation of those fields located within a specified distance of the reference point. From the set of paired values we determine the correlation coefficient and the best-fitting straight line. The latter is the GTR at that position, and the former is a measure of the significance of the derived ratio. This procedure is then repeated for all points on the global grid, yielding maps of the GTR and the correlation coefficient. Unlike previous studies of the GTR on Venus, this approach permits us to make an objective and systematic search for regions with anomalous GTRs as well as areas that do not demonstrate any strong correlation between geoid and topography. These maps can be updated regularly as new harmonic models of the Venus geoid are produced from new Magellan tracking data. This procedure permits the development of a global perspective on the relationship between GTR and venusian surface tectonics.

Gravitational Spreading of High Terrain in Ishtar Terra, Venus

SUZANNE E. SMREKAR AND SEAN C. SOLOMON

Department of Earth, Atmospheric, and Planetary Sciences, Massachusetts Institute of Technology, Cambridge

Magellan altimetry measurements indicate that the mountain belts and plateau margins of Ishtar Terra have topographic slopes in the range 2-30°. Magellan radar images reveal that numerous sets of narrow, closely spaced troughs and lineations, which we interpret as graben and normal faults, are located in many of these regions of high slope. The orientation of many of these graben sets perpendicular to the downslope direction suggests that they formed as a result of gravitational spreading. In several of the mountain belts, the extensional structures are parallel to the apparent direction of shortening, consistent with the interpretation that gravitational spreading occurred while mountain building was still active. To explore the implications of this spreading for the tectonic evolution of Ishtar Terra, we model the process by means of a finite element algorithm for viscoelastic deformation in a vertical section of the crust at the margin of a plateau or broad mountain range. Flow in the crust is assumed to be governed by a nonlinear, depth-dependent rheology. We predict brittle failure and relaxation of topographic relief as functions of time, for ranges of crustal thickness (10-30 km) and thermal gradient (5-25 K/km) and for observed ranges in topographic elevation (1-6 km) and slope (1-30°). This parameter range predicts a large spread in the time scales for initial failure and significant relaxation of relief. For a crustal thickness greater than 10 km, a thermal gradient of 15 K/km or more, and average values of relief (3 km) and slope (3°), the topography relaxes to 25% of its original height in less than 10 m.y. Although initial failure, in the form of normal faulting on the highlands and margin and occasional shallow thrusting in the lowlands, is predicted to occur much earlier, values of horizontal surface strain that are likely to be observable (~1%) do not accumulate until significant relaxation of relief begins. Given the predicted rate of topographic relaxation, either the crust of Ishtar Terra must be anomalous in some way (either much stronger than predicted by standard flow laws or very thin or cold) or the topographic relief and high slopes have been actively built and maintained until times significantly younger than the average crater retention age for Venus of 500 Ma. The large apparent depth of compensation, the abundance of volcanism, and the uncertainty in the local age favor the view that mountain building in Ishtar Terra has occurred until times at least as recent as 10 Ma.

INTRODUCTION

The high terrain on Venus should be subject to significant viscous relaxation on geological time scales [*Weertman*, 1979] because of the planet's high surface temperature (~500°C) and low rate of erosion [*Arvidson et al.*, 1991, this issue]. The highest topography on Venus occurs in the Ishtar Terra region. At the center of Ishtar Terra is Lakshmi Planum, a plateau with elevations 3-4 km above the mean planetary radius. The plateau is surrounded by the mountain belts Danu, Akna, Freyja, and Maxwell montes, which rise an additional 1.5, 3, 3, and 7 km, respectively, above Lakshmi Planum. Maintenance of these extreme elevations may be understood if the topographic relief of Ishtar Terra is geologically young or if the crust is very strong. However, neither of these conditions are clearly satisfied at Ishtar Terra. The average crater retention age for Venus, calculated from the density of impact craters seen in Magellan radar images, is approximately 500 Ma [*Phillips et al.*, 1991a, this issue; *Schaber et al.*, this issue]; on the basis of crater density, Ishtar Terra is not demonstrably younger than the average age. The large value of apparent depth of compensation (180 ± 20 km) for Ishtar Terra indicates some component of dynamic compensation [*Grimm and Phillips*, 1991], but this figure describes the compensation of features with wavelengths of at least 2000 km. Although a dynamic compensation mechanism at depth might be expected to

transmit stresses to the surface and thus contribute to recent changes in topographic relief, the most abrupt changes in elevation in Ishtar Terra occur over distances of tens to hundreds of kilometers and probably do not directly reflect scales of mantle processes. The abundance of volcanism in Ishtar Terra [*Head*, 1990; *Head et al.*, 1991] and particularly in Lakshmi Planum [*Roberts and Head*, 1990a] implies that anomalously low heat flow, and thus relatively high crustal and lithospheric strength, is unlikely.

Magellan radar images (120-210 m resolution) and altimetry data (15-25 km footprint diameter) provide new insights on the stability of the areas of high relief in Ishtar Terra. Numerous sets of lineations interpreted as narrow graben, 0.5-10 km wide, and normal faults are visible in the radar images of the slopes of mountains and on the scarps bordering Lakshmi Planum. Much of the apparent extension appears to be related to topographic slope and elevation, indicating that it is probably the result of gravitational spreading. Magellan altimetry data [*Pettengill et al.*, 1991] show that topographic slope is even higher than indicated by previous data sets [*Pettengill et al.*, 1980; *Barsukov et al.*, 1986]. However, western Maxwell Montes have slopes in excess of 30° yet show no clear evidence of extension. Extreme slopes such as this are very difficult to support unless tectonic forces are actively building the topography.

Even on Earth, where erosion rates are high and surface temperatures are much lower than on Venus, gravitational spreading plays an important role in the evolution of high topography [*Dewey*, 1988]. The high mountains and plateaus associated with the Himalayas and the Andes are prime examples of active gravitational spreading

[*Froidevaux and Ricard*, 1987; *Dewey*, 1988]. Extensional features are observed within and on the margins of the plateaus [*Sebrier et al.*, 1985; *Burchfiel and Royden*, 1985]. In Tibet, which has an average elevation of 5 km, active extension occurs along a set of large (75 by 15 km), north trending graben in the interior of the plateau. From structural evidence, the rate of extension is estimated to be 1% m.y.$^{-1}$ over a distance of 1100 km, corresponding to a rate of east-west spreading of 10 mm/yr [*Armijo et al.*, 1986]. In addition to this Quaternary extension, geologic mapping has revealed fault structures indicating Miocene extension parallel to the direction of shortening [*Burchfiel and Royden*, 1985]. These east trending normal faults extend 800 km along strike and may have experienced as much as several tens of kilometers of displacement [*Burchfiel and Royden*, 1985]. North-south extension has been documented in the Andean Altiplano-Puna Plateau [*Sebrier et al.*, 1985], which is approximately 4 km high. Rates of Quaternary extension [*Sebrier et al.*, 1985] are comparable to those in the Himalayas.

Recent studies of the formation and evolution of mountains have shown that gravitational spreading can be an important driving force for extension. Modeling of areal deformation is made tractable with a quasi three-dimensional, finite element representation of a thin sheet with vertically averaged rheology. *England and Houseman* [1989] employed this method to examine the transition from shortening to extension as a function of thermal conditions and topographic relief in an active orogen. *Bird* [1989] also took this approach, but he included two sheets, one for the crust and one for the mantle, which allows for detachment between the layers. Vertical plane-strain models (numerical and analytical) have been used to model more realistic rheologies or specific aspects of the process of gravitational spreading. *Bird* [1991] and *Kruse et al.* [1991] have looked specifically at the role of flow of the lower crust in balancing stress arising from relief both of the surface and of the crust-mantle boundary within extensional environments. *Braun and Beaumont* [1989] combined elastic, viscoelastic, and elastoplastic rheologies to model the tradeoffs between the timing and magnitude of gravitational spreading and regional vertical and horizontal stresses. Most of these studies have tried to match the thermal and tectonic histories of specific sites either of presently high topography, such as the Andes and Himalayas [*England and Houseman*, 1989], or where high topography in the past is thought to have played an important role in the present tectonics, such as the Basin and Range Province [*Braun and Beaumont*, 1989; *Lynch and Morgan*, 1990; *Kruse et al.*, 1991].

Modeling gravitational spreading on Venus requires a somewhat different approach. The primary constraints are locations of faults identified in radar images relative to the topography, along with broad constraints on the rheology of the crust and lithosphere. Regional tectonic history on Venus can be inferred to some degree from fault patterns observed in radar images [e.g., *Head*, 1990; *Solomon et al.*, 1991, this issue; *Kaula et al.*, this issue], but strain rates and thermal histories are unknown. Thus the goal of modeling is not to constrain the details of the thermal and tectonic history but rather the rheology and state of stress. Specifically, we address the question of how long topography remains after relief-building processes have ceased.

In this study we model gravitational spreading of high topography using a plane-strain, viscoelastic finite element algorithm [*Melosh and Rafesky*, 1980, 1983]. This approach permits the prediction of stress, failure, and strain as a function of time. In Ishtar Terra, extensional faulting is observed to occur both in the interior of the plateau and on the slopes of the plateau and surrounding mountains. We are primarily interested in deformation near the slopes, rather than on the interior of the plateau, for several reasons. First, on the margins of Ishtar Terra, extension is typically the most recent stage of deformation, whereas extensional features near the center of the plateau are often overlain by volcanic deposits or cut by later tectonic features (see discussion below). Normal faulting near the slopes is thus more likely to be related to present topography. Second, the deformation of the plateau as a whole is probably more strongly affected by long-wavelength dynamic compensation, which is poorly understood [*Bindschadler and Parmentier*, 1990; *Grimm and Phillips*, 1991; *Lenardic et al.*, 1991]. Third, including only a portion of the plateau allows for sufficient resolution to predict surface strain on a scale of 1-2 km. As the locations of normal faults and their relationship to the topographic slope provide major constraints for these models, predicting surface strain is an important goal.

In this paper, it is assumed that flow caused by gravitational spreading of high topography occurs primarily in the lower crust and is not strongly influenced by the mantle. This approach is similar to that taken by *Kruse et al.* [1991] in modeling extension in the western United States. Although the strain is greatest in the lower crust, we use the term gravitational spreading to describe both viscous flow in the ductile portion of the crust and the related deformation at the surface. For the rheology of the crust, we adopt a flow law for diabase [*Carlstan*, 1982], and in contrast to the models cited above, we take the viscosity to be depth-dependent. Depth-dependent (or temperature-dependent) rheology is important if the effects of a detachment, or a ductile décollement, are to be included in the model. The stresses created by the process of gravitational spreading are typically small relative to most other tectonic stresses, and some type of weakness must be present to allow significant deformation at the surface. In crystalline rocks, high temperatures at depth in the crust can produce regions that are sufficiently ductile to allow gravitational spreading. Given the high surface temperature on Venus, gravitational spreading above a ductile décollement is likely over a wider range of thermal gradients and crustal thicknesses than on Earth [*Smrekar and Phillips*, 1988]. While the model includes lower crustal flow, we do not model deformation involving a breakaway fault that extends from the lower layer to the surface and allows the upper layer to detach. On Earth, this type of gravity-driven deformation (sometimes referred to as gravitational sliding) is typically confined to areas where a very weak layer, such as shale, is present [*Wiltschko*, 1979]. There is no obvious mechanism for forming such a weak layer on Venus.

SETTING: ISHTAR TERRA

Ishtar Terra (Figure 1) is unique among highland regions on Venus. No other highland area contains a counterpart to the volcanic plateau Lakshmi Planum. The mountain belts Danu, Akna, Freyja, and Maxwell montes surrounding
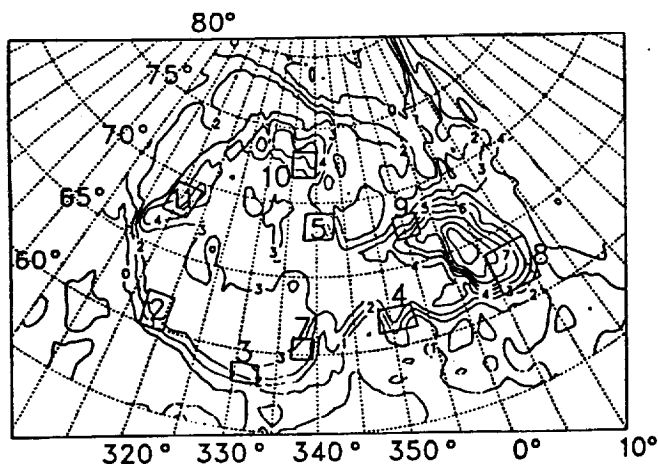
Fig. 1. Simplified Magellan altimetry for Ishtar Terra. The contour interval is 1 km. The datum for all altimetry is a radius of 6051.9 km. One degree of latitude is approximately 105 km. Boxes indicate the locations of the radar images shown in Figures 2-5 and 7-11.

Lakshmi Planum are not found elsewhere on Venus. The highest point on Venus lies within Maxwell Montes, reaching an elevation of over 10 km above the mean planetary radius [Pettengill et al., 1991]. On the periphery of Ishtar Terra, outward from each mountain belt, lie complexly deformed regions classified as tessera terrains. Clotho, Atropos, Itzpapalotl, and Fortuna tesserae are adjacent to Danu, Akna, Freyja, and Maxwell montes, respectively. New Magellan data show details of the deformation in the mountain belts and adjacent tesserae [Solomon et al., 1991, this issue; Kaula et al., this issue].

Pioneer Venus gravity data give an apparent compensation depth of 180 ± 20 km for the long-wavelength (greater than 2000 km) topography of Ishtar Terra [Grimm and Phillips, 1991]. This value is within the range found for many of the highland areas interpreted to be sites of mantle upwelling, or hot spots [Smrekar and Phillips, 1991]. However, Ishtar Terra differs in many ways from areas interpreted as hot spots, which typically display a broad topographic swell, rifting near the summit, and large volcanic constructs. Several other large highlands that have a generally plateaulike topographic profile, such as Ovda, Thetis, Tellus, and Pheobe regiones, have significantly smaller apparent depths of compensation, less than 100 km [Smrekar and Phillips, 1991].

The absolute age of the surface of Ishtar Terra and other areas of Venus is poorly constrained. Using an impactor flux derived from Phanerozoic terrains on Earth, Schaber et al. [1987] find an average crater retention age for the northern 25% of the surface of Venus of 50-160 Ma. Applying a lunar model of impactor flux, in contrast, gives a much larger age of 0.5-1 Ga [Ivanov et al., 1986; Basilevsky et al., 1987; Phillips et al., this issue]. Phillips et al. [this issue] conclude that the overall distribution of impact craters on Venus, as derived from the new Magellan radar data, cannot be distinguished statistically from a random distribution, making it impossible to determine relative dates for individual areas from crater density. However, Phillips et al. [this issue] argue that episodic resurfacing may nonetheless be consistent with the spatially random crater population, and they suggest that the local geological history may be used to infer whether the surface age of a given region differs from

the average for the planet. Roberts and Head [1990a] argue that the abundance of volcanism in Ishtar Terra, and particularly in Lakshmi Planum, favors a resurfacing age that is less than the planetary average value.

A wide range of hypotheses have been proposed for the origin of Ishtar Terra. Among these are mantle upwelling (hot spot) [Pronin, 1986; Grimm and Phillips, 1991], mantle downwelling [Bindschadler and Parmentier, 1990; Lenardic et al., 1991], and horizontal convergence [Head, 1990; Roberts and Head, 1990a]. Each hypothesis must incorporate special circumstances to explain all of the characteristics of Ishtar Terra [Grimm and Phillips, 1990, 1991]. Mantle upwelling most easily explains the gravity signature but requires a lateral contrast in lithospheric strength to produce the surrounding mountain belts. Mantle downwelling can also satisfy the gravity constraint, given the presence of a ductile lower crust which allows for crustal thickening. Peripheral mountain belts may form if the thickening of the crust and lithosphere evolve into a second stage of deformation in which the lithosphere sinks, initiating subduction [Lenardic et al., 1991]. Horizontal convergence can produce the correct arrangement of mountains and plateau but does not satisfy the gravity data; further, the driving forces are not explicit.

Several variations on the three basic mechanisms have been proposed, including multiple episodes of convergence [Head, 1990] and convergence onto a preexisting tessera block [Roberts and Head, 1990a]. The latter hypothesis is, in part, motivated by tectonic features, including ridges and grooves on Lakshmi Planum, that are partially buried by volcanic flows [Head et al., 1990; Roberts and Head, 1990a,b]. The presence of a preexisting tessera block has also been suggested as a means of concentrating stress on the periphery, allowing concentric mountain belts to form during mantle upwelling [Grimm and Phillips, 1990]. Crustal underplating and lithospheric delamination have been suggested as possible mechanisms for the formation of Lakshmi Planum [Roberts and Head, 1990b], but these processes do not account for the mountain belts.

Each of these models was proposed on the basis of radar imaging and altimetry data from Pioneer Venus and Venera 15 and 16. Early analysis of the higher-resolution data from Magellan shows that the tectonics of Ishtar Terra are very complex and cannot easily be interpreted in terms of any of the above models [Kaula et al., this issue]. Further study of the details of the deformational history of Ishtar Terra along with new, higher-resolution gravity data scheduled to be obtained later in the Magellan mission should help to distinguish the relative importance of the various hypotheses.

EVIDENCE FOR GRAVITATIONAL SPREADING

Criteria for Identification of Gravitational Spreading

Gravitational spreading on Venus can be recognized by analogy to features observed on Earth. Although gravitational spreading may produce a variety of fault types [Dewey, 1988; England and Houseman, 1989], we concentrate on identifying extensional features and in particular on identifying graben. As will be shown below, in most cases gravitational spreading is predicted to lead to stresses sufficiently large to cause failure in extension but not

in compression. In mountain belts, which are produced by shortening, extensional strain is a more characteristic manifestation of gravitational spreading than either shearing or shortening. Gravitational spreading stresses generally result in a direction of greatest extensional strain parallel to the regional downslope direction.

Regional stresses may influence the orientation of strain resulting from gravitational spreading. Within actively convergent orogens, the extension direction appears to be controlled by the direction of the regional compressive stress. In the Tibetan plateau, extensional stresses due to gravitational spreading are less than compressive stresses resulting from north-south convergence. Thus recent extension occurs principally in the east-west direction. Similarly, extension in the Altiplano-Puna Plateau occurs in the north-south direction, perpendicular to the direction of convergence.

Distinguishing the nature of a fault from radar data alone is
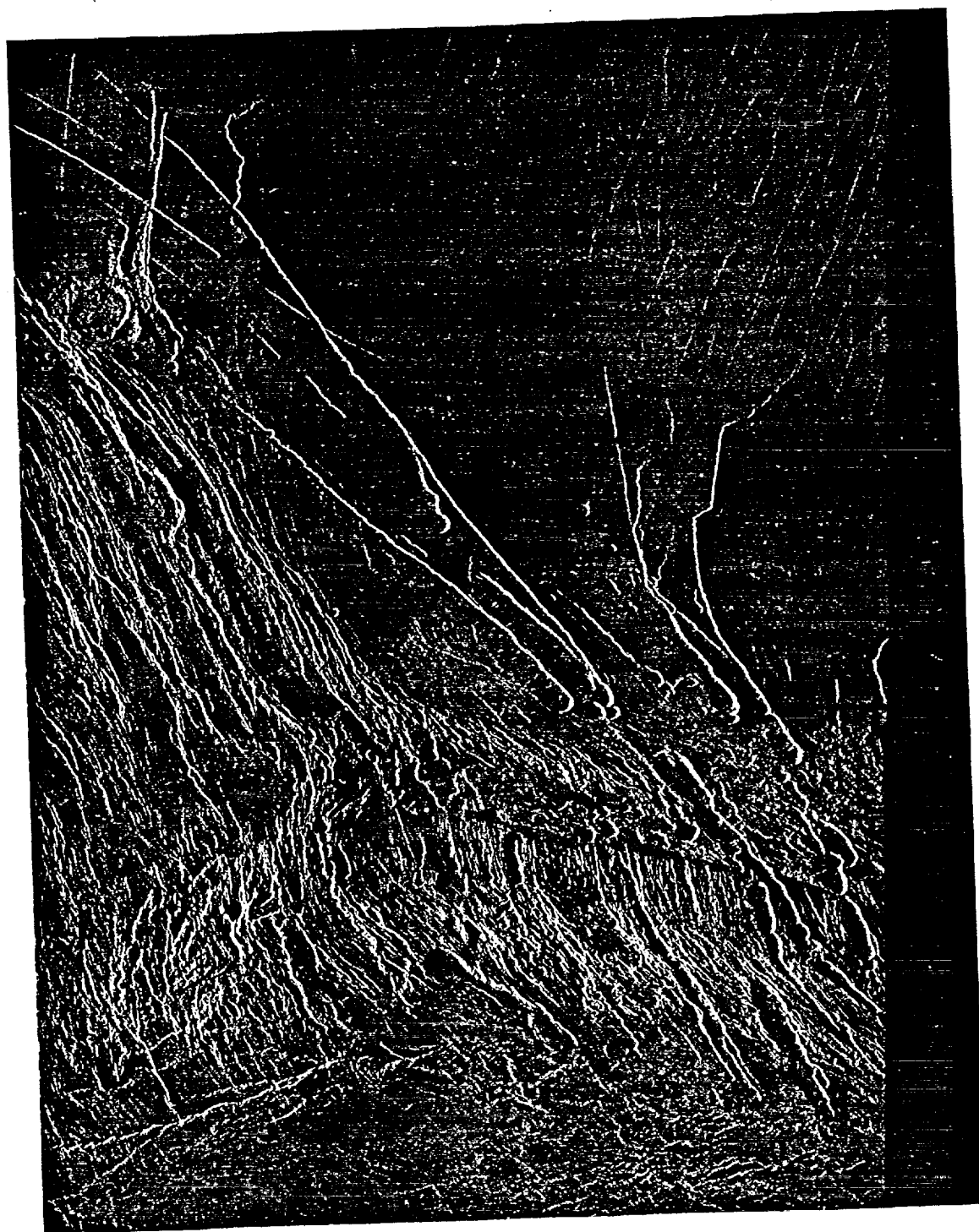
Fig. 2a. Radar image for a portion of western Vesta Rupes. See Figure 1 for location. This and all other radar images in this paper are in sinusoidal equal-area projection, with north to the top. The radar illumination direction is always from the left; the radar incidence angle at the latitudes of these and other images in this paper is 20-30° [Pettengill et al., 1991]. Numerous graben, pit chains, and collapse features trend northwest; most of these features are approximately parallel to the edge of the plateau. Lakshmi Planum appears at the upper right.

often difficult. Characteristics suggestive of extensional faulting include linearity and sense of offset across the fault. Lineations that occur in pairs are a clearer indication of extension. A flat floor between paired, inward facing linear faults is diagnostic of a graben, but these characteristics may not always be present. Some volcanic features also provide an indication of the orientation of the least compressive stress. Chains of volcanic craters, or pits, are magma withdrawal features fed by subsurface dikes that tend to be aligned perpendicular to the direction of least compressive stress [e.g., *Gudmundsson*, 1987]. The pit craters can be so closely spaced that they form a single, elongated depression that resembles a graben except that the sides of the scarps are scalloped rather than straight. Often lava channels extend from one end of the pit chains [see *Head et al.*, 1991, Figure 22].

Estimation of Slopes and Strains

In the areas identified as having experienced gravitational spreading, we estimate topographic slopes and horizontal surface strains. Slopes discussed below are calculated directly from the altimetry data points. Topographic profiles are given along great circles. Points along a profile are found by searching for altimetry observations within a 10-15 km horizontal distance and weighting the observations by their distance from the point on the profile. The locus of a profile is only approximately a straight line on the radar images, which are in sinusoidal projection. Contour maps

accompanying radar images below are created by first reprojecting the altimetric measurements to match the images, then regridding the data onto a regular grid. Gridding and contouring tend to smooth steep slopes. It should also be noted that in regions of high slope the altimetry may include errors due to incorrect identification of the nadir return among multiple returns from different points on the top, base, and flanks of the slope.

Horizontal strains are calculated from the widths and approximate depths of the observed graben. The dip angle of the faults making up the graben walls is assumed to be 60 ± 15°. On the basis of this assumption and the measured widths of graben walls in the radar observations, most of the graben discussed in this paper have estimated depths of 100-300 m. Unpaired lineations with similar widths are taken to be normal faults with throws equal to the depths of nearby graben. Errors in the strain estimates reflect primarily uncertainty in the fault dip angle.

Scarps

Vesta Rupes. Vesta Rupes is a scarp, 2-4 km in elevation, that forms the southwestern boundary of Lakshmi Planum between Danu and Akna montes. Most of Lakshmi Planum slopes gently to the south, but it rises 0.2 -1.5 km near its southern boundary, creating a rim along the plateau edge. The character of deformation changes along the length of Vesta Rupes. To the west of about 320°E, Vesta Rupes is less steep and is cut by numerous, closely spaced graben and collapse features with widths of up to 8 km (Figure 2a).
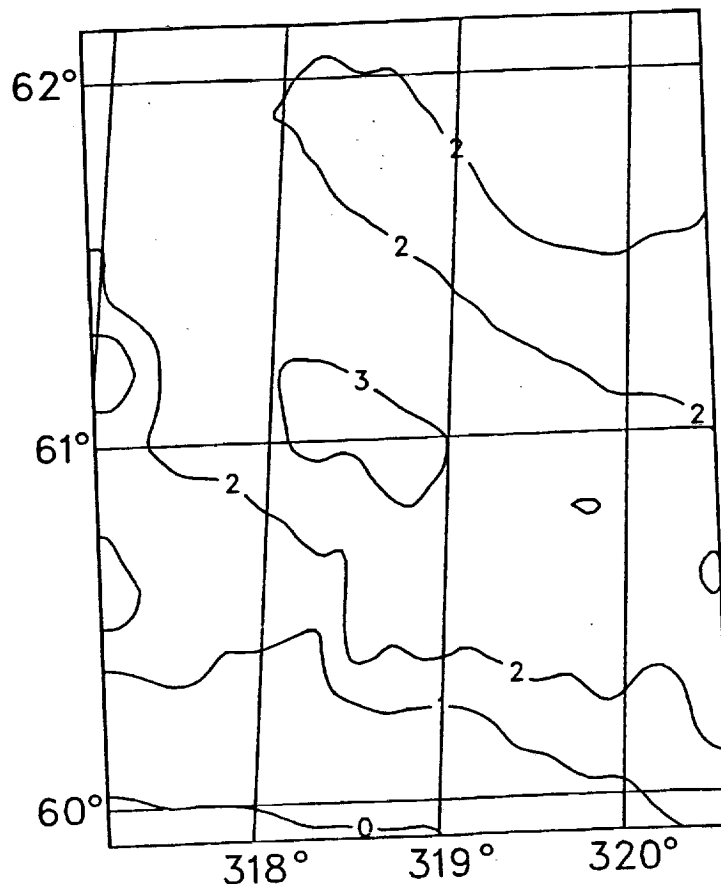

Fig. 2b. Contoured altimetry for the region of western Vesta Rupes shown in Figure 2a. All contour maps are made from the individual altimetry measurements, regridded at 0.1°-0.5° intervals of latitude and longitude. Contour maps that correspond to a radar image are shown in the same projection.
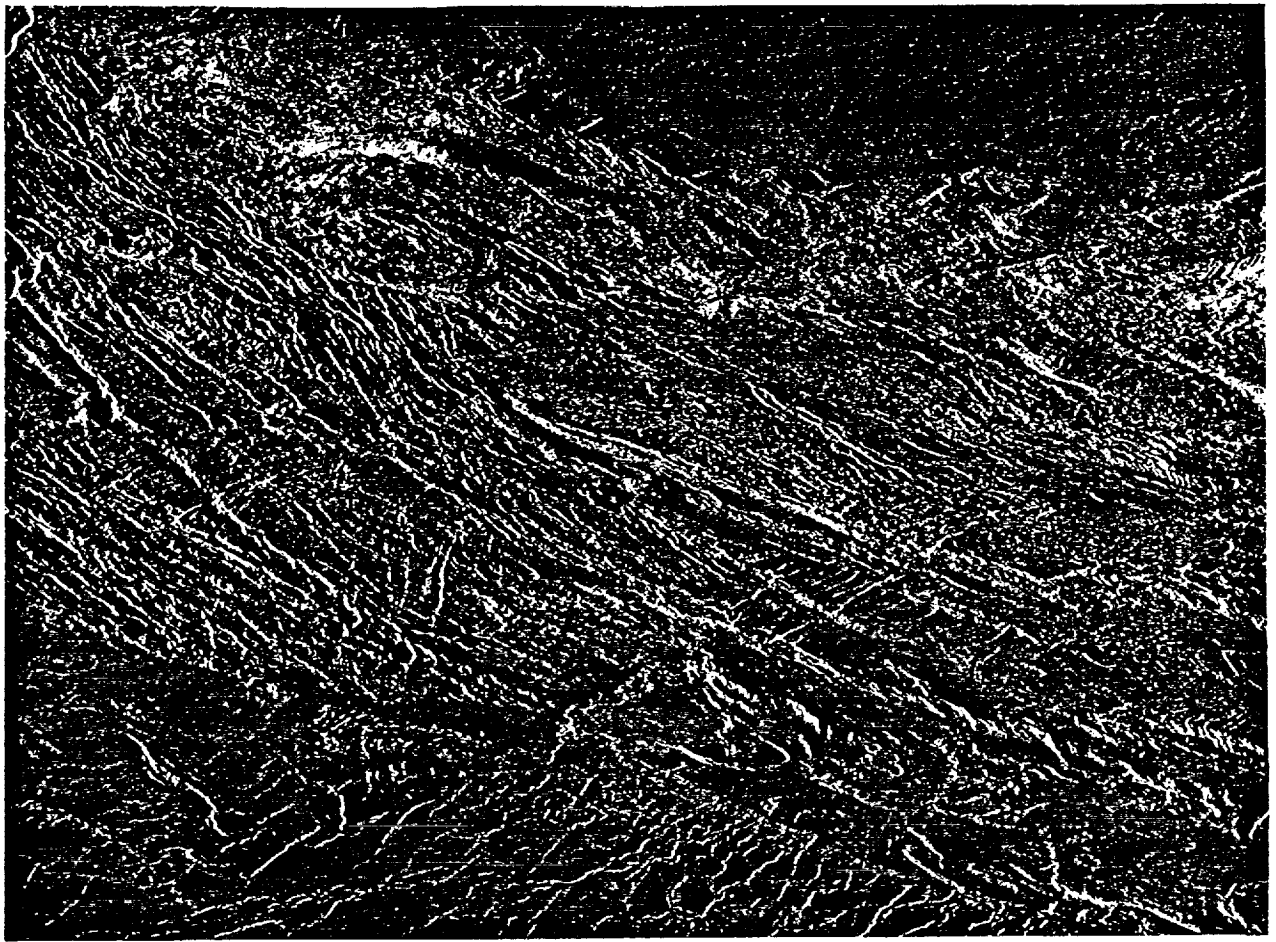
Fig. 3a. Radar image for western Danu Montes and eastern Vesta Rupes. The radar-bright regions near the top are part of the crest of Danu Montes. The plain of Lakshmi Planum appears at the top right. Near the center and lower right of the image are several long, bright, northwest trending lineations that are interpreted to be normal faults. Numerous, narrow, northwest trending paired bright and dark lineations, interpreted to be graben, appear in the central and upper left portion of the image. Both sets of lineations are approximately parallel to the trend of the topographic contours shown in Figure 3b.
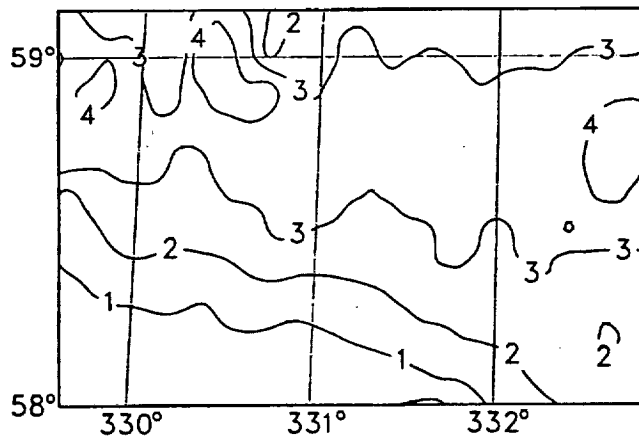

Fig. 3b. Contoured altimetry for the portion of western Danu Montes and eastern Vesta Rupes shown in Figure 3a.

Almost all of the graben and collapse features strike approximately N60°W, which is similar to the regional trend of Vesta Rupes in this area. In the western portion of Figure 2a, the graben parallel the scarp; in the eastern portion, the scarp trends more nearly east-west, and most of the graben

intersect the scarp at an acute angle. The estimated horizontal strain in this area is 2-16%. Numerous pits, collapse features, and lava channels imply that volcanism accompanied extension. In many cases, the extensional features cut each other, often at small angles, suggesting that the stress field evolved over time. This region was postulated to be a site of gravitational sliding on the basis of Venera 15 and 16 radar data by *Bindschadler and Head* [1991]; they also suggested that compressional ridges located 200-600 km to the southwest of Vesta Rupes were formed as a result downslope compression associated with this sliding.

To the east of 321°E, Vesta Rupes drops more steeply to the plains. The easternmost portion of Vesta Rupes is shown in Figure 3. In this region, numerous, narrow (~1 km wide) graben trend approximately perpendicular to the downslope direction. In the extended area, topographic slope is 3.5° over 60 km, and horizontal strain is estimated to be 1-6%. These narrow faults may represent the surface expression of deformation above a detachment. Pit chains, isolated pits, and dark regions which may be flows indicate the presence of volcanism in the area. Some of the narrowly spaced faults and graben cut the radar-bright crest of the western arm of Danu Montes (Figure 3a), suggesting that extension postdates mountain building in this area. In the lower right

of Figure 3, several long (75 km), bright lineations appear to be scarps. These scarps are interpreted as normal faults, as they parallel graben to the west and are collinear with pit chains just to the east of Figure 3. Farther west, there are longer scarps (up to 400 km), parallel to Vesta Rupes, that appear similar to those visible in Figure 3. These features may also be normal faults, possibly due to gravitational spreading.

Southeastern scarp of Lakshmi Planum. The edge of Lakshmi Planum between Danu and Maxwell Montes drops 2-4 km to the plains and has two curved segments, convex toward the plateau (Figure 1). Thus the edge of the plateau can be approximately divided into northeast trending sections and northwest trending sections. Slopes on the northwest trending edges are typically steeper (8.3° over 20 km) than those along the northeast trending edges (4.0° over 45 km), although near 350-351°E there are apparent elevation changes of 2 km between adjacent footprints (14° over 8 km). Figure 4 shows a region where two such trends intersect, near 62°N, 350°E. North to northwest trending graben are perpendicular to the downslope direction in this region and appear to be due to gravitational spreading.

Horizontal strain across the northwest trending graben is estimated to be 1-16%. Numerous pit chains and linear collapse features are interspersed with the graben. These graben occur on the raised rim of the plateau and continue across the slope and onto the plains at the base of the northwest trending scarp (Figure 4). Some of the lineations parallel to the northeast trending segment of the scarp at the eastern edge of the area shown in Figure 4 appear to be graben, but most of the lineations are not paired. If these lineations are normal faults, the estimated strain is 1-4%. The radar look direction is more nearly parallel to the lineations on the northeast trending scarp, however, which may contribute to their subdued appearance. Alternatively, the steeper slopes on the northwest trending scarps may have led to greater downslope extension, or a regional stress field may have inhibited extension on the northeast trending scarps while favoring extension of the northwest trending scarps.

Northeastern scarp of Lakshmi Planum. The edge of Lakshmi Planum between Freyja and Maxwell montes (Figure 5) rises 0.5-1 km above the plains to the west, then drops 2-3 km to the east into a basin (Figure 6). A northwest

Fig. 4a. Radar image for a region that forms the intersection of two curved segments of the southeastern edge of Lakshmi Planum. Numerous north-northwest trending graben, pit chains and collapse features approximately parallel the slope on the northwest trending segment of the edge of the plateau. Fewer lineations, some of which appear to be graben, parallel the northeast trending portion of the edge of the plateau.
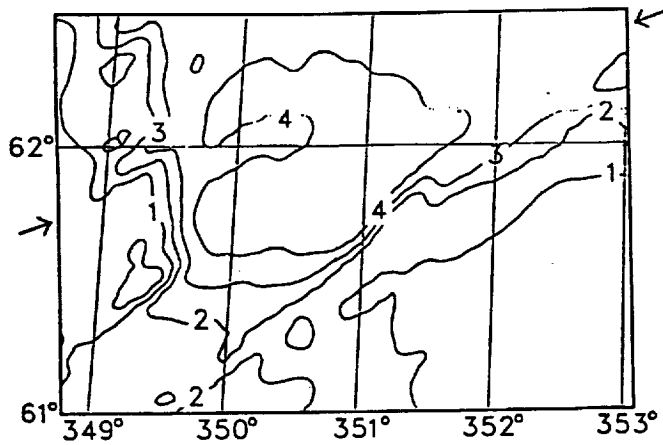
Fig. 4b. Contoured altimetry for the section of the southeastern edge of Lakshmi Planum shown in Figure 4a.

Fig. 4c. Altimetric profile across the southeastern edge of Lakshmi Planum. Location is shown by arrows in Figure 4b.

trending set of graben cuts a series of bright, narrowly spaced ridges that appear to be the result of shortening, as well as several volcanic flows. Both the ridges and the northwest trending graben are parallel to the rim of the plateau. The slope of the western side of the rim is 2.2° over 15 km; slopes to the east are as steep as 13° but are typically 4.5° over 30 km. Extension in this region is the latest stage of deformation and is in the downslope direction, implying a gravitational spreading origin. On the steeper, northeastern slope of the plateau rim, the northwest trending graben are more disrupted than to the southwest, where the graben continue for approximately 50 km onto the plain. Horizontal strain in this area is estimated to be 1-5%. One large, northeast trending trough cuts across the eastern slope of the plateau edge; its trace approximately parallels the local topographic contour.

Mountains

Danu Montes. Several examples of extensional features are visible in Danu Montes, the least elevated of the four mountain ranges rimming Lakshmi Planum. One large graben (10 km wide, 50 km long, 0.5 km deep) occurs at a small angle to the crest of Danu Montes (Figure 7). Apparently compressional ridges that crosscut the southern end of this graben imply that the extension at the crest of the range occurred between episodes of compressional deformation and thus during the shortening that formed Danu Montes. To the north and west of the graben, numerous northwest trending collapse features and lava channels cut northeast trending ridges. The orientation of the collapse features perpendicular to the compressional structures in the northwestern section of the image is consistent with gravitational spreading within an active orogen.

To the north and east of the large graben, a different set of east-west trending pit chains cuts across the ridges at an oblique angle. These chains continue to the east, beyond the area shown in Figure 7, for a total length of about 125 km. Although they do not seem to be related to the topography in the area shown in Figure 7, to the east they are perpendicular to the downslope direction. The collapse features, lava channels, pit chains, and numerous isolated pits provide evidence of multiple episodes of magmatism in the region.
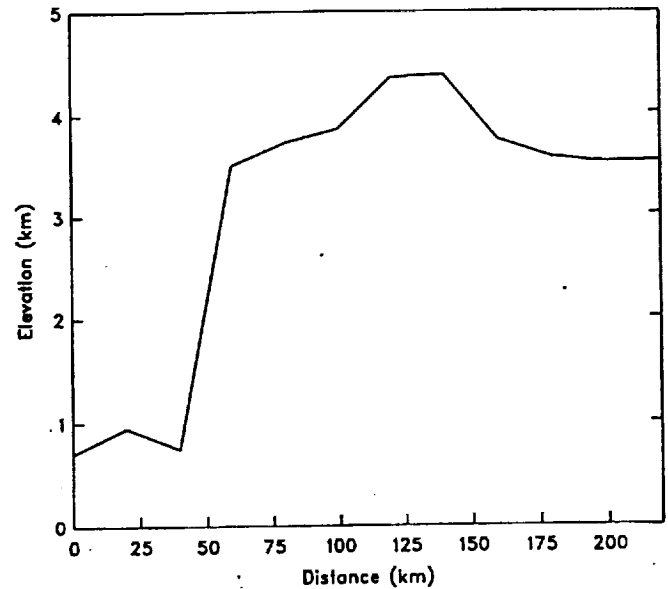
Maxwell Montes. Maxwell Montes contain the highest terrain and steepest slopes on Venus, with a maximum elevation of more than 10 km above mean planetary radius. Interestingly, no graben are obvious on the western slope of Maxwell Montes, where the local slope is as much as 30° over horizontal scales of several tens of kilometers. If unpaired normal faults are present, they are probably interspersed with other faults and folds, making them difficult to identify. *Pronin and Kreslavsky* [1992] interpret many of the topographic troughs on the west side of Maxwell Montes to be graben. Although this is a plausible interpretation, we do not include these troughs in our description of extensional features because none of them have all the characteristics of graben.

Two perpendicular sets of graben occur on the southern slope of Maxwell Montes (Figure 8). The topographic slope in this region is approximately 2°; the elevation drops 6 km to the southeast over a horizontal distance of 350 km. One set of graben is parallel to the downslope direction; the other set is perpendicular to the downslope direction and curves along the southern margin of Maxwell Montes, giving the two sets a radial and concentric pattern. The graben set that trends parallel to the downslope direction is more prominent in the southern, central portion of Figure 8. Horizontal strain is estimated to be 1-17% across the downslope-parallel graben set and 1-9% across the set perpendicular to downslope direction. Northwest trending ridges, interpreted as products of shortening, are also prominent in southern Maxwell Montes. Disrupted, apparently low-relief ridges occur downslope from and approximately parallel to the northeast trending, concentric graben set. These ridges, also interpreted as due to compression, are crosscut by the northwest trending graben.

The concentric set of graben and normal faults, those perpendicular to the downslope direction, are probably a result of gravitational spreading. In many cases the graben cut the northeast trending ridges; in other regions both graben and ridges are disrupted such that it is difficult to
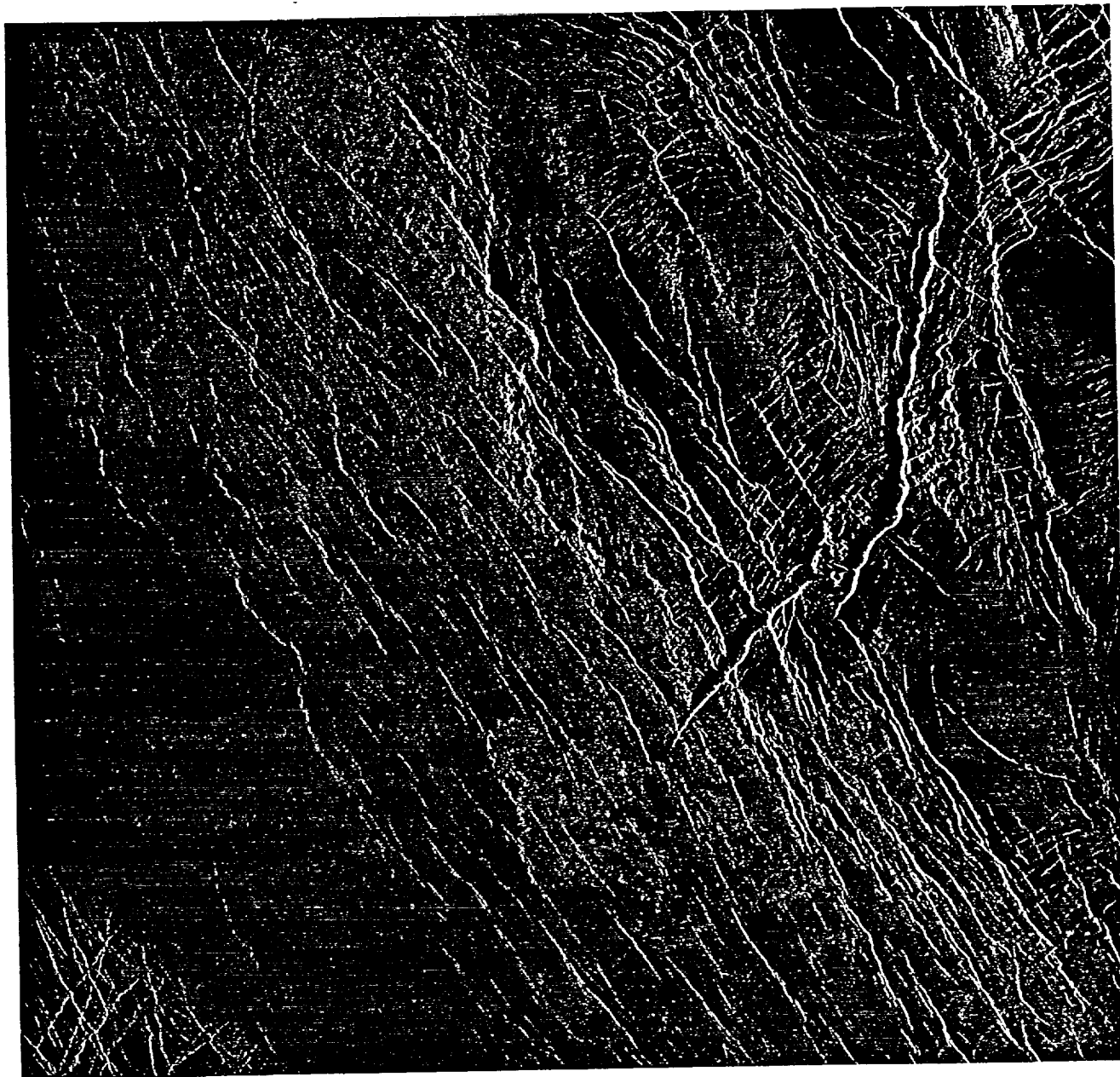
Fig. 5. Radar image for a portion of the northeastern rim of Lakshmi Planum. Altimetry data for this area are shown in Figure 6. Narrow, northwest trending graben are approximately perpendicular to the topographic slope and cut compressional ridges and volcanic flows. A portion of the grooved terrain described by *Roberts and Head* [1990a] appears in the lower left corner.

infer any crosscutting relationship. Patches of both radar-bright and radar-dark material fill areas between the ridges and graben. These regions of locally uniform radar backscatter may be volcanic flows or erosional deposits. In much of Maxwell Montes, as in most of the highlands (see also Figures 3a, 7, 10, and 11a), the emissivity is extremely low [*Tyler et al.*, 1991; *Klose et al.*, this issue]. Thus the radar-bright patches could be areas that are bright because of a high intrinsic reflectivity.

Two sets of narrow graben also occur on the northern flank of Maxwell Montes (Figure 9). A northeast trending set of graben trends perpendicular to the downslope

Fig. 6a. Contoured altimetry for southeastern Freyja Montes and northeastern Lakshmi Planum, including the areas shown in Figure 5 (southern box) and Figure 10 (northern box).

Fig. 6b. Altimetric profile across the region shown in Figure 5. Location is given by arrows outside the southern box in Figure 6a.

Fig. 6c. Altimetric profile across the region shown in Figure 10. Location is given by arrows outside the northern box in Figure 6a.

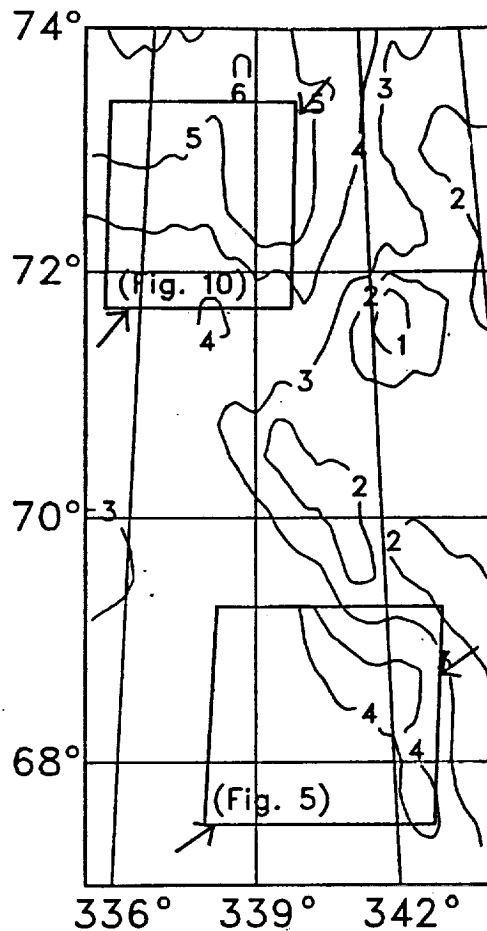direction, suggesting a gravitational spreading origin; a northwest trending set parallels the downslope direction. The age relationship between the two graben sets is unclear. The average slope in this region is 3.8° over a horizontal distance of 80 km, with a drop of 6 km in elevation. The horizontal strain due to extension is estimated to be 2-22% across the northeast trending graben set and 1-6% across the northwest trending set.

Freyja Montes. Numerous northwest trending graben cut across the southern slope of Freyja Montes, near the transitional region which divides the east-west trending ranges in central Freyja Montes from the north-south trending ranges in eastern Freyja Montes. The variably spaced graben trend generally perpendicular to the 3.9° regional topographic slope (measured over 40 km) and continue for approximately 80 km onto the more gently sloped volcanic deposits of Lakshmi Planum (Figure 10). This orientation suggests that the graben likely formed as a result of gravitational spreading. The estimated horizontal strain is 1-6%. These graben cut across the ranges of eastern Freyja Montes and some of the east-west ranges in southern central Freyja Montes. The graben are the latest stage of deformation in this area and cut across lineations interpreted to be folds and thrust faults, as well as an impact crater (Figure 10a). Localized volcanism is not evident in this region, but the smooth, dark plain of Lakshmi Planum is

generally interpreted as a series of volcanic deposits [*Roberts and Head*, 1990a,b].

Extension in central Freyja Montes is more limited in distribution. A set of narrow, closely spaced graben trend north to northwest [*Solomon et al.*, 1991, Figure 14]. The graben occur near the highest elevation in Freyja Montes, but they do not appear to be consistently oriented with respect to the local topographic slope. Typically, they are neither perpendicular to the downslope direction nor parallel to the direction of apparent shortening. In one region, where the graben trend northward, they are perpendicular to radar-light and -dark bands that have been interpreted as compressional ridges [*Crumpler et al.*, 1986; *Head*, 1990]. Their truncation at long lineations and their curved patterns suggest that they have been shortened and probably horizontally sheared [*Solomon et al.*, 1991]. If these graben were formed as a result of gravitational spreading, they have been subsequently deformed such that they are no longer in
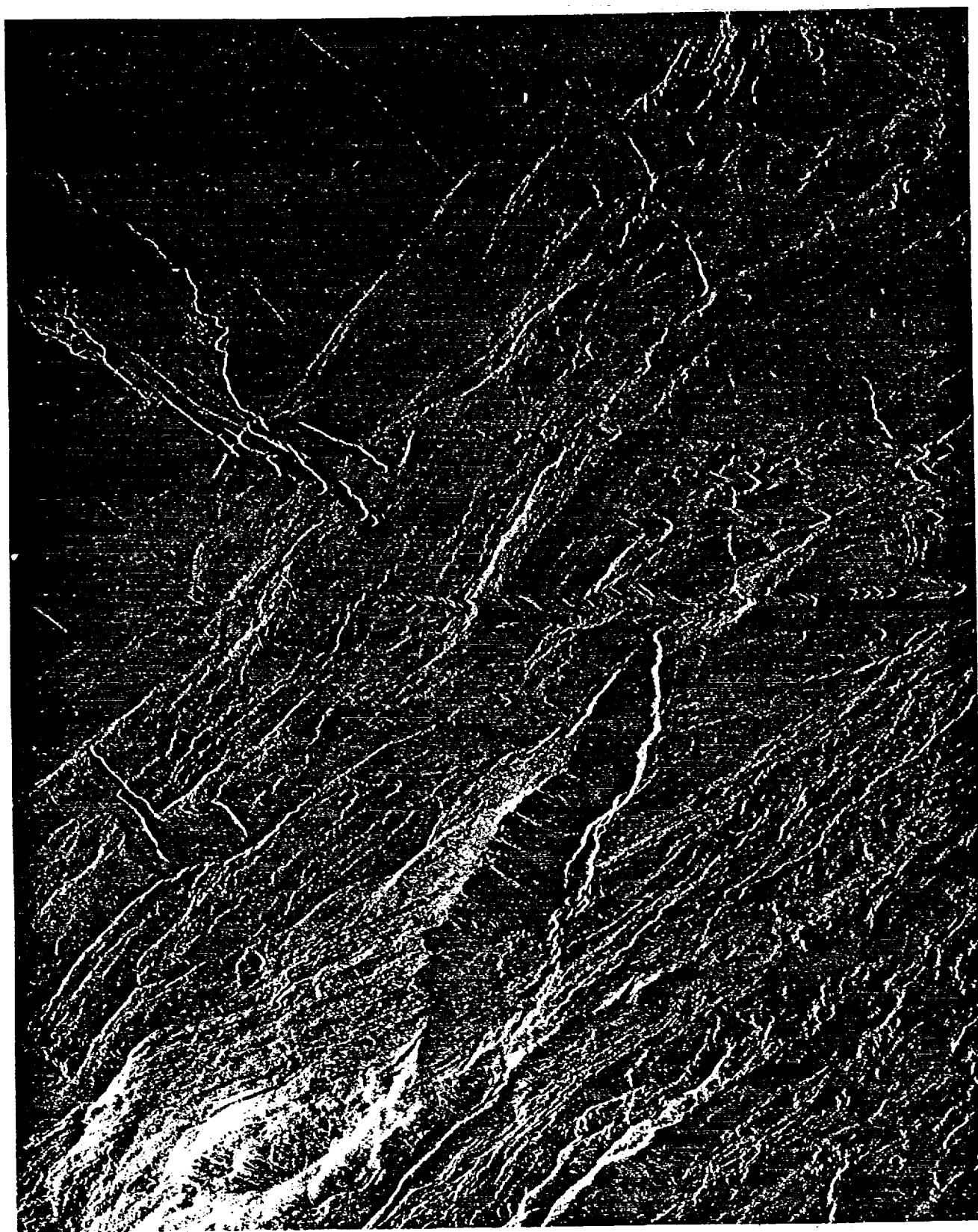
Fig. 7. Radar image of an area about 130 km wide along the northeastern arm of Danu Montes. The highest terrain is in the bright area in the southwest corner of the image. A large graben is located in the center of the image, trending at a small angle to the compressional ridges. Northwest trending collapse features, lava channels, and pit chains cut approximately orthogonally across the ridges. East-west trending pit chains also cut across the ridges.
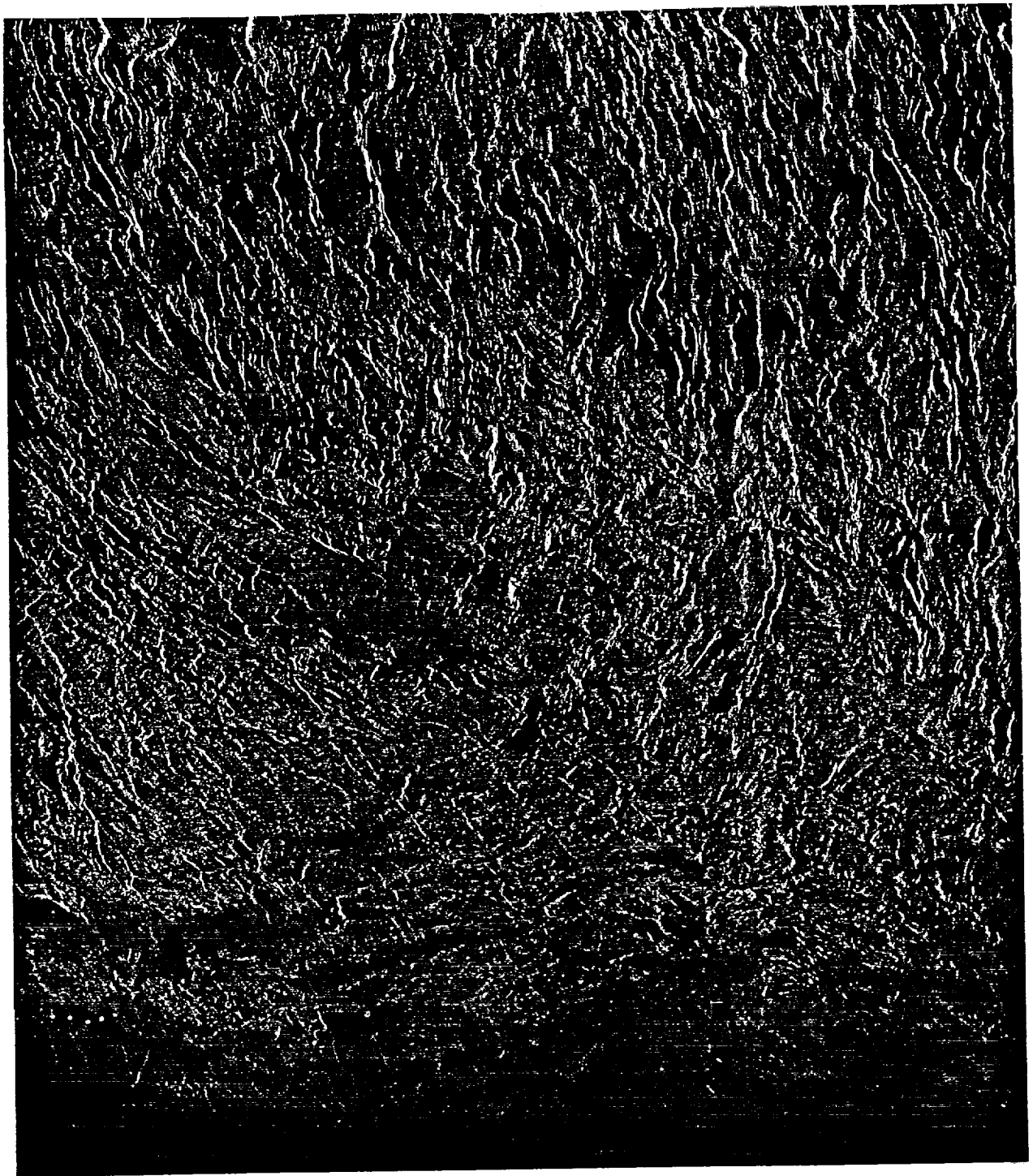
Fig. 8a. Radar image for southeastern Maxwell Montes. Two graben sets occur in this region. One set trends northwest, in the downslope direction; another set generally trends northeast and is approximately perpendicular to slope. Radar-bright regions in this area have very low emissivity relative to the rest of the planet (see text).

their original orientations. No evidence of volcanism is present in this region.

In eastern Freyja Montes there is abundant evidence for extension. Two intersecting graben sets, one trending northwest, the other trending north-south, cover an area approximately 100 km in width by 200 km in length [*Solomon et al.*, 1991, Figure 16]. The northwest trending set appears to be the younger of the two. Local topographic slopes are quite high in portions of this region, up to 11°,

suggesting that gravitational spreading is likely. However, while some of the graben are perpendicular to the downslope direction, others cut across the slope at a variety of angles.

Akna Montes. Extensional faulting in Akna Montes occurs primarily on the western slope. Northwest trending graben and normal faults cut across the northeast trending ridges that have been interpreted as folds and faults [*Crumpler et al.*, 1986; *Head et al.*, 1990] composing the mountain range (Figure 11a). In some cases, the graben are
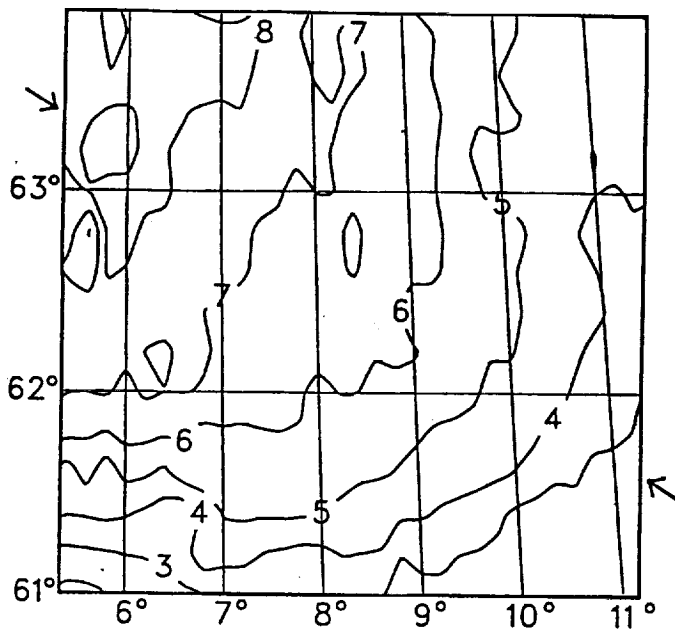
Fig. 8b. Contoured altimetry for the section of southeastern Maxwell Montes shown in Figure 8a.

Fig. 8c. Altimetric profile across southeastern Maxwell Montes. Location shown by arrows in Figure 8b.

perpendicular to the folds, such as in the northern and southernmost portions of Figure 11a; in the central region they cut across the trend of the folds at an acute angle. In the central region, the graben appear curved, due either to undulations in the topography or to deformation after their formation. If these graben are the result of gravitational spreading, their orientation with respect to the topography and the ridges indicates that they formed while the shortening that created Akna Montes was still active. Estimated horizontal strain is 1-14%. Only one small pit is visible in Figure 11a, but many of the ridges in the west appear to be embayed, possibly by volcanic flows. South of the area shown in Figure 11a, at the southern tip of Akna Montes, several large troughs trend approximately perpendicular to the downslope direction, suggesting that they are due to gravitational spreading.

Lakshmi Planum

Lakshmi Planum is dominated by volcanic flows and faulting, much of which is associated with the calderas Colette and Sacajawea. Grooves interpreted as graben are common [*Roberts and Head*, 1990a]. In some areas only graben occur, but in other areas, ridges interpreted to be compressional features are also present. The age relationship between ridges and graben in these areas is unclear [*Roberts and Head*, 1990a]. Both ridges and graben appear to be closely linked to the formation of the surrounding orogenic belts: compressional ridges are often parallel to and graben are typically perpendicular to ridges in adjacent mountains [*Roberts and Head*, 1990a]. Most of the deformed regions are somewhat more elevated than the surrounding plains and thus are only partially flooded by volcanic flows [*Roberts and Head*, 1990a]. A portion of the grooved terrain is visible in the southeastern corner of Figure 5. In this area, one of the two graben sets in the grooved terrain is parallel to the edge of the plateau and to the set of graben farther to the
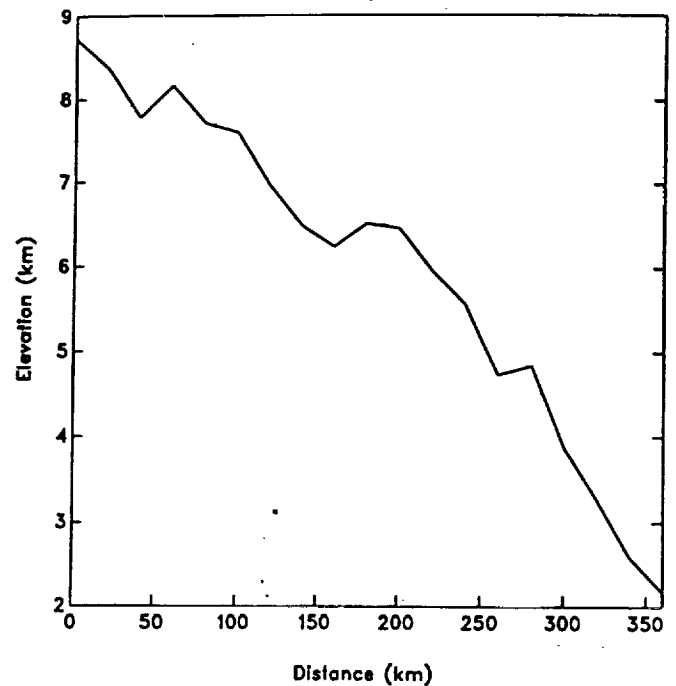
east that we have interpreted to have formed by gravitational spreading. Numerous, large (100 km long by 5 km wide), northeast trending graben intersect the southeastern scarp of Lakshmi Planum. In this region, the graben are not flooded and appear to be the youngest deformational features, sometimes cutting older areas of flooded grooves and ridges. Gravitational spreading can easily lead to extensional faulting in the interior of a plateau such as Lakshmi Planum (see below) and may be responsible for many of the extensional features observed there. The orientation of the many of the graben in the interior of the plateau suggests that if the extension is the result of gravitational spreading, then the spreading occurred during the formation of the adjacent mountain belts.

MODELS

To model the time-dependent stresses and displacements associated with the gravitational spreading described above, we employ the finite element program TECTON [*Melosh and Rafesky*, 1980, 1983]. A two-dimensional, plain-strain representation of the problem is assumed. An example of the initial finite element grid depicting a vertical section of the crust is shown in Figure 12a. The reference crustal thickness, that of the plains, is shown on the right; on the left is a region of elevated topography that we will refer to as the plateau, although it could represent the topography of either a plateau or a broad mountain range. A sloped region, or scarp, connects the plateau and the plains. The boundary conditions are zero vertical and horizontal velocity on the bottom of the grid, a free surface top boundary, and zero horizontal velocity and free slip vertically at the sides. The elements are 1 km high and 2 km wide. We adopt a viscoelastic rheology, a Poisson's ratio of 0.25, and a Young's modulus of 6×10^{10} Pa. The viscosity is calculated as a function of depth from a given flow law (see below) in which
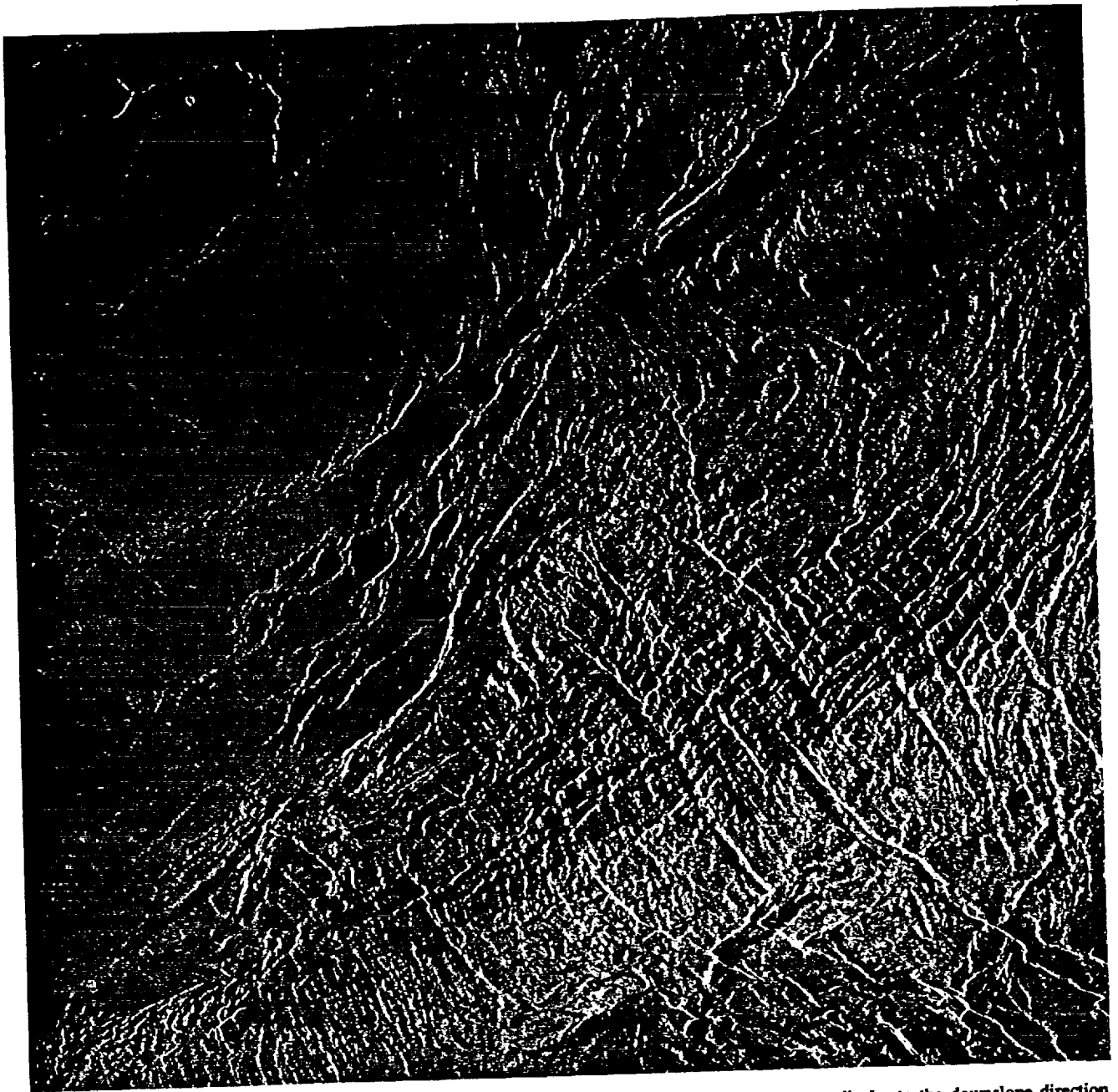
Fig. 9a. Radar image for northwestern Maxwell Montes. The northeast trending graben set is perpendicular to the downslope direction, while the northwest trending set runs generally downslope. A volcanic crater chain that switches orientation is visible in the upper left.

strain rate varies approximately as a power of the deviatoric stress and depends exponentially on the reciprocal temperature. The surface temperature is taken to be 740 K, and a linear thermal gradient is assumed. Each row of elements has the same viscosity, which is equivalent to assuming that the temperature is constant along both the bottom and top of the grid. The thermal gradient is thus less in the plateau than in the plains, by a factor equal to the ratio of the crustal thicknesses. The bottom boundary condition is intended to simulate approximately the effects of an upper mantle layer that is considerably stronger than the lower crust. As an alternative to a lower boundary that is fixed in both the vertical and horizontal directions, we have carried out calculations for a lower boundary fixed in the vertical direction but free horizontally; such a boundary condition is intended to simulate a detachment surface. An actual detachment surface is likely to display behavior somewhere between that of the two boundary conditions.

The choice of a flow law for crustal material is critical to the estimation of time scales for deformation by gravitational spreading. The surface material at the Venera and Vega landing sites in the equatorial plains [Surkov et al., 1984, 1987] has a composition similar to that of basalt or diabase, and many previous studies of crustal deformation on Venus [Grimm and Solomon, 1988; Smrekar and Phillips, 1988; Zuber and Parmentier, 1990; Phillips, 1990; Lenardic et al., 1991] have adopted the flow law of Maryland diabase obtained from the laboratory measurements of Caristan [1982]. Some uncertainty, of course, is always introduced by the extrapolation of creep rates measured in the laboratory to

Fig. 9b. Contoured altimetry for the section of northwestern Maxwell Montes shown in Figure 9a.

Fig. 9c. Altimetric profile across northwestern Maxwell Montes. Location shown by arrows in Figure 9b.

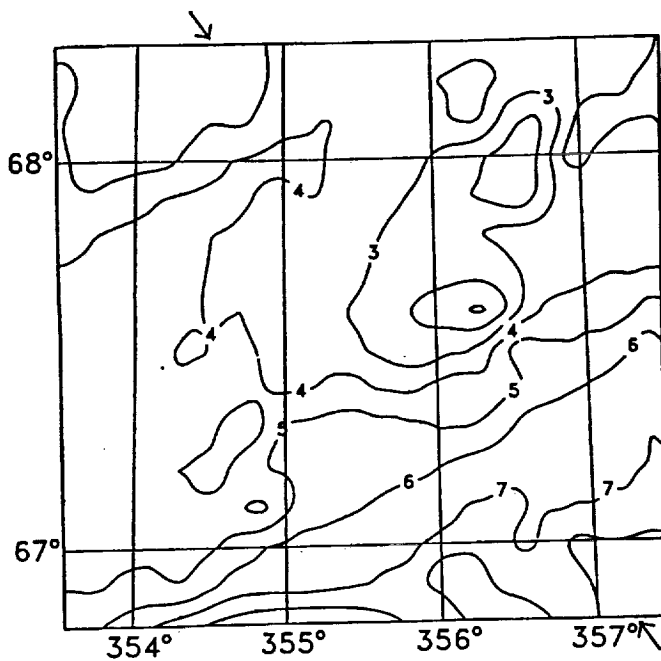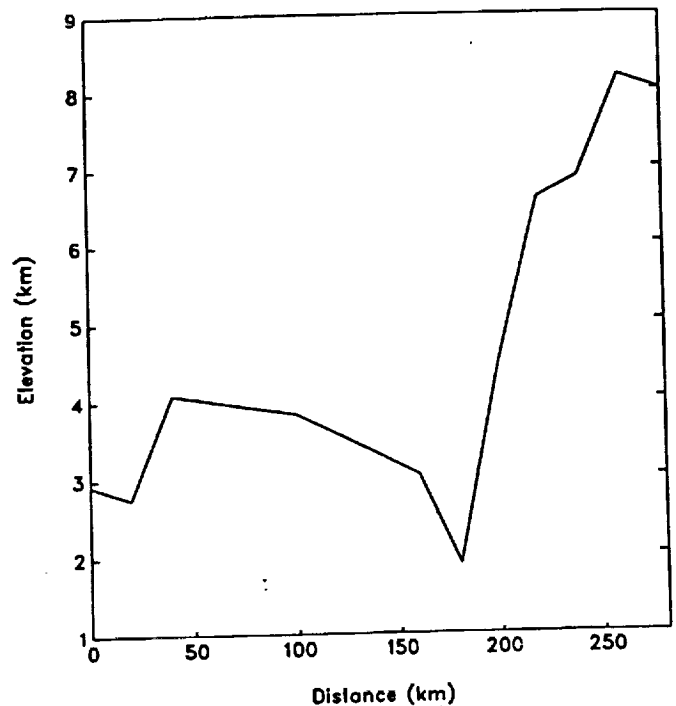flow at geologic strain rates. Further, strain rates in rock can be strongly affected by the presence of water. Because of the extremely low water content of the lower atmosphere of Venus, the Venusian crust is thought to be quite dry [McGill et al., 1983]. Although the samples used by Caristan [1982] were first dried by heating, the retained water content may still be greater than that of the crust on Venus. The presence of partial melt as well as possible microcracking in the laboratory samples used to measure creep rates may have also caused the strength to be underestimated [Caristan, 1982; Evans et al., 1990]. The flow law of Caristan [1982] should thus probably be considered as providing only a lower bound on the strength of the Venusian crust. As an approximate upper bound on the strength of the Venusian crust, we adopt the websterite flow law of Avé Lallement [1978].

We examine stresses and deformation over periods of up to several billion years. Model time steps are scaled by the Maxwell time, which is given by

$$\tau_M = e^{-Q/(RT)} / 2EA_o \, \sigma^{(n-1)} \qquad (1)$$

where Q is the activation energy, R is the gas constant, T is the absolute temperature, E is the Young's modulus, A_o is a flow law constant, and σ is the second invariant of the deviatoric stress tensor. For diabase, $A_o = 6.12 \times 10^{-2}$ MPa^{-n} s^{-1}, $Q = 276$ kJ/mole, and $n = 3.05$ [Caristan, 1982]. The parameters for websterite are $A_o = 3.16 \times 10^{-6}$ MPa^{-n} s^{-1}, $Q = 323$ kJ/mole, $n = 4.3$ (from the data of Avé Lallement [1978] refit by Carter and Tsenn [1987]). The initial time step is taken to be 0.1 τ_M; after 10 time steps at 0.1 τ_M, 10 more time steps are run at 1 τ_M, and so on, typically for 100 time steps. An appropriate time step for the calculations must be small enough to give accurate numerical results. We therefore adopt a value of τ_M given by the basal temperature and a stress σ of 5×10^8 Pa. Actual values of τ_M in the model vary

with stress across the grid and with time, increasing by several orders of magnitude as the stresses relax. The effective viscosity also varies in time and space; stresses from the previous time step (or the initial elastic response in the case of the first time step) are used to estimate the effective viscosity at each time.

The finite element model was tested by comparing the predicted stresses and velocities to those from an analytic solution for one-dimensional (infinitely long, inclined slab) gravitational spreading [Smrekar and Phillips, 1988]. For finite element simulations with both Newtonian and power law, temperature-dependent rheologies, a lower boundary fixed in the vertical and horizontal directions, and side boundaries free in the vertical and horizontal directions, the predictions of the finite element models away from the sides of the grid agree very well with the analytic solutions.

The Mohr-Coulomb criterion for basalt [Handin, 1966] is used to predict failure within each element. The orientation of the principal stresses with respect to the surface determines the type of faulting [Anderson, 1951]. Stresses in our models are not adjusted in response to predicted failure. The horizontal strain is found by comparing element dimensions before and after deformation.

The effects of topographic slope, plateau height, thermal gradient, and crustal thickness on the timing of faulting and the relaxation of relief are evaluated by constructing models with a range of values for these parameters. The ranges of slope (1-30°) and plateau or mountain belt height (1-6 km) correspond to those observed in Ishtar Terra. Scaling the heat flux from Earth to Venus using the planet mass provides an estimate of the average thermal gradient of 10-25 K/km [Kaula and Phillips, 1981; Solomon and Head, 1982; Phillips, 1990]. Most models are run for a thermal gradient of 15 K/km. We include some models with a thermal gradient
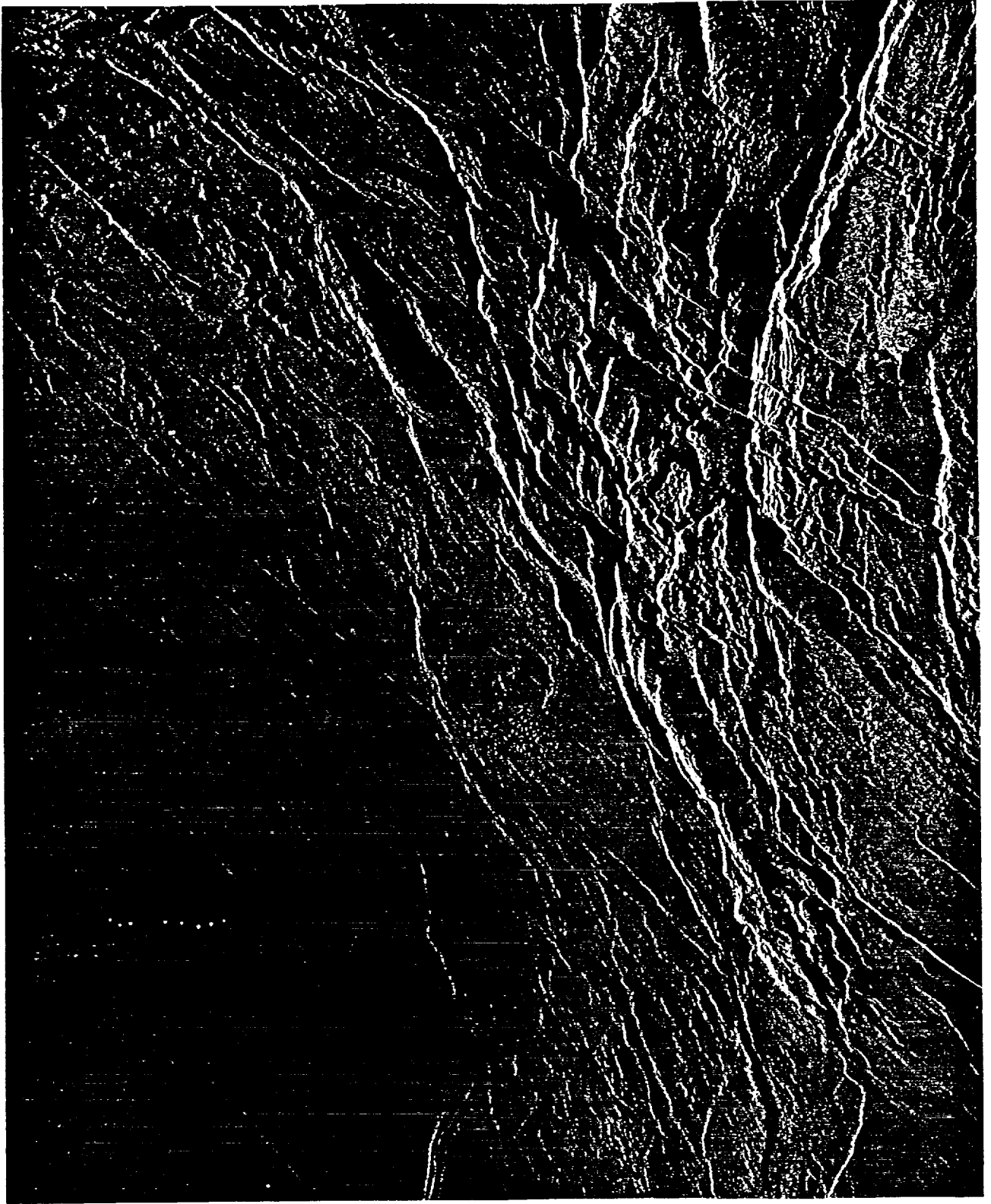
Fig. 10. Radar image of a portion of Freyja Montes. The contoured altimetry and an altimetric profile for this area are given in Figure 6. The northwest trending graben set is approximately perpendicular to the general trend of the topographic slope and represents the latest stage of deformation.

Fig. 11a. Radar image of the central portion of Akna Montes. Northwest trending graben crosscut the northeast trending folds and thrusts of the mountain belt.
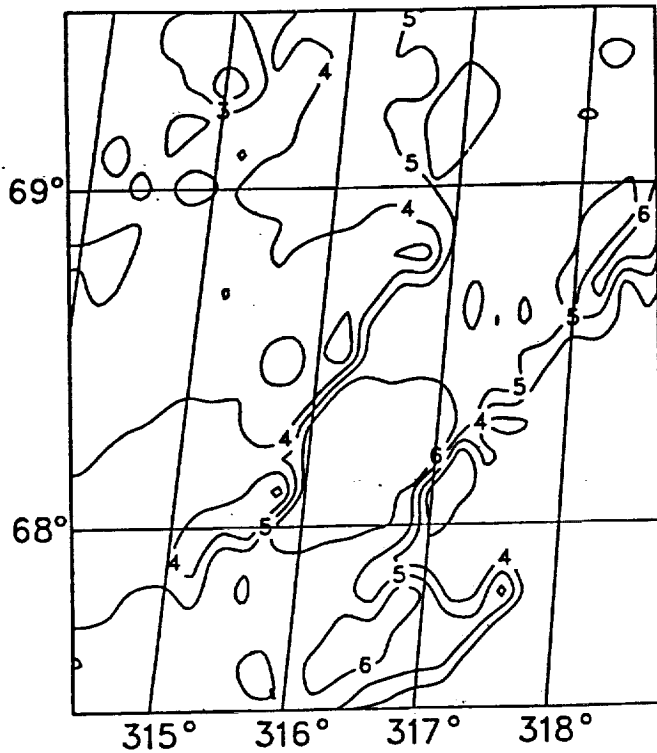
Fig. 11*b*. Contoured altimetry of the central portion of Akna Montes shown in Figure 11*a*.

of 25 K/km, as well as ones with a thermal gradient of 5 K/km to represent the possibility of lower than average heat flow. The range of crustal thicknesses (10-30 km) beneath the plains is consistent with studies of viscous relaxation of impact craters [*Grimm and Solomon*, 1988] and models for the formation of regularly spaced compressional and extensional tectonic features [*Banerdt and Golombek*, 1988; *Zuber and Parmentier*, 1990].

We first present two examples, and then we consider some general results for cases with a range of crustal thickness (10-30 km), thermal gradient (5-25 K/km), plateau height (1-5 km), and scarp slope (1-30°), all under the assumption that the crustal flow law is that of diabase. Finally, we discuss results for three departures from these cases: models with a horizontally free lower boundary condition, intended to simulate a detachment; models with a horizontal velocity boundary condition imposed on one end to mimic a regional tectonic stress; and models in which the crustal flow law is that of websterite.

The history of deformation and failure associated with one model of gravitational spreading is shown in Figure 12. The model incorporates a plateau height of 3 km, a bounding scarp of slope of 3°, a plains crustal thickness of 10 km, and a plains thermal gradient of 15 K/km. The finite element grid is shown at three model times. The first predicted failure (normal faulting) occurs on the plateau and on the top of the slope at approximately 0.1 m.y. (Figure 12*b*). Failure in this model, even at subsequent times, is confined to the plateau and the top of the slope and extends to a depth of only 1 km. Although the greatest compressive principal stress in the plains is horizontal, no thrust faulting is predicted. Significant relaxation of the topography of the plateau, resulting in a decrease in the angle of the slope of the

bounding scarp, does not occur until 100 m.y. (Figure 12*c*). The finite element grid is extended under the plateau and compressed beneath the plains, a result of flow concentrated at the base of the crustal layer. At 100 m.y. the failure criterion is no longer satisfied. The horizontal surface strain increases with time as long as the topography is still relaxing; at 100 m.y. the maximum accumulated horizontal surface strain is approximately 9% and occurs in the plateau.

Failure and relaxation of relief occur much more rapidly for models with thicker crust and a higher plateau. Figure 13 shows the results from such a model with a 30-km-thick crust, a plateau or mountain belt height of 6 km, a surface slope of 30°, and a plains thermal gradient of 15 K/km. A height of 6 km (above Lakshmi Planum) and a slope of 30° are typical of western Maxwell Montes. The first failure on the plateau occurs at approximately 10^{-2} yr; the slope first fails at 10 yr. The pattern of deformation in Figure 13 is quite different from that shown in Figure 12. Failure near the surface of the plateau does not extend to the plateau edge, and failure near the surface of the scarp is at the base of the slope rather than near the top (Figure 13*b*). Thrust faulting in the plains occurs at distances of greater than approximately 40 km from the base of the scarp. The plateau has relaxed to less than 75% of its original elevation by 0.01 m.y. (Figure 13*c*). At this time normal faulting is predicted at depths of up to 3 km beneath the plateau and at depths of 1-2 km near the base of the scarp. Ductile flow, which occurs much more rapidly for thick crust than for thin crust for a given thermal gradient, is greatest at the base of the crust. The region of highest strain is localized in the bottom row of elements, with the greatest deformation occurring beneath the scarp.

The timing of predicted initial normal faulting beneath the plateau is largely controlled by the effective viscosity at the base of the crust. Figure 14 shows the time for the first failure on the plateau as a function of plateau height and crustal thickness. Increasing the crustal thickness from 10 to 20 km or from 20 to 30 km causes failure to occur at times earlier by a factor of 10^2-10^3. There is a large difference in initial failure time for plateau heights of 1 and 3 km (factor of 10^4-10^5), but no more than a factor of 10 difference in failure time for heights between 3 and 5 km. Temperature at the base of the crust increases with crustal thickness, and deviatoric stress near the base of the crust increases with both crustal thickness and plateau elevation. The nonlinear change in predicted failure time is due both to the exponential dependence on temperature and to the power law dependence on deviatoric stress of the effective viscosity.

Crustal thickness and plateau height have similar effects on the timing of initial failure on the scarp. Predicted first failure on the scarp always occurs at the same time as, or somewhat later than, failure on the plateau. Typically, for 10-km-thick crust, failure on the plateau and scarp are simultaneous. For 20- or 30-km-thick crust, the time of first failure on the scarp can lag behind that on the plateau by up to a factor of 10^3. In a few cases, no failure occurs on the scarp, even though failure is predicted on the plateau.

The effect of the slope of the scarp was also studied by comparing cases with a plateau height of 3 km, crustal thicknesses of 10, 20, and 30 km, and slopes of 1°, 3°, 10°, and 30°. For crust of 10 to 20 km thickness, the effect is
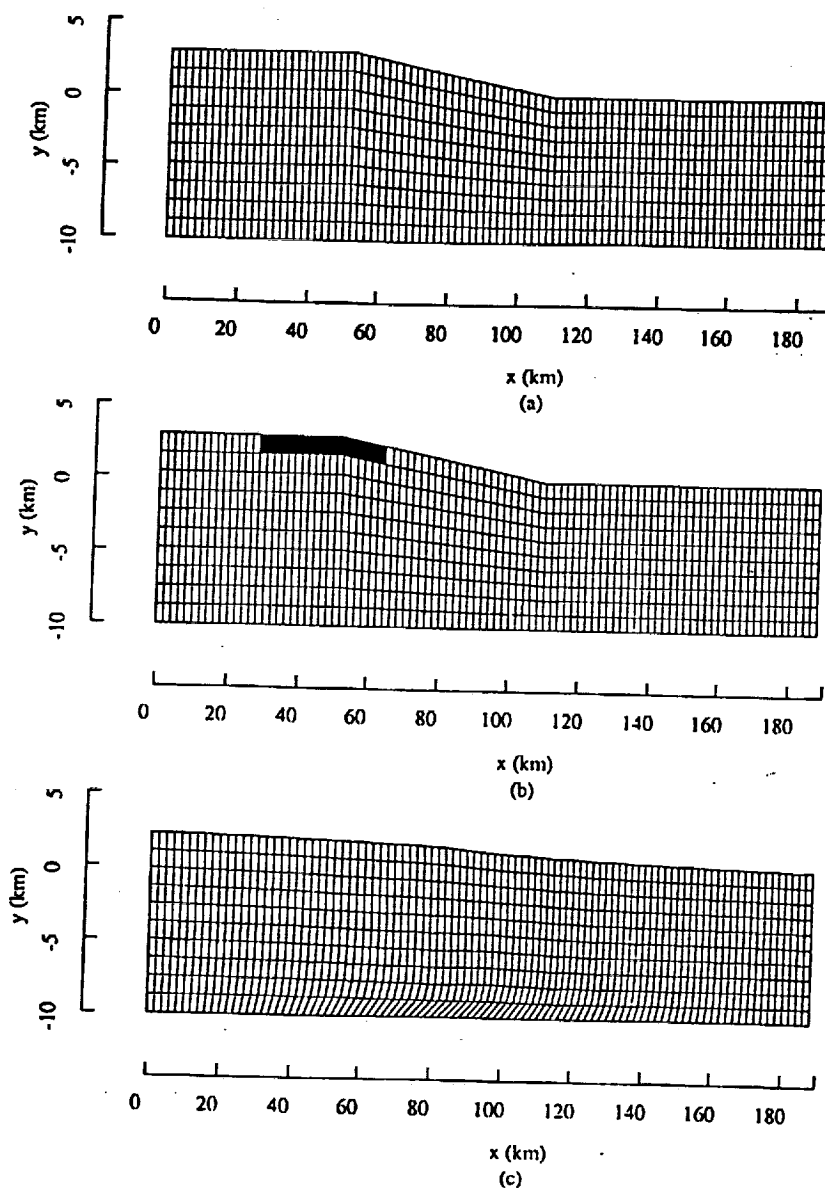
Fig. 12. (a) Initial finite element grid for a model with a plateau elevation of 3 km, a bounding scarp of slope 3°, a crustal thickness beneath the plains of 10 km, and a thermal gradient in the plains of 15 K/km. The vertical exaggeration is 4:1; the elements are 1 km high and 2 km wide. (b) Grid at approximately 0.1 m.y. Elements predicted to have failed are shaded. All predicted failure in this model is extensional. (c) Grid at approximately 100 m.y. The plateau elevation has decreased by approximately 25% from its initial value.

small. For a 1° slope, failure on the plateau is predicted to occur up to a factor of 10 later than for a slope of 3°. Increasing the slope up to 30° does not have a significant effect on initial failure times. For a 30-km-thick crust, the effect of scarp slope, however, is much more pronounced. Increasing slope from 1° to 3° results in a decrease in predicted initial failure time by a factor of 10^3. Between 3° and 10° slope and between 10° and 30° slope, the decreases are factors of 10.

Failure by thrust faulting in the plains is predicted in some cases with plains crustal thicknesses of 20-30 km and plateau heights of more than 1 km. For a given thermal gradient, predicted thrust faulting occurs earlier for larger crustal thickness and plateau height. Initial thrust faulting occurs later than first normal faulting in the plateau by a factor of 10^3-10^4, typically not occurring until the topography begins to relax significantly. In all cases, thrusting occurs at

distances of at least 20-50 km from the base of the scarp and only within the upper 1 km of the plains crust. The width of the zone of predicted thrusting is likely to be controlled by the width of the plains in the model, as thrusting typically continues to the edge of the model.

The accumulated horizontal strain at the surface at the time of predicted first failure is quite low, typically 0.01%. The horizontal strain remains small until the topographic relief begins to relax significantly; strain is approximately 1-25% when the topography has relaxed by 25%. Strain is most strongly affected by crustal thickness, with thinner crust resulting in higher strain. Strain increases typically by a factor of 3-10 for a decrease in crustal thickness from 30 to 10 km. As relaxation of the topographic relief occurs primarily through flow in the lower crust, with a thicker crust near-surface material is less coupled to the deformation at depth and experiences less horizontal strain. The calculated

strains may be underestimates of the actual strain that would be produced by gravitational spreading, inasmuch as the model does not explicitly include strain by faulting. Once a fault forms, deformation may proceed more readily by movement along the fault than by creating a new fault,

leading to higher strain than predicted by these continuum models.

The first predicted extensional failure in the model may not produce strains sufficiently large to be comparable to observed strains. Minimum estimates of horizontal strains
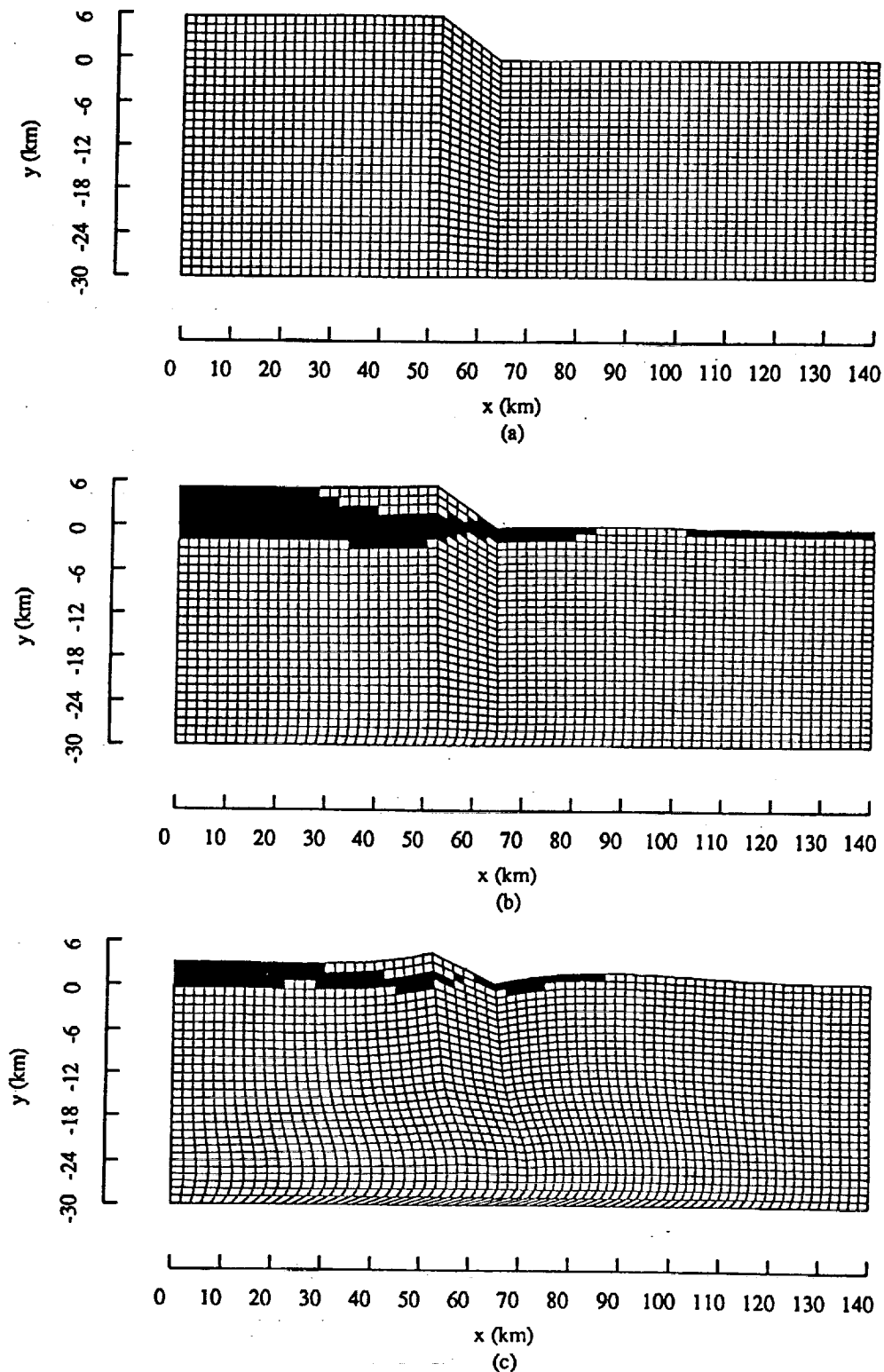
Fig. 13. (a) Initial finite element grid for a model with a plateau elevation of 6 km, a bounding scarp of slope 30°, a plains crustal thickness of 30 km, and a thermal gradient in the plains of 15 K/km. The vertical exaggeration is 2:1; the elements are 1 km high and 2 km wide. (b) Grid at approximately 100 yr. Thrust faulting is predicted in the plains farther than 40 km from the scarp. (c) Grid at approximately 10,000 yr. The plateau elevation has decreased by approximately 25%.
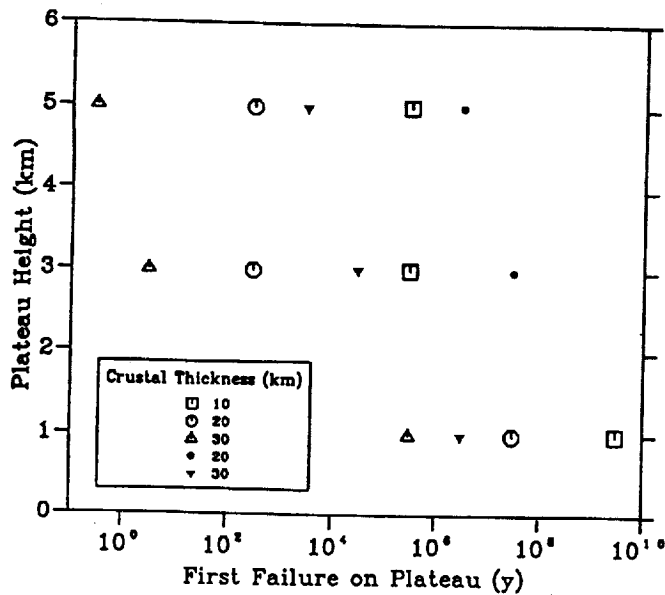
Fig. 14. The time at which failure (by normal faulting) first occurs on the plateau is shown as a function of plateau elevation for three values of plains crustal thickness. The initial slope of the scarp in each model is 3°, and the plains thermal gradient is 15 K/km. Open symbols represent models with a diabase flow law [Caristan, 1982]; solid symbols are for a websterite flow law [Avé Lallement, 1978]. All times in Figures 14-15 are given only to the nearest order of magnitude in seconds.

documented in regions of extension in Ishtar Terra are approximately 5-10%. It is unlikely that a surface strain of 0.01%, as is typical at the time of predicted initial failure, would be recognizable in the radar images as extensional faulting. A resolvable value of horizontal surface strain may be closer to 1%. The models predict that horizontal strain at the surface on the order of 1% is not produced until much later than the time of initial failure. In most cases, 1% accumulated strain at the surface occurs later than initial failure by a factor of 10^2-10^5. For a thermal gradient of 15 K/km, 1% cumulative strain is usually attained in 10^4-10^8 yr, although in some cases with a 30-km-thick crust horizontal surface strain never reaches 1%. As discussed above, the higher the effective viscosity of the crust, the higher the strain. Thus for many cases with a thermal gradient of 25 K/km, 1% horizontal strain at the surface is not reached, even though the topography relaxes significantly.

The timing of relaxation of topographic relief is primarily affected by the crustal thickness and the associated temperature at the base of the crust. The time at which the average elevation in the plateau has relaxed by at least 25% is shown as a function of plateau height and crustal thickness, for thermal gradients of 15 and 25 K/km, in Figure 15. For a given thermal gradient and crustal thickness, predicted relaxation times for plateau heights of 1, 3, and 5 km vary by a factor of 10 at most, with a decrease in relaxation time typically occurring between heights of 1 and 3 km. Typically, a model with a crustal thickness of 20 km will relax faster (by a factor of 100) than a model with a crustal thickness of 10 km. The difference in relaxation time between models with crustal thicknesses of 20 and 30 km is also a factor of 10-100; cases with higher thermal gradient tend to have larger differences. Larger differences in

relaxation time are predicted for models with the same plateau height and crustal thickness but with thermal gradients that differ by 10 K/km, as is consistent with the larger changes in basal temperature. For a thermal gradient of 25 K/km and a plateau height of 1-5 km, all the models are predicted to relax by at least 25% within 100 m.y. for a 10-km-thick crust, 0.1 m.y. for a 20-km-thick crust, and 1000 yr for a 30-km-thick crust. A thermal gradient of 15 K/km gives relaxation times of up to 1 b.y., 100 m.y., and 0.1 m.y. for crustal thicknesses of 10, 20, and 30 km, respectively. This strong dependence on temperature is because the flow is largely controlled by the lowest viscosity in the crustal column, which in turn is controlled by the basal temperature.

An interesting consequence of the relaxation of the topographic relief is the development of topographic profiles that resemble those associated with lithospheric flexure. As the relief in the plateau decreases, the plains at the base of the scarp develop a foredeep and outer rise and are predicted to fail in extension (Figure 13c).

As discussed above, detachment surfaces in regions of gravity-driven deformation on Earth develop most often in layers of soft, sedimentary rocks. Detachment surfaces in crystalline rocks, however, are also known in such structures as thrust belts and metamorphic core complexes [Armstrong and Dick, 1974; Bhattacharya, 1987; Miller et al., 1983]. Although not well understood, mechanisms such as strain softening [Schmid, 1983] are thought to be important in reducing the strength within the detachment zone and localizing deformation. To simulate a weak detachment surface, we use a lower boundary condition that is free in the horizontal direction and fixed in the vertical direction.

Predicted failure times are strongly influenced by the horizontally free lower boundary condition, with failure on the plateau occurring at times earlier by a factor of 10^3-10^6 than those shown in Figure 14. The difference in predicted initial failure time between the horizontally free and fixed lower boundary conditions is least for those cases with a thick crust and high plateau. For these cases, the low viscosity region at the base allows deformation to occur rapidly even with a fixed lower boundary. Differences in the time of significant relaxation of relief between models with different lower boundary conditions are less than for initial failure time. With a horizontally free lower boundary, 25% relaxation of the initial plateau elevation occurs either at the same time as or earlier by as much as a factor of 100 than for models with a fixed lower boundary. Thus if a weak detachment does develop at depth, the times for initial failure and relaxation shown in Figures 14 and 15 will be overestimates.

Regional tectonic forces can strongly influence the time scale of gravitational spreading. To simulate a regional force opposing gravitational spreading, the boundary condition at the plains end of the finite element grid was modified to include a vertically uniform horizontal velocity directed toward the plateau. To avoid failure of the finite element code due to excessive changes in the shape of individual elements, we use a lower boundary condition that is free in the horizontal condition. Two cases were considered. The first included a 20-km-thick crust, a plains thermal gradient of 15 K/km, a plateau height of 3 km, and a scarp slope of 3°; the second included a 30-km-thick crust, a thermal gradient

of 15 K/km, a plateau height of 6 km, and a scarp slope of 30°. Initial extensional failure develops as it would if the velocity boundary condition were zero. In time, however, the shortening induced by a nonzero boundary velocity overcomes the extension driven by the topographic relief, and failure is predicted to occur only by thrust faulting. For both cases, a boundary velocity of 100 mm/yr will prevent gravitational spreading after a period of approximately 10^4 yr. If the velocity is significantly less than this value, there will be little change in the gravitational spreading on geologic time scales from models without an imposed velocity boundary condition.

In a final set of models we incorporated the websterite flow law of *Avé Lallement* [1978] and *Carter and Tsenn* [1987] to simulate a crust much stiffer than would be given by the flow law for diabase. For a fixed lower boundary condition and the same ranges of crustal thickness, thermal gradient, and plateau height, initial failure is predicted to occur later, typically by a factor of 10^4-10^5, than in similar models with a diabase flow law (Figure 14); failure times for thin crust or a low plateau differ by much less (Figure 14). Times for significant relaxation of relief are also much different for a websterite rheology than a diabase rheology. For the same parameter ranges as the cases shown in Figure 15, none of the models with the websterite flow law approached 25% relaxation within 1 b.y. Even with a thermal gradient of 25 K/km, only those models with a crustal thickness of 30 km reached 25% relaxation in 100 m.y. to 1 b.y.

DISCUSSION

The models presented in this study indicate that gravitational spreading is likely to occur in most of the high terrain of Ishtar Terra, on time scales less than the average crater retention age of Venus, for observed values of topographic slopes and elevations and likely values of
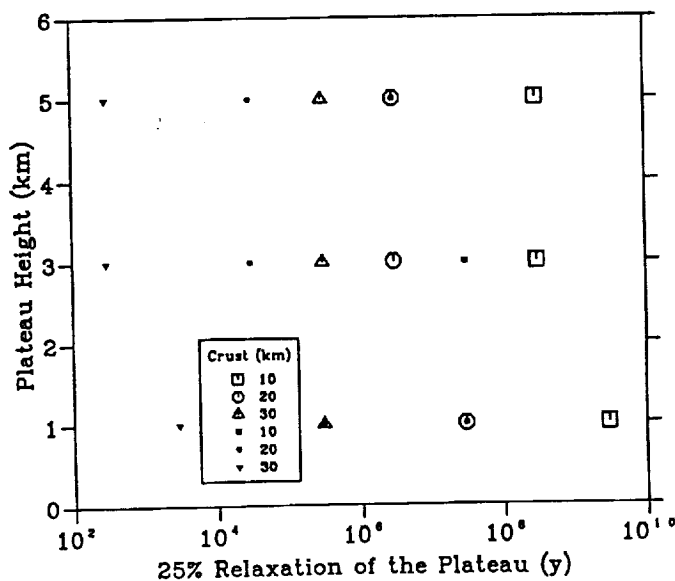

Fig. 15. The time at which the height of the plateau has relaxed by 25% is shown as a function of plateau height for three values of plains crustal thickness. The initial slope of the bounding scarp is 3°. The open symbols are for a plains thermal gradient of 15 K/km; solid symbols are for a thermal gradient of 25 K/km.

crustal thickness and thermal gradient. This result implies that regions of high elevation either have anomalously cold, strong crust or were recently (or are currently) subject to regional tectonic forces that are greater than those driving gravitational spreading. In the former case, this study provides a lower bound on the strength of the crust. In the latter case, the models predict the time period over which high topography has been relaxing. To constrain the rheology or the duration of gravitational spreading, we must make some assumptions about the age of Ishtar Terra and the possible degree of relaxation of the topography. As discussed above, the absolute age of the surface of Ishtar Terra is quite uncertain. As a basis for discussion, we consider ages of 50-500 Ma; the former is the surface age in the northern 25% of the planet derived from a terrestrial impactor flux rate [*Schaber et al.*, 1987], and the latter is the average crater retention age for the planet if the rate of crater production is scaled from the lunar impactor flux rate [*Phillips et al.*, this issue]. As the elevation of Ishtar Terra is much higher than for most of Venus and scarp slopes are generally large, we also make the assumption that the topography has not relaxed significantly. Specifically, we examine model predictions for 25% relaxation of the initial relief. Given that our models may underestimate surface strain, it is reasonable to assume that observable strain will accumulate by the time 25% relaxation of the topography occurs.

Age Constraints

If the crust in Ishtar Terra is not anomalously strong relative to predictions from laboratory measurements on diabase, then regional tectonic forces are likely to have acted to maintain or enhance topographic slope within the last 10^7-10^8 years. For most of the regions where gravitational spreading is believed to have occurred, the relief is approximately 2-3 km; at Maxwell Montes, 5-6 km is a better approximation. For a thermal gradient of 15 to 25 K/km, only those cases with a crustal thickness of 10 km require times of the order of 10-100 m.y. to relax by 25% (Figure 15). For a thermal gradient of 15 K/km, those cases with a 20-km-thick crust relax in less than 10 m.y.; those with a 30-km-thick crust relax in less than 1 m.y. For a thermal gradient of 25 K/km, cases with a 20- or 30-km-thick crust relax within 1 m.y. Almost all cases require 100 m.y. or more to relax by 25% for a thermal gradient of 5 K/km. Thus for thermal gradients of at least 15 K/km and crustal thicknesses greater than 10 km, our models predict 25% relaxation within several million years.

Given the high topography (up to 10 km of relief at Maxwell Montes) and steep slopes, it is likely that some crustal thickening has occurred and that the crustal thickness exceeds 10 km in many areas of Ishtar Terra. The overlap of volcanism and extension in many areas of Ishtar Terra also suggests that the thermal gradient is unlikely to be as low as 5 K/km. Thus the time scales for relaxation imply that orogeny in many areas of Ishtar Terra is likely to have continued until at least several million years ago.

The presence of extensional faulting does not necessarily imply that regional tectonic forces are no longer active. On Earth, episodes of shortening and extension are believed to overlap in time. Examples of this process of

contemporaneous shortening and extension have been documented in the Andes and in the Himalayas. Regional compressional forces act to increase the topographic height and slope to the point where gravitational spreading forces are able to balance the tectonic forces. Once spreading has occurred, the regional compressive forces may again be dominant. In Ishtar Terra examples of apparently contemporaneous extension and shortening are found in Danu, Freyja, and Akna montes (see Figures 7, 10, and 11a, respectively).

Rheological Constraints

Conversely, if we assume that the age of the topography in Ishtar Terra is at least 50 Ma and that no regional tectonic forces have opposed gravitational spreading during that time, then the time scales for relaxation of the topography provide a constraint on the crustal thickness and strength. Topography in Ishtar Terra will not relax by more than 25% over several tens of millions of years if the temperature at the base of the crust is less than approximately 1000 K for a diabase flow law. This temperature corresponds to an effective viscosity at the base of the crust of approximately 10^{11} Pa s^{-1}. For thermal gradients of 15 and 25 K/km, the crust must be 10 km or less in thickness (see Figure 15). Crustal thicknesses of 20-30 km will not relax in several tens of millions of years if the thermal gradient is as low as 5 K/km. As there is evidence for probable gravitational spreading in Ishtar Terra, a maximum time of several billion years for significant relaxation of relief provides an upper bound on the strength of the crust. For 25% relaxation to occur within several billion years, the temperature at the base of the crust must be greater than approximately 880 K, corresponding to an effective viscosity of 10^{12} Pa s^{-1}. For example, a crustal thickness of 10 km and a thermal gradient of 5 K/km will not lead to relaxation on this time scale. If the strength of the crust is closer to that predicted by a websterite flow law, the temperature at the base of the crust must be near 1400 K for significant relaxation to develop within several billion years. Of those models with a websterite flow law, only those with a thermal gradient of 25 K/km and a crustal thickness of 30 km predict significant relaxation within this time scale.

Another potential rheological constraint involves the accumulated horizontal surface strain predicted to develop as the topography relaxes. As shown above, the strain is sensitive to the crustal thickness and thermal gradient, which together control how well coupled flow in the lower crust is to deformation at the surface. Models with a crustal thickness of 30 km develop surface strains that are typically about 0.1-1% at the time when relaxation reaches 25%. Thus if the topography in a region appears to have relaxed but does not exhibit evidence for extensional faulting, it may have a very thick crust. This situation may occur in mountain belts with large crustal roots. However, two factors make application of this constraint very uncertain. The first is the interpretation of predictions of horizontal surface strain by models that do not include the effects of faulting. The second is the uncertainty in the estimate of observed surface strain. This factor does not present as severe a limitation, however, as strain inferred from observations of faulting is more likely to be an underestimate than an overestimate.

Comparison With Observations

The models of gravitational spreading discussed above predict the distribution of faulting, the type and depth of faulting, the horizontal strain, and the shape of the topographic profile. All of these characteristics can be observed or estimated from Magellan altimetry and radar images. The general agreement between the strains estimated from the images and those predicted by the models was discussed above. The models predict that regions of high slope (~10°) will fail first through normal faulting at the base of the slope, while scarps of lower slope will fail first at the top (Figures 12 and 13). In most of the areas of extensional faulting in Ishtar Terra, such simple relationships are not seen. However, in a few areas where extension constitutes the only apparent tectonic activity, the relationship predicted by the models appears to hold. The best example is the southeastern scarp of Lakshmi Planum (Figure 4) along the northwest trending limb of the scarp, which has an average slope of 8°. Downslope extensional strain is visible at the base of the scarp, on the scarp, and at the top of the plateau. Along the northeast trending limb of the scarp, the average slope is approximately 3°, and lineations interpreted as possible normal faults occur only at the top of the scarp.

At the base of the scarps along the southern and southeastern margins of Lakshmi Planum there are frequent sets of long, narrow, anastomosing ridges (e.g., Figures 2a and 4a), which we interpret to indicate crustal shortening of modest magnitude. This type of low-strain, compressional deformation at shallow depths is predicted by the models to occur at distances at least 20-30 km from the base of the scarp. Although these ridges sometimes occur somewhat closer to the base of the bounding scarp of Lakshmi Planum than this range (Figure 4a), their positions and strains are broadly consistent with model predictions.

The range of predicted depths of extensional faulting is 1-10 km beneath the plateau, 1-3 km beneath the scarp, and 1-3 beneath the base of the scarp. Greater plateau elevations and crustal thicknesses result in greater depths of faulting beneath the plateau. The average spacing between normal faults in Ishtar Terra is 1 to 15 km. A greater depth extent of surficial normal faulting would be expected to be reflected in a greater spacing between faults, although this relationship can be complicated by such effects as listric faulting. A general rule of thumb is that the depth extent of faulting is equal to the characteristic fault spacing divided by 2π. This rule gives a depth extent of approximately 0.1 to 2 km. Given the uncertainties in this general rule, this range is in general agreement with the model predictions.

The importance of gravitational spreading on Venus has previously been discounted on the basis of an expected failure pattern which includes a breakaway fault at the top of a slope, extensional faulting on the slope, and shortening at the base of the slope [Bindschadler and Head, 1991]. While such relationships are observed for gravitational spreading in soft sedimentary rocks on Earth [Pederson, 1987], the models in this study do not display this pattern of deformation. Ductile flow at depth does bear some resemblance to a décollement, but strain at the surface remains small. For the cases considered here, lower crustal flow does not lead to a breakaway fault, as surface strains are low and the zone of faulting does not extend to depths of significant flow.

However, in cases where flow extends over much greater distances, it is possible that strains would be sufficient for a breakaway fault to be produced. A breakaway fault has not yet been identified in the Magellan radar images; however, such a fault might be difficult to discern.

As noted above, as the topography relaxes the plateau margin develops a profile resembling that of a flexural bulge. A good example of such profile is observed along the southeastern scarp of Lakshmi Planum (Figure 4c). This profile may reflect upwarping of the plains in response to partial viscous relaxation of the plateau edge. The extensional faulting observed in this area may be due to the upwarping. Profiles which resemble flexural profiles are found in many areas of Venus. In Ishtar Terra, examples are found outward of Uorsar Rupes to the north of Freyja Montes, at western Maxwell Montes, and at eastern Akna Montes [Solomon et al., this issue]. Similar topographic profiles are often found exterior to coronae [Stofan et al., this issue]. Solutions for the elastic or mechanical lithospheric thickness in these regions sometimes greatly exceed expected values for Venus [Sandwell and Schubert, this issue].

As a basis for comparison with estimates of the thickness of the elastic lithosphere derived elsewhere on Venus from topographic profiles assumed to be the result of lithospheric flexure, we fit the topographic profile for the plains portion of our models to the analytical solution for flexure resulting from the superposition of a bending moment applied to the end of a broken elastic plate and a line load on a continuous elastic plate [Sandwell and Schubert, this issue]. An elastic plate thickness of approximately 10 km fits the profile shown in Figure 13c with a root-mean-squared error of 25 m. This value of elastic plate thickness should not be compared directly with values obtained by fitting actual topographic profiles, because our models do not include the effect of deformation in the mantle. Ductile flow of the lithosphere on Venus may be an important process for modifying topography, however, and can lead to profiles similar to those arising from elastic flexure.

Comparison With Gravitational Spreading on Earth

Active gravitational spreading in southern Tibet occurs in the form of approximately 15-km-wide, north-south trending graben with a typical spacing between sets of faults of 200 km. The estimated surface strain in this 1100-km-wide area is 1% [Armijo et al., 1986]. In the Andes, extension occurs across a 400-km-wide area, where fault spacing is approximately 1-20 km; surface strain is also estimated to be 1% [Sebrier et al., 1985]. In contrast, extension in Ishtar Terra is confined to areas not more than 200 km across, and estimated strains are greater, in the range of 5-15%. Average graben widths (1-10 km) and spacings (5-20 km) are comparable to those in the Andes but somewhat less than those in the Himalayas. The greater surface strains on Venus may be a result of a lesser crustal thickness.

Additional Effects

Several effects not included in this study may also influence the process of gravitational spreading. The surface temperature in the mountains is lower than the temperature of 740 K used in this study, as the atmospheric temperature decreases by 7.7 K/km with increasing altitude [Seiff, 1983]. Areas considered in this study have elevations up to 8 km above the mean planetary radius, corresponding to a decrease in temperature of up to 60 K. Although we did not specifically incorporate this difference, the effect is mimicked to some degree because the temperatures at the base and at the surface of the crust are the same under the plateau as under the plains in our models, giving a lower thermal gradient in the plateau. If modeled explicitly, the lower surface temperature would probably result in slightly longer times for predicted initial failure and lower surface strains. However, as discussed above, the temperature at the base of the crust is the primary variable controlling the rate of deformation.

The nature of the compensation of the topography is likely to have a major effect on gravitational spreading. In the models of this study, the topography is not compensated, and no flow occurs deeper than the base of the crust. The long-wavelength topography (>2000 km) of Ishtar Terra has an apparent depth of compensation of 180 km [Grimm and Phillips, 1991], but no information is available on shorter wavelengths. For comparison, the models in this study have horizontal dimensions ranging from 140 to 300 km. Such short-wavelength topography in Ishtar Terra may be isostatically compensated or maintained partly by regional tectonic stresses arising from mantle convection. Flexure is likely to be important at even shorter wavelengths than those considered here.

Compensation of topography by Airy isostasy would lead to shorter times of initial failure and significant relaxation of relief for most of the cases considered. For a crustal density of 3000 kg/m^3 and a mantle density of 3300 kg/m^3, an elevated region is balanced by a crustal root of thickness 10 times that of the excess elevation. Thus, for cases with a 1-km-high plateau, crustal compensation might occur at depths within the range considered (10-30 km), depending on crustal thickness. Higher elevations that are completely compensated by crustal thickness variations would have roots that extend to depths greater than 30 km. The higher temperature at the base of a deep crustal root would lead to more rapid relaxation, if the region is in thermal equilibrium with surrounding areas.

The effect of dynamic compensation is less clear, as the stress field and crustal thickness evolve with time. Mantle upwelling or downwelling may be responsible for compensating the long-wavelength topography of Ishtar Terra and may indirectly compensate shorter-wavelength variations in the topography by inducing variations in stress that can result in differences in crustal thickness. Mantle downwelling beneath a weak crust can produce crustal thickening [Bindschadler and Parmentier, 1990; Lenardic et al., 1991]. Mantle upwelling is typically expected to thin the crust, but if lateral heterogeneities in lithospheric strength are present, crustal thickening over limited regions is also possible [Grimm and Phillips, 1991]. Generation of new crust by partial melting above a zone of upwelling may also increase the crustal thickness [Phillips et al., 1991b]. Thus both upwelling and downwelling models call on crustal thickening to produce the observed topography in Ishtar Terra. Further, the inclusion of stresses due to dynamic processes would require a larger-scale model than considered in this study.

Kiefer and Hager [1991] present a one-dimensional model of gravitational spreading that includes a bottom velocity condition meant to simulate traction on the base of the crust due to mantle downwelling beneath Ishtar Terra. By balancing the flux out of the region due to gravitational spreading, for a fixed topographic slope and elevation, with the flux into the region specified by the bottom boundary condition, they find the bottom velocity that will lead to no net flux. Their results show that for parameters appropriate for the Fortuna Tessera region and basal velocities in the range of 0-500 mm/yr, only anomalously thick or anomalously cold crust will fail to undergo gravitational spreading. Although their model is a steady state calculation, and thus not easily comparable to results from this study, it does suggest that gravitational spreading is possible even in the presence of mantle downwelling.

Incorporating a mantle layer into the study would probably change the results somewhat, even if convection does not contribute significantly to the stress field. *Kruse et al.* [1991] considered the problem of stresses due to high topography in conjunction with regional extension. They found that allowing flow in a mantle layer to accommodate deformation of a crust-mantle boundary caused the crust to thicken beneath extensionally thinned areas at rates 30-50% slower (for crustal thicknesses of 10-30 km) than for the case where a rigid lower crustal boundary was assumed. The results of *Kruse et al.* [1991] may not be directly applicable to Ishtar Terra because they were obtained for constant-viscosity layers in an extensional stress field and for lower temperatures than those appropriate for the crust of Venus, but they do suggest that including the effect of mantle flow would result in somewhat lower relaxation rates than found in this study.

Implications for the Tectonic History of Ishtar Terra

This study indicates that two quite distinct possibilities exist for Ishtar Terra: either the crust is anomalously strong and no regional tectonic forces are required to support the topographic relief or tectonic forces have continued to build the topography and steepen slopes until geologically recent time. Crater retention ages, gravity data, and the relationship between volcanism and tectonism provide independent information.

As discussed above, an absolute surface age for Ishtar Terra is quite uncertain. Crater retention ages are meaningful only for areas much larger than even the large-scale tectonic features of Ishtar Terra [*Plaut and Arvidson*, 1988; *Phillips et al.*, 1991a, this issue]. Geologic information about the surface age is unclear. The 105-km-diameter crater, Cleopatra, in Maxwell Montes is a particularly obvious example of an undeformed impact structure in a region of very high topography [*Phillips et al.*, 1991a]. However, other impact structures in the region have experienced tectonic modification (e.g., extension across the crater visible in Figure 10). As surface strain associated with gravitational spreading is small, this type of deformation may not be very efficient at reducing the crater population or even substantially modifying crater shapes. Thus the estimates of the age for Ishtar Terra and the surrounding region may not provide a strong constraint on the recency or duration of gravitational spreading.

As noted earlier, gravity data for Ishtar Terra indicate that the long-wavelength topography is dynamically supported in the mantle [*Grimm and Phillips*, 1991]. Dynamic compensation, however, does not specifically rule out the possibility of cold crust. Downwelling might have led to thickened, initially cold crust; eventually, however, the crust will equilibrate to more typical temperatures.

A low temperature at the base of the crust in Ishtar Terra may not be consistent with the extent and timing volcanism found in the region. In areas where pits, pit chains, and collapse features overlap with graben and extensional faulting, the volcanism appears to be contemporaneous with gravitational spreading. Of the regions of extensional faulting described in this study, the evidence for volcanism is least strong for Freyja Montes and northern and southern Maxwell Montes. One interpretation is that the crust is anomalously cool and strong because of recent shortening in these regions.

Last, we must also consider the possibility that because the crust on Venus may be extremely dry, the lower crust is much stiffer than indicated by the laboratory flow law obtained for diabase [*Caristan*, 1982]. As demonstrated by models with a websterite flow law, if the rheology is much stiffer, high elevations with moderate crustal thicknesses and thermal gradients might support gravitational stresses for periods of up to several billion years. However, this possibility raises the question of why Ishtar Terra is the only region of extremely high topography preserved over the geologic history of Venus. Under the assumption that gravitational spreading and viscous relaxation of high terrain have been important processes in the recent geologic history of Venus, Ishtar Terra represents a variation on landforms observed elsewhere on the planet. Gravitational spreading is also believed to part of the evolutionary sequence of tesserae and coronae [*Bindschadler et al.*, this issue; *Squyres et al.*, this issue]. One implication of a very stiff crust on Venus would be that the crust could be thicker than previous estimates of 10-30 km.

We favor the hypothesis that many of the areas of greatest relief and steepest slopes in Ishtar Terra have recently been tectonically active. The primary evidence against this interpretation is the estimated crater retention age for Venus. We note, however, that the recency of tectonic activity does not provide a means to distinguish among the major competing hypotheses for the origin of Ishtar Terra. High-resolution gravity data for Ishtar Terra, which are scheduled to be obtained later in the Magellan mission, should provide further constraints on plausible crustal thicknesses and dynamic compensation mechanisms.

Implications for Other Regions of Venus

Other regions of high topography are also candidates for gravitational spreading. Even areas that have relatively low relief are predicted to undergo gravitational relaxation on geologic time scales. Magellan images show evidence of extension, which is of modest magnitude and is the latest stage of deformation, in other highland and tessera terrains. At Alpha Regio, small, widespread graben cut older tectonic features, indicating that distributed extension is the youngest tectonic event [*deCharon et al.*, 1991]. Many of the graben are parallel to the edges of the elevated terrain of Alpha

Regio, suggesting that extension may be a result of gravitational spreading [Bindschadler et al., this issue]. Numerous small troughs, interpreted as graben, postdate apparently compressional features in Ovda Regio [Saunders et al., 1991] and could also result from gravitational spreading of this equatorial highland. Gravitational spreading is also thought to be an important process in the evolution of coronae on Venus [Squyres et al., this issue].

Comparison With Other Studies

In general, the time scales of viscous relaxation predicted by these models compare well with those from other studies of Venus. For example, in this study, we find that a 1-km-high plateau with a surface slope of 3°, a crustal thickness of 20 km, a thermal gradient of 15 K/km, a basal temperature of 1040 K, and a model width (plateau, scarp, and plains) of 150 km relaxes by 25% in approximately 0.1 m.y. In a study of viscous relaxation of impact craters on Venus, Grimm and Solomon [1988] found that the relief for a 140-km-diameter crater would be nearly completely relaxed within 50 m.y., given a 15-km-thick diabase crust over an olivine-rich mantle and a thermal gradient of 15 K/km. Our results are also in general agreement with one-dimensional models of gravitational spreading on Venus, which show that viscous deformation can occur at geologically significant strain rates [Weertman, 1979; Smrekar and Phillips, 1988]. One would expect viscous relaxation on Earth to proceed more slowly than on Venus for a given rheology because of the difference in surface temperature. However, in models of the relaxation of isostatically compensated topography of a given wavelength, Bird [1991] found that relief with an amplitude of 1 km (2 km total relief), a 35-km-thick crust with ductile strength given by a diabase flow law, a horizontal wavelength of 100 km (surface slope ~2°), and a basal temperature of 980 K relaxed by 50% within 2000 yr. This time scale for relaxation is shorter than would be predicted by our models for comparable length scales but higher surface temperature, probably because Bird [1991] included crustal compensation and had a very different model formulation.

CONCLUSIONS

Magellan radar images display abundant evidence for extensional faulting in regions of high elevation and steep topographic slope within Ishtar Terra. We interpret extensional faults oriented generally perpendicular to the downslope direction to be a result of gravitational spreading. Extensional faults that are parallel to the apparent direction of shortening in mountain belts are interpreted as evidence for gravitational spreading within an actively converging orogen. Regions of likely gravitational spreading occur in all of the mountain belts surrounding Ishtar Terra and on the plateau margins of Lakshmi Planum. Horizontal surface strains in these areas are estimated to be 1-20%.

Volcanism is associated with many of these areas of extensional faulting, particularly along the margins of Lakshmi Planum and in Danu Montes. Extensional faulting cuts older folds and thrust faults in Danu, Akna, Freyja and southern Maxwell montes. In Akna, Danu, and Freyja montes, some of the extensional faults have been deformed by later shortening and possibly horizontal shearing, suggesting that extension occurred before the mountain-forming process was complete.

Finite element modeling of the gravitational spreading of high topography by flow in the lower crust shows that failure and relaxation of relief occur on geologically rapid time scales for likely estimates of crustal thickness and thermal gradient. The pattern of predicted failure is consistent with the observations in Ishtar Terra, in that the cumulative horizontal surface strains are low. Extensional faulting is predicted to occur first on the plateau, followed by extension on the slope, and sometimes by thrusting in the plains. Initial failure occurs typically within 0.1 m.y., for a thermal gradient of at least 15 K/km. However, an accumulated horizontal strain of 1%, which is a more plausible threshold for observability in Magellan radar images, does not occur typically until 0.01-100 m.y. A thermal gradient of 5 or 25 K/km shifts the time scales somewhat.

Viscous relaxation of relief is also predicted to occur rapidly. The rates of relaxation depend strongly on the temperature (and thus the effective viscosity) at the base of the crust, as relaxation occurs primarily through flow in the lower crust. For a range of plateau elevations and scarp slopes, relaxation of the topographic relief by 25% occurs within 10^5, 10^8, or 10^{10} yr for crustal thicknesses of 30, 20, or 10 km, respectively, and a thermal gradient of 15 K/km. A thermal gradient of 25 K/km gives relaxation times that are shorter by up to a factor of 10^3; a thermal gradient of 5 K/km gives relaxation times that are larger by a factor of $10-10^4$.

These results indicate that the topographic relief in Ishtar Terra either is supported by crust considerably stronger than indicated by standard flow laws for terrestrial crustal materials, or has been built and maintained by tectonic forces until times less than millions to tens of millions of years. Although an average crater retention age for the high northern latitudes on Venus of 50 Ma to 1 Ga [Ivanov et al., 1986; Schaber et al., 1987; Basilevsky et al., 1987] and an average crater retention age of 500 Ma for the entire planet [Phillips et al., 1991a, this issue] tend to favor the interpretation that the area is comparatively strong and inactive, this age may not be applicable to such small areas as mountain belts and plateau margins. Evidence for widespread volcanism, which appears to be concurrent with extension in many locations, particularly in Lakshmi Planum, may be inconsistent with an anomalously cold crust. The large apparent depth of compensation at Ishtar Terra indicates that the long-wavelength topography is probably dynamically supported [Grimm and Phillips, 1991] and suggests a ready mechanism for recent crustal deformation. In the mountain belts, even partial isostatic compensation by a crustal root would result in crustal thicknesses greater than the largest value used in this study (30 km) and would yield an even more rapid relaxation of relief than obtained here. We therefore favor the hypothesis that regional deformation in the mountain belts and steep plateau margins of Ishtar Terra is geologically young (less than 10 m.y.) and may be ongoing.

REFERENCES

Anderson, E. M., The Dynamics of Faulting and Dyke Formation with Applications to Britain, 2nd ed., 206 pp., Oliver and Boyd, Edinburgh, 1951.

Armijo, R., P. Tapponnier, J. L. Mercier, and Han T. L., Quaternary extension in southern Tibet: Field observations and tectonic implications, J. Geophys. Res., 91, 13,803-13,872, 1986.

Armstrong, R. L., and H. J. B. Dick, A model for the development of thin overthrust sheets of crystalline rock, Geology, 1, 35-40, 1974.

Arvidson, R. E., V. R. Baker, C. Elachi, R. S. Saunders, and J. A. Wood, Initial analysis of Venus surface modification, Science, 252, 270-275, 1991.

Arvidson, R. E., R. Greeley, M. Malin, R. S. Saunders, N. Izenberg, J. J. Plaut, E. R. Stofan, and M. Shepard, Surface modification of Venus as inferred from Magellan observations of plains, J. Geophys. Res., this issue.

Avé Lallement, H. G., Experimental deformation of diopside and websterite, Tectonophysics, 48, 1-27, 1978.

Banerdt, W. B., and M. P. Golombek, Deformational models of rifting and folding on Venus, J. Geophys. Res., 93, 4759-4772, 1988.

Barsukov, V.L., et al., The geology and geomorphology of the Venus surface as revealed by the radar images obtained by Veneras 15 and 16, Proc. 16th Lunar Planet. Sci. Conf., Part 2, J. Geophys. Res., 91, suppl., D378-D411, 1986.

Basilevsky, B. A. Ivanov, G. A. Burba, I. M. Chernaya, V. P. Kryuchkov, O. V. Nikolaeva, D. B. Campbell, and L. B. Ronca, Impact craters of Venus: A continuation of the analysis of data from the Venera 15 and 16 spacecraft, J. Geophys. Res., 92, 12,869-12,901, 1987.

Bhattacharya, A. R., A 'ductile thrust' in the Himalaya, Tectonophysics, 135, 37-45, 1987.

Bindschadler, D. L., and J. W. Head, Tessera terrain, Venus: Characterization and models for origin and evolution, J. Geophys. Res., 96, 5889-5908, 1991.

Bindschadler, D. L., and E. M. Parmentier, Mantle flow tectonics: The influence of a ductile lower crust and implications for the formation of topographic uplands on Venus, J. Geophys. Res., 95, 21,329-21,344, 1990.

Bindschadler, D. L., A. deCharon, K. K. Beratan, S. E. Smrekar, and J. W. Head, Magellan observations of Alpha Regio: Implications for formation of complex ridged terrains on Venus, J. Geophys. Res., this issue.

Bird, P., New finite element techniques for modeling deformation histories of continents with stratified temperature-dependent rheology, J. Geophys. Res., 94, 3967-3990, 1989.

Bird, P., Lateral extrusion of lower crust from under high topography, in the isostatic limit, J. Geophys. Res., 96, 10,275-10,286, 1991.

Braun, J., and C. Beaumont, Contrasting styles of lithospheric extension: Implications for differences between the Basin and Range province and rifted continental margins, in Extensional Tectonics and Stratigraphy of the North Atlantic Margins, edited by A. J. Tankard and H. R. Balkwill, AAPG Mem., 46, 53-79, 1989.

Burchfiel, B. C., and L. H. Royden, North-south extension within the convergent Himalayan region, Geology, 13, 679-682, 1985.

Caristan, Y., The transition from high temperature creep to fracture in Maryland diabase, J. Geophys. Res., 87, 6781-6790, 1982.

Carter, N. L., and M. C. Tsenn, Flow properties of continental lithosphere, Tectonophysics, 136, 27-63, 1987.

Crumpler, L. S., J. W. Head, and D. B. Campbell, Orogenic belts on Venus, Geology, 14, 1031-1034, 1986.

deCharon, A. V., D. L. Bindschadler, K. K. Beratan, and J. W. Head, Geology of Alpha Regio, Venus from Magellan data (abstract), Lunar Planet. Sci., 22, 287-288, 1991.

Dewey, J. F., Extensional collapse of orogens, Tectonics, 7, 1123-1139, 1988.

England, P., and G. Houseman, Extension during continental convergence, with application to the Tibetan Plateau, J. Geophys. Res., 94, 17,561-17,579, 1989.

Evans, B., J. T. Fredrich, and T.-f. Wong, The brittle-ductile transition in rocks: Recent experimental and theoretical progress, in The Brittle-Ductile Transition in Rocks, The Heard Volume, Geophys. Monogr. Ser., vol. 56, edited by A. G. Duba, W. B. Durham, J. W. Handin, and H. F. Wang, pp. 1-20, AGU, Washington, D.C., 1990.

Froidevaux, C., and Y. Ricard, Tectonic evolution of high plateaus, Tectonophysics, 134, 227-238, 1987.

Grimm, R. E., and R. J. Phillips, Tectonics of Lakshmi Planum, Venus: Tests for Magellan, Geophys. Res. Lett., 17, 1349-1352, 1990.

Grimm, R. E., and R. J. Phillips, Gravity anomalies, compensation mechanisms, and the geodynamics of western Ishtar Terra, Venus, J. Geophys. Res., 96, 8305-8324, 1991.

Grimm, R. E., and S. C. Solomon, Viscous relaxation of impact crater relief on Venus: Constraints on crustal thickness and thermal gradient, J. Geophys. Res., 93, 11,911-111,929, 1988.

Gudmundsson, A., Geometry, formation and development of tectonic fractures on the Reykjanes Peninsula, southwest Iceland, Tectonophysics, 139, 295-308, 1987.

Handin, J., Strength and ductility, in Handbook of Physical Constants, edited by S. P. Clark, Jr., Mem. Geol. Soc. Am., 97, 223-289, 1966.

Head, J. W., The formation of mountain belts on Venus: Evidence for large-scale convergence, underthrusting, and crustal imbrication in Freyja Montes, Ishtar Terra, Geology, 18, 99-102, 1990.

Head, J. W., R. W. Vorder Bruegge, and L. S. Crumpler, Venus orogenic belt environments: Architecture and origin, Geophys. Res. Lett., 17, 1337-1340, 1990.

Head, J. W., D. B. Campbell, C. Elachi, J. E. Guest, D. P. McKenzie, R. S. Saunders, G. G. Schaber, and G. Schubert, Venus volcanism: Initial analysis from Magellan Data, Science, 252, 276-288, 1991.

Ivanov, B. A., A. T. Basilevsky, V. P. Kryuchkov, and I. M. Chernaya, Impact craters of Venus: Analysis of Venera 15 and 16 data, Proc. Lunar Planet. Sci. Conf., Part 2, J. Geophys. Res., 91, suppl., D413-430, 1986.

Kaula, W. M., and R. J. Phillips, Quantitative tests for plate tectonics on Venus, Geophys. Res. Lett., 8, 1187-1190, 1981.

Kaula, W. M., D. L. Bindschadler, R. E. Grimm, V. L. Hansen, K. M. Roberts, and S. E. Smrekar, Styles of deformation in Ishtar Terra and their implications, J. Geophys. Res., this issue.

Kiefer, W. S., and B. H. Hager, Mantle downwelling and crustal convergence: A model for Ishtar Terra, Venus, J. Geophys. Res., 96, 20,967-20,980, 1991.

Klose, K. B., J. A. Wood, and A. Hashimoto, Mineral equilibria and the high radar reflectivity of Venus mountain tops, J. Geophys. Res., this issue.

Kruse, S., M. McNutt, J. Phipps Morgan, L. Royden, and B. Wernicke, Lithospheric extension near Lake Mead, Nevada: A model for ductile flow in the lower crust, J. Geophys. Res., 96, 4435-4456, 1991.

Lenardic, A., W. M. Kaula, and D. L. Bindschadler, The tectonic evolution of western Ishtar Terra, Venus, Geophys. Res. Lett., 18, 2209-2212, 1991.

Lynch, H. D., and P. Morgan, Finite-element models of continental extension, Tectonophysics, 174, 115-135, 1990.

McGill, G. E., J. L. Warner, M. C. Malin, R. E. Arvidson, E. Eliason, S. Nozette, and R. D. Reasenberg, Topography, surface properties, and tectonic evolution, in Venus, edited by D. M. Hunten, L. Colin, T. M. Donahue, and V. I. Moroz, pp. 69-130, University of Arizona Press, Tucson, 1983.

Melosh, H. J., and A. Rafesky, The dynamical origin of subduction zone topography, Geophys. J. R. Astron. Soc., 60, 333-354, 1980.

Melosh, H. J., and A. Rafesky, Anelastic response of the Earth to a dip-slip earthquake, J. Geophys. Res., 88, 515-526, 1983.

Miller, E. L., P. B. Gans, and J. Garing, The Snake Range décollement: An exhumed mid-Tertiary brittle-ductile transition, Tectonics, 2, 239-263, 1983.

Pederson, S. A. S., Comparative studies of gravity tectonics in Quaternary sediments and sedimentary rocks related to fold belts, in Deformation of Sediments and Sedimentary Rocks, edited by M. E. Jones and R. M. F. Preston, Geol. Soc. London Spec. Publ., 29, 165-180, 1987.

Pettengill, G. H., E. Eliason, P. G. Ford, G. B. Loriot, H. Masursky, and G. E. McGill, Pioneer Venus radar results: Altimetry and surface properties, J. Geophys. Res., 85, 8261-8270, 1980.

Pettengill, G. H., P. G. Ford, W. T. K. Johnson, R. K. Raney, and L. A. Soderblom, Magellan: Radar performance and data products, Science, 252, 260-265, 1991.

Phillips, R. J., Convection-driven tectonics on Venus, J. Geophys. Res., 95, 1301-1316, 1990.

Phillips, R. J., R. A. Arvidson, J. M. Boyce, D. B. Campbell, J. E. Guest, G. G. Schaber, and L. A. Soderblom, Impact craters on Venus: Initial analysis from Magellan, Science, 252, 288-297, 1991a.

Phillips, R. J., R. E. Grimm, and M. C. Malin, Hot-spot evolution and the global tectonics of Venus, Science, 252, 651-658, 1991b.

Phillips, R. J., R. R. Herrick, R. E. Grimm, R. R. Raubertas, I. C. Sarkar, R. E. Arvidson, and N. Izenberg, Impact crater distribution

on Venus: Implications for planetary resurfacing history, *J. Geophys. Res.*, this issue.

Plaut, J. J., and R. E. Arvidson, Comment on "Impact craters of Venus: A continuation of the analysis of data from the Venera 15 and 16 Spacecraft" by A. T. Basilevsky et al., *J. Geophys. Res.*, *93*, 15,339-15,340, 1988.

Pronin, A. A., The Lakshmi Planum structure as an indicator of asthenospheric horizontal flows on Venus, *Geotectonics*, *20*, 271-280, 1986.

Pronin, A. A., and M. Kreslavsky, A possible mechanism of gravity relaxation on Venus (abstract), *Lunar Planet. Sci.*, *23*, 1113-1114, 1992.

Roberts, K. M., and J. W. Head, Lakshmi Planum, Venus: Characteristics and models of origin, *Earth Moon Planets*, *50/51*, 193-250, 1990a.

Roberts, K. M., and J. W. Head, Western Ishtar Terra and Lakshmi Planum, Venus: Models of formation and evolution, *Geophys. Res. Lett.*, *17*, 1341-1344, 1990b.

Sandwell, D. T., and G. Schubert, Flexural ridges, trenches, and outer rises around Venus coronae, *J. Geophys. Res.*, this issue.

Saunders, R. S., J. W. Head III, R. J. Phillips, S. C. Solomon, R. Herrick, R. Grimm, and E. R. Stofan, Geology of Ovda Regio, Aphrodite Terra, Venus: Preliminary results from Magellan data (abstract), *Lunar Planet. Sci.*, *22*, 1169-1170, 1991.

Schaber, G. G., E. M. Shoemaker, and R. C. Kozak, The surface age of Venus: Use of the terrestrial cratering record, *Solar System Res.*, *21*, 89-93, 1987.

Schaber, G. G., R. G. Strom, H. J. Moore, L. A. Soderblom, R. L. Kirk, D. J. Chadwick, D. D. Dawson, L. R. Gaddis, J. M. Boyce and J. Russell, The geology and distribution of impact craters on Venus: What are they telling us?, *J. Geophys. Res.*, this issue.

Schmid, S. M., Microfabric studies as indicators of deformation mechanisms and flow laws operative in mountain building, in *Mountain Building Processes*, edited by K. J. Hsu, pp. 95-110, Academic, San Diego, Calif., 1983.

Sebrier, M., J. L. Mercier, F. Megard, G. Laubacher, and E. Carey-Gailhardis, Quaternary normal and reverse faulting and the state of stress in the central Andes, *Tectonics*, *4*, 739-780, 1985.

Seiff, A., Thermal structure of the atmosphere of Venus, in *Venus*, edited by D. M. Hunten, L. Colin, T. M. Donahue, and V. I. Moroz, pp. 215-279, University of Arizona Press, Tucson, 1983.

Smrekar, S., and R. J. Phillips, Gravity-driven deformation of the crust on Venus, *Geophys. Res. Lett.*, *15*, 693-696, 1988.

Smrekar, S. E., and R. J. Phillips, Venusian highlands: Geoid to topography ratios and their interpretation, *Earth Planet. Sci. Lett.*, *107*, 582-597, 1991.

Solomon, S. C., and J. W. Head, Mechanisms for lithospheric heat transport on Venus: Implications for tectonic style and volcanism, *J. Geophys. Res.*, *87*, 9236-9246, 1982.

Solomon, S. C., J. W. Head, W. M. Kaula, D. McKenzie, B. Parsons, R. J. Phillips, G. Schubert, and M. Talwani, Venus tectonics: Initial analysis from Magellan, *Science*, *252*, 297-312, 1991.

Solomon, S. C., et al., Venus tectonics: An overview of Magellan observations, *J. Geophys. Res.*, this issue.

Squyres, S. W., D. M. Janes, G. Baer, D. L. Bindschadler, G. Schubert, V. L. Sharpton, and E. R. Stofan, The morphology and evolution of coronae on Venus, *J. Geophys. Res.*, this issue.

Stofan, E. R., V. L. Sharpton, G. Schubert, G. Baer, D. L. Bindschadler, D. M. Janes, and S. W. Squyres, Global distribution and characteristics of coronae and related features on Venus: Implications for origin and relation to mantle processes, *J. Geophys. Res.*, this issue.

Surkov, Yu. A., V. L. Barsukov, L. P. Moskalyeva, and V. P. Kharyukova, New data on the composition, structure, and properties of Venus rock obtained by Venera 13 and Venera 14, *Proc. 14th Lunar Planet. Sci. Conf.*, Part 2, *J. Geophys. Res.*, *89*, suppl., B393-402, 1984.

Surkov, Yu. A., F. F. Kirnozov, V. N. Glazov, A. G. Dunchenko, L. P. Tatsy, and O. P. Sobornov, Uranium, thorium, and potassium in the Venusian rocks at the landing sites of Vega 1 and 2, *Proc. 17th Lunar Planet. Sci. Conf.*, Part 2, *J. Geophys. Res.*, *92*, suppl., E537-540, 1987.

Tyler, G. L., P. G. Ford, D. B. Campbell, C. Elachi, G. H. Pettengill, and R. A. Simpson, Magellan: Electrical and physical properties of Venus' surface, *Science*, *252*, 265-270, 1991.

Weertman, J., Height of mountains on Venus and the creep properties of rock, *Phys. Earth Planet. Inter.*, *19*, 197-297, 1979.

Wiltschko, D. V., A mechanical model for thrust sheet deformation at a ramp, *J. Geophys. Res.*, *84*, 1091-1104, 1979.

Zuber, M. T., and E. M. Parmentier, On the relationship between isostatic elevation and the wavelengths of tectonic surface features on Venus, *Icarus*, *85*, 290-308, 1990.

S. E. Smrekar and S. C. Solomon, Building 54-520, Department of Earth, Atmospheric, and Planetary Sciences, Massachusetts Institute of Technology, Cambridge, MA 02139.

RHEOLOGICAL AND AGE CONSTRAINTS FROM MODELS OF GRAVITATIONAL SPREADING IN ISHTAR TERRA, VENUS;

Suzanne E. Smrekar and Sean C. Solomon, Department of Earth, Atmospheric, and Planetary Sciences, Massachusetts Institute of Technology, Cambridge, MA 02144.

Introduction. Gravitational spreading is expected to lead to rapid relaxation of high relief due to the high surface temperature and associated weak crust on Venus [1,2]. In this study, we use new Magellan radar and altimetry data to determine the extent of gravitational relaxation in Ishtar Terra, which contains the highest relief on Venus and areas of extremely high topographic slope. Within Ishtar Terra, the only mountain belts found on Venus, Akna, Danu, Freyja, and Maxwell, nearly encircle the smooth, high (3-4 km) plateau of Lakshmi Planum. Finite element models of this process give expected timescales of relaxation and failure at the surface. Using modeling results, we attempt to constrain the strength of the crust and timescales of deformation in Ishtar Terra. Below we discuss observational evidence for gravitational spreading in Ishtar Terra, results from the finite element modeling, independent age constraints, and the implications for the rheology and timing of deformation.

Observations. Magellan data have revealed abundant evidence for localized extension throughout Ishtar Terra [3,4]. Many of the observed extensional features are oriented perpendicular to topographic slope, implying that they formed as a result of gravitational spreading. In some of the mountaineous areas, extensional faults occur parallel to the apparent direction of shortening. By analogy with active gravitational spreading on Earth [5], we interpret this extension to indicate gravitational spreading during convergence. Areas of possible gravitational spreading are observed in each of the four mountain belts and along both the southern and northeastern margins of Lakshmi Planum. Horizontal strain in these regions is estimated to be 1-20%; this value may be an underestimate if blocks are rotated along the normal faults. The observational evidence for gravitational spreading in Ishtar Terra is discussed more fully in [4].

Models. We use the finite element algorithym TECTON [6] to model the evolution of gravitational spreading in a vertical section of the crust near the margin of a plateau or the edge of a broad mountain belt. Each model includes an elevated plateau 50 km in width, a sloped margin, and a lowlands region 80 km in width. The code employs a depth-dependent, viscoelastic rheology with non-linear stress dependence and exponential temperature dependence. We adopt a Young's modulus of 6×10^{10} Pa and a Poisson's ratio of 0.25. As a lower bound on the viscous strength, a diabase flow law [7]. Although a diabase compostion is most similar to the composition determined at Soviet lander sites [8], the flow law determined for diabase may underestimate the strength due to partial melting during the experiment [7,9]. For this reason, we also employ a websterite flow law [10] as an upper bound on the crustal strngth. The surface temperature is 740 K and increases linearly with depth. Each row of elements in the grid has the same viscosity, which is equivalent to assuming that the temperature is constant along both the bottom and top of the grid. This results in a somewhat higher thermal gradient in the plains than in the plateau. The boundary conditions are zero vertical and horizontal velocity on the bottom of the grid, a free surface top boundary, and zero horizontal velocity and free vertical slip at the sides. The bottom boundary condition approximates an upper mantle layer that is much stonger than the lower crust. Details of the models are given in [4]. Brittle failure is evaluated using a Mohr-Coulomb criterion. The timing of predicted brittle failure and relaxation of relief are found for ranges of plateau height (1-5 km), plateau margin slope (1-30°), crustal thickness (10-30 km), and thermal gradient (5-25 K/km). Slopes of 1-30° and plateau or mountain belt heights of 1-6 km are observed in Ishtar Terra. Crustal thickness on Venus is predicted to be 10-30 km [11,12]; the average thermal gradient is expected to be 10-25 K/km [13,14].

The rate of deformation is largely controlled by the effective viscosity, and thus the temperature and stress, at the base of the crust. The greatest deformation occurs at the base of the crust, where the viscosity is lowest. Temperature at the base of the crust increases with crustal thickness (for a fixed thermal gradient), and deviatoric stress near the base of the crust increases with both crustal thickness and plateau elevation. The non-linear change in predicted failure and relaxation time is due both to the exponential dependence on temperature and to the power law dependence on deviatoric stress of the effective viscosity.

Failure is predicted to occur when the stresses exceed the Mohr-Coulomb criterion. Initial failure is located on the plateau. In most cases, failure on the slope occurs shortly after failure on the plateau; thrust faulting in the plains occurs typically only for a crustal thickness of 30 km. Figure 1 shows the time for the first failure on the plateau as a function of plateau height and crustal thickness, for a margin slope of 3° and a thermal gradients of 15 K/km. Models with both websterite and diabase flow laws are plotted. No times are shown for models that do not fail within 1 Ga. For cases with a diabase rheology, a large plateau height, and a large crustal thickness fail almost immediately. A plateau height of 1 km and a crustal thicknesses of 10 km can take up to tens of millions of years to fail. With a websterite flow law, no failure occurs unless the crust is a least 20 km thick and the plateau elevation is 1-3 km. Changing the thermal gradient by 10 K/km has a large effect on failure times, with a higher thermal gradient decreasing the failure time by a factor of 100-10,000, and a lower thermal gradient increasing times by a similar factor. When failure is first predicted, the horizontal surface strain is approximately 0.05%. This strain is unlikely to be recognized as normal faulting in Magellan radar images; a strain of 1%, which accumulates once significant relxation of the topograpy begins, is probably a more reasonable value to compare with observations. As faulting is not explicitly modeled, there is some uncertainty in the interpretation of strain after the initial failure. The total strain may be underestimated.

As elevations in Ishtar Terra are among the highest on Venus, we assume that relief has not relaxed by more than 25% of its original value. The time at which the average elevation in the plateau has relaxed by at least 25% is shown as a function of plateau height and crustal thickness, for thermal gradients of 15 and 25 K/km, in Figure 1. For a given thermal gradient and crustal thickness, predicted relaxation times for plateau heights of 1, 3, and 5 km vary by a factor of 10 at most. A 10 km change in crustal thickness leads to a factor of 10-100 change in relaxation time. Larger differences in relaxation time are predicted for models with the same plateau height and crustal thickness but with thermal gradients that differ by 10 K/km, as is consistent with the larger changes in basal temperature. For a thermal gradient of 25 K/km and a plateau height range of 1-5 km, all the models are predicted to relax by at least 25% within 100 My for a 10 km thick crust, 0.1 My for a 20 km thick crust, and 1000 y for a 30 km thick crust. A thermal gradient of 15 K/km gives relaxation times of up to 1 Gy, 100 My, and 0.1 My for crustal thicknesses of 10, 20, and 30 km, respectively.

Discussion. The range of parmeters can be narrowed somewhat by considering the geology and morphology of Ishtar Terra. In areas of possible gravitational spreading, the local topographic slope ranges from 2-15°. For the puposes of discussion, we will assume a slope of at least 3°. Typical local elevation changes are 2-3 km, although elevation changes are as large as 5-6 km in Maxwell Montes. Thus plateau elevations as low as 1 km can be eliminated, especially given that the topography may have relaxed somewhat from its original value. The very steep topographic slopes in many parts of Ishtar Terra suggest that the topography is likely to be at least partially isostatically compensated. As mountains in Ishtar Terra rise 4-10 km above the surrounding lowlands, the crustal thickness is probably greater than 10 km. Further, the abundance of volcanism in Ishtar Terra, as well as the overlap of volcanism and extension in many areas [4], implies that the thermal gradient is unlikely to anomalously low. Values of 15 K/km or more are probably applicable to Ishtar Terra. Using these limits on the parameter range appropriate for Ishtar Terra and assuming a diabase flow law constrains relaxation of the topography by 25% or more to occur within 10 My. This result implies that either the crust is anomalous in some way, thinner, colder, or stronger than expected, or that mountain building processes have maintained the relief in Ishtar Terra until geologically recent times. Next we examine independent information on the age of tectonism in Ishtar Terra to attempt to descriminate between these two hypotheses.

Several types of evidence provide conflicting information on the age of Ishtar Terra. The only available measure of absolute age, the average crater retension age for Venus of 500 My, implies that much of the surface is quite old [15]. Local geological information must be used to determine whether a region is likely to be older or younger than the average age [16]. In Ishtar Terra, the abundance of volcansim, especially in Lakshmi Planum, suggests that the surface may be less than the average age [17]. In many cases, both the shortening in the mountain belts and areas of extension crosscut local volcanism in Lakshmi Planum, implying a younger age for the tectonism

[3,4,16]. At least one impact crater in Ishtar Terra appears to be modified by extension due to gravitational relaxation [4]. However, the 150 km-diameter crater, Cleopatra, lies near the crest of Maxwell Montes and appears undeformed. In addition to surface processes, gravity data suggest that dynamic processes in the mantle are actively supporting the long wavelength topography [8]. These dynamic processes may produce stresses capable of creating the observed short wavelength, high amplitude variations in topography.

Both the gravity data and the majority of the geologic indicators favor the hypothesis that the region is likely to younger than the average crater retension age of Venus, 500 My. On the basis of this information, and the assumptions discusses above regarding the appropriate parameter range for Ishtar Terra, we interpret the results of our modeling to indicate the tectonic processes have maintained the topography until as recently as 10 My, and may still be active.

References. [1] Weertman ; [2] S.E. Smrekar and R.J. Phillips, 1988; [3] S.C. Solomon et al., Science, 252, 297-312, 1991; [4] S.E. Smrekar and S.C. Solomon, J. Geophys. Res., accepted, 1992; [5] R. Armijo et al., J. Geophys. Res., 91, 13,803-13,872, 1986; [6] H.J. Melosh and A. Rafesky, Geophys. J. R. Astron. Soc., 60, 333-354, 1980; [7] Y. Caristan, J. Geophys. Res., 87, 6781-6790, 1982; [8] Surkov et al., Proc. 17th Lunar Planet. Sci. Conf., Part 2, J. Geophys. Res., 92, E537-540, 1987; [9] B. Evans, et al., Geophys. Mono. 56, Am Geophys. Un., pp. 20, 1990; [10] Ave Lallement, H.G., Tectonophysics, 48, 1-27, 1978; [11] R.E. Grimm and S.C. Solomon, J. Geophys. Res., 93, 11,911-111,929, 1988; [12] M.T. Zuber and E.M. Parmentier, Icarus, 85, 290-308, 1990; [13] W.M. Kaula and J.R. Phillips, Geophys. Res. Lett., 8, 1187-1190, 1981; [14] S.C. Solomon and J.W. Head, J. Geophys. Res., 87, 9236-9246, 1982; [15] R.J. Phillips et al., J. Geophys. Res., accepted, 1992; [16] K.M. Roberts and J.W. Head, Earth Moon Planets, 50/51, 193-250, 1990; [17] R.E. Grimm and R.J. Phillips, J. Geophys. Res., 96, 8305-8324, 1991.
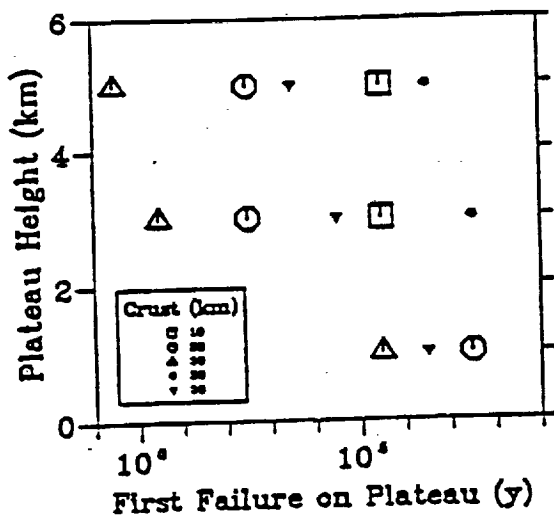
Figure 1.
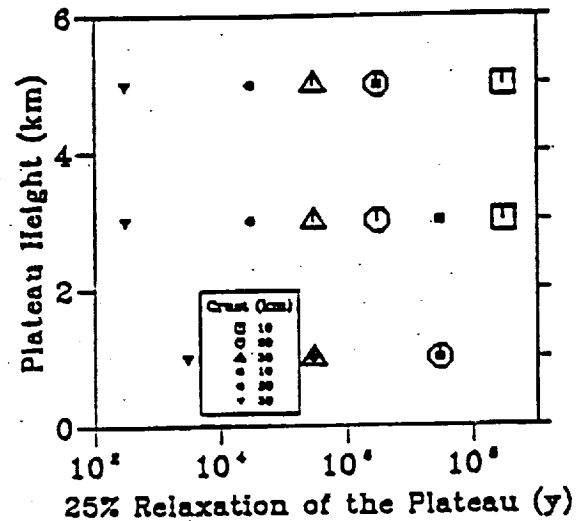
Figure 2.

Figure 1. The time at which failure (by normal faulting) first occurs on the plateau is shown as a function of plateau elevation for three values of plains crustal thickness. The initial slope of the scarp in each model is 3°, and the plains thermal gradient is 15 K/km. Open symbols represent models with a diabase flow law [X]; filled symbols are for a websterite flow law [X] Times in Figures 1 and 2 are determined to the nearest order of magnitude.

Figure 2. The time at which the height of the plateau has relaxed by 25% is shown as a function of plateau height for three values of plains crustal thickness. The initial slope of the bounding scarp is 3°. The open symbols are for a plains thermal gradient of 15 K/km; filled symbols are for a thermal gradient of 25 K/km.

Tectonic Processes on Venus: Comparisons and Contrasts with the Earth

Sean C. Solomon

Department of Earth, Atmospheric, and Planetary Sciences

Massachusetts Institute of Technology

Cambridge, MA 02139

Radar imaging and altimetry data from the Magellan mission have revealed a diversity of deformational features at a variety of spatial scales on the Venus surface. The plains of Venus record a superposition of distinct episodes of deformation, typically manifested in areally distributed strain of modest magnitude and coherent over hundreds of kilometers. Ridge belts and mountain belts represent successive degrees of lithospheric shortening and crustal thickening. As on Earth, mountain belts show widespread evidence for lateral extension and collapse both during and following orogeny. Large-scale extensional structures include the quasi-circular coronae and broad rises with linear rift zones, both sites of significant volcanic flux. Few large-offset strike-slip faults have been observed, but limited local horizontal shear is accommodated across many zones of crustal shortening. Several large-scale tectonic features have topographic slopes in excess of 20° over a 10-km scale; because of the tendency for such slopes to relax by ductile flow in the lower crust, such regions are likely to be tectonically active. In general, Venus is tectonically unlike Earth's oceanic regions, with their large rigid plates and deformation confined to narrow plate boundaries, but actively deforming continental regions provide a closer analogue. The styles and distribution of tectonic deformation on Venus may be consequences of three differences from Earth: the absence of a hydrological cycle and significant erosion, strong coupling of mantle convection to the upper mantle portion of the lithosphere, and a high surface temperature and thus a significantly shallower onset of ductile behavior in the crust.

THE TECTONICS OF VENUS: AN OVERVIEW; Sean C. Solomon, Department of Earth, Atmospheric, and Planetary Sciences, Massachusetts Institute of Technology, Cambridge, MA 02139.

Introduction. While the Pioneer Venus altimeter, Earth-based radar observatories, and the Venera 15-16 orbital imaging radars provided views of large-scale tectonic features on Venus at ever-increasing resolution [1-3], the radar images from Magellan constitute an improvement in resolution of at least an order of magnitude over the best previously available [4]. A summary of early Magellan observations of tectonic features on Venus has been published [5], but data available at that time were restricted to the first month of mapping and represented only about 15% of the surface of the planet. Magellan images and altimetry are now available for more than 95% of the Venus surface. Thus a more global perspective may be taken on the styles and distribution of lithospheric deformation on Venus and their implications for the tectonic history of the planet [6].

Generalizations. Tectonic features on Venus are widespread and diverse, and comparatively few regions are undeformed. Areas lacking tectonic features at Magellan resolution are restricted to relatively young volcanic deposits and the younger impact craters and associated ejecta. Most of the surface, during at least some period over approximately the last 500 My [7,8], has experienced horizontal strain sufficient to fault or fold near-surface material.

Tectonic activity on Venus has continued until geologically recent time, and most likely the planet is tectonically active at present. Several arguments support this inference. The great relief and steep slopes of the mountains and plateau scarps of Ishtar Terra and of the equatorial chasm systems are difficult to reconcile with long-term passive support by crustal strength. Because of the high surface temperature on Venus, temperatures at which crustal rocks fail by ductile flow should be reached at much shallower depths than on Earth [9,10]. Numerical models suggest that areas of high relief and steep slope in the Ishtar region should spread under self-gravity by ductile flow of the weak lower crust on time scales less than about 10 My [11]. Thus the processes that build relief and steepen slopes must have been active within the last 10 My. Further, a number of features produced by geological processes that have operated more or less steadily during the past 500 My show evidence of subsequent tectonic activity. About one third of all preserved impact craters on Venus have throughgoing faults and fractures, and 1 in 12 are extensively deformed [8]. The longest lava channel on the plains of Venus does not progress monotonically to lower elevations downstream, indicating that differential vertical motions have occurred since the channel was formed [12].

Compared with the Earth, horizontal displacements on Venus over the last 500 My have been limited. Most of the tectonic features require modest strains and horizontal displacements of no more than a few tens to perhaps a few hundreds of kilometers. Plains thousands of kilometers across record horizontal strains of order 10^{-2} or less. The great rift systems of Beta and Atla Regiones need have extended no more than a few tens of kilometers, on the basis of topographic profiles, extended features such as the crater Somerville in Devana Chasma, and analogy with continental rifts on Earth [13]. For compressional features, the amount of crustal thickening can be estimated from topographic relief and isostatic considerations, but this approach provides only a lower bound on horizontal displacements if any crustal material is recycled into the mantle at zones of underthrusting. For ridge belts 100 km in width and with up to 1 km of relief, horizontal displacements of no more than 100 km are required for crustal thicknesses of 10-20 km beneath the adjacent plains [14,15]. Mountain belts are exceptional in that greater horizontal displacements are required. For a two- to four-fold thickening of the crust beneath the 500-km width of Maxwell Montes, the implied minimum horizontal displacement is 1000-2000 km.

Unlike the Earth, Venus does not show evidence for a global system of nearly rigid plates with horizontal dimensions of 10^3-10^4 km separated by narrow plate boundary zones a few kilometers to tens of kilometers across. Predictions prior to Magellan that Aphrodite Terra would show features analogous to terrestrial spreading centers and oceanic fracture zones [16] are now seen to be incorrect. Evidence for shear is present in the ridge and fracture belts and in the mountain belts, but the shearing tends to be broadly distributed and to accompany horizontal stretching or shortening. Few clear examples have yet been documented of long, large-offset strike-slip faults

such as those typical of oceanic and many continental areas on Earth; two such features have been identified in the interior of Artemis Corona [17]. A number of the chasm systems of Venus have arcuate planforms, asymmetric topographic profiles, and high relief [18] and have been likened to deep-sea trenches on Earth [17]. These include Dali and Diana Chasmata [17] and the moat structure of Artemis Corona; such trenches may be the products of limited underthrusting or subduction of lithosphere surrounding large coronae [19]. Elsewhere, however, chasm systems of somewhat lesser relief display more linear segments and more nearly symmetric topographic profiles, such as Devana Chasma, and on the basis of small-scale morphology are clearly extensional rifts.

Much of the tectonic behavior on Venus appears to be more reminiscent of actively deforming continental regions than of oceanic regions on Earth. In particular, as in tectonically active continental areas, deformation is typically distributed across broad zones one to a few hundred kilometers wide separated by comparatively stronger and less deformed blocks having dimensions of hundreds of kilometers. On Earth, the continental lithosphere in tectonically active areas is weaker than typical oceanic lithosphere because of the greater thickness of more easily deformable crust. As noted above, because of the higher surface temperature on Venus, the likely comparable lithospheric thermal gradients on Venus and Earth [20,21], and the strong temperature dependence of ductile behavior, the lithosphere on Venus should behave in a weak manner for crustal thicknesses less than are typical of continental regions on Earth.

Status of Models. A major challenge in unravelling the tectonic evolution of Venus is to understand the interaction between mantle convection and the lithosphere. The hotspot [22] and coldspot [23] models for the formation and evolution of major highlands on Venus are distinguishable on the basis of the predicted sequence of events and the time-dependent relationship between topography and gravity. Both models face difficulties in their present forms, however, at least partly because both the rheology of the upper crust of Venus and the observed patterns of magmatism and deformation are more complex than current models for the deformation and magmatic response of the crust to mantle flow. Any global tectonic model, of course, must also consider the formation and characteristics of the lowlands, including the large apparent depths of isostatic compensation [22] and relatively recent lowland volcanism [24]. All dynamical models to date require special pleading to explain Ishtar Terra. Both the rifted, volcanically active highlands and at least the larger coronae are generally regarded as sites of upwelling mantle flow and magma generation by pressure-release partial melting of mantle material. These two classes of features, however, have very different tectonic and morphological manifestations at the Venus surface. If both are products of mantle upwelling, then multiple scales of mantle convection are indicated and the different morphologies of the two classes of features must be related to differences in the geometry, buoyancy flux, or duration of flow in the two types of upwelling regions. The assessment of existing dynamical models for the tectonic evolution of Venus and the development of the next generation of models will require an understanding of geological relationships at all scales, from the highest resolution available to global patterns. High-resolution measurements of the global gravity field later in the Magellan mission will provide key data for testing and refining models.

References: [1] H. Masursky et al., *J. Geophys. Res.*, 85, 8232, 1980; [2] D.B. Campbell et al., *Science, 221*, 644, 1983; [3] V.L. Barsukov et al., *Proc. Lunar Planet. Sci. Conf. 16th*, D378, 1986; [4] G.H. Pettengill et al., *Science, 252*, 260, 1991; [5] S.C. Solomon et al., *Science, 252*, 297, 1991; [6] S.C. Solomon et al., *J. Geophys. Res.*, in press, 1992; [7] R.J. Phillips et al., *Science, 252*, 288, 1991; [8] G.G. Schaber et al., *J. Geophys. Res.*, in press, 1992; [9] J. Weertman, *Phys. Earth Planet. Inter., 19*, 197, 1979; [10] S.C. Solomon and J.W. Head, *J. Geophys. Res., 89*, 6885, 1984; [11] S.E. Smrekar and S.C. Solomon, *J. Geophys. Res.*, in press, 1992; [12] V.R. Baker et al., *J. Geophys. Res.*, in press, 1992; [13] G.E. McGill et al., *Geophys. Res. Lett., 8*, 737, 1981; [14] R.E. Grimm and S.C. Solomon, *J. Geophys. Res., 93*, 11,911, 1988; [15] M.T. Zuber and E.M Parmentier, *Icarus, 85*, 290, 1990; [16] J.W. Head and L.S. Crumpler, *Science, 238*, 1380, 1987; [17] D. McKenzie et al., *J. Geophys. Res.*, in press, 1992; [18] P.G. Ford and G.H. Pettengill, *J. Geophys. Res.*, in press, 1992; [19] D.T. Sandwell and G. Schubert, *J. Geophys. Res.*, in press, 1992; [20] S.C. Solomon and J.W. Head, *J. Geophys. Res., 87*, 9236, 1982; [21] R.J. Phillips and M.C. Malin, *Ann. Rev. Earth Planet. Sci., 12*, 411, 1984; [22] R.J. Phillips et al., *Science, 252*, 651, 1991; [23] D.L. Bindschadler et al., *J. Geophys. Res.*, in press, 1992; [24] J.W. Head et al., *Science, 252*, 276, 1991.

The Tectonic and Volcanic Evolution of Venus: Catastrophic or Gradual?

Sean C. Solomon (DTM, Carnegie Institution of Washington, 5241 Broad Branch Road, N.W., Washington, DC 20015)

Radar imaging and altimetry data from the Magellan mission have yielded important new constraints on the tectonic and volcanic history of Venus and on its internal dynamics. The planet lacks global plate tectonics, but a number of chasm systems and corona moat structures have arcuate planforms, asymmetric topographic profiles, and relief analogous to deep-sea trenches on Earth and may be products of limited lithospheric underthrusting or subduction. Several lines of evidence point to a crust and upper mantle stronger than would be predicted by simple extrapolation from Earth and the 450 K greater surface temperature; these include the unrelaxed depths of impact craters, apparently large values of elastic lithosphere thickness, and large ratios of gravity to topography. The density of impact craters indicates an average crater retention age of about 500 My, but no more than 5% of the recognized craters have been volcanically embayed. This last observation has led to the proposal that Venus has been subjected to one or more global resurfacing events, the latest about 500 My ago, and that the volcanic flux during intervals between such events has been low. That more recent tectonic activity has been widespread, however, is indicated by the high relief and slopes of mountains, chasm walls, and plateau margins; the significant fraction (0.3) of impact craters deformed by younger faults; and the post-formational vertical deformation of long channels. Interior dynamical scenarios advanced to account for episodic volcanic resurfacing include catastrophic overturn of a global lithosphere thickened by cooling or compositional buoyancy and strongly time-dependent mantle convective heat flux. Outgassing considerations and analogy with Earth and other terrestrial planets, however, suggest that such catastrophic models are unlikely. If the mantle of Venus cooled more efficiently than that of Earth because of, say, different boundary conditions, a different flow law, or a different degree of layering, then the planet may in the last 500 My have attained lesser mantle temperatures, lower mantle heat flux, and a significantly lesser rate of magma production than Earth yet still display evidence for ongoing convection and active tectonics. Such a "cold Venus" scenario would be broadly consistent with observations yet be characterized by a gradual volcanic and tectonic evolution.

Keeping that youthful look

Sean C. Solomon

THE record of impact cratering on Venus, recently revealed from high-resolution radar imaging by the Magellan spacecraft, has been interpreted as indicating that the planet underwent catastrophic global resurfacing about 500 million years ago[1]. Although other interpretations of the crater characteristics have been suggested[2], the possibility of geologically rapid global resurfacing on the planet that most resembles our own in terms of mass, density and bulk composition has generated widespread interest: what mechanisms could cause such a catastrophe? Several ideas were discussed at the Fall Meeting of the American Geophysical Union last month*.

The average age of Venus's surface has been estimated from the number of larger impact craters (the planet's thick atmosphere has tended to protect it from the smaller bodies that would give craters smaller than 30 km in diameter) and from the cratering rate on Earth and the Moon, or from estimates of the number of asteroids whose orbits cross that of Venus[3]. The answer, 500 million years[1,2] (a tenth of the age of the Solar System), is not in itself remarkable for a planet which, like the Earth, has a hot, dynamic interior — despite the absence of significant erosion. What is remarkable is that the craters at all sizes are indistinguishable from a random population (that is, spatial variations in crater density are not larger than those due to chance) and almost none has been significantly modified by tectonic strain or by volcanic flows beyond the crater rim[1,2] (Fig. 1), even though Magellan images show volcanic and tectonic features to be nearly ubiquitous on Venus.

The interpretation of Schaber and others[1] is that most of the surface dates from the end of a global resurfacing event that ceased about 500 million years ago, and that the small fraction of craters volcanically embayed or modified by deformation indicate that volcanic and tectonic activity has since been at much lower levels. Phillips and colleagues[2] have argued that a correlation of locations of modified craters with areas of low crater density and an inverse correlation between crater density and Magellan radar backscatter (a quantity elevated in regions of high topography and high roughness, both thought to be signatures of comparative geological youth) indicate that the Venus surface exhibits a spectrum of ages. (The paucity of small craters, however, hampers the use of crater density in determining the relative ages of geological units, a method used with the other solid planets and satellites.) Phillips et al. have described an alternative model in which resurfacing occurs episodically in small patches a few hundred kilometres in extent, with a characteristic time between events of the order of 10^5 years (Fig. 2).

Nonetheless, the catastrophic hypothesis and its possible mechanisms have captured the lion's share of the attention. At the meeting, D. L. Turcotte (Cornell University) proposed that global lithospheric overturn operates episodically on Venus, and that for the past 500 million years the lithosphere has been cooling and mechanically stable. Although the mechanism for stabilization of the lithosphere is not an explicit component of Turcotte's scheme, he argues that a cool and thick lithosphere is in better agreement (than one in steady-state conductive equilibrium) with the large values obtained from topographic profiles for the rigidity of the lithosphere at sites of presumed lithospheric bending[4] and with the large ratio of long-wavelength gravity anomaly to long-wavelength topographic relief at highland areas[5].

Parmentier and Hess[6], following Stevenson and Bittker[7], have recently suggested that lithospheric stabilization may occur on Venus because of a decrease in the density of lithospheric mantle following melt extraction. But they add that the cooling
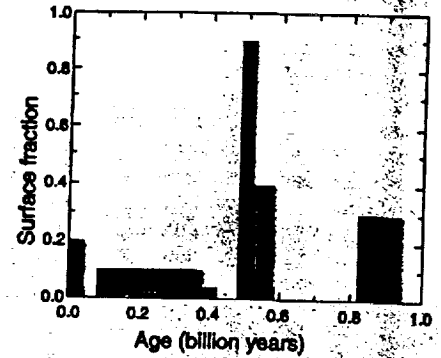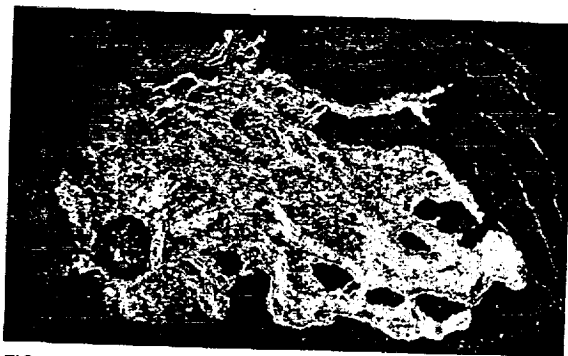

FIG. 1 Magellan radar image of an impact crater on Venus, approximately 70 km in diameter. Radar-bright, rough-textured ejecta extending up to 60 km from the crater rim and the remarkable bright flow features extending more than 300 km from the crater walls are thought to date from the impact[1] and have not been modified to any significant degree by later deformation or volcanism outside the crater (although the generally radar-dark, smooth floor of the crater may contain younger volcanic deposits).

FIG. 2 Two schematic distributions of surface age on Venus. With catastrophic resurfacing[1] (green histogram), most of the surface is about 500 million years old, but small areas have younger ages. With episodic resurfacing[2] (red histogram), there is a more widespread distribution of surface ages from 0 to approximately 1,000 million years. Both possibilities are broadly consistent with the distribution and states of preservation of impact craters on Venus. (Courtesy of R. J. Phillips.)

of such a layer may subsequently raise its density to the point where it becomes unstable. Global overturn of this unstable layer, which would sink back into the mantle, would be followed by partial melting of the upper mantle, global resurfacing, and the gradual development of a new buoyant layer and another extended period of stability. In simple one-dimensional models of this process, the time between lithospheric instability events is 300–500 million years.

Others point to time-variable mantle convection rather than lithospheric instability as a mechanism for global resurfacing. An early effort to simulate such convection on Venus[8] led to models in which the characteristic flow speed and mantle heat flux showed large variations (by factors of 2–10) at intervals of 100–200 million years. J. Arkani-Hamed (McGill University) reported improved calculations with better spatial resolution which are still time-varying but which show significantly weaker fluctuations of the order of several tens of a per cent. V. Steinbach (Cologne University) drew attention to the potential role of upper-mantle phase transitions in governing the radial character of mantle convection in the large terrestrial planets[9]. He and D. Yuen argue that such phase transitions promote the formation of distinct convecting layers in the upper and lower mantle, but that as the Rayleigh number (governing vigour of flow) in the mantle decreases in response to core cooling, whole-mantle convection tends to become favoured over layered convection. If Venus cooled more rapidly than the Earth early in its history, it may now

PRECEDING PAGE BLANK NOT FILMED

have a smaller mantle Rayleigh number and may have gone through a transition to whole-mantle convection, while the Earth may still be characterized by layered mantle flow. Such a transition would have been accompanied by overturn of the upper mantle, the upward transport of heat, and probably by global resurfacing.

The lithospheric instability models as applied to date for Venus suffer from being one-dimensional — global synchroneity is imposed by assumption. Even if such instability mechanisms do operate, it is likely that different parts of the planet will be at different stages in the stabilization and destabilization sequence, and whole-planet temporal variations will be smoothed out by such regional differences. For both lithospheric and mantle-convection mechanisms, attention needs to be given to all the terrestrial planets as a group. Both the Earth and Mars have gone through episodes of great magmatic activity, presumably an indication of variable mantle convective flux, but neither planet shows any evidence of rapid, complete global resurfacing during the past 4,000 million years, and nor do Mercury or the Moon.

Global resurfacing by large-scale overturn of the lithosphere or upper mantle should result in efficient outgassing of the upper mantle; consideration of the ^{40}Ar abundance of Venus's atmosphere suggests that any such widespread outgassing was restricted to times much earlier than 500 million years ago[10].

Finally, remember that there are alternatives to the catastrophic model that seem to be equally consistent with the characteristics of impact craters on Venus[2]. Further study of the Magellan images of impact features and continued development of dynamic models of the planet's interior should sharpen the competing hypotheses and may lead to an improved understanding of mantle convection and melting on all of the terrestrial planets, including the Earth. □

Sean C. Solomon is in the Department of Terrestrial Magnetism, Carnegie Institution of Washington, Washington DC 20015, USA.

1. Schaber, G. G. et al. J. geophys. Res. 97, 13257–13301 (1992).
2. Phillips, R. J. et al. J. geophys. Res. 97, 15923–15948 (1992).
3. Shoemaker, E. M., Wolfe, R. F. & Shoemaker, C. S. Lunar planet. Sci. 22, 1253–1254 (1991).
4. Sandwell, D. T. & Schubert, G. J. geophys. Res. 97, 16069–16083 (1992).
5. Smrekar, S. E. & Phillips, R. J. Earth planet. Sci. Lett. 107, 582–597 (1991).
6. Parmentier, E. M. & Hess, P. C. Geophys. Res. Lett. 19, 2015–2018 (1992).
7. Stevenson, D. J. & Bittker, S. S. Lunar planet. Sci. 21, 1200–1201 (1990).
8. Arkani-Hamed, J. & Toksöz, M. N. Phys. Earth planet Inter. 34, 232–250 (1984).
9. Steinbach, V. & Yuen, D. A. Geophys. Res. Lett. 19, 2243–2246 (1992).
10. Matsui, T. & Tajika, E. Lunar planet. Sci. 22, 863 (1991).

A Tectonic Resurfacing Model for Venus; Sean C. Solomon, Department of Terrestrial Magnetism, Carnegie Institution of Washington, Washington, DC 20015.

Two remarkable aspects of the population of impact craters on Venus are that craters at all sizes are indistinguishable from a random population [1] and that the vast majority of craters have not been significantly modified by tectonic strain or by volcanic flows external to the crater rim [1,2], despite evidence from Magellan images that volcanic [3] and tectonic [4] features are widespread on Venus. One interpretation of these observations [2] is that most of the surface dates from the end of a catastrophic global resurfacing event that ceased about 500 My ago, and that the small fraction of craters volcanically embayed or modified by deformation indicates that volcanic and tectonic activity subsequent to that time has been at much lower levels. An alternative model, in which resurfacing occurs episodically in patches a few hundred kilometers in extent and there is a wider spectrum of surface ages, also appears to be consistent with the characteristics of impact craters on Venus [1]. A number of potential mechanisms for catastrophic resurfacing of Venus have been proposed, ranging from geologically sudden convective destabilization of the global lithosphere [5,6] to strongly time-dependent heat flux and melt generation in the underlying mantle [7-9]. In most of these geophysical models, resurfacing occurs implicitly or explicitly by volcanism. We explore here the hypothesis that, at least in the geologically recent history of Venus, the primary resurfacing mechanism has been tectonic deformation rather than volcanism. We show how such a hypothesis provides at least as good an explanation of a wide range of observations as do volcanic resurfacing models. Finally, we explore the implications of the tectonic resurfacing hypothesis for the controversy over the recent resurfacing history of the planet.

Key Observations. Any model for resurfacing on Venus should be consistent with the following observations: (i) The average crater retention age of the surface is about 500 My [1,2,10]. (ii) As noted above, the distribution of craters of all sizes is not distinguishable at high confidence from that of a random population [1]. (iii) Only about 5% of the craters are embayed by volcanic flows exterior to the rim [1,2]. (iv) About one third of the craters have been deformed subsequent to the impact event [2]; for approximately 10% of the craters the post-impact deformation has been extensive [1,2]. (v) There is some tendency for modified craters to be located in areas of low crater density [1]. (vi) There is a weak inverse correlation between crater density and radar backscatter; i.e., smooth plains have some tendency to be more densely cratered than radar-bright regions of high topography and/or high roughness [1]. (vii) The most common radar-bright regions on Venus are the intensely deformed complex ridged terrain, or tessera, that make up large areas of many highland regions [11] and occur pervasively as small exposed inliers in many lowland plains units [4]. (viii) Deformation on Venus tends to be broadly distributed rather than concentrated into narrow zones as on Earth; Venus lacks a global system of tectonic plates [4]. (ix) Topography and gravity are strongly correlated at long wavelengths [12]; many major features have a large gravity-to-topography ratio (GTR) and apparent depth of compensation [13]. (x) Evidence for tectonic activity substantially more recent than 500 My ago, in addition to the large number of deformed craters, includes the great relief and steep slopes of the mountain belts and plateau scarps of Ishtar Terra and of the equatorial chasm systems [4, 14] and elevation profiles indicating differential vertical movements along major channels [15]. (xi) Evidence that the crust and upper mantle of Venus may be stronger than predicted by simple extrapolation from Earth and the 450 K greater surface temperature include the apparently unrelaxed depths of impact craters [2] and large values of elastic lithosphere thickness derived from flexural models of topographic profiles across the margins of coronae [16]. (xii) The ^{40}Ar abundance of the Venus atmosphere is a factor of 4 less than that on Earth as a fraction of planet mass [17], suggesting that any widespread outgassing such as might accompany large-scale overturn of the global lithosphere [5,6] or upper mantle [8] was restricted to times significantly earlier than 500 My ago [18]. (xiii) While episodes of widespread volcanism at a flux greater than the long-term average for the planet have been documented for Mars [19] and Earth [20], none of the other terrestrial planets have been subjected to a global volcanic resurfacing event over the last 4 Gy.

Tectonic Resurfacing Hypothesis. An important difference between Venus and all of the other terrestrial planets is its high surface temperature. Characteristic time scales for ductile deformation

of crustal and mantle material are known to vary exponentially with reciprocal temperature, so for a given thermal gradient and stress field, high rates of flow are expected to be reached at much shallower levels on Venus than on other terrestrial planets. The large values of GTR and apparent depth of compensation on Venus have been taken as evidence that Venus lacks an asthenosphere or upper mantle low-viscosity channel and that mantle convective stresses couple strongly to the overlying lithosphere [21]. In the absence of plate tectonics, these stresses should give rise to lithospheric strains that are broadly coherent over large regions. For a sufficiently weak lower crust, rates of lower crustal deformation and consequently of surface strain can be high.

Prior to the era of Venus history now preserved, therefore, if the surface temperature was comparable to that at present, the higher heat flow associated with early planetary cooling and enhanced levels of radiogenic heat production and a mantle convective vigor at least that of the present should have led to geologically rapid rates of crustal deformation over most, if not all, of the surface. Such an era would have been characterized by a nearly global extent of complex ridged terrain and few impact craters sufficiently undeformed as to be recognizable from surface images. At some point in the evolution of Venus, however, heat flow will decline to levels sufficiently low that the ductile strength of the lower crust will increase rapidly with small increments of additional cooling. Subsequent to that transition, which might appear to be rapid relative to the geological record, rates of deformation will be substantially less, and both volcanic deposits and impact craters will persist for long intervals with at most modest deformation of landforms. The observations enumerated above are consistent with this hypothesis if this transition from rapid to modest rates of surface strain accumulation occurred about 500 My ago.

Implications for Resurfacing History. The tectonic resurfacing hypothesis leads to some simple predictions that are germane to the resurfacing controversy. If Venus were laterally uniform in both crustal thickness and heat flow, then the transition in surface strain rates would occur with global synchroneity. That is, there would be a rapid change on a planetary scale from high rates of resurfacing to low rates, as is called for by the catastrophic resurfacing model [2], although no true catastrophe - and certainly no global outpouring of magma - is involved. While the assumption of uniform crustal thickness and heat flow is unreasonable, the unimodal hypsometric distribution for Venus suggests that a large fraction of the Venus surface may not depart greatly from this assumption; i.e., an apparently "catastrophic" change is not a bad first approximation. Departures from a globally uniform change in resurfacing rates are to be expected, however. In particular, highland regions, whether they owe their elevations primarily to greater than average crustal thickness or to enhanced temperatures at depth, should persist as regions of high strain rate long after the rate of deformation in lowland plains regions has dropped to modest levels. Lowlands should thus be preferred sites for the preservation of relatively undeformed volcanic deposits and impact craters, as is observed [1,3,4].

Conclusions. The hypothesis that most resurfacing on Venus has occurred by tectonic rather than volcanic processes can account for many of the important characteristics of the planet. The unusual cratering record on Venus is seen in this light to be a consequence primarily of the atmospheric greenhouse and the effect of the high surface temperature on the rheology of the crust. The hypothesis leads to the view that the resurfacing history should contain elements of both the "catastrophic" and "episodic" scenarios for crater removal, with approximately coeval stabilization of lithosphere beneath plains regions but more recent tectonic activity concentrated in highlands.

References. [1] R.J. Phillips et al., *JGR, 97,* 15923, 1992; [2] G.G. Schaber et al., *JGR, 97,* 13257, 1992; [3] J.W. Head et al., *JGR, 97,* 13153, 1992; [4] S.C. Solomon et al., *JGR, 97,* 13199, 1992; [5] E.M. Parmentier and P.C. Hess, *GRL, 19,* 2015, 1992; [6] D.L. Turcotte, *Eos Trans. AGU, Fall Suppl., 73,* 329, 1992; [7] J. Arkani-Hamed and M.N. Toksöz, *PEPI, 34,* 232, 1984; [8] V. Steinbach and D.A. Yuen, *GRL, 19,* 2243, 1992; [9] J. Arkani-Hamed, *Eos Trans. AGU, Fall Suppl., 73,* 332, 1992; [10] E.M. Shoemaker et al., *LPS, 22,* 1253, 1991; [11] D.L. Bindschadler et al., *GRL, 17,* 171, 1990; [12] W.L. Sjogren et al., *JGR, 88,* 1119, 1983; [13] S.E. Smrekar and R.J. Phillips, *EPSL, 107,* 582, 1991; [14] S.E. Smrekar and S.C. Solomon, *JGR, 97,* 16121, 1992; [15] V.R. Baker et al., *JGR, 97,* 13421, 1992; [16] D.T. Sandwell and G. Schubert, *JGR, 97,* 16069, 1992; [17] T.M. Donahue and J.B. Pollack, in *Venus,* p. 1003, Univ. Ariz. Press, 1983; [18] T. Matsui and E. Tajika, *LPS, 22,* 863, 1991; [19] K.L. Tanaka et al., *PLPSC 18th,* 665, 1988; [20] R.L. Larson, *Geology, 19,* 547, 1991; [21] R.J. Phillips, *GRL, 13,* 1141, 1986.

The Resurfacing Controversy for Venus: An Overview and a Mechanistic Perspective

Sean C. Solomon (DTM, Carnegie Institution of Washington, 5241 Broad Branch Road, N.W., Washington, DC 20015)

Two remarkable aspects of the population of impact craters on Venus are that craters at all sizes are indistinguishable from a random population and that most craters have not been significantly modified by tectonic strain or by volcanic flows external to the crater rim, despite evidence from Magellan images that volcanic and tectonic features are widespread on Venus. One interpretation of these observations is that most of the surface dates from the end of a catastrophic global resurfacing event that ceased about 500 My ago, and that the small fraction of craters volcanically embayed or modified by deformation indicate that volcanic and tectonic activity subsequent to that time has been at much lower levels. A competing scenario, in which resurfacing occurs episodically in patches a few hundred kilometers in extent and there is a wider spectrum of surface ages, also appears to be consistent with the characteristics of impact craters on Venus. While geological and statistical studies of the crater population on Venus offer some promise for distinguishing between these two hypotheses, consideration of the possible mechanisms of catastrophic and episodic resurfacing provides an independent perspective. Potential mechanisms for catastrophic resurfacing of Venus range from geologically sudden convective destabilization of the global lithosphere to strongly time-dependent heat flux and melt generation in the underlying mantle. For most of these mechanisms, resurfacing occurs implicitly or explicitly by volcanism. An alternative hypothesis is that, at least in the geologically recent history of Venus, the primary resurfacing mechanism has been tectonic deformation rather than volcanism. Because the rate of surface strain should be controlled by the temperature-dependent strength of the lower crust, a geologically rapid transition in surface strain rates should be the natural result of planetary cooling. This transition would occur at comparable times for areas of similar crustal thickness and heat flow (e.g., plains), but would be delayed for regions of thicker or hotter crust (highlands). The end of the era of high rates of tectonic resurfacing could thus appear as a "catastrophe" over the 80% of the planet with an elevation within 1 km of the mean, while continued deformation would give rise to "episodic" resurfacing to much younger times in the highlands, a result consistent with lower crater densities seen in highland regions.

Plains Tectonism on Venus:
The Deformation Belts of Lavinia Planitia

STEVEN W. SQUYRES and DAVID G. JANKOWSKI

Center for Radiophysics and Space Research, Cornell University, Ithaca, New York

MARK SIMONS, SEAN C. SOLOMON, BRADFORD H. HAGER

Department of Earth, Atmospheric, and Planetary Sciences, Massachusetts Institute of Technology, Cambridge

GEORGE E. MCGILL

Department of Geology and Geography, University of Massachusetts, Amherst

High-resolution radar images from the Magellan spacecraft have revealed the first details of the morphology of the Lavinia Planitia region of Venus. A number of geologic units can be distinguished, including volcanic plains units with a range of ages. Transecting these plains over much of the Lavinia region are two types of generally orthogonal features that we interpret to be compressional wrinkle ridges and extensional grooves. The dominant tectonic features of Lavinia are broad elevated belts of intense deformation that transect the plains with complex geometry. They are many tens to a few hundred kilometers wide, as much as 1000 km long, and elevated hundreds of meters above the surrounding plains. Two classes of deformation belts are seen in the Lavinia region. "Ridge belts" are composed of parallel ridges, each a few hundred meters in elevation, that we interpret to be folds. Typical fold spacings are 5–10 km. "Fracture belts" are dominated instead by intense faulting, with faults in some instances paired to form narrow grabens. There is also some evidence for modest amounts of horizontal shear distributed across both ridge and fracture belts. Crosscutting relationships among the belts show there to be a range in belt ages. In western Lavinia in particular, many ridge and fracture belts appear to bear a relationship to the much smaller wrinkle ridges and grooves on the surrounding plains: Ridge morphology tends to dominate belts that lie more nearly parallel to local plains wrinkle ridges, and fracture morphology tends to dominate belts that lie more nearly parallel to local plains grooves. We use simple models to explore the formation of ridge and fracture belts. We show that convective motions in the mantle can couple to the crust to cause horizontal stresses of a magnitude sufficient to induce the formation of deformation belts like those observed in Lavinia. We also use the small-scale wavelengths of deformation observed within individual ridge belts to place an approximate lower limit on the venusian thermal gradient in the Lavinia region at the time of deformation.

INTRODUCTION

Of the many linear tectonic features known to be present on Venus prior to the Magellan mission, most attention was devoted to the spectacular mountain belts found in the Maxwell Montes and elsewhere [e.g., *Campbell et al.*, 1983; *Barsukov et al.*, 1986; *Basilevsky*, 1986]. It has also been known, however, that there is considerable evidence for tectonism on the venusian plains. The "ridge belts" described on the basis of Arecibo and Venera 15/16 data are particularly good examples. In Venera 15/16 images they are most abundant in Atalanta Planitia, a lowland region in the northern hemisphere. Like the highland mountain belts, ridge belts were inferred to consist of subparallel ridges and grooves. However, they appeared to be elevated comparatively little above the surrounding plains. The ridges and grooves that form them are approximately parallel to the margins of the belts, and can be continu-

ous along strike for hundreds of kilometers. Spacings of individual ridges, as determined from the low-resolution Arecibo and Venera 15/16 data, were seen to be typically a few tens of kilometers. The belts in Atalanta Planitia are themselves crudely parallel, with typical belt-to-belt spacings of 300–400 km. In some locations, both in Atalanta and elsewhere, individual ridges and furrows not organized into belts also were observed. A compressional origin for the ridge belts was the most widely accepted hypothesis prior to Magellan [e.g., *Barsukov et al.*, 1986; *Crumpler et al.*, 1986], although an extensional origin also was suggested [*Sukhanov and Pronin*, 1989].

The first deformation belts on the venusian plains observed by the Magellan spacecraft have been those on Lavinia Planitia, in Venus's southern hemisphere. *Solomon et al.* [1991] presented a preliminary description of some of the belts of Lavinia. They noted that there were two classes of belts and concluded that both had a compressional origin. In this paper we discuss the belts of Lavinia in detail, using improved data and expanded imaging coverage. Because the Magellan images have shown the belts to have significantly greater mor-

phologic diversity than was apparent in previous data sets, we have followed *Solomon et al.* [1991] by adopting the general term "deformation belts" for these features, retaining the term "ridge belt" for one of the morphologic subtypes.

In preparing this paper, we have primarily made use of three Magellan data products: full-resolution mosaicked image data records (F-MIDRs), compressed mosaicked image data records (C1-MIDRs), and global topographic data records (GTDRs). F-MIDRs are synthetic aperture radar (SAR) image mosaics that retain the full spatial resolution of the radar system, sampled at 75 m/pixel. C1-MIDRs contain the SAR data resampled at 225 m/pixel. Altimetry is taken from GTDRs, which contain measurements of local planetary radius made by the Magellan altimeter, sampled to a uniform planetary grid and spatially filtered for smoothing. The along-track spatial resolution of the altimeter varies from about ~8 km near the equator to ~20 km at high latitudes, and the across-track resolution varies similarly from ~13 to ~30 km [*Pettengill et al.*, 1991]. Due to a software error, the altimetric results for Lavinia and

elsewhere presented by *Solomon et al.* [1991] are incorrect at small spatial scales, and we present improved altimetric data here.

GEOLOGIC UNITS

Most of Lavinia Planitia is seen in the Magellan C1-MIDR 45S350, shown in Figure 1. Several geologic units, defined on the basis of radar brightness, small-scale texture, characteristics and abundance of superposed structural features, and apparent relative ages, can be distinguished in this area. Because the SAR incidence angle in this region averages about 25°, the radar return relates primarily to wavelength-scale roughness and, less commonly, to meter-scale and larger slopes; the effects of compositional variations should be minor. Consequently, many, and perhaps most, of the geological units are distinguished by differences in surface characteristics rather than differences in inherent material properties. For some units, such as lobate flows, radar units very likely correspond to those defined using more conventional geological criteria. Other units, however,
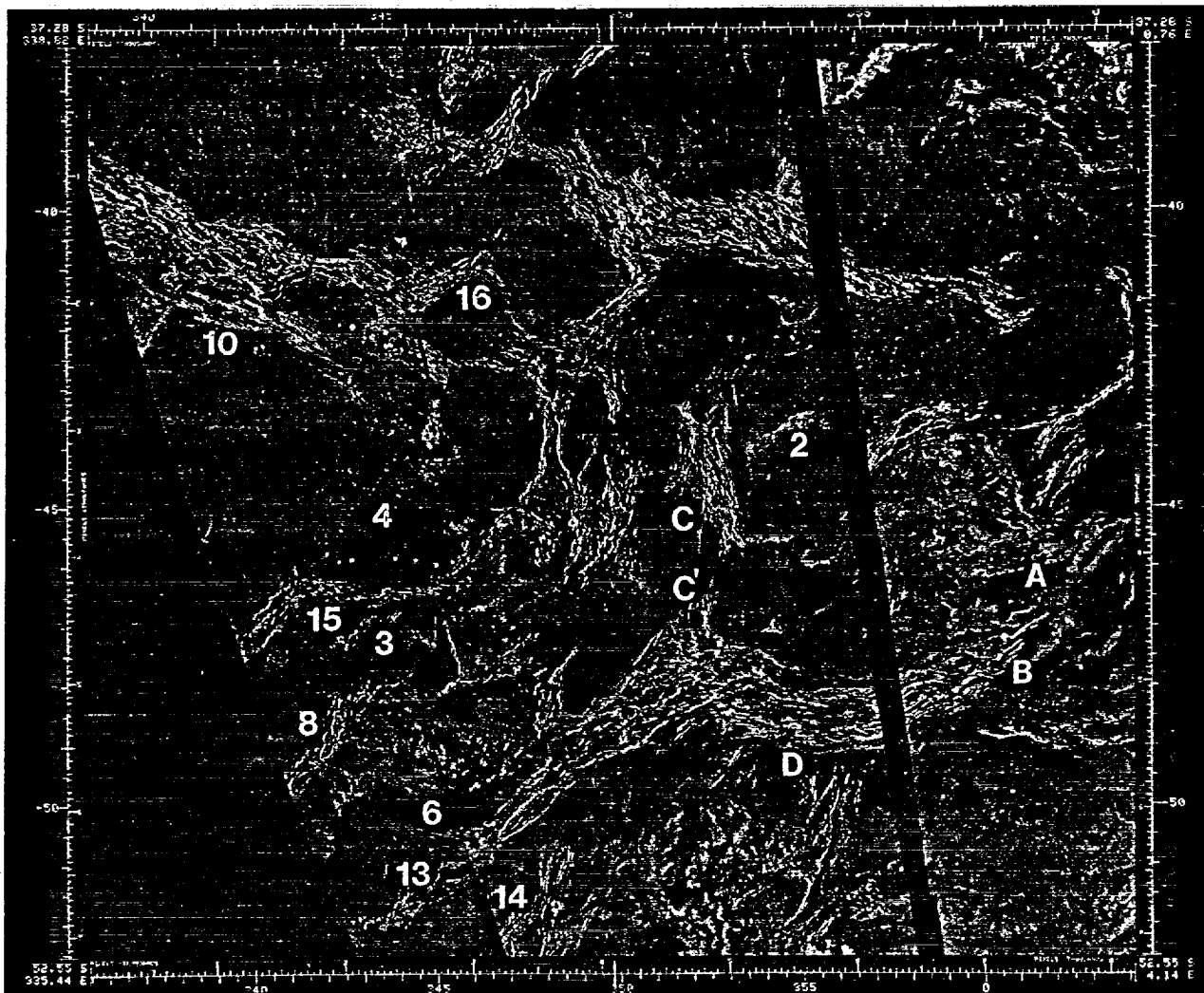

Fig. 1. Magellan radar mosaic of Lavinia Planitia, in sinusoidal equal-area projection. The image is centered at 45°S, 350°E, and the width of the image is 1843 km. Letters refer to features discussed in the text. Numbers give the locations of other figures. As for all other radar mosaics in this paper, north is at the top and the radar illumination direction is from the left.

may represent similar materials that have experienced different structural evolutions, with consequently different surface textures at centimeter and meter scales.

We divide the terrains of Lavinia Planitia into four broad groups: complex ridged terrains (CRT), textured terrains, regional plains, and digitate plains. We have defined one CRT unit, one textured unit, two regional plains units, and one digitate plains unit. The following paragraphs describe the units in approximate order from oldest to youngest.

Complex Ridged Terrain

CRT occurs in Lavinia Planitia as scattered inliers surrounded and embayed by younger plains deposits (Figure 2). These inliers are characterized by a strong linear trend of kilometer-scale or narrower ridges and troughs, with a weaker secondary trend of lineaments at a high angle to the strong primary trend present locally. CRT is much brighter than surrounding plains on the SAR images unless the plains are intensely fractured.

Textured Terrain

Many areas in Lavinia are as radar-bright as CRT but do not exhibit the same kilometer-scale ridge-and-trough pattern. In places, it is possible to resolve a very regular fabric of bright lines at a scale of about 400 m, and it is this fabric that gives this material its textured appearance (Figure 3). At the scale of the Magellan SAR images, this fabric can be considered penetrative. The structural cause of the fabric cannot be determined, but a uniformly spaced set of joints is one possibility. Textured terrain occurs in two distinct physiographic forms: (1) as plains that are significantly brighter than adjacent regional plains materials, and (2) as long, narrow ridges generally grouped together into ridge belts (see below). Crosscutting and embayment relationships in some instances indicate that textured terrain is younger than CRT and older than regional plains. Nevertheless, both textured terrain and regional

Fig. 2. Complex ridged terrain, exposed through younger plains materials. Width of the image is 190 km. See Figure 1 for location.

Fig. 3. Textured terrain. Width of the image is 150 km. See Figure 1 for location.

plains are of variable brightness, and therefore there are places where it can be difficult to define the contact between them. The penetrative fabric and, indeed, the overall textured aspect are not evident in places where textured terrain is intermediate in character between well-defined textured terrain and bright mottled plains.

Regional Plains

The areally dominant terrain type in Lavinia Planitia consists of moderately radar-dark to moderately radar-bright plains. Regional plains materials are most likely of volcanic origin, but morphologic forms resembling flows are rare.

Mottled plains. These are moderately bright to locally bright plains with a "blotchy" or mottled texture at kilometer and smaller scales (Figure 4). They are generally characterized by abundant superposed wrinkle ridges (see below). In places, mottled plains include large numbers of small shields or domes from a few to about 20 km in diameter. Locally, it is possible to define two members of mottled plains that differ in radar brightness. At many such locations it is the brighter and apparently older of the two members that includes the small shields and domes, which are surrounded by the darker and apparently younger member (Figure 4).

Dark plains. These are plains that are darker, have more uniform radar backscatter, and have fewer super-

Fig. 4. Mottled plains materials. Darker member in the lower right appears to surround small domes and shields in the lighter member in the upper left. Also note abundant wrinkle ridges. Width of the image is 155 km. See Figure 1 for location.

posed wrinkle ridges than mottled plains. Dark plains commonly occur as small patches adjacent to or within fracture belts (see below), where they are superposed on the fractures. In other places, however, dark plains appear to grade into the dark member of the mottled plains (Figure 4).

Digitate plains

This unit consists of complexes of digitate to locally lobate flows, many attaining lengths of hundreds of kilometers (A in Figure 1). Most of these flows are brighter on the SAR image, and hence probably rougher at centimeter scales, than all other plains units. Feeder channels (or collapsed lava tubes) are apparent in several places, and many flow complexes can be traced upslope to sources of apparent volcanic origin. Superposed wrinkle ridges are sparse, and flow patterns clearly indicate that adjacent deformation belts already existed as topographic ridges when these flows were emplaced.

TECTONIC FEATURES

Wrinkle Ridges

Most of the plains areas of Lavinia contain long, narrow, sinuous linear features that appear brighter than the background plains (Figure 4). These features are generally less than 1 km wide and a few tens of kilometers long, although some reach widths of several kilometers and lengths in excess of 100 km. Typical spacings range from several to about 20 km and locally up to 50 km. Where the topography of these features can be inferred from brightness variations in the SAR images, they are clearly seen to have positive relief, although most appear as simple sinuous bright lineaments. We interpret these features as compressional ridges, analogous to the wrinkle ridges commonly seen on the lunar maria and Martian ridged plains [e.g., *Plescia and Golombek*, 1986; *Watters*, 1988].

The wrinkle ridges of Lavinia Planitia show strong preferred orientations within subareas of the region (Figure 5a). A very strong NNE-SSW trend is apparent in the western portion of the map, while the trend is N-S in the central portion and NNW-SSE in the northeast portion. These trends are also evident in rose diagrams of ridge segment orientations (Figure 5b).

Wrinkle ridges appear to have formed throughout the evolution of plains, because all plains units have them, including digitate plains. However, there is a clear decrease in the number of ridges from mottled plains to dark plains to digitate plains; that is, there is a decrease in ridge concentration with decreasing inferred age. Furthermore, the trends of the ridges appear related to locality rather than stratigraphic age because the dominant trend of the sparse ridges on digitate plains is similar to the dominant trend of the more abundant ridges on adjacent regional plains. These relationships suggest that ridge formation is an ongoing process related to local stress fields that did not change significantly during the deposition of the various plains materials. Although local stress fields varied geograph-
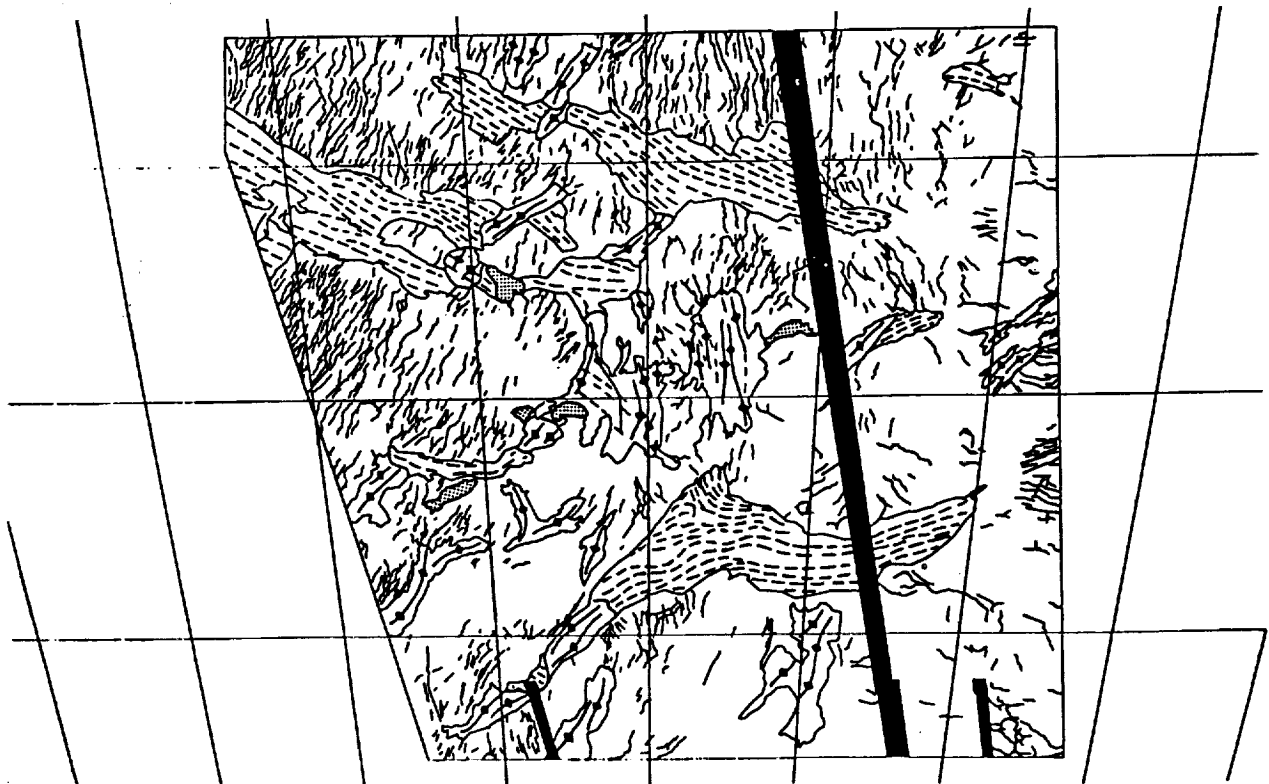

Fig. 5a. Map of wrinkle ridges (lines on plains) and deformation belts in Figure 1. For fracture belts, fracture trends are shown by dashed line patterns; for ridge belts, ridge trends are shown by lines with diamond symbols. Shaded regions are complex ridged terrain.
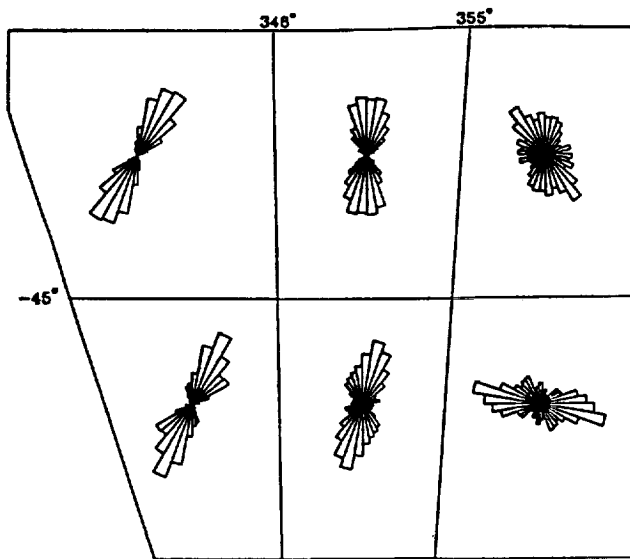
Fig. 5b. Rose diagrams of wrinkle ridge orientations in six sub-areas of Figure 1. Diagrams are normalized to have equal total lengths.

ically during plains formation, they apparently did not vary substantially with time in any one locality.

Grooves

Over much of the western part of Lavinia Planitia are WNW trending radar-bright lineaments. They are geometrically distinct from the wrinkle ridges in that they are both longer and substantially straighter. In many instances they are too narrow to be resolved as anything but radar-bright lines, but where they can be resolved they are seen to be narrow grooves (Figure 6). Lengths from 25 to 75 km are common in some areas, while lengths of 150 to 200 km are common in others. A few grooves have lengths exceeding 500 km. Spacings are also variable. The longest grooves (lengths exceeding 200 km) show typical spacings of 30 to 100 km. Heavily deformed regions show typical spacings of 1 to 3 km. Groove widths are generally about 300 to 700 m. There are no instances of these grooves cutting digitate flows, but it is not clear if this is because the flows are younger or simply because these grooves were never formed in the eastern portions of Lavinia where such flows occur. The grooves clearly are younger than mottled and dark plains. Abutting relationships with wrinkle ridges suggest that some ridges are older than adjacent grooves, some younger. We interpret these grooves to be narrow grabens.

A map of grooves in Lavinia Planitia shows the parallel nature of the grooves in the western part of the region (Figure 7). It is noteworthy that in all areas where grooves are present, their orientations are perpendicular to those of the wrinkle ridges. Thus, a significant section of Lavinia Planitia is characterized by a distinctive pattern of orthogonal compressional and extensional features on the plains between the deformation belts.
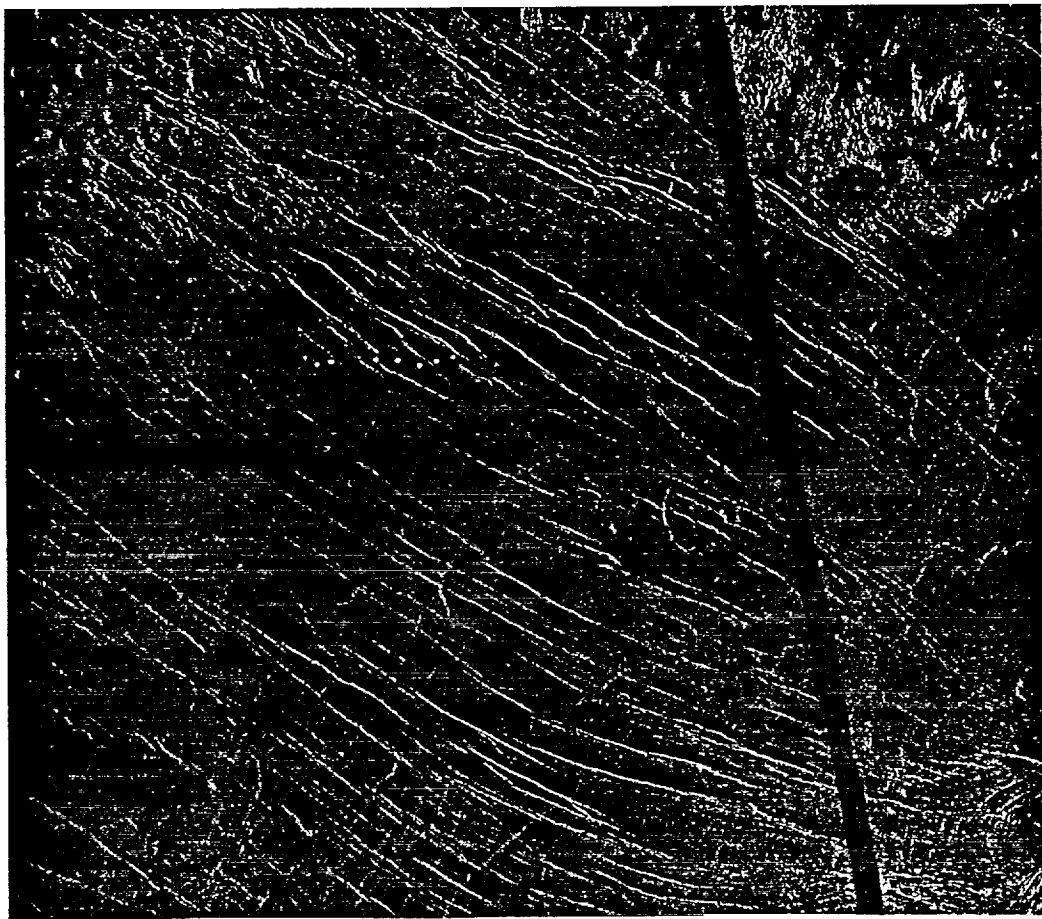

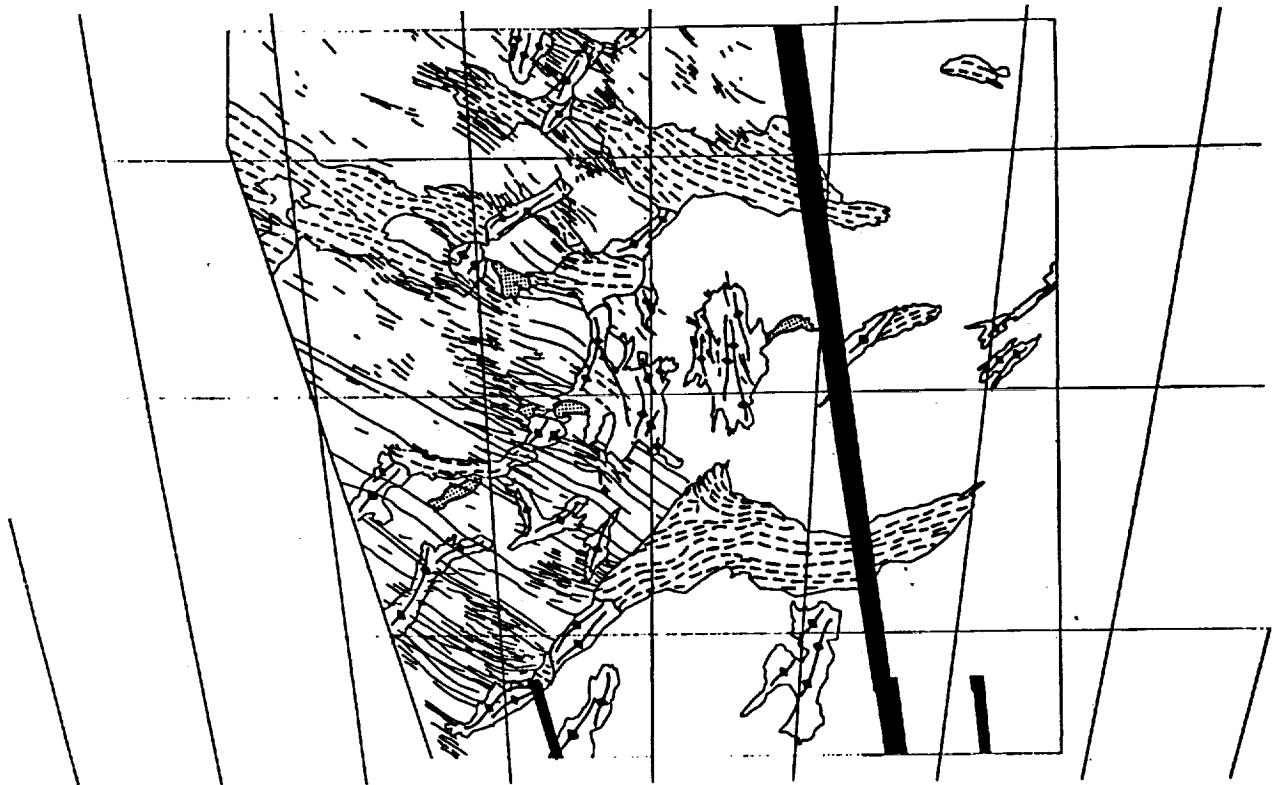Fig. 6. Grooves on the plains. Width of the image is 205 km. See Figure 1 for location.

Fig. 7a. Map of grooves (lines on plains) and deformation belts in Figure 1. For fracture belts, fracture trends are shown by dashed line patterns; for ridge belts, ridge trends are shown by lines with diamond symbols. Shaded regions are complex ridged terrain.
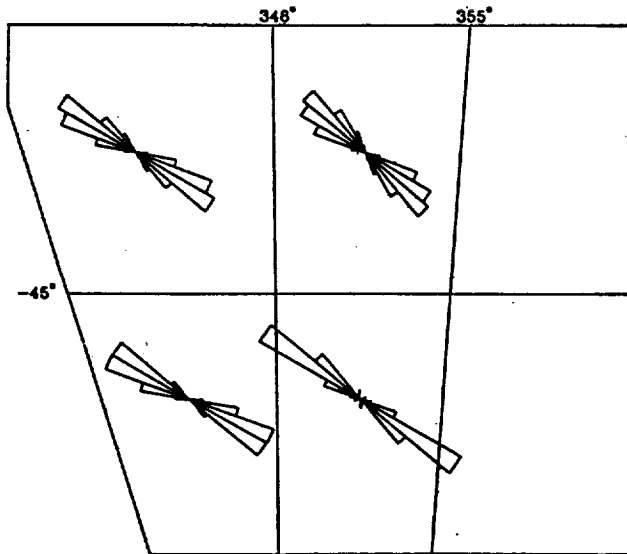

Fig. 7b. Rose diagrams of groove orientations in six subareas of Figure 1. Normalization is as in Figure 5b.

Ridge Belts

The most obvious tectonic features of Lavinia Planitia are the prominent deformation belts that transect much of the surface. These belts take two very distinct forms, which we call ridge belts and fracture belts. An example of a ridge belt is shown in Figure 8. The ridges that compose them can vary considerably in width both from one to the next in a given belt and along the length of a single ridge. The maximum width observed

is about 10 km, and more typical widths are a few kilometers. Some ridges appear symmetric in cross section, while others appear steeper on one flank than the other. A smooth, archlike profile is most common, but some ridges show a narrow, rugged secondary ridge superimposed on the crest or on one flank of the arch, as is common for lunar wrinkle ridges. The ridges are typically rather sinuous and commonly bifurcate and merge along strike, producing a complex anastomosing pattern. Some ridges appear to consist of textured terrain material, but in most places the unit involved is not apparent.

It would be desirable to construct detailed topographic profiles across ridge belts, but the individual ridges are too narrow to be resolved by the Magellan altimeter, and the single SAR view obtained during the first mapping cycle does not permit stereo analysis. There is, however, one approach that can be used to construct such profiles. One of the belts (Figure 8) is cut by several of the tectonic grooves discussed above. While these grooves appear very straight where they lie on the adjacent plains, they take on a distinctive cuspate curvature as they cross each ridge in the belt. It is likely that this curvature is an effect of the radar viewing geometry; the low radar incidence angle at this latitude (about 23°) results in the groove, as it passes across the elevated ridge, appearing displaced in the direction of the spacecraft.

If we make the assumption that the grooves are actually straight in map view as they cross the ridges, we can use the apparent local deviation of the groove
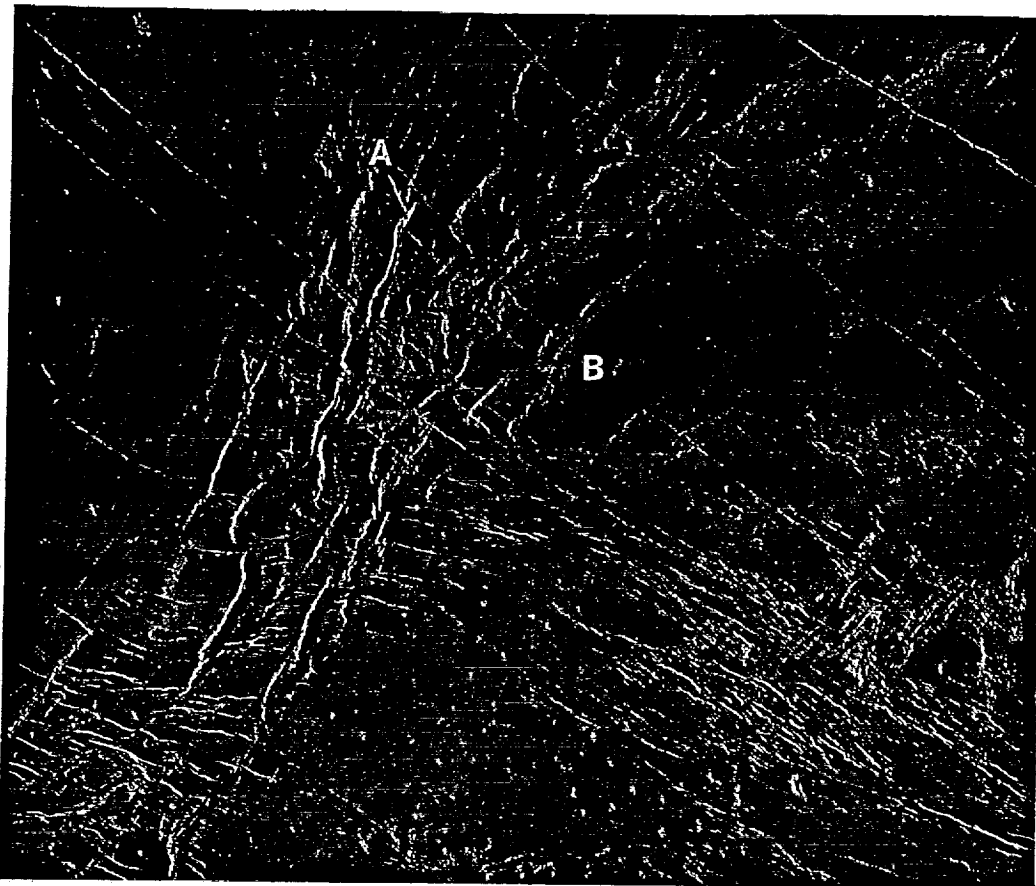
Fig. 8. A ridge belt. Width of the image is 205 km. See Figure 1 for location. A and B are endpoints of the topographic profile in Figure 9.

trend, plus a knowledge of the radar viewing geometry, to construct a topographic profile. Such a profile is shown in Figure 9. Most of the ridges in this profile are fairly symmetric, with archlike profiles, widths of several kilometers, and heights of 200-300 m. (This approach to producing a topographic profiles is, of course, fundamentally limited by the correctness of the assumptions on which it is based. The detailed heights and shapes of the ridges in the profile may be fairly accurate, since grooves elsewhere tend to be very straight on scales comparable to the ridge width. The overall height of the belt in the profile, however, should not be regarded as accurate, since subtle curvature of the grooves over length scales of many tens of kilometers is common.)

The individual ridges within ridge belts differ little in appearance from the largest wrinkle ridges, except that they tend to be less sinuous. Because both types of ridges are inferred to result from compressional deformation, this similarity is not too surprising. Where ridge belts deforming textured terrain are embayed by plains materials with wrinkle ridges, large, young wrinkle ridges can be distinguished from older ridges of the belt. The possibility must be entertained, however, that ridge belts can evolve from wrinkle ridges and thus be younger than the adjacent regional plains at some locations.

Fracture Belts

The other class of deformation belts found in Lavinia

Planitia is the fracture belt (Figure 10). In contrast to ridge belts, fracture belts are dominated by a complex pattern of linear to arcuate faults and fractures. Many faults appear singly, but others are paired to
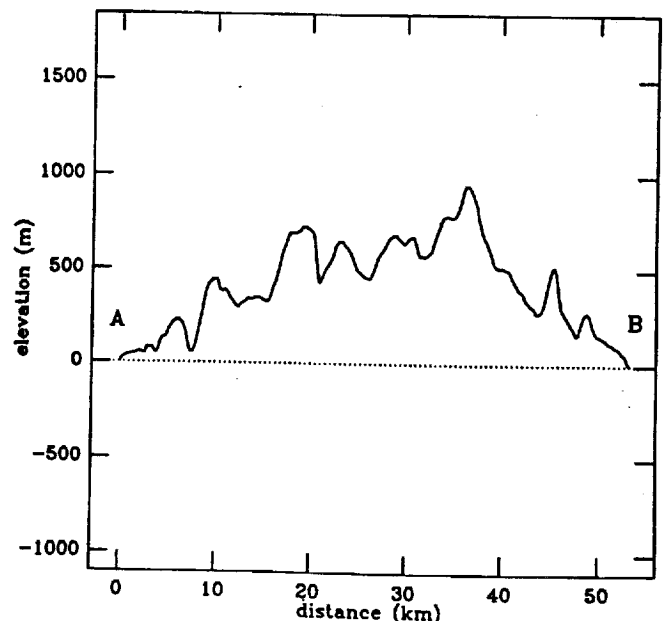

Fig. 9. Inferred topographic profile across the ridge belt in Figure 9, constructed from the apparent displacement of a groove as it crosses the belt.

form grooves with widths ranging from a few kilometers down to the resolution limit of the images. The faults commonly display complex anastomosing and crossing patterns that indicate repeated or progressive deformation. Where fracture belts change trend, or where belts bifurcate or merge, the pattern of faults is especially intricate.

In general, fracture belts deform mottled plains materials but not dark plains materials. The obvious diversion of flows and of channels in digitate flow fields around some fracture belts in eastern Lavinia (B in Figure 1) and the truncation of the fractures by flows indicate quite clearly that these fracture belts are older than the digitate flow fields.

A noteworthy aspect of a few of the fracture belts is that in some parts of them two distinct scales of deformation are observed. Faults are spaced very closely (typically a few hundred meters) almost everywhere they are present in fracture belts. However, in a few locales these closely spaced faults are concentrated in bands of intense deformation that are separated by nearly undeformed materials. The bands typically are spaced 20-30 km apart. It was reported by *Solomon et al.* [1991] that these bands of intense deformation co-incided with local highs in the altimetry, and this was interpreted to mean that the faulting might be a consequence of brittle deformation across the crests of anticlines. However, as mentioned above, this inference was based on incorrectly processed altimetric data. In Figure 11 we present the same altimetric scan across one of the fracture belts, Hippolyta Linea, that was shown by *Solomon et al.* [1991], here using the reprocessed altimetry. It now appears that the intensely fractured bands within the belts are not higher than the adjacent materials; if anything, they may be lower. Definitive treatment of this problem will have to await acquisition and processing of stereographic data, but at present the idea that the bands coincide with anticlinal crests appears uncertain. An alternative possibility is that the bands are regular concentrations of extensional deformation caused by necking instabilities.

Much of the faulting that is so prominent in the fracture belts is similar in appearance, though much greater in density, to the faulting on the plains that forms the grooves there. In fact, there are a number of instances (e.g., Figures 1 and 10 and Figure 17 below) where faulting in fracture belts continues onto the plains, at much lower density, to form widely spaced grooves. As is the
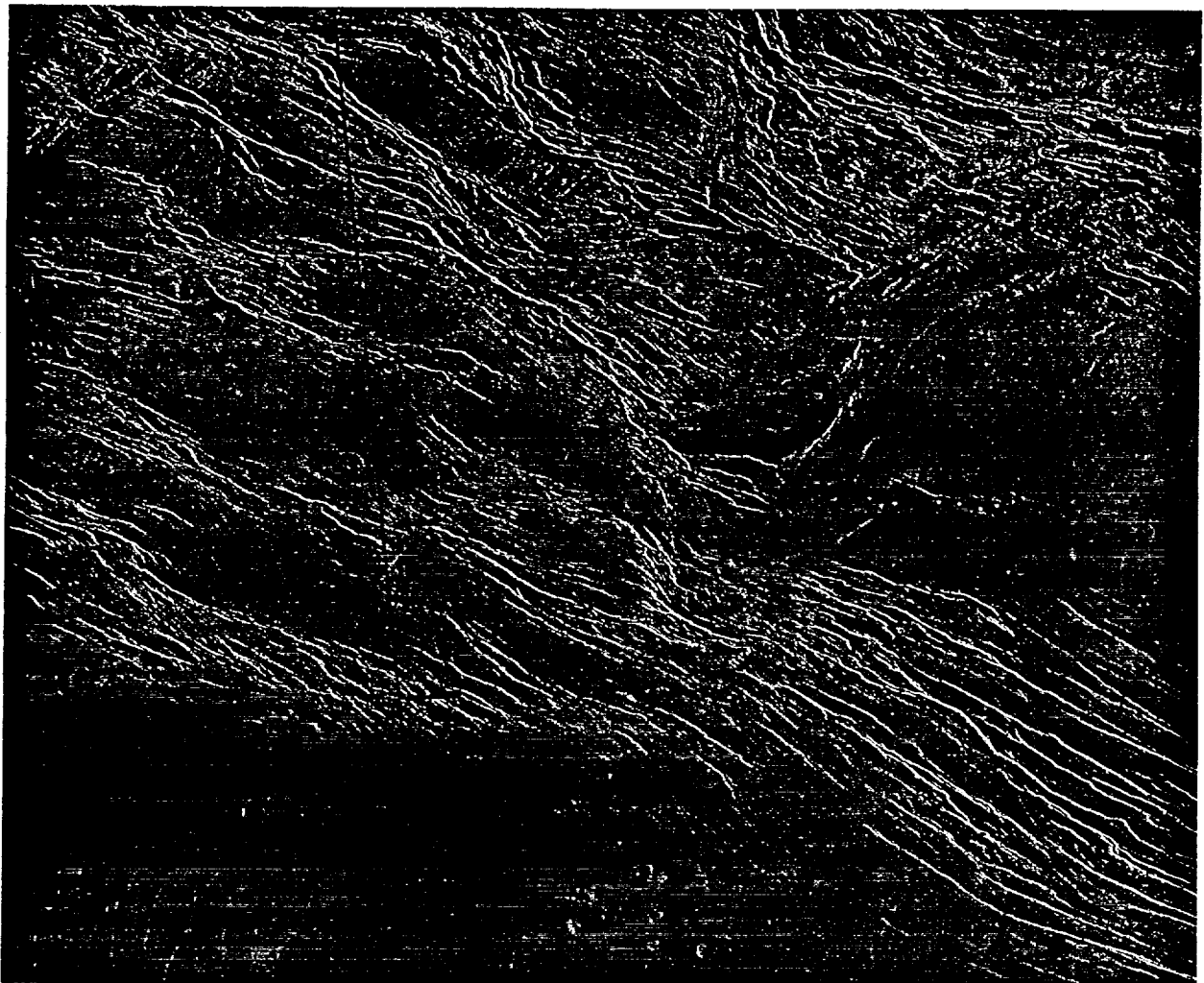

Fig. 10. A fracture belt. Width of the image is 260 km. See Figure 1 for location. The altimeter ground track for orbit 415 is shown. Arrows correspond in position to arrows in Figure 11.
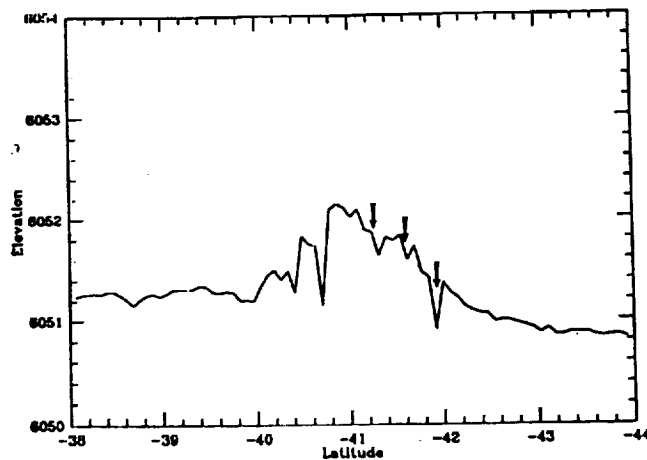
Fig. 11. Altimetry data from orbit 415. Arrows correspond in position to arrows in Figure 10.

case for the ridge belts and the wrinkle ridges, then, there appears to be a close relationship between faulting in fracture belts and the formation of grooves.

ALTIMETRY

Magellan altimetry data have also provided the first detailed look at the topography of Lavinia Planitia. Figure 12 presents a topographic contour map for the Lavinia region. Overall, Lavinia is a broad, low plain, lying at a typical planetary radius of about 6050.5 km. The regional topography rises gradually by more than 1 km to the northwest, northeast, and southeast. The general rise in elevation to the east continues well beyond the edge of our map and culminates in a line of several large coronae south of Alpha Regio [Stofan et al., this issue]. A prominent characteristic of the altimetry of Lavinia is that both types of deformation belts are elevated above the surrounding plains.

The fracture belts appear in general to reach higher elevations than the ridge belts. A number of the fracture belts reach elevations that are as much as 1 km above the level of the adjacent plains, and elevations 500 m above the plains within fracture belts are the norm. Particularly high elevations commonly are found in complex and intensely deformed regions present at bends and junctions in fracture belts. In contrast, maximum relief of 200-300 m is more typical for the ridge belts, and some of the ridge belts are not evident at all in the altimetric data. Some care must be exercised in interpretation of the altimetry, however, as determination of surface elevation for a given altimeter pulse can depend sensitively on both the large-scale and small-scale surface roughness within the pulse footprint. Roughness on a large scale can cause multiple echoes that severely complicate the range-finding algorithm. Roughness on a small scale can result in a surface scattering law that deviates from the one assumed in fitting the shape of the leading edge of an echo, again affecting the range-finding process. In any case where two terrains of significantly different roughness are observed, systematic variations in elevation between them must be treated with caution.
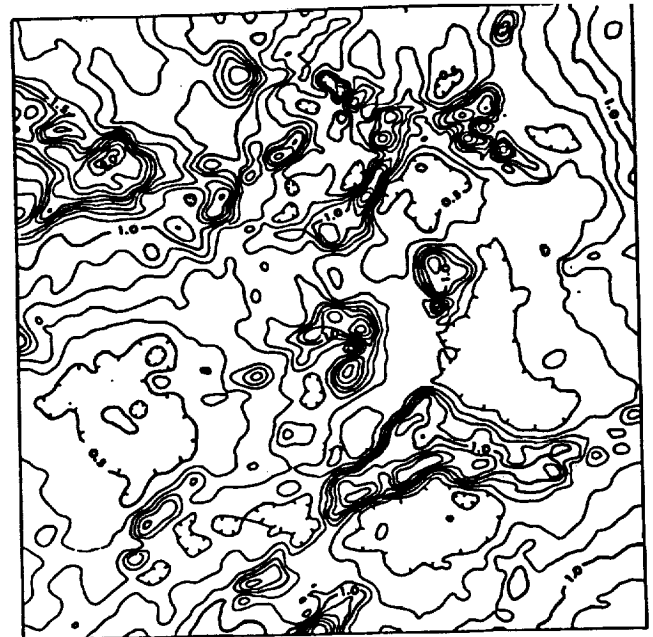
Lavinia: Contour Interval = 100m
Latitude: 44.2S - 50.9S
Longitude: 347.8E - 356.9E (at north edge)

Fig. 12. Topographic contour map for the area covered by Figure 1, in sinusoidal equal-area projection. Elevations are referenced to a planetary radius of 6050.0 km.

GEOLOGIC RELATIONSHIPS

Evidence for Horizontal Shear in Deformation Belts

Solomon et al. [1991] presented two pieces of evidence for modest amounts of horizontal shear parallel to the axes of deformation belts. These are shown in Figures 8 and 10. In Figure 8, an old set of plains grooves exhibits an S-shaped bend consistent with distributed left-lateral shear as it crosses the ridge belt. In Figure 10, the fracture belt exhibits a number of instances where paired faults form rhombohedral downdrops, in a manner similar to what is seen in terrestrial settings where extension is coupled with shear. In this instance, the inferred sense of horizontal shear across the belt is right-lateral.

There are several other instances in Lavinia Planitia where patterns developed within deformation belts can be interpreted as very large-scale analogs of familiar kinematic indicators seen in terrestrial shear zones. One of these (Figure 13) shows a series of S-shaped minor folds along the lengths of individual ridges within a ridge belt. S folds of this geometry are indicative of left-lateral (sinistral) movement and in this instance would imply sinistral shearing parallel to the length of the ridge belt. The belt showing the S folds terminates to the SSW against a contact with mottled plains, and there is no indication of sinistral slip within these plains. Consequently, the inferred belt-parallel sinistral slip must be older than the mottled plains. It either represents a late stage in the development of the ridge belt or implies that the ridge belt is transpressional (com-

Fig. 13. S-shaped folds in a ridge belt, with orientations consistent with left-lateral shearing of the belt. Width of the image is 120 km. See Figure 1 for location.
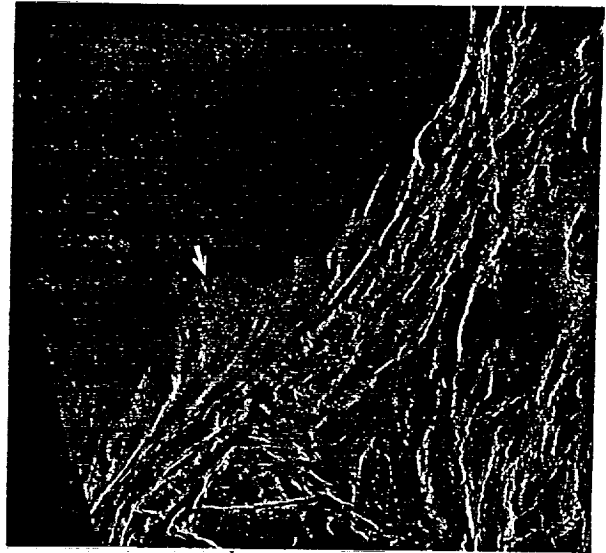

Fig. 14. Penetrative fabric in textured terrain that is distorted with a geometry consistent with right-lateral shear across a ridge belt. Width of the image is 125 km. See Figure 1 for location.

pression plus sinistral shear) rather than purely compressional in origin.

A second example of a possible kinematic indicator (Figure 14) involves the distortion of well-developed penetrative fabric in textured terrain as the fabric impinges on a throughgoing, strongly lineated boundary of a ridge belt. This boundary abruptly truncates all structures within the belt and is interpreted to be a shear zone. If this inference is correct, the distortion of the fabric at this location implies a right-lateral (dextral) sense of shear.

Age Relationships Among Belts

The deformation belts in Lavinia did not all form contemporaneously. Instead, they show some significant variability in age, both with respect to the plains materials surrounding them and with respect to one another. As noted above, a number of belts, particularly in western Lavinia, appear to deform the same material that constitutes the adjacent plains, with little or no subsequent volcanism. In the ridge belts, the transition from dark or mottled plains adjacent to the belt to the textured terrain of the belt is not necessarily a stratigraphic one in all cases; we cannot rule out the possibility that in some instances the texturing simply resulted from the folding of the plains material. However, there are other very clear instances where belts are embayed and partially buried by lavas that postdate the belt deformation. The N-S fracture belt at C in Figure 1 is one of these, and it may have once been contiguous with another aligned and partially buried N-S belt at C'.

An example of a clear crosscutting relationship involving two belts is shown at D in Figure 1. Here a N-S belt has been largely buried by lavas, and these lavas have in turn been deformed to form an E-W belt that crosscuts the N-S one. This case in particular demonstrates that belt formation in Lavinia took place over an extended period of time, during which which belt formation episodes were interleaved with plains volcanic events.

Regional Tectonic Trends

As noted above, there are two classes of deformation

belts in the Lavinia region, and each appears related to tectonic features on the intervening plains. Specifically, ridges of the ridge belts are morphologically similar to and in some cases contiguous with plains wrinkle ridges, and faults of the fracture belts are similar to and in some cases contiguous with plains grooves. In some parts of Lavinia, however, these relationships may be more fundamental, as suggested by Figures 5 and 7. The morphologic form taken by each deformation belt, ridge belt or fracture belt, appears related in many instances to the orientation of the belt with respect to the orthogonal tectonic features on the adjacent plains. Belts whose orientations are closest to those of the plains grooves in their vicinity tend to be fracture belts, while those whose orientations are closest to those of local wrinkle ridges tend to be ridge belts. Even more notably, there are instances, as in Figure 15, where a single belt changes from one trend to the other, and in so doing also changes tectonic style from one belt type to the other. In addition, there are some belts (e.g., Figure 16) where both ridges and fractures are common within the belt and where the ridges lie parallel to local plains wrinkle ridges and the fractures lie orthogonal to them and parallel to local plains grooves.

There are exceptions to this relationship. The most obvious one is the N-S fracture belt at C in Figure 1. In this same belt, some ridges also are present and lie parallel to fractures, rather than perpendicular to them. Other belts departing from the general relationship occur farther to the east. Despite these exceptions, the relationship described above appears sufficiently prevalent, particularly in western Lavinia, that it must be accounted for in some fashion. The belts in central and eastern Lavinia that deviate from the general pattern are in most cases very clearly buried and embayed by younger volcanic deposits and perhaps are formed in a stress field distinct from the one responsible for most of the wrinkle ridges and grooves.
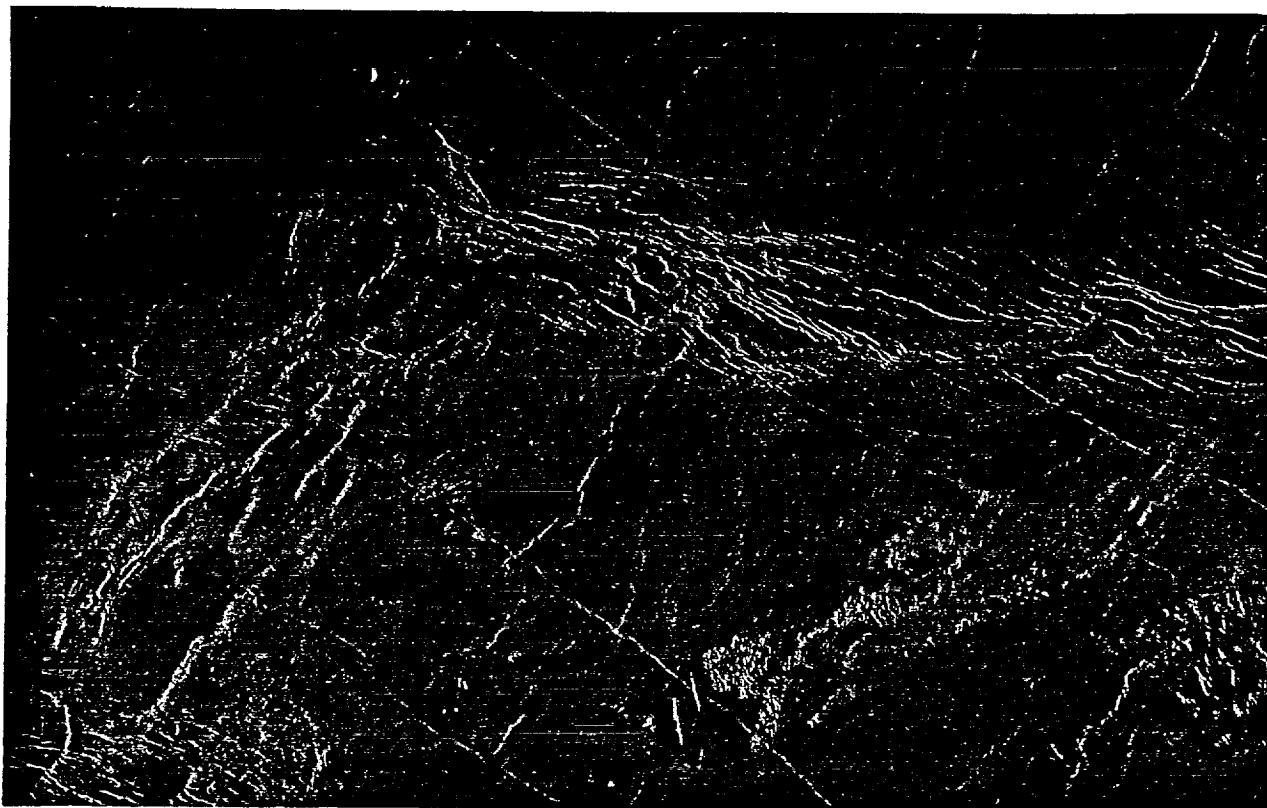
Fig. 15. A deformation belt that changes from a ridge belt to a fracture belt along its length. Width of the image is 290 km. See Figure 1 for location.

DISCUSSION

Geologic Evolution of Lavinia Planitia

The description above of geologic units and tectonic features in Lavinia Planitia leads us to some preliminary interpretations:

Regional tectonic pattern on the plains. The orthogonal pattern of compressional wrinkle ridges and extensional grooves that transects the plains units over much of Lavinia Planitia is remarkable in its regularity and in both its spatial and temporal extent. These characteristics indicate that at least the near-surface materials of Lavinia have been subjected to a stress field that has been generally uniform, both spatially and temporally, for much of the region's history. This conclusion is not unique to Lavinia, since a variety of regular tectonic patterns are observed on the plains elsewhere on the planet [*Solomon et al.*, 1991, this issue].

It is tempting to think of the wrinkle ridges and grooves on the plains as the simple manifestations of thrust faulting and normal faulting, respectively, and this interpretation may well be correct. If so, it has some interesting implications. A common approach to predicting faulting style from stress field descriptions is that of *Anderson* [1951]. With the Anderson faulting criteria, however, no single set of values of the three principal stresses σ_1, σ_2, and σ_3 simultaneously predicts orthogonal grabens and thrust faults. Applying Anderson criteria rigorously, one can obtain either thrust faults or grabens from a given stress field orientation, but not both.

Orthogonal thrust faults and grabens may both be formed, according to Anderson criteria, if the two stress components in the plane of the surface maintain their relative values but vary appropriately with respect to the vertical stress. One way this could take place would be for the in-plane stresses to vary relative to the vertical stress over time. Another would be if fault initiation for the two classes of features took place at different depths [*Golombek*, 1985], near the surface for thrust faults and at depth for grabens, so that in the former case the vertical stress is σ_3 and in the latter case it is σ_1. (The depth is limited, however, since many grabens are very narrow.)

In either of these scenarios there is a stress state, intermediate in either time or depth, for which Anderson criteria would predict strike-slip faulting. Clear evidence for strike-slip faulting is rare on Venus (and indeed on most of the terrestrial planets save Earth), and is lacking entirely on the plains of Lavinia. One explanation offered for the absence of strike-slip motion on other planets is that layered mechanical discontinuities concentrate stress, and hence fault initiation, at certain depths (and hence at certain confining stresses) where faults with styles other than strike-slip tend to be initiated [*Golombek*, 1985]. Another possibility is simply physical restriction of lateral movement. A planet has
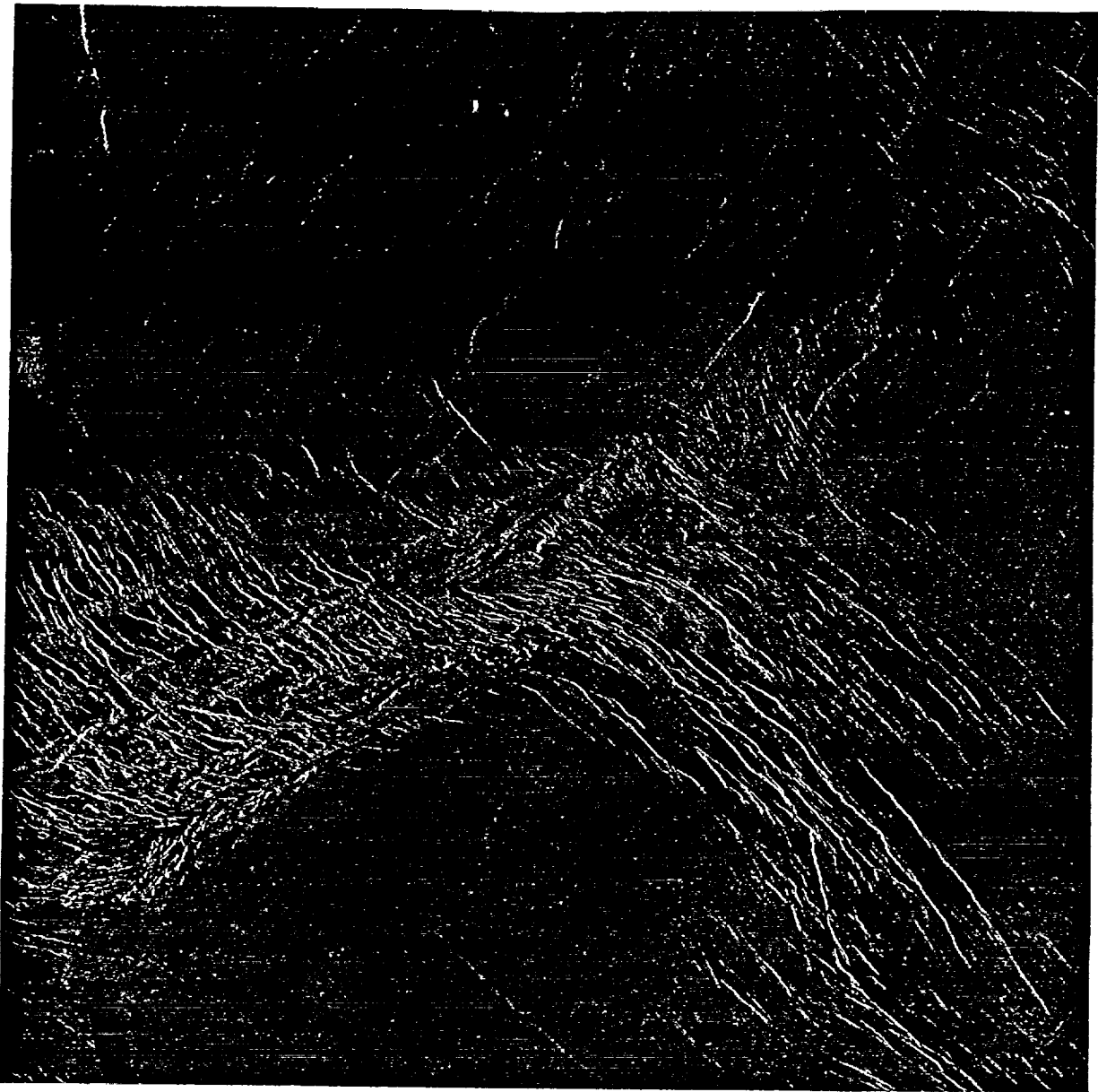
Fig. 16. A deformation belt that exhibits both ridges and fractures, with approximately orthogonal orientations. Width of the image is 240 km. See Figure 1 for location.

a free surface and a ductile region at depth, so thrust and normal faulting within the strong upper crust can always be accommodated by vertical motions, and the stress at the base of a fault cutting the entire strong upper layer can relax by ductile flow. On a one-plate planet or within the interior of a single lithospheric plate, however, there may be restrictions on the extent of horizontal strain, and stress relaxation at the ends of strike-slip faults will not be comparable to that for dip-slip faults. It may be that such restrictions inhibit most large-scale (i.e., easily observed) strike-slip motions in Lavinia. Schultz and Zuber [1991] have recently suggested that in situations where the lithosphere is vertically loaded, tensile failure rather than shear failure may relieve much of the stress and may suppress the zone in which shear failure criteria predict strike-slip faulting.

Deformation belts. In contrast to pre-Magellan expectations, we now know that there are two distinct classes of deformation belts (ridge belts and fracture belts) in Lavinia. A particularly important question is whether or the not ridge belts and fracture belts both owe their origin to a similar mechanism. Evidence suggesting that they do includes geometric similarities between the two classes of belts (widths, positive topographic signatures, patterns traced across the plains) and, particularly, the observation that a few belts undergo a transformation from ridge morphology to fracture morphology along their length. Similar changes in morphology along the length of a belt occur in the deformation belts of Atalanta Planitia as well [Solomon et al., this issue]. It is clear, however, that whatever the underlying cause of belt formation, the surface tectonic

expressions of ridge and fracture belts are markedly different.

Because of the gross similarities of both types of belts, and particularly because both are elevated, one reasonable working hypothesis is that both result from belt-normal crustal shortening and thickening [*Solomon et al.*, 1991]. In the case of the ridge belts, this argument is straightforward: the ridges are interpreted to be folds formed by ridge-normal compression. In the case of the fracture belts, however, the argument is really based only on the altimetry. All of the belts lie higher than the surrounding plains and hence are attributed in this interpretation to a thickening, via belt-normal shortening, of the buoyant crust.

A difficulty with the idea that both types of belts share a common origin is that the most straightforward interpretation of the observed tectonic features in the fracture belts runs directly counter to this interpretation. While near-surface materials in the ridge belts have been deformed to produce folds, the same materials in fracture belts are intensely faulted in what appears to be a manifestation of near-surface extension. One could interpret these belts, then, as being wholly extensional features, with the uplift a consequence of lithospheric heating or igneous intrusion. Alternatively, in the compressional interpretation, the observed faulting could be the consequence of stretching of brittle surface materials across the crest of an archlike uplift whose underlying origin is compressional. The strongest argument that both belt types owe their origin to the same process may be that single belts exist that exhibit both morphologies, depending on their local trend.

While the great extent and uniformity of the orthogonal tectonic pattern of Lavinia indicate that the near-surface materials there have been subjected to a stress field of significant spatial and temporal regularity, the deformation belts of Lavinia, in contrast, are geometrically very irregular and can change trend substantially along their length, bifurcating and merging to form an intricate pattern. If there is a single underlying belt formation process, then the irregular orientations of the belts with respect to the orthogonal pattern of the plains suggest that this process is not related in a simple manner to the one responsible for the near-surface stresses expressed on the plains. The morphologic manifestation of each belt nonetheless commonly depends on the orientation of the belt with respect to the tectonic pattern of the plains: ridge belts form where the belt is perpendicular to the regional compressive stress, and fracture belts form where the belt is perpendicular to the regional extensional stress. In both cases there apparently can be some distributed shear across the belt, as indeed is likely to be the case when the belt axis is not perfectly orthogonal to any principal stress.

The source of stress responsible for formation of the deformation belts of Lavinia is not known, but mantle convection must be considered the prime candidate. It has been suggested that the Venusian mantle may lack an Earth-like asthenosphere [e.g., *Phillips*, 1990]. If this is the case, convective stresses can couple strongly to the lithosphere and can lead to deformation of the lithosphere at wavelengths comparable to the spacing of the Lavinia deformation belts [*Zuber*, 1987, 1990].

The surface manifestation of convective stresses, however, will also depend on the rheologic structure of the crust. A model in common use for crustal and upper mantle rheology on Venus involves a crust of basaltic composition overlying an olivine-rich mantle. This configuration can lead to a layered rheologic structure, with a strong upper crust, a ductile lower crust, a strong upper mantle, and ductile mantle material below [*Zuber*, 1987; *Banerdt and Golombek*, 1988]. A weak lower crust may be relatively ineffective in transmitting convective stresses to the upper crust.

We cannot presently answer the question of whether the mantle motions and resultant stresses that led to formation of the two classes of belts in the Lavinia region were fundamentally the same. In some respects the interpretation of the data is more straightforward if they were not, since the surface morphologic expressions of the two belt types are quite different. However, we have already noted the arguments for the view that both belt types share a common underlying origin, and these arguments appear fairly persuasive. Because the pattern of the belts is so complex, stresses produced in the strong upper mantle by convection must also have been complex, both spatially and temporally. The stresses that produced surface deformation on the plains, however, must have been spatially and temporally quite regular. The surface stress field must therefore have resulted from the superposition of (1) stresses generated by mantle convection and transmitted across the ductile lower crust with (2) stresses in the strong upper crust of unknown origin that were much more regular in space and time. The former stresses are expressed at the surface primarily by the elevated belts themselves. The latter stresses must have dominated the in-plane components of stress in near-surface materials, controlling both the orientation of the plains tectonic features and the style of deformation within the belts. A mixed stress field of this sort might be enabled by a ductile lower crust that incompletely transmits stresses from the upper mantle to the upper crust.

Our observations of the Lavinia region raise a number of questions:

1. What process is responsible for the stress field that produced the orthogonal tectonic pattern on the plains, both here and elsewhere on Venus?

2. What process is responsible for the stresses that produced the elevated deformation belts, and for the concentration of the deformation into discrete belts?

3. What do the dominant wavelengths of deformation, both within and among the belts, indicate about the mechanical properties of the venusian crust and mantle?

4. If the two classes of belts share a common origin, is there a fully self-consistent stress distribution and history that can produce the deformation observed?

5. If the two classes of belts have fundamentally different origins, why are they so similar in some respects? Why are there belts with both characteristics, and especially belts that change style along their length? Why are the fracture belts different from rift zones elsewhere on the planet?

In the two sections that follow, we make a first attempt to address questions 2 and 3 above. The others

will be left for consideration in future work.

Dynamical Models for Belt Formation

We have argued above that the large-scale morphology of deformation belts, and of the ridge belts in particular, may be consistent with the hypothesis that these features are products of lithospheric shortening and crustal thickening. This was also the conclusion reached by most investigators prior to the Magellan mission, and previous workers have postulated this shortening to be the result of convective downwelling centered beneath lowlands regions [Zuber, 1990; Bindschadler et al., 1990; Phillips et al., 1991]. In this section we use finite element models to investigate quantitatively the relationship between mantle convection and crustal deformation, with particular emphasis on the conditions favoring the formation of deformation belts.

The geometry and characteristic spacing of the deformation belts of Atalanta Planitia suggest that these features result from lithospheric instabilities induced by horizontal extensional or compressional stress [Zuber, 1987]. There are two characteristic scales of deformation associated with these belts: one describing the spacing of features (e.g., ridges) within the belts, and one describing the spacing of the belts themselves.

Linear stability analysis indicates that two scales of deformation can arise given sufficient compression or extension if the lithosphere is rheologically stratified, i.e., if a weak lower crustal layer is sandwiched between a relatively strong upper mantle and a strong upper crust. A stress-dependent rheology is required for the instabilities to grow. Zuber [1990] suggests that the compressional stresses required to induce the instabilities may be supplied by mantle convection. This hypothesis requires that the stresses associated with the motions of the mantle couple into the overlying crust. The high correlation of long-wavelength topography and gravity and the large apparent depths of compensation suggest that Venus lacks an upper-mantle low-viscosity zone [Kiefer et al., 1986; Bills et al., 1987; Phillips et al., 1991; Smrekar and Phillips, 1991]. If so, then mantle convection should indeed couple strongly to the lithosphere, and patterns of mantle flow should have recognizable signatures in surface topography and deformation [Phillips, 1986, 1990].

On the basis of analytical models of convection-induced crustal flow [e.g., Bindschadler and Parmentier, 1990; Schmeling and Marquart, 1990], the crust may be regarded as having two responses to convective
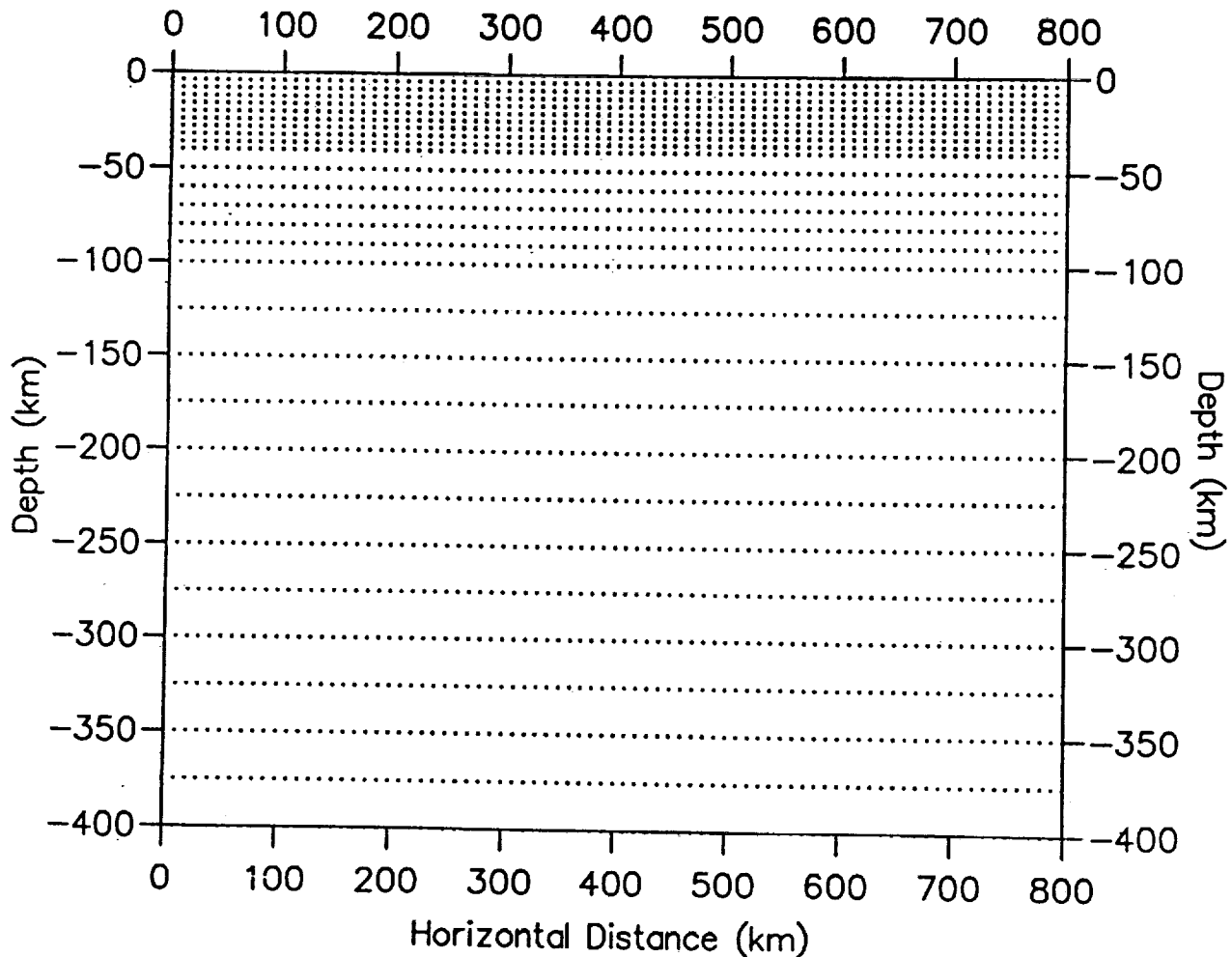

Fig. 17. The finite element mesh used for calculations of convectively induced deformation of the crust. The mesh is 28 by 80 elements with a highest vertical resolution of 4 km in the upper 40 km.

downwelling. The first is a "flexural" response, during which the surface and crust-mantle boundary can be thought of as deforming "in phase." Following this mode of deformation, the crust responds by thickening, and eventually the surface and the crust-mantle boundary become anticorrelated.

Simons et al. [1991] have proposed that deformation belts like the ones observed in Lavinia Planitia can form during the transition from the initial flexural response to the later phase of crustal thickening, and we expand on this suggestion here. We illustrate this proposal by means of idealized finite-element models of the dynamic interaction between the crust and mantle. The crust and mantle in these models are treated as viscous fluids, and a modified version of the two-dimensional Cartesian finite-element program ConMan [*King et al.*, 1990] is employed. A passive marker chain tracks the crust-mantle interface and permits variation in the crustal buoyancy as well as specification of different crustal and mantle rheologies. In addition to the flow field, the stress field in the lithosphere and the surface topography are readily calculated.

We use an irregular finite element mesh that is 28 elements high and 80 elements wide (Figure 17). Our maximum resolution is in the 40-km-thick top layer, where each element is 4 km high and 10 km wide. In all, the mesh is 800 km in the horizontal dimension and 400 km in the vertical dimension. We impose free-slip boundary conditions on the top and side walls, with no flow through these walls. On the bottom boundary, flow is constrained to be vertical, with no deviatoric normal stress permitted. In effect, this last boundary condition gives us a virtual 800 km by 800 km box. The surface topography is calculated from the vertical stresses on the top wall of the box. Top and bottom temperatures are fixed at 500°C and 1250°C, respectively. Initially, we impose a linear temperature gradient across the thermal boundary layer and set the rest of the mantle to be nearly isothermal with a small sinusoidal temperature perturbation imposed throughout the box to initiate flow.

Our exploratory models have a constant viscosity mantle overlain by a crust of greater constant viscosity. As noted above, the viscosity in the actual Venusian crust and mantle is likely to vary with depth; in these simple models the higher viscosity crust is intended to represent a strong surface layer capable of being deformed by stresses induced by mantle convective motions. We adopt a reference mantle viscosity of 10^{21} Pa s, a crustal density of 3000 kg m^{-3}, and a mantle density of 3300 kg m^{-3}. We use initial crustal thicknesses of 12 and 25 km, and ratios of crustal viscosity to mantle viscosity of 25, 50, and 100. In all these models, convection produces horizontal compressive stresses in the lithosphere that overlies downwelling mantle and extensional stresses in the lithosphere that overlies upwelling mantle. As the convective vigor increases, so does the magnitude of the compressive stress over the downwelling, with stress in the crust reaching values in excess of 100 MPa in about 100 m.y. (Figure 18). Note that the rate of increase in compressive stress decreases with increasing crustal viscosity. This is because the stronger the crust, the more the development of the
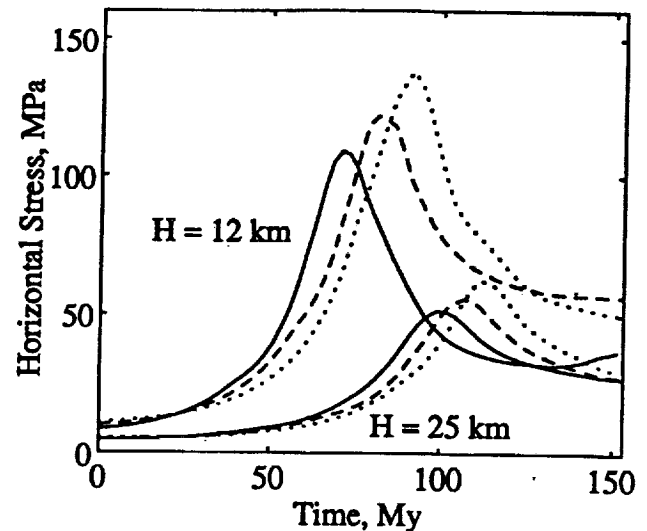

Fig. 18. Development of horizontal compressive stress versus time in models of convectively induced crustal deformation. Stress is measured at the top right-hand (downwelling) side of the model. Models shown include crust/mantle viscosity ratios of 25 (solid line), 50 (dashed line), and 100 (dotted line), and a crustal thickness *H* of 12 or 25 km. Note the similarities among the curves and the peak in compressional stress.

convective instability in the mantle driving the deformation is impeded. We also find that the magnitude of the peak compressive stress achieved above the downwelling increases with higher viscosities and/or with thinner initial crustal layers; the stronger the crustal lid, the larger the tractions from mantle convection supported by the crust. Since force balance on the crust requires that shear traction integrated along the base be balanced by normal stresses integrated through its thickness, the thinner the crust, the larger the horizontal stresses.

The topography over the downwelling undergoes a complex evolution in these models (Figure 19). Initially, the effect of stresses induced by downgoing mantle dominates, producing topographic lows. After reaching a minimum, the topography grows due to the isostatic contribution from the thickened crust. We suggest that if the deformation belts are the result of compressive stress and that mantle convection is the source of this stress, then the belts will develop at or before the time of maximum horizontal compressive stress. This time corresponds to the transition from decreasing to increasing topography.

Theory derived by *Biot* [1961] shows that horizontal compression of a buoyant viscous plate overlying a viscous substratum will have a dominant wavelength that depends on the difference in layer densities $\Delta\rho$, the ratio of viscosities η_c/η_m, the applied stress P, and the layer thickness H_c. For values of the quantity $P/(\Delta\rho g H_c)$ less than about 7, the amplification of folds becomes insignificant. For one of our models described above, with $\eta_c/\eta_m = 100$, $H_c = 12$ km, $\Delta\rho = 300$ kg/m^3, and $P = 100$ MPa, the dominant wavelength is about 100 km. However, these parameters are near the threshold conditions for significant fold amplitudes.

Our initial results show that coupling of convective motions to the lithosphere will cause significant crustal
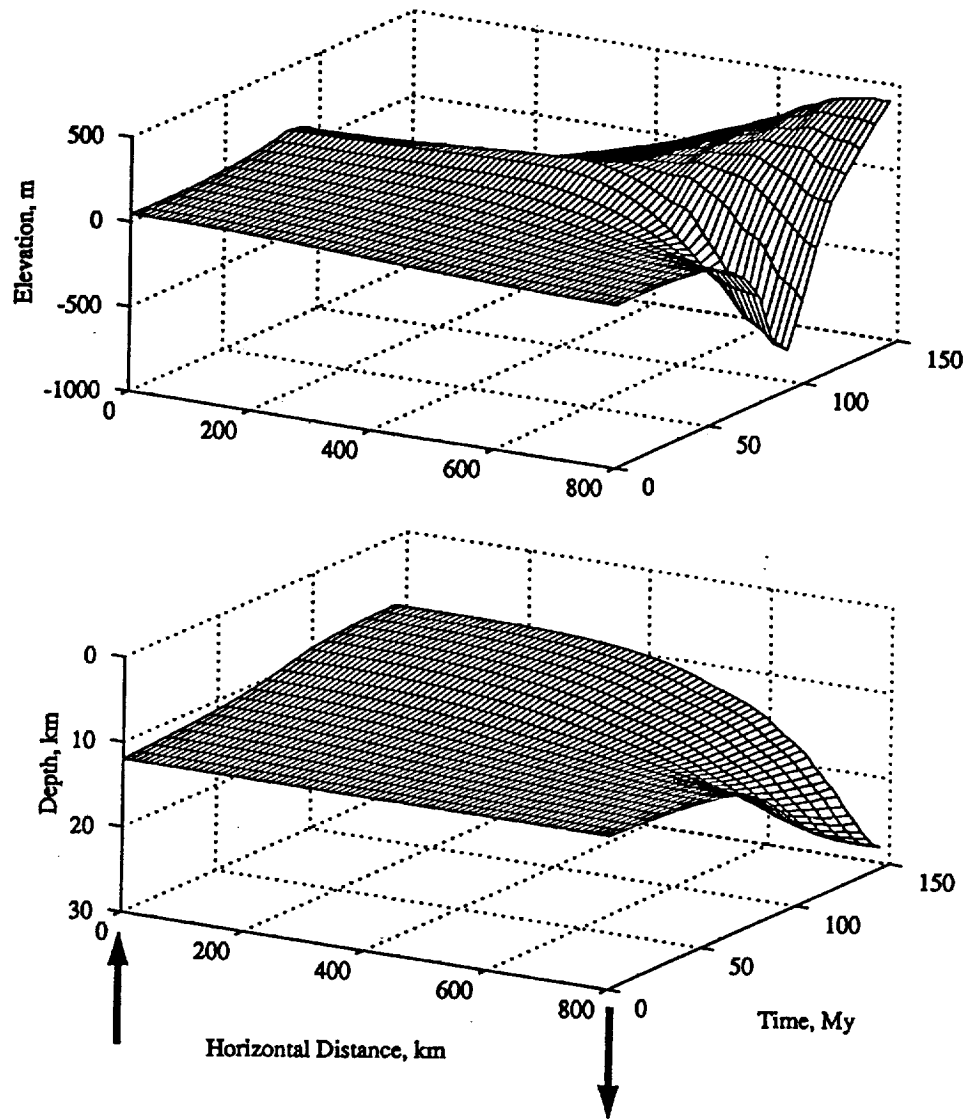
Fig. 19. Evolution of surface elevation (top) and the depth to the crust-mantle interface (bottom) with time for a model of crustal deformation induced by mantle convection. Note the initial decrease in elevation over the zone of downwelling (downward arrow), followed by an eventual increase in elevation. Note also the steady increase in crustal thickness over the zone of downwelling. The initial crustal thickness, H_c, is 12 km, and the ratio of crustal viscosity to mantle viscosity is 70.

deformation. This deformation is complex and highly time dependent. Our results are preliminary, and modeling with more realistic rheologies is in progress. However, the simple rheologies assumed here are sufficient to generate stress fields that, together with simple theory [Biot, 1961], predict the predominant wavelength of deformation seen in Lavinia Planitia. This theory may also explain why the belts are only generated for a finite period of time before they become overwhelmed by larger-scale deformation.

Buckling Within Individual Ridge Belts

We have argued that the ridge belts observed on Lavinia Planitia are fold belts, formed by buckling of a strong upper crust in response to ridge-normal compression. If this interpretation is correct, then we may use observations of ridge geometry, along with a simple mechanical model of buckling, to place some quantitative

constraints on the structure of Venus's crust at the time of ridge formation. We model the ridges here as having formed due to a buckling instability in an elastic layer with a depth-dependent yield strength subjected to a compressive end force. Our general approach follows that of Banerdt and Golombek [1988]. We consider the strength of the venusian lithosphere to be determined by two deformation mechanisms: brittle failure and ductile flow [see Brace and Kohlstedt, 1980]. At a given depth, the local pressure and temperature determine the yield stress for each mechanism; the lithospheric strength is taken to be the weaker of the two.

In our modeling, the critical differential stress for brittle failure is taken to be $\tau = \mu\sigma_n$ [Byerlee, 1978], where τ and σ_n are the shear and normal stresses, respectively, and μ is the coefficient of friction. The critical differential stress for ductile flow is derived from the

creep equation $\dot{\varepsilon} = A\sigma^n \exp(-Q/RT)$, where $\dot{\varepsilon}$ is the strain rate, σ is the differential stress, R is the gas constant, T is the absolute temperature, and Q and n are experimentally determined constants. We take values for these constants appropriate for dry diabase [*Caristan*, 1982].

An example of a lithospheric strength profile for horizontal compression calculated from the above models is given by the heavy solid line in Figure 20. The strength increases linearly with depth near the surface (in the brittle regime) due to the increasing lithostatic stress and then decreases exponentially (in the ductile regime) due to the thermal gradient. For this figure we use a surface temperature of 720 K, a thermal gradient (assumed constant) of 15 K km^{-1}, and a strain rate of 10^{-15} s^{-1}. Now, consider how the strength profile of Figure 20 responds to an applied stress of of 70 MPa (the dashed vertical line in the figure). Only those depths with a lithospheric strength exceeding the applied stress (between Z_t and Z_b) will support the entire stress load elastically. Depths above Z_t will only support part of the load elastically (up to the yield stress) and will undergo brittle failure. Depths below Z_b will only support part of the load and will undergo ductile creep.

At the crust-mantle boundary, a change in composition can create another rheologic transition. Mantle material on Venus has been assumed in most models to be olivine-rich in composition and hence to possess much higher yield stresses than the crust, leading to another brittle-ductile failure envelope in the upper mantle [e.g., *Zuber*, 1987; *Banerdt and Golombek*, 1988]. In line with the calculations above, this deeper strong zone could be responsible for longer wavelengths of deformation on Venus. Here we only consider short-wavelength folding and take it to be a function only of the crustal

failure envelope, neglecting the potential influence that the coupling between the crust and mantle discussed in the previous section could have on the stress field.

An elastic plate overlying an inviscid fluid will buckle if subjected to a sufficiently large compressive end load. The critical force required is given by [*Turcotte and Schubert*, 1982, p. 124]

$$F_c = \left[\frac{Eh^3 \rho g}{3(1-\nu^2)}\right]^{1/2}, \tag{1}$$

where E, h, and ν are the Young's modulus, thickness, and Poisson's ratio of the plate, respectively, ρ is the fluid density, and g is the gravitational acceleration. Given this force, the elastic plate will deform with a characteristic wavelength

$$\lambda = 2\pi \left[\frac{Eh^3}{12(1-\nu^2)\rho g}\right]^{1/4}. \tag{2}$$

This simple buckling model was adapted by *McAdoo and Sandwell* [1985] to the more complicated case for which the elastic plate possesses a brittle-ductile strength envelope as discussed above. They found that equations (1) and (2) hold quite well if the plate thickness is set equal to the thickness of the "elastic core", defined as the region for which the strength of the lithosphere exceedes the applied stress (i.e., the thickness of the region between Z_t and Z_b in Figure 20). This approach avoids the unreasonably high critical buckling stresses found when finite strength envelope is ignored. The critical load for this model is determined by equating the left side of equation (1), now taken as an integral over the entire thickness of the crust of the supported stress, to the right side of equation (1), with the elastic core thickness set as the effective plate thickness. Since both sides of the equation depend upon the applied stress, the critical load and corresponding buckling wavelength must be solved iteratively. In all of our calculations, the derived critical buckling stress is smaller than the maximum lithospheric strength; therefore an elastic core exists and buckling occurs before complete lithospheric failure.

The dominant wavelength of folding determined by the above model depends on three parameters: the crustal thickness, the thermal gradient, and the strain rate. Figure 21 shows contour plots of the dominant wavelength of folding, in kilometers, as a function of these parameters. In each plot, one parameter is held constant. Figure 21a assumes a thermal gradient of 25 K km^{-1}; Figure 21b assumes a strain rate of 10^{-16} s^{-1}; Figure 21c assumes a crustal thickness of 10 km. All results are calculated assuming a surface temperature of 720 K, a density for the ductile lower crust of 2800 kg m^{-3}, a Young's modulus of 100 GPa, and a Poisson's ratio of 0.25.

Figure 21 shows that the folding wavelength is not very sensitive to the crustal thickness, particularly for thicknesses greater than about 10 km. This is a result of the rapid dropoff in lithospheric strength (see Figure
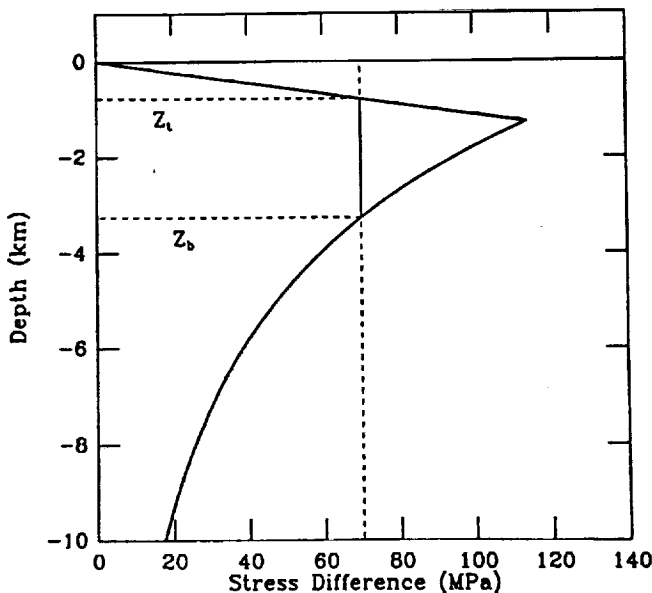

Fig. 20. A typical strength envelope for the venusian crust, showing strength as a function of depth, with an upper regime controlled by frictional failure on faults and a lower regime controlled by ductile flow. Calculations are for a dry diabase rheology, a surface temperature of 720 K, a thermal gradient of 15 K km^{-1}, and a strain rate of 10^{-15} s^{-1}.

20) due to ductile creep. The bottom of a thick crust contributes very little strength to the crust, and therefore has comparatively little influence on the folding mechanics. As the crustal thickness decreases, the folding wavelength shows more and more of a dependence, with the thinnest crust yielding the shortest wavelengths. Of course, the development of a second, longer wavelength of deformation does depend strongly on crustal thickness [Zuber, 1987, 1990].

The thermal gradient and strain rate both can have a significant effect on the folding wavelength. Increasing the thermal gradient decreases the wavelength, while increasing the strain rate increases the wavelength. Of course, as Figure 21c demonstrates, the folding wavelength can remain essentially constant as the combination of a relatively large strain rate and thermal gradient is varied to a relatively small strain rate and thermal gradient. This behavior is a consequence of the form of the creep law for the ductile deformation. Increasing the thermal gradient and decreasing the strain rate both lower the ductile yield stress of the crust, thinning the lithosphere and decreasing the resulting folding wavelength.

In Figure 21d, we have set the folding wavelength to 8 km, a value representative of ridge spacing in the ridge belts of Lavinia Planitia. This allows us to vary all three of the key model parameters simultaneously. The contours show the thermal gradient required, in kelvins per kilometer, to produce folding with a wavelength of 8 km, as a function of strain rate and crustal thickness. Ultimately, we would like to be able to use this plot to constrain the thermal gradient in Lavinia at the time of deformation. In order to do this, however, we need to know the strain rate involved in ridge belt formation. Given the geometry of the belts and typical estimates of the age of the Venusian surface, a strain rate corresponding to 10% shortening per 100 m.y. is probably an extreme lower limit; this value is 8×10^{-17} s^{-1}. Taking this as the strain rate, Figure 21d yields a minimum thermal gradient of ~30 K km^{-1}. This value is somewhat greater than previous estimates obtained by similar arguments [Zuber, 1987, Banerdt and Golombek, 1988]. The difference is attributable to the ability of Magellan to resolve buckling features with smaller wavelengths than were inferred from low-resolution data. Although Figure 21d suggests that the
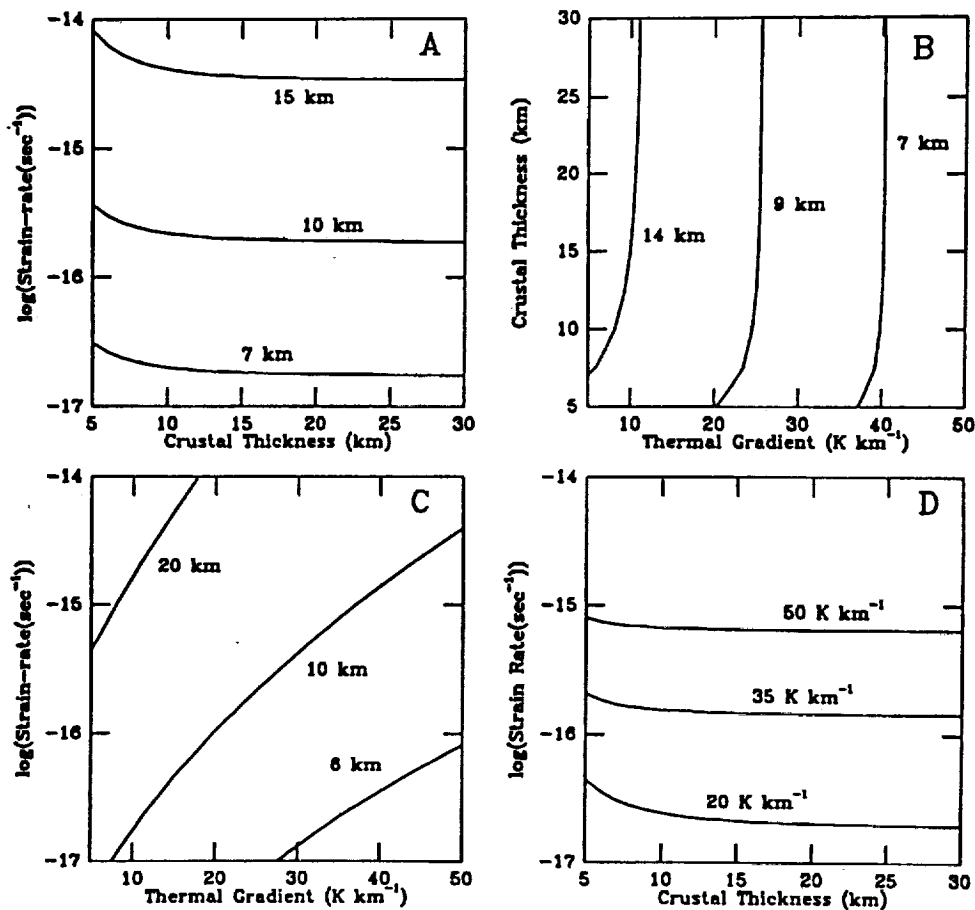

Fig. 21. Results of buckling calculations for the Venusian crust. (a) Dominant buckling wavelength as a function of strain rate and crustal thickness, assuming a thermal gradient of 25 K km^{-1}. (b) Dominant buckling wavelength as a function of crustal thickness and thermal gradient, assuming a strain rate of 10^{-16} s^{-1}. (c) Dominant buckling wavelength as a function of strain rate and thermal gradient, for a crustal thickness of 10 km. (d) Thermal gradient as a function of strain rate and crustal thickness for a buckling wavelength (8 km) typical of the values observed in the ridge belts of Lavinia Planitia.

crustal thickness is not well constrained, the thickness of the elastic core is well constrained, with a value near about 200 m over the entire parameter space.

As noted above, these results assume complete decoupling between the crust and mantle. If some degree of coupling does exist, as we assumed in the convection model above, the buckling wavelengths presented here would increase [Banerdt and Golombek, 1988], leading to still higher inferred thermal gradients. Conversely, the buckling wavelengths would decrease if lithospheric strengths are reduced near the brittle-ductile transition by semibrittle deformation processes [Kirby, 1980]. Finally, we note that there is significant uncertainty in the choice of creep law parameters for the Venusian crust and that changes in a number of parameters chosen could have a significant effect on the results.

CONCLUSIONS

The Magellan spacecraft has provided the first detailed look at the deformation belts of the Venusian lowland plains. In some ways, these observations appear consistent with pre-Magellan expectations. The belts are elevated zones of intense tectonic deformation, and plausible arguments may be made that they are the consequence of crustal shortening and thickening. The observed scales and spacings of the belts may yield information about the strength properties of the lower crust and upper mantle, and the spacings of tectonic features within the belts may carry information about the strength properties of the upper crust [Zuber, 1987, 1990]. However, there are some surprises as well, the most notable one being the fact that there are two distinct types of belt morphology. We ultimately must understand the reasons for these differing morphologies, and how they may be related to the orthogonal pattern of smaller deformational features that transects the plains. Perhaps the most important part of this process will be the examination of future Magellan data. These data for Lavinia will include additional SAR images at incidence angles that will allow stereographic determination of topography, along with high-resolution mapping of the planet's gravity field. Moreover, images of other deformation belts, particularly those in Atalanta Planitia, have only recently become available for detailed study. A systematic comparison of the deformation belts throughout Venus will provide a foundation for further modeling of belt formation and evolution.

REFERENCES

Anderson, E.M., The Dynamics of Faulting and Dyke Formation With Applications to Britain, 2nd ed., 206 pp., Oliver and Boyd, Edinburgh, 1951.

Banerdt, W. B., and M. P. Golombek, Deformational models of rifting and folding on Venus, J. Geophy. Res., 93, 4759-4772, 1988.
Barsukov, V. L. et al., The geology and geomorphology of the Venus surface as revealed by the radar images obtained by Veneras 15 and 16, Proc. Lunar Planet. Sci. 16th, Part 2, J. Geophys. Res., 91, Suppl., D378-D398, 1986.
Basilevsky, A.T., A.A. Pronin, L.B. Ronca, and V.P. Kryuchkov, Styles of tectonic deformation on Venus: Analysis of Venera 15 and 16 data, Proc. Lunar Planet. Sci. Conf., 16th, Part 2, J. Geophys. Res.91, Suppl., D399-D411, 1986.
Bills, B.G., W.S. Kiefer, and R.L. Jones, Venus gravity: A harmonic analysis, J. Geophys. Res., 10,335-10,351, 1987.
Bindschadler, D. L., and E. M. Parmentier, Mantle flow tectonics: The influence of a ductile lower crust and implications for the formation of topographic uplands on Venus, J. Geophys. Res., 95, 21,329-21,344, 1990.
Bindschadler, D.L., G. Schubert, and W.M. Kaula, Mantle flow tectonics and the origin of Ishtar Terra, Venus, Geophys. Res. Lett., 17, 1345-1348, 1990.
Biot, M. A., Theory of folding of stratified viscoelastic media, and its implications for tectonics and orogenesis, Bull. Geol. Soc. Am., 72, 1595-1620, 1961.
Brace, W. F., and D. L. Kohlstedt, Limits on lithospheric stress imposed by laboratory experiments, J. Geophy. Res., 85, 6248-6252, 1980.
Byerlee, J., Friction of rocks, Pure Appl. Geophys., 116, 615-626, 1978.
Campbell, D. B., J. W. Head, J. K. Harmon, and A. A. Hine, Venus: Identification of banded terrain in the mountains of Ishtar Terra, Science, 221, 644, 1983.
Caristan, Y., The transition from high temperature creep to fracture in Maryland diabase, J. Geophys. Res., 87, 6781-6790, 1982.
Crumpler, L.S., J. W. Head, and D. B. Campbell, Orogenic belts on Venus, Geology, 14, 1031-1034, 1986.
Golombek, M.P., Fault type predictions from stress distributions on planetary surfaces: Importance of fault initiation depth, J. Geophys. Res., 90, 3065-3074, 1985.
Kiefer, W. S., M.A. Richards, B.H. Hager, and B.G. Bills, A dynamic model of Venus's gravity field, Geophys. Res. Lett., 13, 14-17, 1986.
King, S. D., A. Raefsky, and B. H. Hager, ConMan: Vectorizing a finite element code for incompressible two-dimensional convection in the Earth's mantle, Phys. Earth Planet. Inter., 59, 195-207, 1990.
Kirby, S. H., Tectonic stresses in the lithosphere: Constraints provided by the experimental deformation of rocks, J. Geophys. Res., 85, 6353-6363, 1980.
McAdoo, D. C., and D. T. Sandwell, Folding of oceanic lithosphere, J. Geophys. Res., 90, 8563-8569, 1985.
Pettengill, G. H., P. G. Ford, W.T.K. Johnson, R. K. Raney, and L. A. Soderblom, Magellan: Radar performance and data products, Science, 252, 260-265, 1991.
Phillips, R.J., A mechanism for tectonic deformation on Venus, Geophys. Res. Lett., 13, 1141-1144, 1986.
Phillips, R. J., Convection-driven tectonics on Venus, J. Geophys. Res., 95, 1301-1316, 1990.
Phillips, R. J., R. E. Grimm, and M. C. Malin, Hot-spot evolution and the global tectonics of Venus, Science, 252, 651-658, 1991.
Plescia, J.B., and M.P. Golombek, Origin of planetary wrinkle ridges based on study of terrestrial analogs, Geol. Soc. Am. Bull, 97, 1289-1299, 1986.
Schmeling, H., and G. Marquart, A mechanism for crustal thinning without lateral extension, Geophys. Res. Lett., 17, 2417-2420, 1990.
Schultz, R.A., and M.T. Zuber, The paradox between predicted and observed occurrences of faults surrounding planetry surface loads (abstract), Eos Trans. AGU, 72, 285, 1991.
Simons, M., S.C. Solomon, and B.H. Hager, Dynamic models for ridge belt formation on Venus (abstract), Lunar Planet. Sci., 21, 1263-1264, 1991.
Smrekar, S.E., and R.J. Phillips, Venusian highlands: Geoid to topography ratios and their implications, Earth Planet. Sci. Lett., 107, 582-597, 1991.
Solomon, S.C., J.W. Head, W.M. Kaula, D. McKenzie, B. Parsons, R.J. Phillips, B. Parsons, G. Schubert, and M. Talwani,

Venus tectonics: Initial analysis from Magellan, *Science*, *252*, 297-312, 1991.

Solomon, S.C., et al., Venus tectonics: An overview of Magellan observations, *J. Geophys. Res.*, this issue.

Stofan, E.R., V.L. Sharpton, G. Schubert, G. Baer, D.L. Bind-schadler, D.M. Janes, and S.W. Squyres, Global distribution and characteristics of coronae and related features on Venus: Implications for origin and relation to mantle processes, *J. Geophys. Res.*, this issue.

Sukhanov, A.L., and A.A. Pronin, Ridged belts on Venus as extensional features, *Proc. Lunar Planet. Sci.*, *19th*, 335-348, 1989.

Turcotte, D. L., and G. Schubert, *Geodynamics, Applications of Continuum Physics to Geologic Problems*, 450 pp., John Wiley, New York, 1982.

Watters, T.R., Wrinkle ridge assemblages on the terrestrial planets, *J. Geophys. Res.*, *93*, 10,236-10,254, 1988.

Zuber, M. T., Constraints on the lithospheric structure of Venus from mechanical models and tectonic surface features, *Proc. Lunar Planet. Sci. Conf. 17th, Part 2, J. Geophys. Res.*, *92*, Suppl., E541-E551, 1987.

Zuber, M. T., Ridge belts: Evidence for regional- and large-scale deformation on the surface of Venus, *Geophys. Res. Lett.*, *17*, 1369-1372, 1990.

B.H. Hager, M. Simons, and S. C. Solomon, Department of Earth, Atmospheric, and Planetary Sciences, Massachusetts Institute of Technology, Cambridge, MA 02139.

D. G. Jankowski and S. W. Squyres, Center for Radiophysics and Space Research, Cornell University, Ithaca, NY 14853.

George E. McGill, Department of Geology and Geography, University of Massachusetts, Amherst, MA 01003.